XV ural international winter school on physics of semiconductors

The articles published in this issue pertain to material presented in lectures and reports at the XV Ural International Winter School on Physics of Semiconductors.

The tradition of holding winter schools on semiconductor physics in the Urals began in 1966. They were conducted by the staff of the Institute of Metal Physics of the Ural Division of the Russian Academy of Sciences with the participation of other academic institutes and the Ural University, and for more than 20 years were produced and directed by Acad. I. M. Tsidil'kovskiĭ (1928–2001). His approach to the selection of the main subject matter for the schools was to choose the most current research topics at the given time in the rapidly changing face of the physics of electronic phenomena in semiconductors. He encouraged the participation of a large number of lecturers and young people from research centers all over Russia and also Ukraine, Poland, and other countries.

The latest session of this school was held February 16–21, 2004 at Kyshtym in the Chelyabinsk Region. The program was devoted largely to research on low-dimensional electron systems in semiconductor heterostructures. In addition, considerable attention was devoted to semiconducting compounds doped with transition-element impurities, to the properties of systems possessing high-temperature superconductivity, and to structural aspects of the physics of semiconductor crystals. The participants included leading specialists in various fields, who presented over 20 invited lectures and reviews, authors of original research, and young scientists.

The articles published here reflect the main content of the program and in their nature and the character of the problems addressed fit the profile of the journal *Low Temperature Physics*. They may be divided thematically into three sections.

The first section contains papers devoted to the electronic properties of two-dimensional and layered structures. Among the main news in this area is the observation of giant quantum oscillations of the magnetoresistance of two-dimensional electron layers in a microwave field. A review of the research on this effect is given by Lyapilin and Patrakov. They set forth the main theoretical methods and approaches proposed for describing effects of this kind. In a separate, original paper they develop a possible interpretation of the effect. Research results on the electronic properties of low-dimensional structures created on the basis of different allotropic forms of carbon has also been attracting considerable interest of late. Results in this field are summarized in the review article by Kulbachinskii, who discusses the Shubnikov–de Haas effect, weak localization of current carriers, superconductivity, and a number of other phenomena characteristic of such structures. The papers by Yakunin *et al.*, Sheregii *et al.*, and Arapov *et al.* are devoted to problems of the physics of conduction and galvanomagnetic phenomena in two-dimensional electron layers of semiconductor heterostructures. A topical theoretical question related to this group of problems is to determine the character of the energy spectrum of the current carriers in double quantum wells, the solution of which is the subject of the paper by Alshanskii and Yakunin. The observation of novel optical effects arising as a result of the excitation of charged excitons—bound states of three current carriers—in heterostructures based on cadmium telluride is the subject of the paper by Gaj and co-workers. The paper by Dvurechensky, Nikiforov, Pchelyakov, Teys, and Yakimov is of considerable interest for those who study heterostructures; it deals with the technique for growing germanium- and silicon-based heterostructures by molecular beam epitaxy. Also in that section is the paper by Ponomarev and coauthors, basically devoted to the experimental aspects of the justification of the low-dimensional character of the conduction in crystals of compounds belonging to the class of high-T_c superconductors.

The papers in the second section of this issue pertain to the electronic properties of semiconductor crystals containing impurities of transition elements. New results of optical studies of a wide-gap compound (zinc selenide) containing chromium and iron impurities are presented in the paper by Godlewski and coauthors. Other papers are devoted to the effects of impurities on conduction and to galvanomagnetic phenomena. The paper by Nesmelova and coauthors is devoted to a detailed discussion of the large set of experimental data obtained on manganese donor impurities in mercury telluride. The resonance scattering of electrons with impurities is the subject of the paper by Okulov.

Some interesting new results in the physics of doped semiconductors have been obtained recently in the region of the low-temperature structural phase transitions. Such results are the presented in the papers published in the third section of this issue. The characteristic anomalies connected with the appearance of a phase transition in lead telluride containing gallium impurities are discussed by Khokhlov and coauthors on the basis of an analysis of impedance measurements. Gudkov and coauthors report the observation of features of the ultrasonic parameters, giving evidence of a low-temperature phase transition, in zinc selenide containing nickel impurities. Tikhomirova and Babushkin present material from studies of a structural phase transition in ammonium halides. Also in that section are papers by Robouch, Sheregii, and Kisiel and by Chukalina, Funke, and Dubrovskii, devoted to developing a theoretical interpretation of the experimental data on the structure of semiconductor crystals.

Altogether the contents of this special issue give an idea of the active research in a number of areas of semiconductor physics. It is hoped that the materials presented will be useful to the readers of *Low Temperature Physics*.

V. I. Okulov

LOW-DIMENSIONAL AND SUPERCONDUCTING SYSTEMS

Electronic properties and superconductivity of low-dimensional carbon structures

V. A. Kulbachinskiĭ*

M. V. Lomonosov Moscow State University, Department of Physics of Low Temperatures and Superconductivity, Moscow 119992, Russia
(Submitted May 20, 2004)
Fiz. Nizk. Temp. **30**, 1105–1114 (November 2004)

A review of research on the electronic properties of low-dimensional structures based on various modifications of carbon is presented. The following effects are discussed: the Shubnikov–de Haas effect in graphite intercalation compounds (GICs) of the acceptor type, superconductivity of GICs of the donor type, weak localization and superconductivity of carbon fibers, the negative magnetoresistance of a carbon foil obtained by pressing of exfoliated graphite, and the superconductivity and spectroscopy of new heterofullerides. © *2004 American Institute of Physics.* [DOI: 10.1063/1.1819856]

INTRODUCTION

In this article we discuss the electronic properties and superconductivity of various low-dimensional carbon structures such as graphite intercalation compounds (GICs), carbon fibers, foils pressed from exfoliated graphite, and fullerides.

In graphite and in GICs the sharp difference between the interaction energies between atoms belonging to the same layer and atoms of adjacent layers leads to high anisotropy of the physical properties. The graphite structure corresponds to hexagonal, perfectly planar layers. The carbon atoms in the layer are bound by strong covalent bonds, with a C–C distance between carbon atoms in the layer b_0 equal to 0.1415 nm. The distance between layers at room temperature is $d_0 = 0.33538$ nm.[1] The interaction between them is brought about by weak van der Waals forces. This crystal structure permits different atoms and molecules to be intercalated in the interplane space to form a new class of GICs in which the lattice consists of plane layers of carbon alternating with the intercalated substance, or intercalate. These compounds exhibit typically metallic properties, have a high electrical conductivity, and some of them are superconductors.[2,3] A great many GICs have now been synthesized and are under active investigation. GICs are used to make infrared polarizers, monochromators for low-energy neutrons, wavelength-tunable optical filters, electrochemical devices in optical displays, heat-shielding systems, etc.

GICs can be divided into two broad classes: donor and acceptor. The redistribution of the electron density between the intercalate molecules and the carbon atoms in a GIC of the acceptor type gives rise to an additional number of delocalized holes in the graphite layers. Acceptor compounds are formed in the intercalation of such substances as halogens, metal halides, and oxygen. Donor compounds are formed in the intercalation of alkali or alkaline-earth metals into a graphite host. Examples of donor compounds are C_4K, C_8Li, C_8Ca, C_4Hg, and others. Acceptor compounds are of more complex composition, e.g., $C_{16}Br_2$, $C_{20}FeCl_3$, $C_{16}ICl$, $C_{24}^+HSO_4^- \cdot 2H_2SO_4$, $C_{24}^+NO_3^- \cdot 3HNO_3$, and others.[4–7]

GICs in which the interlayer space is alternately filled with two different intercalates are also known. These are so-called heterocompounds, typical examples of which are GICs with $CuCl_2$ and ICl or $FeCl_3$ and ICl.[6,8] They expand even further the possibilities of obtaining new materials with a unique set of physicochemical characteristics.

The intercalation of acceptors entails a significant (by a factor of 2–3) increase in the distance between graphite layers, and the characteristic graphitic order of alternation of the layers can be disrupted. A distinctive feature of GICs is the possibility of inserting an intercalate only between every second or every third, etc., layer of graphite, creating GICs of different so-called stages. The number of stages N is equal to the number of graphite networks between nearest intercalate layers. The identity period I_c of a GIC is given by the formula

$$I_c = d_i + (N-1)d_0, \tag{1}$$

where N is the number of stages and d_i is the thickness of an intercalate layer.

The kinetics of intercalation is extraordinarily interesting. Initially a high-stage GIC forms, and then, by passage through mixtures of the different stages, GICs of lower and lower stages progressively form, ultimately reaching the first stage (if the given intercalate forms a stage-1 GIC). As an example, Fig. 1 shows the time dependence of the relative resistivity in the basal plane of a graphite single crystal during the *in situ* intercalation of sulfuric acid. Simultaneous x-ray diffraction studies showed that each minimum corresponds to the formation of a pure stage in the sequence from 5 to 1, after which the irreversible overoxidation of the graphite host occurs, and the resistivity increases severalfold.[9]

The electrical conductivity of GICs has a high anisotropy, $\eta = \sigma_a/\sigma_c$, which in pure graphite has the value 10^3–10^4; in GICs of the acceptor type it increases to 10^5–10^6 (Ref. 5).

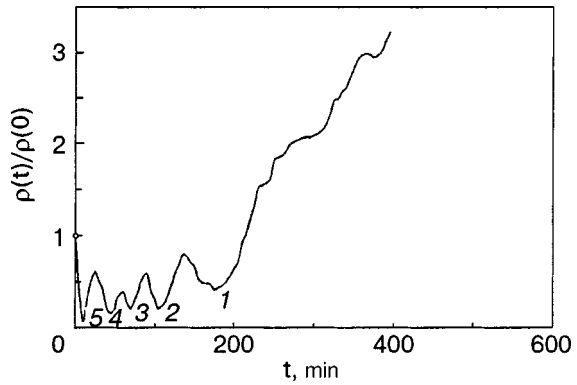

FIG. 1. Relative change in resistivity of a graphite sample during the intercalation of H_2SO_4. The minima are labeled by the number of the corresponding pure stage formed.

Fullerenes have attracted attention since their discovery by the English scientist Kroto and his co-workers in 1985.[10] They succeeded in synthesizing a number of new allotropic forms of carbon C_n (where n is an integer from 38 to 120), among which the C_{60} molecule turned out to be the most common and stable. It consists of 20 hexagons and 12 pentagons. The name *fullerene* is in honor of the architect Buckminster Fuller, who designed the dome of the United States Pavilion at the Montreal Exposition in 1967 in the form of conjoined pentagons and hexagons.

There was an extraordinary upsurge in interest in fullerenes in 1990, when a group of scientists led by Krätschmer and Hoffman[11] successfully synthesized solid fullerene in the form of microcrystals (which have been given the name *fullerites*). Usually the crystals have an fcc lattice, but an hcp lattice is also possible. In the crystal C_{60} molecules are bound by van der Waals forces. The intercalation of fullerene by alkali metal ions gives *fullerides* of composition A_3C_{60} (A=Li, Na, K, Rb, Cs).[12] Less than a year after Krätschmer and Hoffman's paper appeared, superconductivity with $T_c=18$ K was observed in the potassium fulleride.[13] The discovery of superconductivity in other fullerides soon followed. The highest superconducting transition temperature observed to date, $T_c=33$ K, was recorded in the compound $RbCs_2C_{60}$ (Ref. 14) and, under pressure, in Cs_3C_{60} ($T_c=40$ K).[15]

In this article we review the electronic properties and superconductivity of GICs, carbon fibers, foils, and novel heterofullerides.

PROPERTIES OF GRAPHITE INTERCALATION COMPOUNDS

Supermetallic conductivity

The high conductivity of GICs in the basal plane, σ_a, is determined by the composition of the intercalate, the grade of graphite, and the number of stages of the GIC. The most famous papers for the creation of GICs with supermetallic conduction are those of Vogel and coauthors.[16] The conductivity rises with increasing intercalate content, reaching the usual maximum for a stage-3 GIC, mainly for compounds with metal halide intercalates.[17] In the so-called heterointercalation compounds, i.e., GICs with alternating layers of different intercalates, even the stage-1 GICs have high metallic conductivity.[6,18] As an example, in Fig. 2a we show the conductivity in the basal plane, σ_a (left scale), and the hole density p (right scale) for GICs with intercalates of ICl and $CuCl_2$ and for the heteroGIC $C_{10}CuCl_2\cdot 0.6ICl$. It is clearly seen that the value of the conductivity is correlated with the hole density. Figure 2b shows the conductivity in the basal plane for GICs of stages 1–5 with a sulfuric acid intercalate.[19]

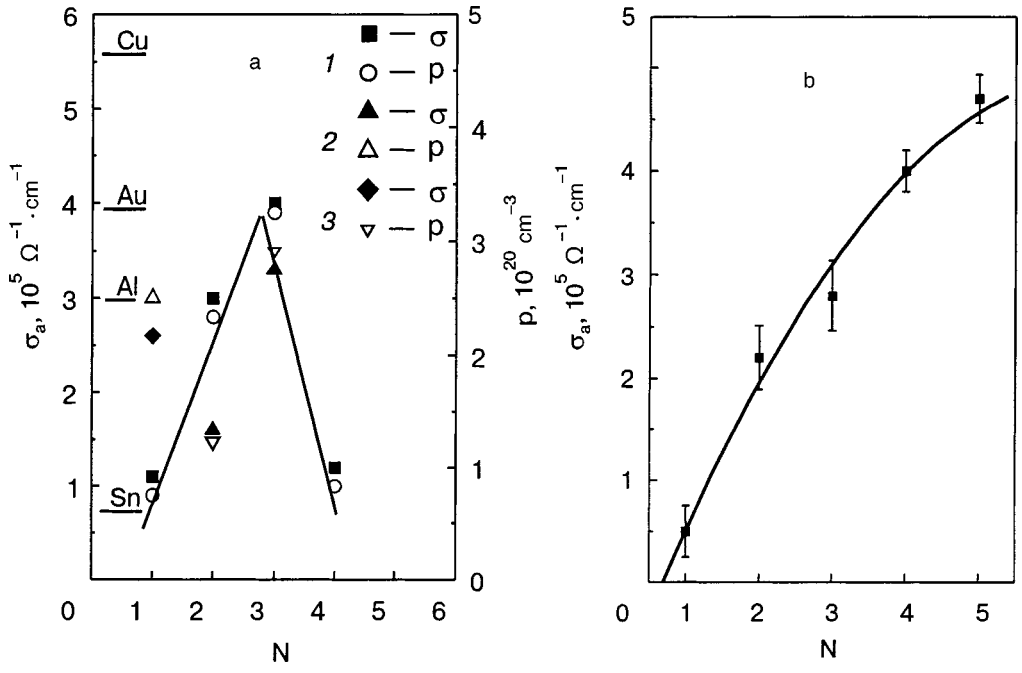

FIG. 2. Basal-plane conductivity σ_a and hole density p at room temperature versus the stage number N: for the GICs $C_{8N}ICl$ (*1*) and $C_{5N}CuCl_2$ (*2*) and for the heteroGIC $C_{10}CuCl_2\cdot 0.6ICl$ (*3*). The conductivities of several metals are shown for comparison (a). The conductivity of the H_2SO_4 GIC (b).

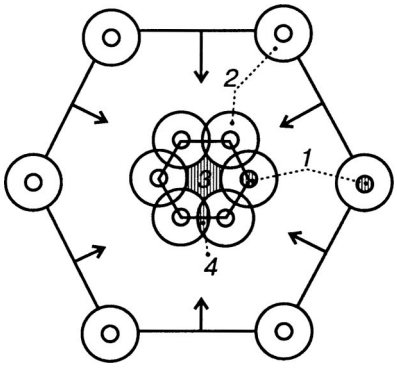

FIG. 3. Cross section of the hexagonal Brillouin zone of a GIC with two initial coaxial cylindrical Fermi surfaces along the edges *1* and *2*. The arrows indicate the decrease in size of the Brillouin zone when an intercalate superlattice commensurate with the graphite lattice appears.

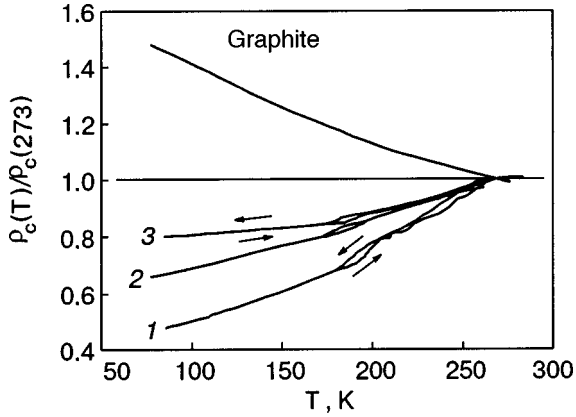

FIG. 4. Relative change in the resistivity along the *C* axis in graphite and in sulfuric acid GICs of stages 1–3. The curves are labeled by the number of the stage.

Phase transitions of the "order–disorder" type

When the temperature is lowered below the temperature of synthesis of the GIC there is a transition of the intercalate from the liquid phase to a crystalline or amorphous phase. At the transition temperature T_c a superlattice commensurate or incommensurate with the graphite lattice can appear. Such superlattices have been observed in GICs with H_2SO_4 (Ref. 20), with AsF_5 (Ref. 21), and with $SbCl_5$ (Refs. 22–25). In the GIC with H_2SO_4 the sulfuric acid anions form a hexagonal superlattice that is commensurate with the graphite lattice but with a greater period. Here the initial hexagonal Brillouin zone of the GIC decreases proportionally, as is shown in Fig. 3. In the initial Brillouin zone the Fermi surfaces are coaxial cylinders located at the edges (they are denoted *1* and *2* in Fig. 3). When a commensurate superlattice of the intercalate appears, the Brillouin zone contracts proportionally (zone folding effect). Then in the new zone the sections labeled *3* and *4* appear, giving rise to new frequencies in the oscillations of the magnetoresistance, although new groups of current carriers do not appear. This follows from a comparison of the data on the Hall effect and the Shubnikov–de Haas effect.

The phase transition can be observed by different methods (e.g., NMR), but the simplest way is to measure the resistivity perpendicular to the layers (along the C axis), ρ_C, which undergoes a jump at the phase transition.[26] As an example, in Fig. 4 we show the temperature dependence of the relative change in the resistivity along the *C* axis (perpendicular to the layers) in sulfuric acid GICs of different stages, and, for comparison, the curve for graphite. The transition temperature depends on the stage (in the given case of an H_2SO_4 GIC we have $T_c \approx 187$ K for the first stage, $T_c \approx 180$ K for the second stage, and $T_c \approx 178$ K for the third. Analogous transitions are observed in nitric acid GICs.[27]

Shubnikov–de Haas effect in GICs

High-quality GIC crystals exhibit quantum oscillations of the magnetoresistance—the Shubnikov–de Haas (SdH) effect.[7,28] Many GICs of the acceptor type have a cylindrical Fermi surface, which corresponds to a purely two-dimensional character of the energy spectrum. As an example, in Fig. 5a we show the SdH effect at liquid helium temperatures for samples of HNO_3 GICs of stages 1–4. The Fourier spectra of the oscillations are shown in Fig. 5b. The

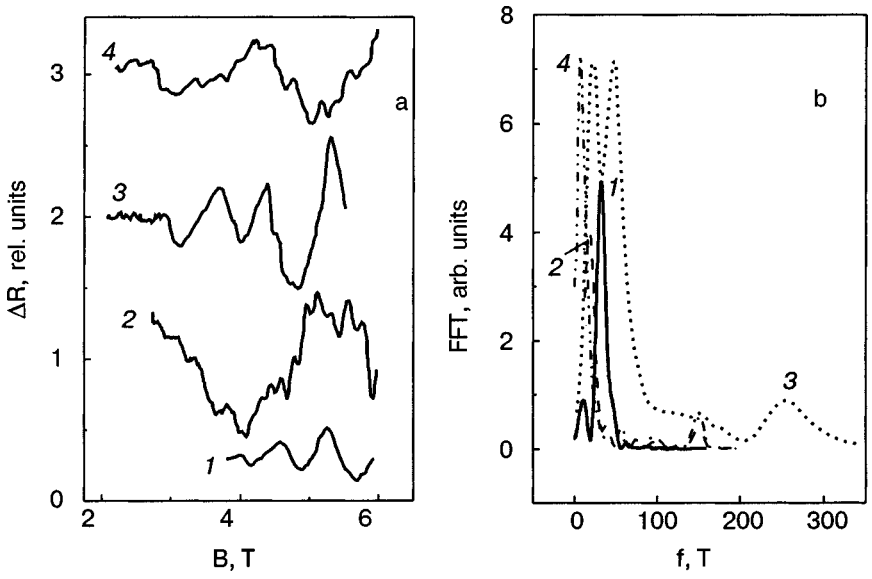

FIG. 5. Shubnikov–de Haas oscillations of nitric acid GICs of stages 1–4 (a) and their Fourier spectra (b). The curves are labeled by the stage number.

TABLE I. Parameters of nitric acid GICs.

HNO_3, %	Synthesis time, h	I_c, nm	P_{osc}, 10^{21} cm^{-3}	S^1_{extr}, 10^{13} cm^{-2}	S^2_{extr}, 10^{13} cm^{-2}	S^3_{extr}, 10^{13} cm^{-2}
98	1	0.798	0.04	2.99	–	–
98	0.5	1.121	0.16	3.40	14.30	–
85	1	1.456	0.21	2.40	4.30	23.80
83	1.5	1.807	0.08	0.57	14.30	–

Fourier spectrum has one oscillation frequency in a first-stage, two in a second-stage, and three in a third-stage GIC. The Fourier spectrum of a fourth-stage GIC has a frequency corresponding to pure graphite and a high frequency. From the frequencies of the quantum oscillations of the transverse magnetoresistance one determines the extremal sections S_{extr} of the Fermi surface and the density of current carriers, P_{osc}. If it is assumed that the Fermi surface consists of smooth cylinders, the carrier density P_{osc} can be determined from the formula

$$P_{osc}=\frac{4\sum S^k_{extr}}{(2\pi\hbar)^2[d_i+(N-1)d_0]}. \tag{2}$$

The factor of 4 in expression (2) takes into account the Pauli principle and the fact that in a GIC, two cylinders of the Fermi surface, with cross sections S^k_{extr}, fall within each band of index k (the summation is over the several filled bands). Some parameters of nitric acid GICs are presented in Table I.

Energy spectrum of GICs

In 1980 Blinovskii and Rigo proposed a model of the energy spectrum of low-stage GICs of the acceptor type.[29–31] In the framework of that model a stage-1 GIC is treated as a system of equivalent noninteracting graphite layers, i.e., the system is purely two-dimensional. The dispersion relation for a stage-1 GIC of the acceptor type has the form

$$E_{c,v}=\pm\frac{3}{2}\gamma_0 b_0 k, \tag{3}$$

where γ_0 is a parameter describing the interaction of nearest-neighbor carbon atoms in the layer.

For second-stage GICs, in the subsystem of two graphite layers one considers only the interaction between neighboring carbon atoms in the basal plane (the parameter γ_0) and between nearest atoms in adjacent planes (described by the parameter γ_1). The dispersion relation for the valence band and conduction band are written

$$E_1\cong -E_{V_1}=E_{C_1}=\frac{1}{2}\{-\gamma_1+[\gamma_1^2+9\gamma_0^2b_0^2k^2]^{1/2}\}, \tag{4}$$

$$E_2\cong -E_{V_2}=E_{C_2}=\frac{1}{2}\{\gamma_1+[\gamma_1^2+9\gamma_0^2b_0^2k^2]^{1/2}\}. \tag{5}$$

For third-stage GICs the graphite layers are no longer equivalent with respect to to the intercalate, and a parameter δ, characterizing the difference in the potential energy of the carbon atoms of the outer and inner layers, appears in the calculations. For a stage-3 GIC the energy spectrum consists of six branches:

$$E_1^{c,v}=\delta\pm|x|, \tag{6}$$

$$E_2^{c,v}=\pm\{\delta^2+\gamma_1^2+|x|^2-[\gamma_1^4+(4\delta^2+2\gamma_1^2)|x|^2]^{1/2}\}^{1/2}, \tag{7}$$

$$E_3^{c,v}=\pm\{\delta^2+\gamma_1^2+|x|^2+[\gamma_1^4+(4\delta^2+2\gamma_1^2)|x|^2]^{1/2}\}^{1/2}, \tag{8}$$

where $|x|=3\gamma_0 b_0 k$; δ is a parameter that depends on the distribution of excess charge between the inner and outer layers of graphite. Three of the branches of the energy spectrum lie in the conduction band, and three in the valence band. From a comparison of the experimental and theoretical data on optical reflection in GICs it has been established that $\delta\approx 0.2$ eV. At that value of the parameter δ an excess charge of approximately $z=0.15$ is redistributed to the inner graphite layer. A uniform distribution of charge between the three graphite layers would correspond to $z=1/3$. We note that in the case of complete screening of the inner graphite layer a frequency corresponding to pure graphite should appear in the SdH oscillations of a stage-3 GIC.

The Blinovskii–Rigo model is of course a simplification, but it gives a rather good description of the optical reflection data for low-stage GICs of the acceptor type. In that model the Fermi surface of a first-stage ($N=1$) GIC of the acceptor type consists of two smooth cylinders lying along the edges of the hexagonal Brillouin zone (it is usually depicted as 6 cylinders, along all of the axes, so that the total volume of the Fermi surface for each zone is $6/3=2$). The Fermi surface of a stage-2 GIC in the case of strong acceptors consists of coaxial cylinders (two in each zone), and for a stage-3 GIC, in the case of a large Fermi energy, the number of coaxial cylinders can be equal to three, i.e., if three bands are filled (there are 6 cylinders in all). The experimental data on the SdH effect in nitric acid GICs correspond well to the spectrum (3)–(8): in a stage-1 GIC there is one hole band (one oscillation frequency is observed), in a stage-2 GIC two hole bands are filled (two frequencies are observed), and in a stage-3 GIC, three hole bands (3 oscillation frequencies) (see Fig. 5). Using formulas (3)–(8) and the experimental values of the cross section of the Fermi surface for a stage-1 GIC (see Table I), one can calculate the value of the Fermi energy E_F. For stage 1 a Fermi energy $E_F=0.21$ eV is obtained; for stage 2, $E_F=0.42$ eV; for stage three, $E_F=0.75$ eV.

Experimentally, however, in a number of GICs, even of the first stage, a Fermi surface in the form of corrugated cylinders is observed.[6] This means that the structure cannot be considered purely two-dimensional. For such GICs the energy spectrum should include dispersion with respect to the third direction. Such a spectrum has the form[6,32]

$$E_{1,2}=\pm\gamma_1^*\cos\Phi-\sqrt{\gamma_1^{*2}\cos^2\Phi+\eta^2k^2}, \tag{9}$$

where $\Phi = k_z I_c/2$, $\eta = \sqrt{3} a \gamma_0^*/2$. The parameter γ_1^* describes the interaction of conducting graphite layers in a GIC and determines the three-dimensionality of the spectrum. The Fermi surface in the case of such a spectrum will be two coaxial corrugated cylinders with the following cross sections at $k_z = 0$:

$$S_{1,2}^k = \frac{\pi |E_F| (|E_F| \pm 2\gamma_1)}{\eta^2}. \tag{10}$$

Donor GICs

Donor GICs are formed in the intercalation of alkali metals into graphite. In 1965 a group of scientists led by Hannay discovered superconductivity of KC_8, RbC_8, and CsC_8 GICs at ultralow temperatures.[33] A review of the superconducting properties of donor GICs can be found in the monograph cited as Ref. 3. We note that in a magnetic field parallel to the C axis (perpendicular to the layers) those GICs have properties corresponding to type-I superconductors, while in a magnetic field in the plane of the layer they are type-II superconductors. The highest transition temperature $T_c = 0.55$ K has been observed in the stage-1 GIC C_8K. Subsequently, in ultradense stage-1 GICs (i.e., those with significantly more potassium ions per carbon atom than in C_8K) synthesized under pressure, the value of T_c has been raised substantially, e.g., to 1.5 K in C_6K (Ref. 34) and to $T_c \approx 4.2$ K in C_4K (Ref. 35). In amalgams of thallium and in superconducting bismuth GICs of composition $C_{4n}MTl_{1.5}$ ($n = 1, 2$; M = K, Rb) T_c lies in the interval from 0.7 to 4 K. For example, $T_c = 2.56$ for $C_4KTl_{1.5}$ and $T_c = 4.05$ for $C_4CsBi_{1.5}$ (Ref. 3).

ELECTRICAL PROPERTIES OF CARBON FIBERS AND FOILS

Weak localization of current carriers in a carbon foil

Disordered carbon materials are excellent objects for studying transport and magnetotransport at low temperatures. Such objects include carbon foil obtained by pressing of exfoliated graphite.[36] First the graphite is intercalated by sulfuric acid, for example. Then a thermal shock is created—rapid heating to 900 °C—whereupon exfoliation of the GIC occurs, the volume increasing by tens of times. Then by pressing one can create a foil whose properties will depend on the oxidation time of the graphite by the sulfuric acid, the subsequent heat treatment, and other controllable factors. Such a foil has interesting galvanomagnetic properties. Low-temperature growth of the resistivity, which is characteristic of weak localization, and negative magnetoresistance in low magnetic fields are observed. As an example, Fig. 6 shows curves of the magnetoresistance at different temperatures for a carbon foil obtained by pressing of exfoliated graphite. The negative magnetoresistance in the majority of cases is described quantitatively by either the original theory of quantum corrections to the conductivity[37,38] or by a modified theory extended beyond the diffusion limit.[39] In the latter case the change of the conductivity in a magnetic field can be described by the function

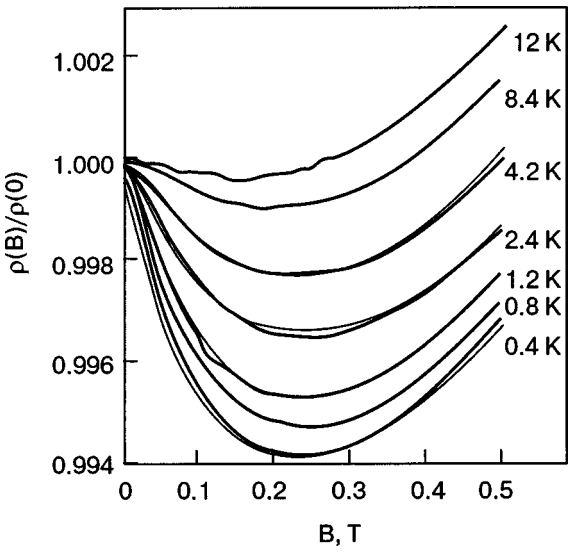

FIG. 6. Relative magnetoresistivity of a carbon foil at different temperatures. The curves drawn with a fine line show a fit according to formula (11).

$$\Delta\sigma(B) = -\frac{e^2}{2\pi^2\hbar} \frac{b}{(1+\gamma)^2} \sum_{n=0}^{\infty} \frac{\psi_n^3(b)}{1+\gamma-\psi_n(b)}, \tag{11}$$

where $b = 2el^2B/(1+\gamma)^2\hbar$, and $\psi_n(b)$ are the Laguerre polynomials:

$$\psi_n(b) = \int_0^{\infty} \exp(-(x + bx^2/4)) L_n(bx^2/2)\, dx. \tag{12}$$

The curves of the Whitman and Schmidt theoretical dependence [formula (11)] conform well to the experimental data[40] (the fine lines in Fig. 6), making it possible to obtain the temperature dependence of the main parameter of the theory—the dephasing time τ_φ of the wave function of the current carriers (Fig. 7).

Carbon fibers

There is still another type of carbon material in which weak localization of the current carriers is observed—carbon fibers.[41–43] Since the structure inherent to graphite is preserved in the fibers, weak localization corresponds to a two-dimensional character of the conduction. Figure 8 shows the temperature dependence of the resistance of two types of

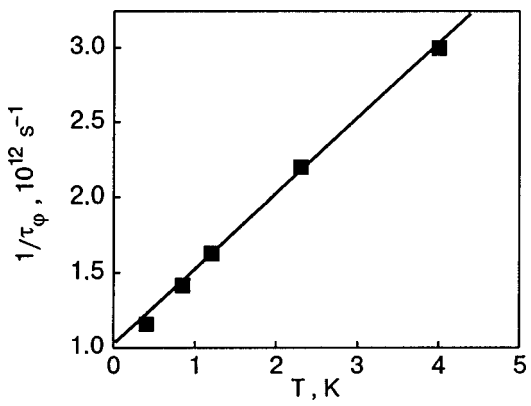

FIG. 7. Temperature dependence of the dephasing time of the wave function of the current carriers.

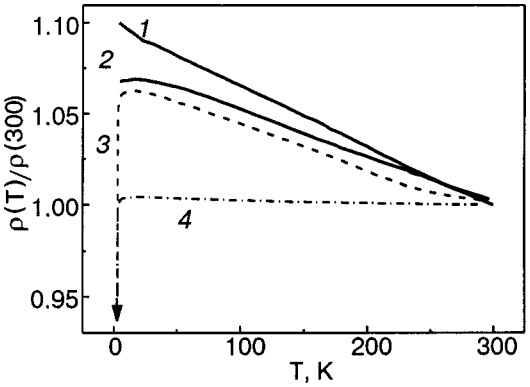

FIG. 8. Temperature dependence of the relative change of the resistivity of single carbon fibers obtained from viscose (*1,3*) and coal tar (*2,4*) in the initial state (*1,2*) and after intercalation and heat treatment (*3,4*).

fibers (obtained from viscose and coal tar). The resistance increases as the temperature is lowered, as is characteristic of weak localization (curves *1* and *2*). These isolated fibers were intercalated and heat treated, after which the localized growth of the resistivity on decreasing temperature persisted, but around 4 K the fibers underwent a transition to the superconducting state (see Fig. 8, curves *3,4*).[44–46]

ELECTRONIC AND SUPERCONDUCTING PROPERTIES OF FULLERIDES

Superconductivity of heterofullerides

Recently a method has been developed for synthesizing heterofullerides of the Fe and Cu groups with the composition K_2MC_{60} (Refs. 47 and 48). Some of them exhibit superconducting properties.[49] For example, Fig. 9 shows the temperature dependence of the magnetic susceptibility χ for fullerides with M=Fe, Ni, Cu. Also shown in Fig. 9 is the $\chi(T)$ curve for the well-known superconductor K_3C_{60}, which was synthesized simultaneously for purposes of comparison.

It follows from the studies done that fullerides of composition K_2MC_{60} (M=Ag, Cu, Co) and $KM_2^{2+}C_{60}$ (M =Co, Ni, Fe) are not superconductors. Fullerides of composition K_2CoC_{60}, and KCo_2C_{60} exhibited a paramagnetic signal on cooling to 4.2 K.

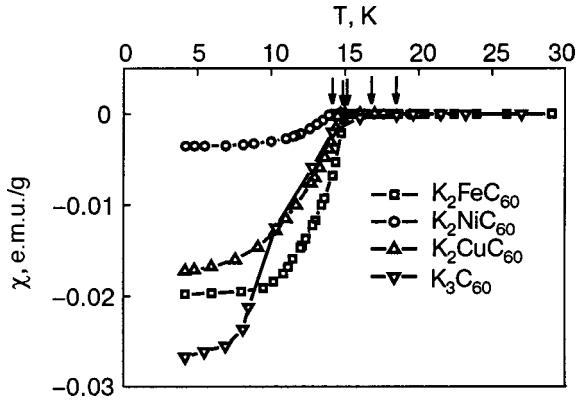

FIG. 9. Temperature dependence of the magnetic susceptibility χ of fullerides of composition K_2MC_{60} (M=Fe, Ni, Cu) and, for comparison, K_3C_{60}.

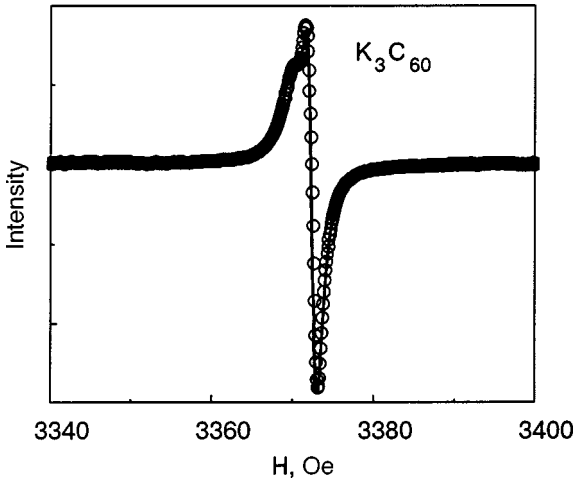

FIG. 10. EPR spectrum of K_3C_{60} at a temperature of 15 K.

Superconducting heterofullerides of composition K_2MC_{60} have lower superconducting transition temperatures T_c than K_3Co_{60}, and the crystal lattice constant a of the heterofullerides studied is smaller than that of K_3C_{60}, apparently because substitution of the potassium ion by an ion of smaller diameter decreases the lattice constant. Thus there is a correlation between the superconducting transition temperature and the crystal lattice constant: a decrease of a leads to a decrease of T_c.

Electron paramagnetic resonance

Figure 10 shows the typical EPR spectrum of this fulleride, measured in K_3C_{60} at 15 K.[50] The asymmetric signal has two components, which are well approximated by Lorentzian lines (solid curve). The two components are due to conduction electrons in the anions C_{60}^{3-}, C_{60}^{3-}–O–C_{60}^{3-}, and others. Figure 11 shows the EPR spectra of K_2NiC_{60} and K_2CoC_{60} at various temperatures. A characteristic feature of these EPR spectra is that the amplitude of the resonance increases with decreasing temperature. Interestingly, the g factors of the heterofullerides K_2NiC_{60} and K_2CoC_{60} at temperatures of 20 K and below (where the signal is clearly seen) are equal to 1.9996 ± 0.0003 and 1.9986 ± 0.0003, respectively. The g factor of the heterofulleride $K_2Fe^{3+}C_{60}$ at these same temperatures is 1.9965 ± 0.0001. These values are somewhat smaller than the g factors of K_3C_{60}. The two lines in the ER spectrum of K_3C_{60} gives values of 2.001 and 2 for the g factors of the wide and narrow lines, respectively.

For $T<T_c$ one observes fluctuations of the background signal, while these fluctuations are absent at temperatures above T_c. It is seen in Fig. 11 that fluctuations of the background signal are also observed in K_2CoC_{60} at temperatures of 3 and 6 K, although superconductivity is not observed in that fulleride.

Raman scattering spectra

The Raman scattering spectra of the fullerides K_2MC_{60} (M=Fe, Ni, Co) are shown in Fig. 12, together with the spectrum of K_3C_{60} for comparison. It has been found[51] that of the ten lines that are characteristic for the spectrum of the pure fullerite [standard notation $A_g(1,2)$ and $H_g(1-8)$], the

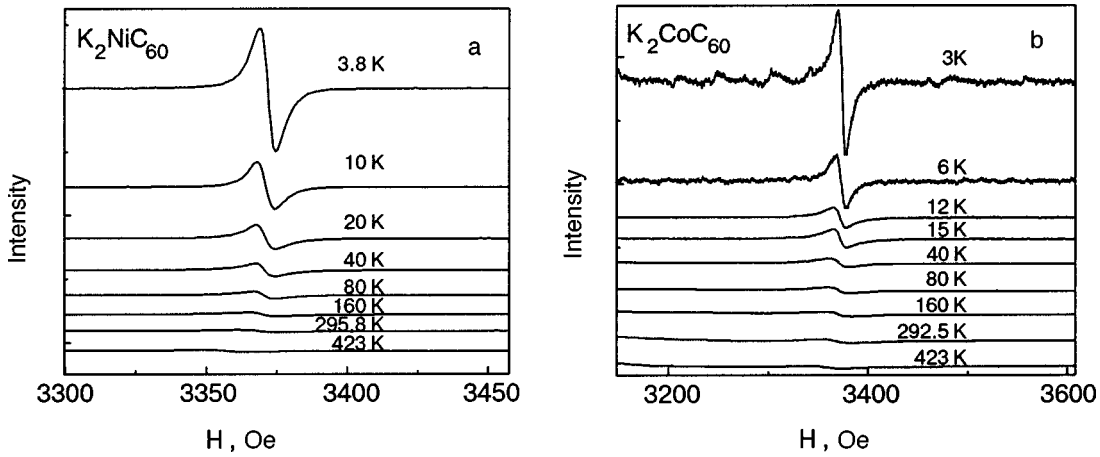

FIG. 11. Temperature dependence of the EPR signal from K_2NiC_{60} (a) and K_2CoC_{60} (b).

modes $H_g(5,6,7)$ are missing in the spectrum of K_3C_{60}. In addition, the lines $H_g(2,4,8)$ and $A_g(1,2)$ are shifted relative to their positions in the spectrum of pure fullerite C_{60}. The lines $H_g(1)$ and $H_g(3)$ do not change position. Characteristically, all of the shifts are in the direction of smaller wave number. This attests to a lowering of the energy of certain phonon modes upon intercalation of metal atoms in fullerite. Of the seven phonon modes observed in the spectrum of K_3C_{60}, there are actually only three intense lines in the heterofullerides: $A_g(1, 2)$ and $H_g(1)$ (see Fig. 12). These lines are present in the spectra of all heterofullerides of composition K_2MC_{60} ($M=Fe^{2+}$, Fe^{3+}, Ni, Co). The other four lines are much less intense than $A_g(1, 2)$ and $H_g(1)$. The position of almost all the lines in the spectra of the heterofullerides corresponds to the position of those lines in the spectrum of K_3C_{60}. A difference is observed in the position of $A_g(2)$ and $H_g(2)$. For example, in the spectra of K_2MC_{60} with $M=Fe^{2+}$, Fe^{3+} and of K_3C_{60} the line $H_g(2)$ has a wave number of $430\ cm^{-1}$, while in the spectrum of K_2MC_{60} with M=Ni, Co this line is shifted leftward to $415\ cm^{-1}$. From the position of the line $A_g(2)$ in the fullerides one can assess the charge state of the C_{60} molecule.

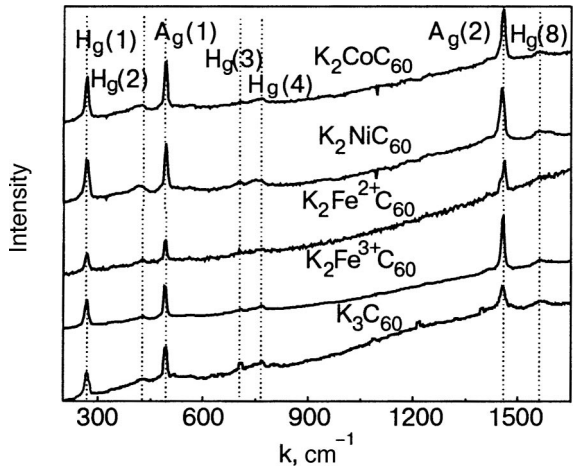

FIG. 12. Raman scattering spectra of fullerides of composition K_2MC_{60} (M=Fe, Ni, Co) and K_3C_{60}. The dotted lines indicate the positions of the peaks of the main phonon modes.

A shift of the line $A_g(2)$ is observed not only in the spectrum of $K_2Fe^{2+}C_{60}$ but also in K_2NiC_{60}. In the latter fulleride the $A_g(2)$ line is shifted by about $3\ cm^{-1}$ to smaller wave number. This indicates that the charge of the C_{60} molecule in this fulleride is nearly one electron charge higher than in K_3C_{60}.

CONCLUSION

In summary, graphite intercalation compounds are low-dimensional conducting materials that can be classified as synthetic metals. Some of them, like the fulleride allotropic forms of carbon, exhibit superconductivity. Carbon foils and fibers are also extraordinarily interesting objects of study. Suitably treated, they exhibit weak localization effects and superconductivity. The synthesis of new allotropic forms of carbon, e.g., carbon nanotubes, the properties of which could not be discussed in this review article, and the recently discovered superconductivity of diamond[52] hold great promise for research on graphite-based materials.

*E-mail: kulb@mig.phys.msu.ru

[1] R. E. Franklin, Acta Crystallogr. **3**, 253 (1951).
[2] S. V. Shulepov, *Physics of Carbon-Graphite Materials* [in Russian], Metallurgiya, Moscow (1972).
[3] H. Zabel and S. A. Solin (eds.), *Graphite Intercalation Compounds II*, Vol. 18 of Springer Series in Materials Science, Springer–Verlag Berlin, Heidelberg (1992).
[4] A. Herold, NATO ASI Ser., Ser. B **172**, 3 (1987).
[5] M. S. Dresselhaus, in *Theoretical Aspects and New Developments in Magneto-Optics*, NATO ASI Ser. B **16**, 102 (1980).
[6] V. V. Avdeev, V. Ya. Akim, N. B. Brandt, V. N. Davydov, V. A. Kulbachinskii, and S. G. Ionov, Zh. Eksp. Teor. Fiz. **94**, 188 (1988) [Sov. Phys. JETP **67**, 2496 (1988)].
[7] V. A. Kulbachinskiĭ, N. E. Sorokina, S. V. Kuvshinnikov, and S. G. Ionov, Fiz. Tverd. Tela (St. Petersburg) **45**, 2161 (2003) [Phys. Solid State **45**, 2264 (2003)].
[8] V. A. Kulbachinskii, S. G. Ionov, S. A. Lapin, and V. V. Avdeev, J. Phys. (France) **2**, 1941 (1992).
[9] S. A. Lapin, *Energy Spectrum, Transport Properties, and Localization of Current Carriers in Graphite Intercalation Compounds of the Acceptor Type* [in Russian], Candidate's Dissertation, M. V. Lomonosova Moscow State University, Moscow (2000).
[10] H. W. Kroto, J. R. Heath, S. C. O'Brien, R. F. Curl, and R. E. Smalley, Nature (London) **318**, 162 (1985).

[11] W. Krätschmer, L. D. Lamb, K. Fostiropoulos, and D. R. Hoffman, Nature (London) **347**, 354 (1990).
[12] R. C. Haddon, A. F. Hebard, M. J. Rosseinsky, D. W. Murphy, S. J. Duclos, K. B. Lyons, B. Miller, J. M. Rosamilia, R. M. Fleming, A. R. Kortan, S. H. Glarum, A. V. Makhija, A. J. Muller, R. H. Eick, S. M. Zahurak, R. Tycko, G. Dabbagh, and F. A. Thiel, Nature (London) **350**, 320 (1991).
[13] A. F. Hebard, M. J. Rosseinsky, R. C. Haddon, D. W. Murphy, S. H. Glarum, T. T. M. Palstra, A. P. Ramirez, and A. R. Kortan, Nature (London) **350**, 600 (1991).
[14] K. Tanigaki, I. Hirosawa, T. W. Ebbesen, J. Mizuki, K. Shimakawa, Y. Kubo, J. S. Tsai, and S. Kuroshima, Nature (London) **356**, 419 (1991).
[15] T. T. M. Palstra, O. Zhou, Y. Iwasa, P. E. Sulewski, R. M. Fleming, and B. R. Zegarski, Solid State Commun. **93**, 327 (1995).
[16] See, for example, F. L. Vogel, Carbon **17**, 255 (1979).
[17] N. B. Brandt, V. A. Kul'bachinskii, O. M. Nikitina, V. V. Avdeev, V. Ya. Akim, and S. G. Ionov, Pis'ma Zh. Tekh. Fiz. **13**, 302 (1987) [Sov. Tech. Phys. Lett. **13**, 388 (1987)].
[18] N. B. Brandt, V. A. Kul'bachinskii, O. M. Nikitina, V. V. Avdeev, V. Ya. Akim, S. G. Ionov, and K. N. Semenenko, Fiz. Nizk. Temp. **13**, 1213 (1987) [Sov. J. Low Temp. Phys. **13**, 685 (1987)].
[19] V. A. Kul'bachinskiĭ, S. A. Lapin, N. E. Fadeeva, I. V. Nikol'skaya, and V. V. Avdeev, Vest. Mosk. Un-ta, Ser. 2, Khimiya **31**, 37 (1990).
[20] N. B. Brandt, V. A. Kul'bachinskiĭ, S. A. Lapin, V. V. Avdeev, I. V. Nikol'skaya, and N. E. Fadeeva, Fiz. Tverd. Tela (Leningrad) **32**, 94 (1990) [Sov. Phys. Solid State **32**, 51 (1990)].
[21] E. McRae, J. F. Mareche, M. Levaurain, G. Furdin, and A. Herold, J. Phys. Chem. Solidi **38**, 957 (1987).
[22] Y. Yoshida and S. Tanuma, J. Phys. Soc. Jpn. **54**, 702 (1985).
[23] H. Zaleski, P. K. Ummat, and W. R. Datars, Phys. Rev. **35**, 2958 (1987).
[24] R. Clarke, M. Elzinga, J. N. Gray, H. Homma, D. T. Morelli, M. J. Winokur, and C. Uher, Phys. Rev. **26**, 5250 (1982).
[25] H. Homme and R. Clarke, Phys. Rev. **31**, 5865 (1985).
[26] V. V. Avdeev, N. B. Brandt, S. G. Ionov, S. V. Kuvshinnikov, V. A. Mukhanov, and K. N. Semenenko, Izv. Akad. Nauk SSSR, Neorg. Mater. **21**, 1219 (1985).
[27] A. R. Ubbelohde, Proc. R. Soc. London, Ser. A **304**, 72 (1968).
[28] V. A. Kulbachinskii, S. G. Ionov, S. A. Lapin, and A. de Visser, Phys. Rev. B **51**, 10313 (1995).
[29] J. Blinowski, Nguyen Hy Hay, C. Rigaux, J. P. Vieren, R. Le Toullec, G. Furdin, A. Herold, and J. Melin, J. Phys. **41**, 47 (1980).
[30] J. Blinowski and C. Rigaux, J. Phys. **41**, 667 (1980).
[31] Nguyen Hy Hay, J. Blinowski, C. Rigaux, and R. Letoullec, Synth. Met. **3**, 99 (1981).
[32] V. Ya. Akim, V. N. Davydov, V. A. Kul'bachinskiĭ, and O. M. Nikitina, JETP Lett. **45**, 724 (1987).
[33] N. B. Hannay, T. H. Geballe, B. T. Matthias, K. Andres, P. Schmidt, and D. MacNair, Phys. Rev. Lett. **14**, 225 (1965).
[34] V. V. Avdeev, O. V. Zharikov, V. A. Nalimova, A. V. Pal'nichenko, and K. N. Semenenko, Zh. Éksp. Teor. Fiz. **92**, 1423 (1987) [Sov. Phys. JETP **65**, 800 (1987)].
[35] V. V. Avdeev, O. V. Zharikov, V. A. Nalimova, A. V. Pal'nichenko, and K. N. Semenenko, JETP Lett. **43**, 484 (1986).
[36] V. A. Kulbachinskii, S. G. Ionov, V. V. Avdeev, N. B. Brandt, S. A. Lapin, A. G. Mandrea, I. V. Kuzmin, and A. de Visser, J. Phys. Chem. Solids **57**, 893 (1996).
[37] B. L. Altshuler and A. G. Aronov, in *Modern Problems in Condensed Matter Sciences*, Vol. 10, A. L. Efros and M. Pollak (eds.), North-Holland, Amsterdam (1985).
[38] P. A. Lee and T. V. Ramakrishnan, Rev. Mod. Phys. **57**, 287 (1985).
[39] H. P. Wittmann and A. Schmid, J. Low Temp. Phys. **69**, 131 (1987).
[40] R. T. F. van Schaijk, A. de Visser, S. G. Ionov, V. A. Kulbachinskii, and V. G. Kytin, Phys. Rev. B **57**, 8900 (1998).
[41] L. Piraux, J.-P. Issi, J.-P. Michenaud, E. McRae, and J. F. Mareche, Solid State Commun. **56**, 567 (1985).
[42] N. B. Brandt, V. A. Kul'bachinskiĭ, O. M. Nikitina, and S. M. Chudinov, Fiz. Nizk. Temp. **12**, 1115 (1986) [Sov. J. Low Temp. Phys. **12**, 630 (1986)].
[43] N. B. Brandt, V. A. Kul'bachinskiĭ, O. M. Nikitina, and S. M. Chudinov, Fiz. Tverd. Tela (Leningrad) **29**, 263 (1986) [Sov. Phys. Solid State **29**, 151 (1986)].
[44] N. B. Brandt and V. A. Kul'bachinskiĭ, Pis'ma Zh. Tekh. Fiz. **14**, 1687 (1988) [Sov. Tech. Phys. Lett. **14**, 734 (1988)].
[45] V. A. Kulbachinskii, Phys. Status Solidi **151**, 1687 (1988).
[46] V. A. Kulbachinskii, Synth. Met. **41–43**, 2697 (1991).
[47] B. M. Bulychev, A. A. Dityat'ev, S. G. Ionov, V. A. Kulbachinskii, V. G. Kytin, and V. N. Bezmelnitsin, Mol. Cryst. Liq. Cryst. **310**, 149 (1998).
[48] B. M. Bulychev, V. I. Privalov, and A. A. Dityat'ev, Russ. J. Inorg. Chem. **45**, 931 (2000).
[49] B. M. Bulychev, R. A. Lunin, A. V. Krechetov, V. A. Kulbachinskii, V. G. Kytin, K. V. Poholok, K. Lips, and J. Rappich, J. Phys. Chem. Solids **65**, 337 (2004).
[50] J. Robert, P. Petit, T. Yildirim, and J. E. Fischer, Phys. Rev. B **57**, 1226 (1998).
[51] P. Zhou, K. A. Wang, P. C. Eklund, G. Dresselhaus, and M. S. Dresselhaus, Phys. Rev. B **48**, 8412 (1993).
[52] E. A. Ekimov, V. A. Sidorov, E. D. Bauer, N. N. Mel'nik, N. J. Curro, J. D. Thompson, and S. M. Stishov, Nature (London) **428**, 542 (2004).

Translated by Steve Torstveit

Conductivity of a two-dimensional electron gas in magnetic field in the presence of microwave radiation

I. I. Lyapilin* and A. E. Patrakov

Institute of Metal Physics of the Ural Division of the Russian Academy of Sciences, Sofia Kovalevskaya St., 18, Ekaterinburg 620219, Russia

(Submitted May 24, 2004)
Fiz. Nizk. Temp. **30**, 1115–1132 (November 2004)

The experimental observations of novel behavior of the kinetic properties of a two-dimensional electron gas in the presence of microwave radiation are reviewed, and the various theoretical models that have been proposed for explaining them are described. © *2004 American Institute of Physics.* [DOI: 10.1063/1.1819857]

1. INTRODUCTION

The transport-related properties of two-dimensional electron systems (2DESs) in a perpendicular magnetic field were investigated rather widely in the late 1960s and early 1970s.[1,2] The studies showed that microwave radiation at frequencies ω slightly higher than the cyclotron frequency ω_c or its harmonics $N\omega_c$ (N is an integer) can lead to absolute negative conductance in a 2DES. Investigation of the nonlinear photoconductivity in the microwave range due to the photon-assisted scattering of electrons on impurities was the subject of Refs. 3.

Renewed interest in the theoretical investigation of nonlinear transport phenomena arose in connection with the publication of new experimental results on very pure 2DES samples. Recent studies by two experimental groups[4–6] have revealed that the resistance of a two-dimensional electron gas (2DEG) with high mobility in GaAs/AlGaAs heterostructures subjected to microwave irradiation at frequency ω exhibits some new behavior of its dependence on temperature, microwave power, etc. In the presence of microwave radiation, peculiar oscillations of the longitudinal magnetoresistance arise in two-dimensional systems at large occupation numbers. Unlike the Shubnikov–de Haas oscillations, which depend on the ratio of the chemical potential μ to the cyclotron frequency ω_c, the oscillations caused by microwave radiation depend on the ratio of the radiation frequency ω to the cyclotron frequency ω_c. With increasing radiation intensity the minimum values of the resistance approach zero.

In this review article we discuss the results of experimental studies and various theoretical models proposed to explain the new behavioral regularities observed in the kinetic properties of a two-dimensional gas.

2. EXPERIMENT

Let us begin with a description of the results of the first experimental studies[4,6] in which these behaviors were observed.

The first experiment[4] was done using a very pure sample of $Al_{0.24}Ga_{0.76}As/GaAs/Al_{0.24}Ga_{0.76}As$ (a quantum potential well). The parameters of the sample were: quantum well width 300 Å, sample dimensions 5×5 mm, electron mobility $\mu=2.5\times10^7$ cm^2/(V·s), and electron density $n_e=3.5\times10^{11}$ cm^{-2}.

Let us consider the experimental setup in Ref. 4. The sample with the 2DEG was in a weak ($B=0-2$ kG) magnetic field perpendicular to the surface and was simultaneously subjected to an electromagnetic field of the millimeter range ($f=35-150$ GHz). The wave vector of the electromagnetic waves was perpendicular to the surface of the sample. The power of the electromagnetic radiation was from 10 to 20 mW. The experiment was done in the temperature interval 0.5–6 K. The geometry of the experiment is shown in the inset to Fig. 1.

The longitudinal resistance R_{xx} and Hall resistance R_{xy} were measured as functions of the magnetic induction (Fig. 1). The measurements of the Hall resistance $R_{xy}(B)$ gave a close to linear dependence on the induction and were insensitive to the radiation—this is the well-known nonquantum Hall effect. For the longitudinal resistance R_{xx} the presence of the the electromagnetic field led to substantially different dependence on the induction B. For example, in the absence of the electromagnetic field, Shubnikov–de Haas oscillations are observed. In the presence of the electromagnetic field the sharp oscillations of the longitudinal resistance R_{xx} are observed at significantly lower fields and with a different period in $1/B$.

Analysis showed that the period of these oscillations (with respect to $1/B$) depends on the frequency of the electromagnetic waves. The governing parameter is the ratio of the electromagnetic wave frequency ω to the cyclotron frequency ω_c. It is stated in Ref. 4 that the maxima of the longitudinal resistance are observed at $\omega/\omega_c=1,2,3,\ldots$ and the minima at $\omega/\omega_c=3/2,\ 5/2,\ 7/2,\ldots$.

The longitudinal resistance of the sample measured at the most pronounced minima is equal to zero within the limits of experimental error. At the maxima it is higher than the resistance of the sample in the absence of electromagnetic waves (sometimes by 5 times or more).

Figure 2 shows the dependence of R_{xx} on ω_c/ω for different frequencies of the electromagnetic radiation incident on the sample. It is seen that the positions of the maxima and minima of R_{xx} for the different frequencies coincide. With increasing temperature (Fig. 3) the zero resistance parts be-

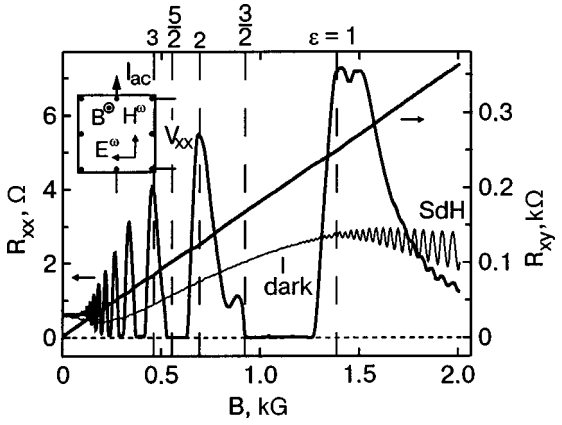

FIG. 1. Resistance versus magnetic induction: heavy lines—in the presence of electromagnetic radiation in the millimeter range ($f=57$ GHz) at $T=1$ K; fine-line curve—in the absence of radiation. The vertical dashed lines correspond to integer and half-integer values of $\varepsilon=\omega/\omega_c$. The inset shows the geometry of the sample, the position of the electrical contacts in a typical case, and the orientation of the current I, magnetic induction B, and the electric and magnetic fields of the electromagnetic wave. (This figure was taken from Ref. 4.)

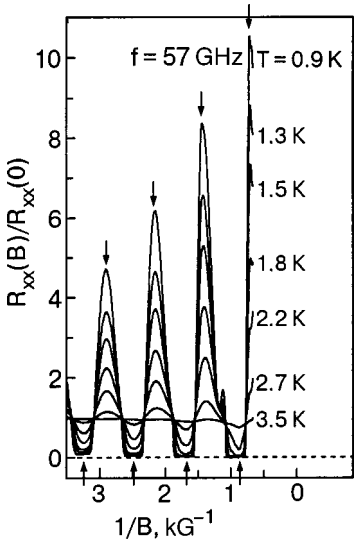

FIG. 3. $R_{xx}(B)/R_{xx}(0)$ versus $1/B$ in the presence of millimeter-range microwave radiation at different T from 0.9 to 3.5 K. The arrows pointing upward indicate the positions of the minima. (This figure was taken from Ref. 4.)

come narrower and eventually vanish, and the height of the peaks decreases as well.

Analogous results on the change in the longitudinal and Hall resistances were obtained in Ref. 6, in which samples in the form of Hall strips of width $50\ \mu\text{m}\leqslant\ell\leqslant200\ \mu$m and square samples up to $\sim3\times3$ mm in size, prepared from high-quality GaAs/AlGaAs heterostructures with an electron density $n(4.2\text{ K})\approx3\times10^{11}\ \text{cm}^{-2}$ and mobility $\mu(1.5\text{ K})\approx1.5\times10^{7}\ \text{cm}^2/(\text{V}\cdot\text{s})$. The measurements were made at radiation frequencies $27\text{ GHz}\leqslant f\leqslant115$ GHz, radiation powers up to 1 mW (i.e., much lower than in Ref. 4), and helium temperatures. The dependence of R_{xx} on B is presented in Fig. 4.

In Ref. 6 a different result for the position of the minima and maxima of the resistance oscillations was obtained as compared to Ref. 4: the minima were observed at $B_{\min}^{-1}/\delta=[4/(4j+1)]^{-1}$ and the maxima, at $B_{\max}^{-1}/\delta=[4/(4j+3)]^{-1}$, where $j=1,2,3,\ldots$. Here δ, the oscillation period in $1/B$, coincides with the value $B_f^{-1}=(\omega m^*c/e)^{-1}$ to within the experimental error.

Figure 5 shows the frequency dependence of the oscillations of the longitudinal resistance. Approximation of the data by a product of a sinusoid times a damped exponential shows that the oscillation frequency F increases linearly with electromagnetic radiation frequency f, and the damping parameter of the oscillations as functions of B^{-1} is independent of f. An estimate of m^* with the use of the formula $dF/df=2\pi m^*c/e$ gives $m^*/m=0.067$, which agrees with other estimates of the electron effective mass in GaAs.

The amplitude of the radiation-induced resistance oscillations also increases with increasing radiation power. At the same time, the shape of the resistance oscillations is insensitive to the value of the current (Fig. 6).

It was stated in Ref. 6 that the observed behavior of the resistance is independent of the type of electrical contacts,

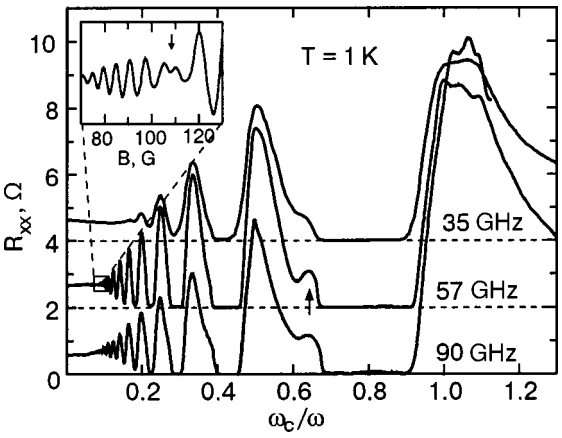

FIG. 2. Dependence of $R_{xx}(T=1\text{ K})$ on ω_c/ω in the presence of electromagnetic radiation of different frequencies (for clarity the graphs have been shifted with respect to each other along the vertical). The vertical arrow shows the additional peak. The inset shows the graph corresponding to a frequency of 57 GHz and weak magnetic fields. Beats can be seen at $B\leqslant0.1$ kG. (This figure was taken from Ref. 4.)

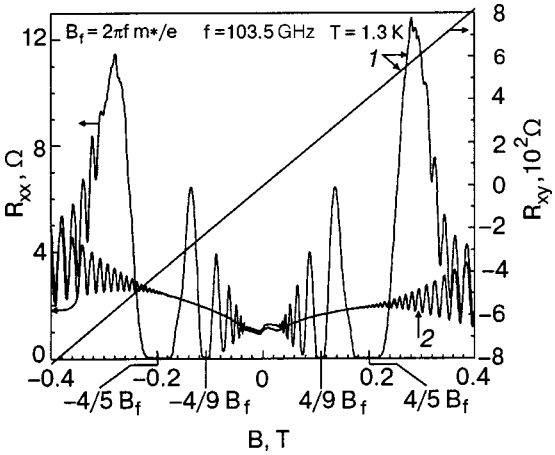

FIG. 4. Curves of $R_{xx}(B)$ and $R_{xy}(B)$ in the presence (*1*) and absence (*2*) of electromagnetic radiation. (This figure was taken from Ref. 6.)

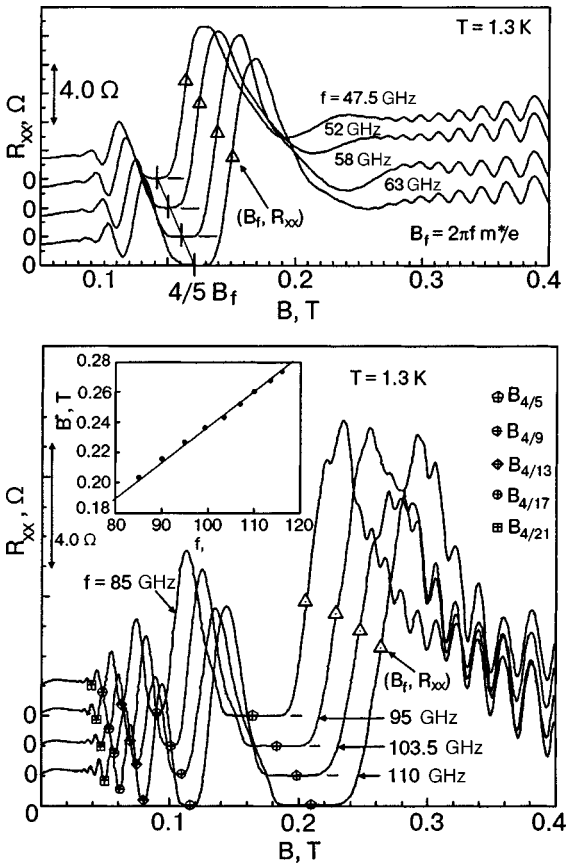

FIG. 5. Evolution of the radiation-induced zero-resistance states upon a change in the radiation frequency. a—At frequencies in the range up to 63 GHz the zero-resistance state appears at $4/5B_f$. The triangles denote the values of R_{xx} at the magnetic field $B_f = \omega m^* c/e$ at which the oscillatory curves have neither maxima nor minima. b—At higher frequencies the zero-resistance state appears around $4/5B_f$ and $4/9B_f$. Inset: B^* was calculated from the first five resistance minima according to the formula $B^* = \Sigma_{j=1}^{5}\{[4j+1/4]B_{4/(4j+1)}\}/5$, with the result $dB^*/df = 2.37$ mT/GHz. (This figure was taken from Ref. 6.)

the shape of the sample, the orientation of the current with respect to the polarization vector of the electromagnetic radiation, and the value of the current.

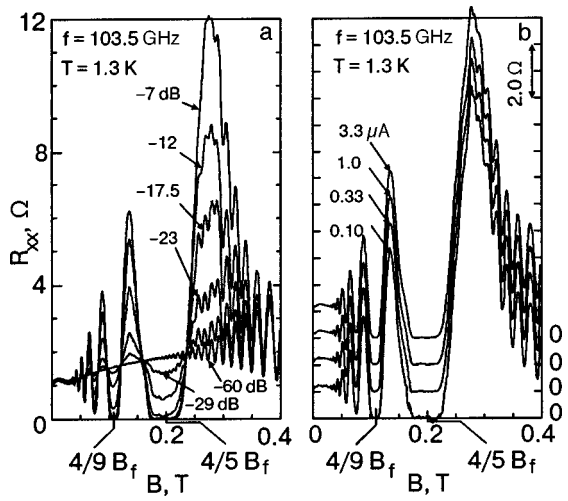

FIG. 6. Amplitude of the radiation-induced oscillations as a function of the magnetic induction for different radiation powers (a) and for different values of the current (b). (This figure was taken from Ref. 6.)

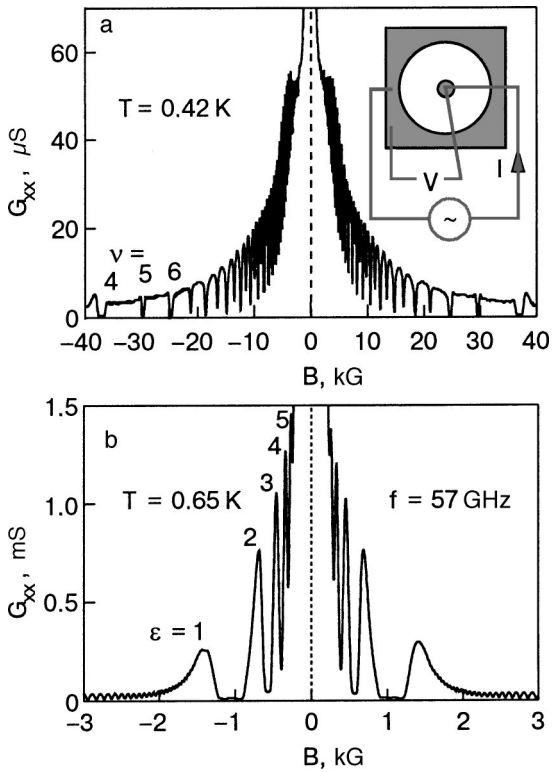

FIG. 7. a—Magnetoresistance of a Corbino sample in the absence of microwave radiation (the sharp Shubnikov–de Haas oscillations at low magnetic fields and the minima of the integer quantum Hall effect at high magnetic field). b—Conductance oscillations under microwave irradiation (at the first minimum a state with vanishingly low conductance is observed). (This figure was taken from Ref. 5).

A state with exponentially low conductivity brought on by microwave radiation has also been observed in Corbino samples with a high mobility of the two-dimensional charge carriers.[5] The samples were $Al_{0.24}Ga_{0.76}As/GaAs/Al_{0.24}Ga_{0.76}As$ quantum wells 25 nm wide, with δ-doped Si layers situated 80 nm above and below the quantum wells. The density and mobility of the electron gas were 3.55×10^{11} cm^{-2} and 1.28×10^7 cm^2/(V·s) at $T = 5$ K. Corbino samples with an inner diameter of 0.5 mm and an outer diameter of 3 mm were made on a square of $\sim 4 \times 4$ mm.

As is seen in Fig. 7a, in the absence of microwave radiation the Drude conductivity of the sample exhibits sharp Shubnikov–de Haas oscillations with changing magnetic field for $B \geqslant 1.5$ kG, and vanishing conductivity at the quantum Hall effect minima for $B \geqslant 10$ kG. Figure 7b shows a plot of the conductance at a microwave power of 10 μW and frequency 57 GHz. Strong oscillations of the conductance are seen in the region of low magnetic fields. In a region around the strongest minimum of the oscillations (at $B = 1.05$ kG) a state with vanishingly small conductance is observed. The evolution of the conductance under microwave irradiation at different frequencies but equal power $P \approx 10$ μW at temperature $T = 0.65$ K is shown in Fig. 8. It is seen that the strong oscillations and the state with vanishingly small conductance are observed at all frequencies.

To determine the activation energy associated with the minima, curves of $R_{xx}(B)/R_{xx}(0)$ versus $1/T$ were constructed in Refs. 4 and 6 (see Figs. 9 and 10). These temperature curves are characteristic of activational processes:

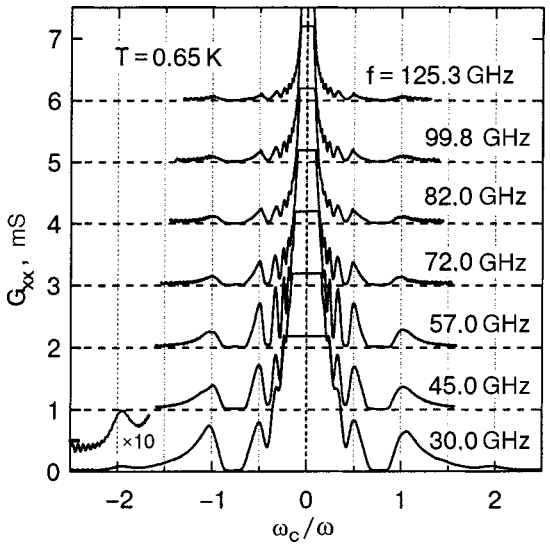

FIG. 8. Conductance oscillations in a Corbino sample at various frequencies of the microwave radiation (the amplitude of the oscillations decreases with increasing radiation frequency). The graphs have been shifted relative to each other along the vertical. (This figure was taken from Ref. 4.)

$R_{xx} \propto \exp(-\kappa/2T)$, where κ is the activation energy. This relation holds in a range of resistances whose upper and lower boundaries differ by more than a factor of 10. The pertinent energy scales for the given problem include the separation between Landau levels $\hbar\omega_c$, the energy $\hbar\omega$ of a quantum of the radiation, and the Landau level broadening πT_D, where T_D is the Dingle temperature. All of these energies are lower than the calculated activation energy (not over 20 K in Ref. 4). We note that there are no other arguments in favor of an activational transport mechanism besides the shape of the $R_{xx}(B)/R_{xx}(0)$ versus $1/T$ curve.

Among the novel effects observed is unusual behavior of the longitudinal magnetoresistance in the low field region $B \leqslant 0.02$ T. For example, in the experiments of Ref. 4, which

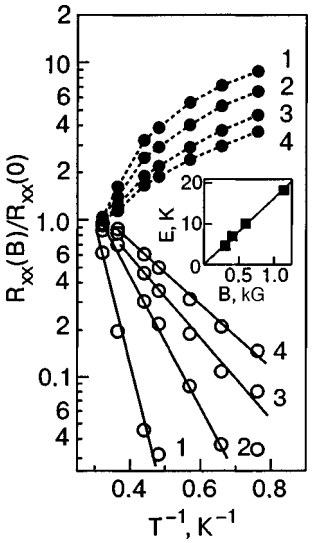

FIG. 9. $R_{xx}(B)/R_{xx}(0)$ versus $1/T$ at the sequence of minima (unfilled symbols) and maxima (filled symbols) at $j=1, 2, 3, 4$. The solid lines are an approximation by the law $R_{xx}(T) \propto \exp(-E/T)$. The inset shows the values of the fitting parameter E as a function of B. (This figure was taken from Ref. 4).

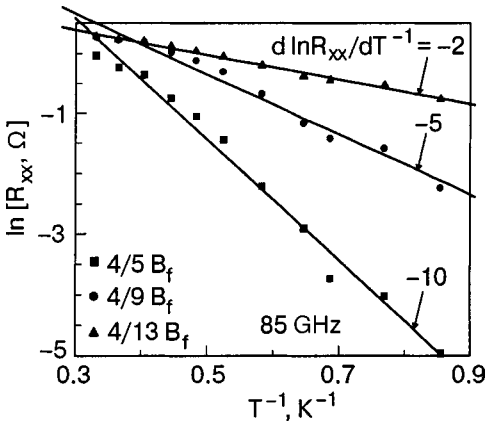

FIG. 10. Natural logarithm of the resistance as a function of inverse temperature. Here $\kappa/2k_Bt \approx 10$ K for the state $4/5B_f$ at 85 GHz. (This figure was taken from Ref. 6.)

were done on GaAs/AlGaAs heterostructures (with an electron mobility $\mu = 25\times10^6$ cm^2/(V·s) and electron density $n_e = 3.5\times10^{11}$ cm^{-2}), the amplitude of the magnetoresistance oscillations was observed to vanish at $B = 110$ G. As the magnetic field was decreased further, the amplitude of the oscillations grew again (see the inset in Fig. 2). This feature of the magnetoresistance was interpreted as beats. An analogous effect was observed in the experiments of Ref. 6, which were done on GaAs/AsGaAs heterostructures with electron mobility $\mu = 15\times10^6$ cm^2/(V·s) and $n_e = 3\times10^{11}$ cm^{-2}. Vanishing of the amplitude of the oscillations was observed around $B = 240$ G (see Fig. 11). According to Ref. 6, the magnetic field strength at which the amplitude of the magnetoresistance oscillations vanishes is independent of the frequency of the external radiation. The observed "beats" were attributed to "zero-spin splitting" due to the spin–orbit interaction.[7,8]

3. THEORY

The experimental observation of "giant" oscillations of the magnetoresistance of two-dimensional electron systems under microwave irradiation and the experimentally observed[4,6] vanishing of the electrical resistance and the transition to "dissipationless" states in a 2DES placed in a mag-

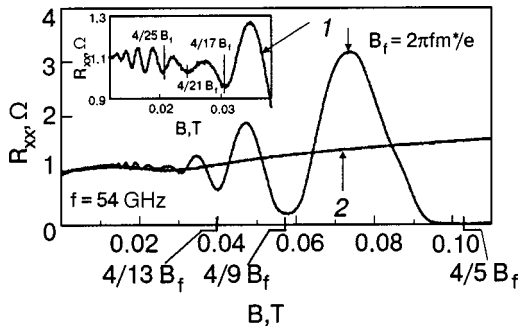

FIG. 11. Dependence on B of the resistance R_{xx} of a 2DEG in a GaAs/AlGaAs heterostructure in the presence (*1*) and absence (*2*) of electromagnetic radiation. The beats visible in the resistance oscillations are shown on an expanded scale in the inset. (This figure was taken from Ref. 6.)

netic field have elicited numerous attempts to explain the nature of these effects and have led to a new wave of theoretical studies.[9–16]

Let us begin our discussion of the theoretical models used in analyzing the results of Refs. 4 and 6 with a microscopic model based on consideration of the probabilities of transition between Landau levels under the influence of radiation; this model describes the origin of the resistance oscillations and explains their period and phase. We consider this class of models from the example of the first papers.[10,11]

The authors of Ref. 10 begin with a study of a simplified model that can be used to establish a simple physical picture of the problem.

The electronic states of the 2DEG in a perpendicular magnetic field **B** are the Landau levels $\varepsilon_n = n\omega_c$, where $\omega_c = eB/m^*c$, n is a non-negative number, and m^* is the effective mass of an electron in the semiconductor. Here $\hbar = 1$ and a constant energy shift of $\omega_c/2$ has been dropped. When an electron absorbs a photon, it acquires an energy ω. In the absence of disorder the conductivity is independent of the distribution of the electrons over Landau levels (the Kohn theorem),[17] so that the electrons excited by the photons cannot give an additional contribution to the dc current. In the presence of disorder the Landau levels broaden. We denote the eigenstates in the absence of disorder as $\psi_\alpha(\mathbf{r})$, with eigenenergies ε_α. When an electron absorbs a photon it acquires an energy ω. In the presence of disorder the excited electrons can be scattered by impurities. To second order in the radiation the frequency at which the electron is scattered from the initial state α' to the final position $\mathbf{r}$ is

$$w_{\alpha'}(\mathbf{r}) = 2\pi \sum_{\alpha} |\psi_\alpha(\mathbf{r})|^2 \delta(\varepsilon_\alpha - \varepsilon_{\alpha'} - \omega) |\langle \alpha | eE\hat{x} | \alpha' \rangle|^2, \quad (1)$$

where $\langle \alpha | eE\hat{x} | \alpha' \rangle$ is a matrix element of the electric dipole operator of the radiation field. The additional current density due to the radiation is

$$\Delta J_x(\mathbf{R}) = -e \int d\varepsilon d^2\Delta\mathbf{r} [n_F(\varepsilon) - n_F(\varepsilon+\omega)] \times \sum_{\alpha'} |\psi_{\alpha'}(\mathbf{r}')|^2 \delta(\varepsilon - \varepsilon_{\alpha'}) w_{\alpha'}(\mathbf{r}) \Delta x. \quad (2)$$

Here $\mathbf{R} = (\mathbf{r}+\mathbf{r}')/2$, $\Delta\mathbf{r} = \mathbf{r} - \mathbf{r}' = (\Delta x, \Delta y)$. For the average over the disorder (denoted by an overbar) we have

$$\Delta J_x(\mathbf{R}) = -2\pi e \int d\varepsilon d^2\Delta\mathbf{r} [n_F(\varepsilon) - n_F(\varepsilon+\omega)] \times \mathcal{N}(\mathbf{r}, \varepsilon+\omega) \mathcal{N}(\mathbf{r}', \varepsilon) M(\mathbf{r}, \mathbf{r}') \Delta x. \quad (3)$$

Here $\mathcal{N}(\mathbf{r}, \varepsilon) = \overline{\Sigma_\alpha |\psi_\alpha(\mathbf{r})|^2 \delta(\varepsilon - \varepsilon_\alpha)}$ is the average local density of states, which for high Landau levels satisfies the relation $\mathcal{N}(\varepsilon + m\omega_c) = \mathcal{N}(\varepsilon)$; $M(\mathbf{r}, \mathbf{r}') > 0$ is determined by separating these factors of the density of states and is assumed to be independent of the energies ε and $\varepsilon + \omega$ and is a function of $|\Delta\mathbf{r}|$ alone.

The dc field E_{dc} is directed along the x axis. It is assumed that the field influences Eq. (3) only through $\mathcal{N}(\mathbf{r}, \varepsilon) = \mathcal{N}(\varepsilon - eE_{\rm dc}x)$. The energy spectrum in the field E_{dc} is illustrated in Fig. 12. For finding the linear response we expand to first order in E_{dc} and find the longitudinal conductivity σ_{xx}. The radiation-induced change in the longitudinal conductivity is proportional to the integral of the partial derivative $(\partial(\mathcal{N}(\mathbf{r}, \varepsilon+\omega)\mathcal{N}(\mathbf{r}', \varepsilon))/\partial\Delta x)_{\mathbf{R}}$.

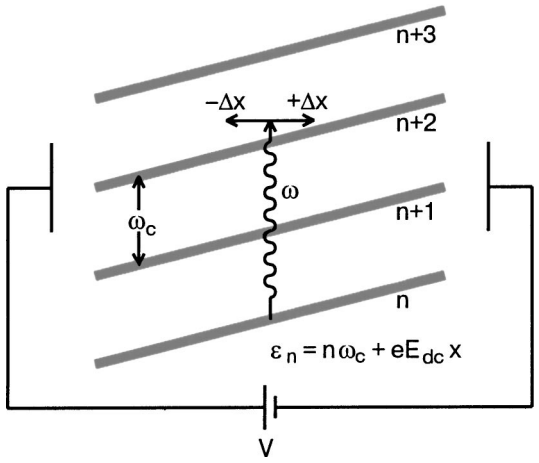

FIG. 12. The Landau levels are tilted by an applied dc bias voltage. Electrons absorb photons and acquire an energy ω. The electrons excited by photons are scattered by disorder and shift to the right or left by a distance $\pm\Delta x$. If the final density of states to the left is greater than the density of states to the right, then the dc current increases. In the opposite case, it decreases.

The density of states is modeled by the expression $\mathcal{N}(\varepsilon) = \mathcal{N}_0 + \mathcal{N}_1 \cos(2\pi\varepsilon/\omega_c)$. For ω/ω_c large in comparison with $\mathcal{N}_0/\mathcal{N}_1$ one obtains the result

$$\Delta\sigma_{xx} \propto -\sin(2\pi\omega/\omega_c) \quad (4)$$

with a positive coefficient. This form, which resembles the derivative of the density of states $(\partial\mathcal{N}/\partial\varepsilon|_{\varepsilon=\omega}$ arises because the main contribution is given by the initial states around the center of the broadened Landau level, which are scattered into empty broadened levels, and the accessible phase space increases or decreases for positive or negative Δx depending on the change of the energy ω modulo ω_c (see Fig. 12). It follows from experiment that σ_{xy} is almost a hundred times larger than σ_{xx} and does not change noticeably under irradiation. Therefore inversion of the conductivity tensor gives $\rho_{xx} \approx \rho_{xy}^2 \sigma_{xx}$, the oscillations of which have experimentally observable period and phase.

The analysis in Ref. 10 shows that disorder plays a central role and can be sufficient for obtaining radiation-induced oscillations. A calculation of the conductivity with the use of the diagrammatic technique (the Kubo formula) including the radiation and disorder but neglecting electron–electron interactions will be sufficient for reproducing the effect. The calculations of Ref. 10 give $\rho_{xx} < 0$ in the region of magnetic fields where the zero-resistance states is observed.

Analogous arguments are made in Ref. 11. It was shown that the state with negative resistance is also the result of a nontrivial structure of the density of states of the two-dimensional system. The theory of Ref. 11 modeled a tunnel junction sample to which the sum of dc and ac voltages are applied (see Fig. 13).[18] The ac voltage $V_{ac} = \Delta \cos \omega t$ applied to the junction models the microwave radiation in the real experiment.

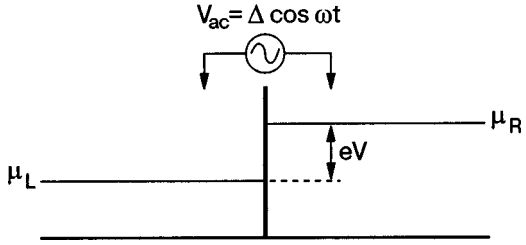

FIG. 13. Model of a quantum tunnel junction. A dc bias voltage V and an ac field $V_{ac}=\Delta\cos\omega t$ are applied to a structureless tunnel junction. The ac field models the microwave radiation.

A calculation of the conductivity with the use of the model density of states

$$\rho(\varepsilon)=\left(1+\lambda\cos\frac{2\pi\varepsilon}{\hbar\omega_c}\right)\rho_0, \tag{5}$$

leads to the following result:

$$\frac{\sigma(T)}{\sigma_0}=\sum_{n=-\infty}^{\infty}J_n^2\left(\frac{\Delta}{\hbar\omega}\right)\left[1+\frac{\lambda^2}{2}\cos\left(2\pi n\frac{\omega}{\omega_c}\right)-n\pi\lambda^2\frac{\omega}{\omega_c}\sin\left(2\pi n\frac{\omega}{\omega_c}\right)\right]+g\left(\frac{\mu}{\hbar\omega_c},T\right), \tag{6}$$

where $\sigma_0=e^2D\rho_0^2$, and $g(\mu/\hbar\omega_c,T)$ is the contribution of the Shubnikov–de Haas oscillations, which falls off rapidly at finite temperatures.

The amplitude of the oscillations in Ref. 11 is independent of temperature. This means that the temperature dependence that is observed experimentally must be due to the temperature dependence of the density of states. We note that the theory developed in Ref. 11 also predicts an oscillatory character of the magnetoresistance, with a period and phase that agree with the observations.[6] Furthermore, it predicts an N-shaped current–voltage (I–V) characteristic for the zero-resistance state.

The results of the conductivity calculations carried out in Ref. 11 for a more realistic density of states,

$$\rho(\varepsilon)=\left[1+2\exp\left(-\frac{\pi}{\omega_c\tau_f}\right)\cos\frac{2\pi\varepsilon}{\hbar\omega_c}\right]\rho_0, \tag{7}$$

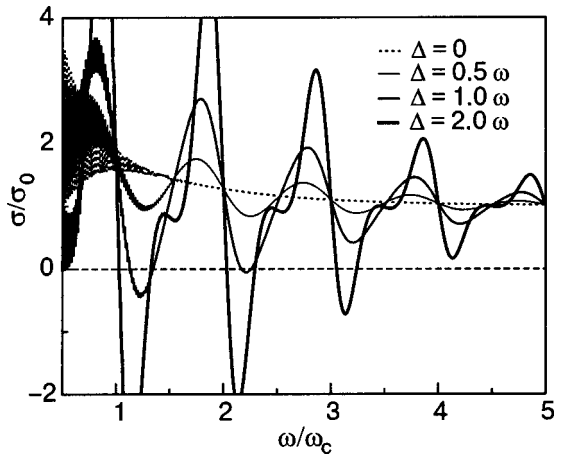

FIG. 14. Dependence of the conductivity on ω/ω_c at different values of the radiation intensity. The parameters are taken from Ref. 10: $\mu=50\hbar\omega$, $kT=0.25\hbar\omega$, $\omega\tau_f=6.25$.

are presented in Fig. 14. We note that the positions of the maxima and minima of the photoconductivity depend on the radiation power; this explains the discrepancy between the results of Refs. 4 and 6.

It follows from the models considered above that the appearance of new oscillations is due to photon-assisted transport phenomena in the presence of an oscillatory density of states, which can also lead to negative conductivity at sufficiently high radiation power. There remains the legitimate question of whether the rather strong interaction between the radiation field and the 2DES in a magnetic field has been adequately studied.

In Ref. 19 a theory was developed in which the interaction of the radiation and electrons is taken into account exactly, while the scattering on impurities is treated by perturbation theory. The main result for the theory developed in Ref. 19 consists in the renormalization of the density of states, for which the following expression was obtained:

$$\rho'(\varepsilon)=\Sigma\rho(\varepsilon+n\hbar\omega)J_n^2\left[\frac{eE}{\hbar}X_j\left(\frac{1}{\omega}+\frac{\omega}{\omega_c^2-\omega^2}\right)\right], \tag{8}$$

where $\rho(\varepsilon)$ is the density of states in the absence of radiation, and X_j is the coordinate of the center of the harmonic oscillator.

The zero-bias conductivity is described here by the same expression as in Ref. 11, but with a different argument of the Bessel function, which exhibits resonance behavior that was absent in the framework of perturbation theory. For the density of states (in the absence of radiation) with the broadening of the Landau levels taken into account (5), the photon-assisted conductivity gives rise to slow oscillations as a function of the inverse magnetic field: $\propto\sin(2\pi n\omega/\omega_c)$, whereas the usual Shubnikov–de Haas oscillations are fast: $\propto\sin(2\pi\mu/\hbar\omega_c)$, where μ is the chemical potential. It is clear that the slow and fast oscillations can be observed separately if the chemical potential is much higher than the temperature ($\mu\gg T$) and the temperature is not too low in comparison with the distance between Landau levels: $kT/\hbar\omega_c\sim 1$. This is precisely the regime in which the experiments have been done.

In this regime the contribution to the conductivity due to photons has the form

$$\frac{\sigma-\sigma_{SdH}}{\sigma_0}=\frac{\lambda^2}{2}\sum_{n=-\infty}^{\infty}J_n^2\left(\frac{eE}{\hbar}\Delta X_j\left(\frac{1}{\omega}+\frac{\omega}{\omega_c^2-\omega^2}\right)\right)\times\left[\cos\left(2\pi n\frac{\omega}{\omega_c}\right)-2\pi n\frac{\omega}{\omega_c}\sin\left(2\pi n\frac{\omega}{\omega_c}\right)-1\right], \tag{9}$$

where $\sigma_0=e^2D\rho_0^2$; σ_{SdH} is the conductivity in the absence of radiation, which is none other than the conductivity in the usual Shubnikov–de Haas effect; σ_{SdH} can be determined as the conductivity at $E=0$; $\Delta X_j\simeq 2\sqrt{2n+1}\,\alpha$ (α is the magnetic length).

A straightforward analysis shows that, together with the oscillations of the first harmonic ($n=1$) there should also be noticeable oscillations of the other harmonics ($n\geqslant 2$) near $\omega\simeq\omega_c$. The observation of additional harmonics was mentioned in Ref. 4. It should be noted that that paper made

some theoretical predictions as to the zero-resistance state in the vicinity of half filling of the lowest Landau level; this state is due to photon-assisted transport processes in the presence of an oscillatory density of states, which is analogous to the zero-resistance state of electrons in low magnetic fields.

An approach based on calculation of the probability of transitions between broadened Landau levels is now the most generally accepted. However, although it explains many of the observed features of the photoresistance oscillations, it does this ''too well.'' There is no clear explanation for why a weak magnetoplasma resonance[20] is observed instead of photoresistance oscillations in samples with lower mobility under otherwise equal conditions.

The influence of an rf field on the conduction of a 2DEG in a quantizing magnetic field at low temperatures was considered in 1986.[21] The proposed mechanism for the formation of the photocurrent is the same as that proposed in Ref. 10. In Ref. 21 the scatterers were assumed to be impurities. Using the Kubo formula (the rf field was taken into account in the second order of perturbation theory), the authors obtained a formula for the dependence of the photocurrent on the radiation frequency in the vicinity of the harmonics of the cyclotron frequency. It was found that the sign of the photocurrent is opposite to the sign of the deviation $\Delta\omega$ of the radiation frequency from the nearest harmonic of the cyclotron frequency, i.e., the dependence of the photoconductivity on the frequency of the microwave radiation has an oscillatory character. We stress once again that, according to Ref. 21, t photoconductivity equals zero for $\Delta\omega=0$, in agreement with the experimental results of Ref. 6 but not with those of Ref. 4. The correction for the rf field to the Hall component of the current in the approximation used in Ref. 21 is equal to zero. In addition, the authors mention that absolute negative conductivity (ANC) can be realized near the cyclotron resonance (see Refs. 22 and 23).

The photoconductivity due to photon-assisted scattering on impurities in multiphoton processes in a magnetic field in the presence of microwave and dc electric fields was considered in Ref. 12. It was shown in the framework of the theory developed there that the value of the maxima and minima of the microwave radiation is a nonmonotonic function of the microwave radiation power and the electric field.

The authors proceed from the expression for the radiation-induced dissipative current:

$$j_{\rm ph}=j_{\rm ph}^{\rm (inter)}+j_{\rm ph}^{\rm (intra)}, \tag{10}$$

where $j_{\rm ph}^{\rm (inter)}$ is the contribution due to transitions of electrons between Landau levels of different numbers as a result of the microwave radiation, while the second term on the right-hand side of (10) is the change of the dissipative current component due to transitions within each Landau level. The probability of these processes is a function of the total dc electric field and ac field of the microwave radiation.

For the transition probabilities between electron states (N,k_x,k_y) and (N',k_x+q_x,k_y+q_y) in the presence of a total electric field $\mathbf{E}=(E,0,0)$ perpendicular to the magnetic field $\mathbf{H}=(0,0,H)$ and an ac field $\mathbf{E}_\Omega=(\mathcal{E}e_x,\mathcal{E}e_y,0)$, polarized in the plane of the system (e_x and e_y are components of the polarization vector of the microwave radiation), the authors of Ref. 12 use the formula

$$W_{N,k_x,k_y;N',k_x+q_x,k_y+q_y}=\frac{2\pi}{\hbar}\sum_M \mathcal{N}_i|V_q|^2\left|Q_{N,N'}\left(\frac{L^2q^2}{2}\right)\right|^2 J_M^2(\xi_\Omega(q_x,q_y))\times\delta[M\hbar\Omega+(N-N')\hbar\Omega_c+eEL^2q_y]. \tag{11}$$

Here N is the number of the Landau level, k_x and k_y are the quantum numbers of the electron, q_x and q_y are the changes in them due to photon-assisted scattering on impurities, $q=\sqrt{q_x^2+q_y^2}$, $e=|e|$ is the electron charge, $\mathcal{N}_i$ is the impurity concentration, $V_q\propto q^{-1}\exp(-d_iq)$ is the matrix element of the electron–impurity interaction, which takes into account the localization of the electrons in the direction of the z axis, where d_i is the distance between the 2DES and the δ-doped layer. The functions characterizing the overlap of the initial and final states of the electrons are

$$Q_{N,N'}(\eta)=P_N^{(N'-N)}(\eta)\exp(-\eta/2),$$

$P_N^{(N'-N)}(\eta)\propto L_N^{(N'-N)}(\eta)$, where $L_N^{\Lambda}(\eta)$ is a Laguerre polynomial, $J_M(\xi_\Omega(q_x,q_y))$ are Bessel functions,

$$\xi_\Omega(q_x,q_y)=\frac{e\mathcal{E}}{m}\frac{|q_xe_x+q_ye_y-i(\Omega_c/\Omega)(q_xe_y-q_ye_x)|}{|\Omega_c^2-\Omega^2|}, \tag{12}$$

where m is the effective mass of an electron.

In the Ohmic regime for a 2DES with $\beta\equiv 2d_i/L<1$ (the case of short-range impurities) the authors of Ref. 12 obtained the following expression:

$$j_{\rm ph}^{\rm (inter)}\propto E\Gamma\exp\left[Pf\left(\frac{\Omega}{\Omega_c}\right)\right]\times\left\{I_1\left(Pf\left(\frac{\Omega}{\Omega_c}\right)\right)\sum_\Lambda\frac{\Theta_\Lambda(\Lambda\Omega_c-\Omega)}{[(\Lambda\Omega_c-\Omega)^2+\Gamma^2]^2}\right\}+I_2\left(Pf\left(\frac{\Omega}{\Omega_c}\right)\right)\sum_\Lambda\frac{\Theta_\Lambda(\Lambda\Omega_c-2\Omega)}{[(\Lambda\Omega_c-2\Omega)^2+\Gamma^2]^2}+\ldots\Bigg\}, \tag{13}$$

where $P=p_\Omega/\overline{p_\Omega}$ is the normalized microwave radiation power, $f(\omega)=\omega(1+\omega^2)/(1-\omega^2)^2$, and $I_M(\eta)$ is a modified Bessel function.

It follows from the analysis done in the present paper that the height of the maximum and depth of the minimum near the cyclotron resonance (and around its harmonics) increase with increasing radiation power. At high powers the height of the maximum and depth of the minimum saturate and begin to decrease. The height of the first one-phonon maximum (depth of the minimum) for $\Lambda=1$ and $M=1$ falls off when the microwave radiation power exceeds a certain threshold value. In that range of radiation power the maxima (minima) corresponding to resonances of higher order can be comparable to the maximum (minimum) near the cyclotron resonance. At large values of the power the two-photon resonance maxima (minima) can increase faster than those due to one-photon absorption processes. Furthermore, in the vicinity of $\Omega/\Omega_c=1.5$ a relatively weak maximum and minimum corresponding to the two-photon transition ($M=2$ and $\Lambda=3$) appear. These results, as was noted in Ref. 12, agree with the experimental data.[4,6]

In comparatively strong total electric fields $E>E_b$, when transitions between high-numbered Landau levels give the main contribution to the photoconduction mechanism under consideration in the microwave range, the authors of Ref. 12 obtain

$$j_{\rm ph}^{(\rm inter)}\propto\sum_{\Lambda,M}\Theta_\Lambda\mathcal{R}_M\left(\xi_\Omega,\frac{\infty|\Lambda\Omega_c-M\Omega|}{eEL}\right)\times\left[\frac{\hbar(\Lambda\Omega_c-M\Omega)}{eE^2L}\right]\exp\left[-\frac{\hbar^2(\Lambda\Omega_c-M\Omega)^2}{2(eEL)^2}\right],\tag{14}$$

where

$$\mathcal{R}_M(z,y)=\int_0^\infty dx J_M^2(z\sqrt{x^2+y^2})\times\frac{\exp[-\beta\sqrt{x^2+y^2}-(x^2+y^2)/2]}{(x^2+y^2)^{3/2}}.\tag{15}$$

It follows from Eq. (14) that conduction in the presence of microwave radiation in a high electric field also has an oscillatory character, with maxima and minima at $\Omega/\Omega_c=\Lambda-\delta^{(+)}$ and $\Omega/\Omega_c=\Lambda+\delta^{(-)}$, respectively, for transitions involving one photon, and at $\Omega/\Omega_c=[\Lambda-\delta^{(+)}]/M$ and $\Omega/\Omega_c=[\Lambda+\delta^{(-)}]/M$ for transitions involving the absorption of M photons. Here $\delta^{(+)}\simeq\delta^{(-)}\simeq eEL/\hbar\Omega_c=E/E_c$. The width of the maxima and minima under discussion increase linearly with E as $\Delta^{(+)}\simeq\Delta^{(-)}\simeq 2.24E/E_c$, whereas their height is proportional to E^{-1}.

As was noted in Ref. 12, the model describes the following features of the conduction in a 2DES acted on by microwave radiation and a magnetic field: zero photoconductivity at the cyclotron resonance and its harmonics; the position of the maxima and minima of the photoconductivity in the vicinity of resonances with absolute negative conductivity at the maxima; nonlinear dependence of the photoconductivity on the radiation power, characterized by slowing of the growth, saturation, and even a decrease in the value of the maxima and minima with increasing microwave radiation power; a shift and broadening of the maxima and minima of the photoconductivity with increasing microwave radiation power and electric field.

As we have said, the dissipative transport of electrons in the direction parallel to the electric and perpendicular to the magnetic field occurs on account of ''hops'' of the centers of the Larmor orbits of the electrons due to scattering processes. However, the probability of such scattering with a spatial displacement ξ of the center of the Larmor orbit greater than the quantum Larmor radius $L=(c\hbar/eH)^{1/2}$ is exponentially small. Because of this, such scattering processes will be efficient, and the microwave radiation-induced change in the dissipative component of the current (i.e., the photocurrent) significant, only in the immediate vicinity of the resonances, $|\Omega-\Lambda\Omega_c|\lesssim\max\{eEL/\hbar,\Gamma\}$, where Γ characterizes the broadening of the Landau levels.[12] Thus at small $eEL/\hbar$ and Γ the intervals $\Omega-\Lambda\Omega_c$ in which ANC due to photon-assisted scattering occurs are rather narrow. One should therefore estimate the contribution of other scattering mechanisms.

In Ref. 13 the dissipative components of the conductivity (mobility) tensor of a 2DES were calculated on the assumption that the main scattering mechanisms were the photon-assisted scattering of electrons on piezoelectric acoustic phonons. The energies of the electron states in a 2DES in crossed magnetic and electric fields (in neglect of the Zeeman splitting) are given by the expression

$$\varepsilon_{N,\xi}=\left(N+\frac{1}{2}\right)\hbar\Omega_c+eE\xi.\tag{16}$$

In the standard approach (see, e..g., Refs. 1, 3, 24, and 25) the dissipative current $j_D(E)$ in a 2DES is written in the form[12]

$$j_D(E)=\frac{e}{\hbar}\sum_{N,N'}f_N(1-f_{N'})\int d^2\mathbf{q}q_y|V_\mathbf{q}|^2|Q_{N,N'}(L^2q_\perp^2/2)|^2\{\mathcal{N}_q\delta[(N-N')\hbar\Omega_c+\hbar\omega_q+eEL^2q_y]$$
$$+(\mathcal{N}_q+1)\delta[(N-N')\hbar\Omega_c-\hbar\omega_q+eEL^2q_y]+I_\Omega(q_x,q_y)\mathcal{N}_q\delta[\hbar\Omega+(N-N')\hbar\Omega_c+\hbar\omega_q+eEL^2q_y]$$
$$+I_\Omega(q_x,q_y)(\mathcal{N}_q+1)\delta[\hbar\Omega+(N-N')\hbar\Omega_c-\hbar\Omega_q+eEL^2q_y]\}.\tag{17}$$

Here f_N is the filling factor of the Nth Landau level, given by the Fermi distribution function; $\mathbf{q}=(q_x,q_y,q_z)$, $\omega_q=sq$, and $\mathcal{N}_q=[\exp(\hbar\omega_q/T)-1]^{-1}$ are, respectively, the phonon wave vector, frequency, and distribution function; s is the speed of sound, $q=\sqrt{q_x^2+q_y^2+q_z^2}$, $q_\perp=\sqrt{q_x^2+q_y^2}$, $\delta(\omega)$ is the form factor of the Landau level, which at small Γ can be replaced by a Dirac delta function; $|V_\mathbf{q}|^2\propto q^{-1}\exp(-l^2q_z^2/2)$ characterizes the piezoelectric coupling of electrons with acoustic phonons (since that coupling is assumed to be the most important in these 2DESs at low temperatures),[2] l is the localization width of the electron in the direction of the z axis, perpendicular to the plane of the 2DES ($l\ll L$), and $|Q_{N,N'}(L^2q_\perp^2/2)|^2=|P_N^{N'-N}(L^2q_\perp^2/2)|^2\exp(-L^2q_\perp^2/2)$ is the matrix element determined by the overlap of the wave functions of the electron before and after the hop caused by scattering, and $|P_N^{N'-N}(L^2q_\perp^2/2)|^2$ is proportional to the Laguerre polynomial.

The value of $I_\Omega(q_x,q_y)$ is proportional to the power of the incident microwave radiation. It characteristics the effect

of the radiation on the motion of the electron in the plane of the system. For unpolarized microwave radiation[1] $I_\Omega(q_x,q_y)=\mathcal{I}_\Omega L^2(q_x^2+q_y^2)$, with $\mathcal{I}_\Omega=(\mathcal{E}_\Omega/\tilde{\mathcal{E}}_\Omega)^2$, where $\mathcal{E}_\Omega$ is the amplitude of the electric field of the microwave radiation and is assumed smaller than some characteristic $\tilde{\mathcal{E}}_\Omega$ of the microwave field. The latter assumption means that the amplitude of the oscillations of the center of the Larmor orbit in the microwave radiation field is smaller than L, and the emission processes involving the participation of more than one photon of the microwave radiation are unimportant.

The first two terms in Eq. (17) correspond to the electron–phonon interactions, while the third and fourth correspond to such interactions accompanied by absorption of a photon. As is seen from (17), at resonances $\Omega=(N'-N)\Omega_c$ the contribution of photon-assisted processes in the dissipative conductivity goes to zero (see Refs. 17, 26). The characteristic amplitude can be written as[27]

$$\tilde{\mathcal{E}}_\Omega=\frac{\sqrt{2}m\Omega|\Omega_c^2-\Omega^2|L}{e\sqrt{\Omega_c^2+\Omega^2}}. \tag{18}$$

In the immediate vicinity of the cyclotron resonance $\Omega=\Omega_c$ the value of $\tilde{\mathcal{E}}_\Omega$ is limited by the broadening of the Landau levels. Formula (18) becomes incorrect, and $\tilde{\mathcal{E}}_\Omega$ can be estimated as $\tilde{\mathcal{E}}_\Omega\simeq\sqrt{2}m\Omega\Gamma/e$.

In Ref. 13 the conductivity was written in the form $\sigma(E)\simeq\sigma_{\rm dark}+\sigma_{\rm ph}$, where $\sigma_{\rm dark}$ is independent of $\mathcal{I}_\Omega$, whereas $\sigma_{\rm ph}\propto\mathcal{I}_\Omega$ (this expansion is valid for $eE|\xi|\ll\hbar|\Omega-\Lambda\Omega_c|<\hbar\Omega,\hbar\Omega_c$).

As a result of calculations under the additional assumptions $N\gg1$ and $L\Omega_c/s\gg1$, the authors arrive at the formulas

$$\sigma_{\rm dark}\propto\overline{G}\left(\frac{\hbar s}{TL}\right)\left(\frac{s}{L\Omega_c}\right)\exp\left(-\frac{\hbar\Omega_c}{T}\right)\exp\left(\frac{l^2\Omega_c^2}{2s^2}\right), \tag{19}$$

where $\overline{G}\simeq1/2\sqrt{2\pi}N_m$ (N_m is the number of the Landau level directly beneath the Fermi surface),

$$\sigma_{\rm ph}^{(\Lambda)}\propto-\mathcal{J}_\Omega\frac{d}{Ldq}\left[\exp\left(-\frac{l^2q^2}{2}\right)H^{(\Lambda)}(q)\mathcal{N}_q\right]\Bigg|_{q=-q_\Omega^{(\Lambda)}} \tag{20}$$

for $\Omega-\Lambda\Omega_c<0$ and

$$\sigma_{\rm ph}^{(\Lambda)}\propto-\mathcal{J}_\Omega\frac{d}{Ldq}\left[\exp\left(-\frac{l^2q^2}{2}\right)H^{(\Lambda)}(q)(\mathcal{N}_q+1)\right]\Bigg|_{q=q_\Omega^{(\Lambda)}} \tag{21}$$

for $\Omega-\Lambda\Omega_c>0$. Here

$$H^{(\Lambda)}(q)\simeq\sum_{N=N_m-\Lambda+1}^{N_m}f_N(1-f_{N+\Lambda})H_N^{(\Lambda)}(q),$$

$$H_N^{(\Lambda)}(q)=\int_0^{Lq}dtt^5\frac{\exp\left[\dfrac{(l^2-L^2)}{2L^2}t^2\right]}{\sqrt{L^2q^2-t^2}}|P_N^\Lambda(t^2/2)|^2,$$

giving

$$H_N^{(\Lambda)}(q)\simeq3[2\sqrt{2\pi}(1-l^2/L^2)^{5/2}NLq]^{-1}\simeq3(2\sqrt{2\pi}NLq)^{-1}$$

and $H_N^{(\Lambda)}(q)\simeq3(Lq)^4/32N$

for $Lq\gg1$ and $1/\sqrt{2N}<Lq<1$, respectively.

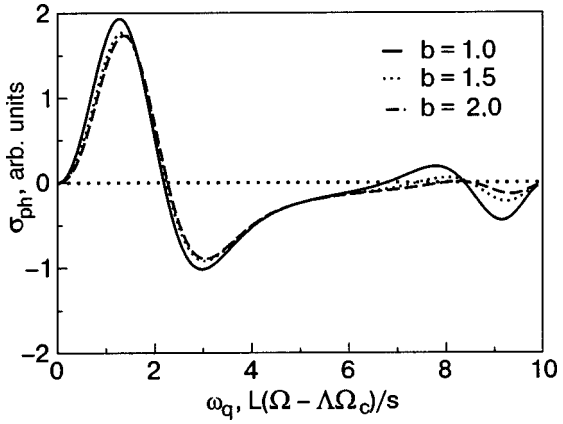

FIG. 15. Dependence of the photoconductivity $\omega_{\rm ph}$ on the normalized frequency of the microwave radiation in the interval $\Lambda\Omega_c\leqslant\Omega\leqslant(\Lambda+1)\Omega_c$.

It is seen from formula (19) that the expression for $\sigma_{\rm dark}$ contains a small exponential factor $\exp(-\hbar\Omega_c/T)$, which arises because the conductivity in the absence of radiation is due to absorption of acoustic phonons with energy $\hbar sq$ close to the distance between Landau levels, the electrons undergoing a transition from the almost filled Landau level (just under the Fermi level, $N=N_m$) to the next, almost empty one. However, the number of such phonons for $T\ll\hbar\Omega_c$ is small. The frequency of processes involving the emission of acoustic phonons accompanying transitions of electrons from the upper Landau level is also exponentially small because of the low occupation of that level and the Pauli exclusion principle.

The photoconductivity given by formulas (20) and (21) as a function of the frequency of the microwave radiation exhibits pronounced oscillations, in which a change of sign occurs. At the resonances $\Omega=\Lambda\Omega_c$ the photoconductivity $\sigma_{\rm ph}=0$. The dependence of the photoconductivity on the microwave radiation frequency, calculated according to formulas (20) and (21) for $L\Omega_c/s=10$, $l/L=0.1$, and various values of the parameter $b=\hbar s/TL$, is presented in Fig. 15.

The negative sign of $\sigma_{\rm ph}$ due to photon-assisted scattering on acoustic phonons near resonances for $\Omega\lesssim\Lambda\Omega_c$ and in the intervals $\Lambda\Omega_c<\Omega<(\Lambda+1)\Omega_c$ is explained as follows. When $\Omega\lesssim\Lambda\Omega_c$, transitions of electrons between Landau levels, which contribute to $\sigma_{\rm ph}^{(\Lambda)}$, are accompanied by the absorption of acoustic phonons with energies $\hbar\omega_q\simeq\Lambda\Omega_c-\Omega$, which are rather small. In this situation the probability of photon-assisted absorption of a phonon decreases with decreasing phonon energy $\hbar\omega_q\propto q$. Since the energies of the phonons absorbed near resonance are small, the difference between values of $\mathcal{N}_q$ with rather small and very close values of q is inconsequential. Because of this, the frequency of absorption of acoustic phonons with $\hbar\omega_q$ not much greater than $\hbar(\Lambda\Omega_c-\Omega)$ exceeds the frequency of absorption of acoustic phonons with $\hbar\omega_q\lesssim\hbar(\Lambda\Omega_c-\Omega)$. In the first case the displacement of the center of the Larmor orbit of the electron is $\delta\xi=\hbar(\Omega-\Lambda\Omega_c+\omega_q)/eE>0$, and so the electron's potential energy change $\delta\varepsilon>0$, and such an electron scattering event therefore gives a negative contribution to the

dissipative current, i.e., it leads to ANC. Contrarily, near the resonances but for Ω slightly greater than $\Lambda\Omega_c$, scattering events with $\delta\xi<0$ predominate.

An analogous model of photoconduction in a quantizing magnetic field was proposed in Ref. 24. It considers optical rather than acoustic phonons and ignores processes that do not involve the participation of photons. The conclusions that the photocurrent is an oscillatory function of the frequency of the microwave radiation and that absolute negative conductivity can occur are still reached even when these simplifications are made.

4. OTHER MICROSCOPIC MODELS

The theoretical schemes considered above presuppose that the observed features of the photoresistance result from *bulk* effects. A fundamentally different approach to the explanation of the resistance oscillations is proposed in Ref. 15. Based on an analysis of the experimental features,[4,6] another possible scenario was put forward, based on the development of the microwave radiation-induced drift instability near the edge of the sample. The author proceeds from the standard picture of the Landau levels, bending upward near the edge and intersecting the Fermi level. The role of the microwave radiation in this case reduces to a redistribution of electrons over quantum states near the edge of the system, where electrons occupying higher energy levels and moving along the boundary (skipping orbits) with an increased velocity (in comparison with the situation in the absence of radiation) appear. In sum, we have a typical situation for the development of drift instabilities in a plasma. For finding the spectrum of the plasma waves the authors of Ref. 15 used the equation[28]

$$\omega - qV = \pm \frac{\omega_p'}{\sqrt{\epsilon(q,\omega)}}, \tag{22}$$

which under the condition $\epsilon(q,\omega)<0$ can give unstable solutions (here $\epsilon(q,\omega)$ is the dielectric function, ω_p' is the plasma frequency in the beam). The dielectric function of a two-dimensional system in a magnetic field has the form $\epsilon(q,\omega)=1+2\pi i\sigma_{xx}(q,\omega)q/\omega\kappa$, where the wave-vector and frequency-dependent conductivity is[29]

$$\sigma_{xx}(q,\omega)=\frac{n_s e^2}{m\omega_c}\,\frac{\omega+i\gamma}{i\omega_c}\left(\frac{2}{qr_c}\right)^2\sum_{k=1}^{\infty} k\,\frac{k^2 J_k^2(qr_c)}{k^2-[(\omega+i\gamma)/\omega_c]^2} \tag{23}$$

and r_c is the cyclotron radius.

As we see, the dielectric function becomes negative in some frequency intervals *above* the harmonics of the cyclotron frequency (instability regions). Solving equation (22) with respect to q at a fixed (real) frequency ω and with $\omega_p' \ll \omega_p$, one can find an expression for the imaginary part of the wave vector $q''(\omega)$, which characterizes the instability growth rate. Figure 16 shows $q''(\omega)$ as a function of magnetic field for typical experimental parameters of Ref. 6.

A comparison of Fig. 16 with Fig. 6a shows that the instability region coincides with intervals of B in which the zero-resistance states were observed experimentally (and negative photoresistance was observed at higher harmonics of the cyclotron frequency; an analogous plot using the data of Fig. 1 gives the same result). A feature of the instability plot in Fig. 16 is that the "strength" of the instability decreases rather slowly with increasing number of the harmonic, in qualitative agreement with experiment. Further, the curves in Fig. 16, constructed for different scattering frequencies, show that the growth of the electron mobility promotes the development of instability, and that also agrees with Refs. 4 and 6. We note that the number of electrons moving along the edge with a velocity that is increased by the influence of the microwave radiation is proportional to $\exp(-W/T)$, and that is also in qualitative agreement with the power dependence and temperature dependence of the photosignal at the minima of R_{xx}.

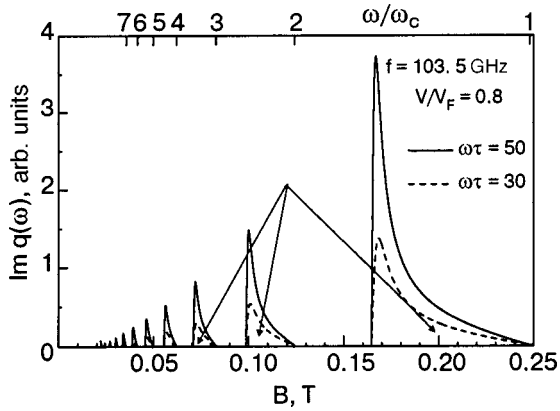

FIG. 16. Instability growth rate as a function of magnetic field for the parameters of Ref. 30, velocity $V/V_F=0.8$, and two different scattering frequencies. The numbers on the upper axis label the positions of the harmonics of the cyclotron frequency. The arrows indicate regions of instability.

It is also supposed by the author of the model under consideration that it resolves the paradox associated with the magnetoplasma resonance with $q\simeq 1/w$ in the new experiments: whereas in Ref. 20 the wave vector of the two-dimensional plasmons was determined by the width w of the sample, in the new experiments the characteristic wave vectors are fixed by the conditions of instability and the weak "bulk" magnetoplasma resonance is not seen against the background of the giant oscillations arising as a result of the edge contribution. An argument in favor of this picture is the relatively weak bulk magnetoplasma resonance observed in Ref. 4 instead of the relatively weak oscillations of R_{xx}.

The author assumes that the arguments he offers reflect the basic physics of the phenomena: the existence of instability in intervals where $\epsilon(q,\omega)>0$. The results of Ref. 15 are in qualitative agreement with the dependence of the photoresistance on the power and frequency of the microwave radiation, temperature, magnetic field, and mobility.

Another approach to the explanation of the observed oscillations of the conductance is proposed in Ref. 16. The authors of Ref. 16 assume that the magnetoresistance features observed in Refs. 4 and 6 are determined by the microwave radiation-induced change of the electron distribution function. Because of the oscillation of the density of states due to the Landau quantization, the correction to the distribution function also acquires an oscillatory character. This gives a contribution to the dc conductivity which oscillates with variation of ω/ω_c. We note that an analogous model

but in zero magnetic field was considered in Ref. 31.

The authors of Ref. 16 start from the expression for the conductivity

$$\sigma_{\rm ph}=2\int d\varepsilon\,\sigma_{dc}(\varepsilon)[-\partial_\varepsilon f(\varepsilon)], \tag{24}$$

where $f(\varepsilon)$ is the electron distribution function and $\sigma_{dc}(\varepsilon)$ determines the contribution of the electrons with energy ε to the dissipative transport processes. In the leading approximation[16,32] one has $\sigma_{dc}(\varepsilon)=\sigma_{dc}^D\tilde{\nu}^2(\varepsilon)$, where $\tilde{\nu}(\varepsilon)=\nu(\varepsilon)/\nu_0$ is the dimensionless density of states, $\nu_0=m/2\pi$ is the density of states per spin in the absence of magnetic field (we are assuming that $\hbar=1$), and $\sigma_{dc}^D=e^2\nu_0 v_F^2/2\omega_c^2\tau_{\rm tr}$ is the Drude conductivity per spin.

The main assumption of Ref. 16 is that all of the effects are due to the nontrivial energy dependence of the nonequilibrium distribution function of the conduction electrons, which satisfies the kinetic equation

$$\mathcal{E}_\omega^2\frac{\sigma^D(\omega)}{2\omega^2\nu_0}\sum_{\pm}\tilde{\nu}(\varepsilon\pm\omega)[f(\varepsilon\pm\omega)-f(\varepsilon)]$$
$$+\mathcal{E}_{dc}^2\frac{\sigma_{dc}^D}{\nu_0\tilde{\nu}(\varepsilon)}\frac{\partial}{\partial\varepsilon}\left[\tilde{\nu}^2(\varepsilon)\frac{\partial}{\partial\varepsilon}f(\varepsilon)\right]=\frac{f(\varepsilon)-f_T(\varepsilon)}{\tau_{\rm in}}. \tag{25}$$

Here $\sigma^D(\omega)$ is the Drude conductivity per spin for alternating current. If it is assumed that $|\omega\pm\omega_c|\tau_{\rm tr}\gg 1$ it is given by the expression

$$\sigma^D(\omega)=\sum_{\pm}\frac{e^2\nu_0 v_F^2}{4\tau_{\rm tr}(\omega\pm\omega_c)^2}. \tag{26}$$

In the right-hand side of Eq. (25) the inelastic processes are taken into account in the relaxation time approximation; $f_T(\varepsilon)$ is the Fermi distribution.

The main results of the authors pertain to the case of overlapping broadened Landau levels (the density of states $\tilde{\nu}=1-2\delta\cos(2\pi\varepsilon/\omega_c)$, where $\delta=\exp(-\pi/\omega_c\tau_q)\ll 1$, where τ_q is the single-particle relaxation time in the absence of magnetic field). When the smallness of δ is taken into account, the authors obtain for the oscillatory part of the distribution function

$$f_{\rm osc}(\varepsilon)=\delta\frac{\omega_c}{2\pi}\frac{\partial f_T}{\partial\varepsilon}\sin\frac{2\pi\varepsilon}{\omega_c}\frac{\mathcal{P}_\omega\dfrac{2\pi\omega}{\omega_c}\sin\dfrac{2\pi\omega}{\omega_c}+4\mathcal{Q}_{dc}}{1+\mathcal{P}_\omega\sin^2\dfrac{\pi\omega}{\omega_c}+\mathcal{Q}_{dc}}. \tag{27}$$

Here dimensionless units have been introduced for the dc and ac electric fields:

$$\mathcal{P}_\omega=\frac{\tau_{\rm in}}{\tau_{\rm tr}}\left(\frac{e\mathcal{E}_\omega v_F}{\omega}\right)^2\frac{\omega_c^2+\omega^2}{(\omega^2-\omega_c^2)^2},$$
$$\mathcal{Q}_{dc}=\frac{2\tau_{\rm in}}{\tau_{\rm tr}}\left(\frac{e\mathcal{E}_{dc}v_F}{\omega_c}\right)\left(\frac{\pi}{\omega_c}\right)^2, \tag{28}$$

where $\tau_{\rm tr}$ is the transport relaxation time for $B=0$, and $\tau_{\rm in}$ is the inelastic relaxation time. The magnetic field is assumed to be classically strong, i.e., $\omega_c\tau_{\rm tr}\gg 1$.

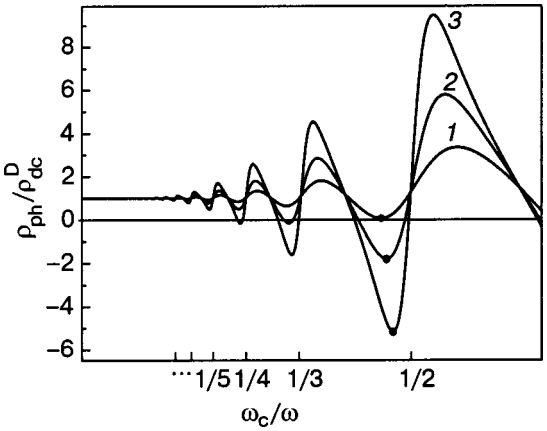

FIG. 17. Photoresistivity (normalized to the Drude value in the absence of radiation) for overlapping Landau levels as a function of ω_c/ω at a fixed value $\omega\tau_q=2\pi$ and different values of the microwave radiation power $\mathcal{P}_\omega^{(0)}$: 0.24 (*1*), 0.8 (*2*), 2.4 (*3*).

The following expression is obtained for the oscillatory part of the conductivity:

$$\frac{\sigma_{\rm ph}}{\sigma_{dc}^D}=1+2\delta^2\left[1-\frac{\mathcal{P}_\omega\dfrac{2\pi\omega}{\omega_c}\sin\dfrac{2\pi\omega}{\omega_c}+4\mathcal{Q}_{dc}}{1+\mathcal{P}_\omega\sin^2\dfrac{\pi\omega}{\omega_c}+\mathcal{Q}_{dc}}\right]. \tag{29}$$

In the linear response regime ($\mathcal{E}_{\rm dc}\to 0$) and for not too high a field of the microwave radiation, Eq. (29) gives a correction to the dark dc conductivity $\sigma_{dc}=\sigma_{dc}^D(1+2\delta^2)$, which is linear in the power of the microwave radiation:

$$\frac{\sigma_{\rm ph}-\sigma_{dc}}{\sigma_{dc}}=-4\delta^2\mathcal{P}_\omega\frac{\pi\omega}{\omega_c}\sin\frac{2\pi\omega}{\omega_c}. \tag{30}$$

Formula (29) also permits consideration of effects which are nonlinear both in the dc and in the ac electric field. The evolution of the dependence of the photoconductivity $\sigma_{\rm ph}$ on B with increasing microwave radiation power $\mathcal{P}_\omega^{(0)}=\mathcal{P}_\omega(\omega_c=0)$ is shown in Fig. 17.

The I–V characteristics of the system at sufficiently high radiation power are N-shaped:

$$\mathcal{P}_\omega>\mathcal{P}_\omega^*=\left(4\delta^2\frac{\pi\omega}{\omega_c}\sin\frac{2\pi\omega}{\omega_c}-\sin^2\frac{\pi\omega}{\omega_c}\right)^{-1}.$$

In the limit of large $\mathcal{E}_{dc}$ the conductivity is close to the Drude value and is therefore positive. The value of the dc electric field at which $\sigma_{\rm ph}$ changes sign is determined by the condition $\mathcal{Q}_{dc}=(\mathcal{P}_\omega-\mathcal{P}_\omega^*)/\mathcal{P}_\omega^*$ and is equal to

$$\mathcal{E}_{dc}^*=\sqrt{\mathcal{E}_\omega^2-\mathcal{E}_\omega^{*2}}\left[\frac{\omega_c^4(\omega^2+\omega_c^2)}{2\omega^2(\omega^2-\omega_c^2)}\right]^{1/2}$$
$$\times\frac{1}{\pi}\mathrm{Re}\left(4\delta^2\frac{\pi\omega}{\omega_c}\sin\frac{2\pi\omega}{\omega_c}-\sin^2\frac{\pi\omega}{\omega_c}\right)^{1/2}, \tag{31}$$

where $\mathcal{E}_\omega^*$ is the threshold value of the ac field at which the zero-resistance state is realized.

It should be noted that the results of Ref. 16 on the whole are also in agreement with the experimental observations.[4,6] The observed temperature dependence of the photoresistance at the maxima agrees well with the predicted

T^{-2} behavior. Typical parameters $\omega/2\pi \simeq 50-100$ GH, $\tau_q \simeq 10$ ps give $\omega\tau_q \simeq 0.5-1.0$ (overlapping Landau levels), and the experimental data are actually analogous to those shown in Fig. 17. For $T \sim 1$ K and $\varepsilon_F \sim 100$ K we find $\tau_\varepsilon^{-1} \sim 10$ mK, which is much smaller than $\tau_q^{-1} \sim 1$ K, as is assumed in the theory. Finally, for a microwave radiation power ~ 1 mW and an area of the sample ~ 1 cm^2 the dimensionless power is $\mathcal{P}_\omega^{(0)} \sim 0.005-0.1$, which is considerably lower than the predicted result for overlapping Landau levels (Fig. 17). The reason for this discrepancy must still be explained.

Obviously the conductivity is ''sensitive'' to irradiation only if Kohn's theorem is violated.[17] It is usually assumed that the cause of this violation is a random impurity potential. The authors of Ref. 14 considered a model in which Kohn′s theorem is violated for an ''internal'' reason, viz., because of a slight nonparabolicity of the electron spectrum:

$$\varepsilon(p) = \frac{p^2}{2m}\left(1 - \frac{p^2}{2mE_0}\right), \tag{32}$$

where m is the effective mass, and E_0 is an energy of the order of the width of the forbidden band. The corresponding expression for the velocity

$$\mathbf{v} = \frac{\mathbf{p}}{m}\left(1 - \frac{p^2}{mE_0}\right) \tag{33}$$

is obtained by differentiating the energy with respect to momentum.

In the model of Ref. 14 a negative σ_d arises under linear polarization of the ac field $\mathcal{E}\cos\omega t$. Let us write the classical equation of motion of an electron in an ac magnetic field **B** and dc and ac electric fields:

$$\frac{d\mathbf{p}}{dt} + \frac{\mathbf{p}}{\tau} - \frac{e}{c}[\mathbf{v}\times\mathbf{B}] = e\mathbf{E} + e\mathcal{E}\cos\omega t, \tag{34}$$

(τ is the relaxation time).

The authors of Ref. 14 seek a solution of (34) in the form

$$p_x(t) + ip_y(t) = \mathcal{P}_0 + \mathcal{P}_+ \exp(i\omega t) + \mathcal{P}_- \exp(-i\omega t). \tag{35}$$

Solving a system of equations for $\mathcal{P}_0$, $\mathcal{P}_+$, $\mathcal{P}_-$ on the assumption that $\mathcal{P}_0 \ll \mathcal{P}_+$, $\mathcal{P}_-$, $\omega \approx \omega_c |\mathcal{P}_-| \ll |\mathcal{P}_+|$ (but keeping $\mathcal{P}_-$ in lowest order), they obtain for the longitudinal and Hall conductivities

$$\sigma_d = \frac{ne^2}{m\omega_c}\left[\frac{1}{\omega_c\tau} - \left(\frac{\delta m}{2m}\right)\frac{\Omega\tau\sin 2\theta - \cos 2\theta}{\omega_c\tau}\right], \tag{36}$$

$$\sigma_t = \frac{ne^2}{m\omega_c}\left[1 - \left(\frac{\delta m}{2m}\right)\frac{\Omega\tau\cos 2\theta + \sin 2\theta}{\omega_c\tau}\right], \tag{37}$$

where

$$\frac{\delta m}{m} = \frac{|\mathcal{P}_+|^2}{mE_0} = \frac{(e\mathcal{E}\tau)^2}{4mE_0[1 + (\Omega\tau)^2]} \tag{38}$$

is a small relative correction to the electron mass due to the radiation and to the nonparabolicity of the spectrum,

$$\Omega = \omega - \omega_c + \frac{\omega_c|\mathcal{P}_+|^2}{mE_0} \ll \omega_c$$

is the deviation of the frequencies of the microwave radiation from the shifted cyclotron frequency in the ac field, n is the electron density, and $\mathcal{P}_+ = e\mathcal{E}\tau/2(1 + i\Omega\tau)$.

Here the condition under which the diagonal conductivity will be negative has the form

$$\frac{|\Omega|}{\omega_c} > \frac{2}{\omega_c\tau}\left(\frac{m}{\delta m}\right). \tag{39}$$

This condition is consistent with the assumptions $|\Omega| \ll \omega_c$ and $\delta m/m \ll 1$.

In the limit of a pure electron gas $\tau \to \infty$ formulas (36) and (37) simplify to

$$\sigma_d = -\frac{ne^2}{m\omega_c}\frac{(e\mathcal{E})^2}{8mE_0\Omega\omega_c}\sin 2\theta, \tag{40}$$

$$\sigma_t = \frac{ne^2}{m\omega_c}\left[1 - \frac{(e\mathcal{E})^2}{8mE_0\Omega\omega_c}\cos 2\theta\right]. \tag{41}$$

We note that the relaxation time τ drops out not only from σ_t but also from the diagonal conductivity. This means that the momentum relaxation necessary for dissipative transport processes is provided by scattering on the microwave field, which is coupled with the translational motion through the nonparabolic term in the dispersion relation.

Several experimental facts cannot be described in the framework of the model under discussion: the model does not give the frequency dependence of the conductivity in the entire range of frequencies (in particular, it is difficult to generalize to the case $\omega \approx n\omega_c$); the result (36), (37) for the longitudinal conductivity contains dependence on the polarization of the radiation, in contradiction with experiment.[6]

5. INSTABILITY OF ONE-DIMENSIONAL STATE OF A 2DES

The decisive result in the preceding discussions consists in the existence of regimes of magnetic field and microwave radiation power for which the longitudinal conductivity calculated in the linear response theory is negative:

$$\sigma_{xx} < 0. \tag{42}$$

However, at the same values of the cyclotron frequency and microwave radiation frequency for which the model considered above gives $\sigma_{xx} < 0$, experimentally one observes a state with zero resistivity or zero conductivity.

It was shown in Ref. 30 that formula (42) is in itself sufficient for explaining the state with zero dc resistivity observed in Refs. 4 and 6, irrespective of the details of the microscopic mechanism that leads to the validity of that formula. One uses in it the following relation between the local dc electric field **E** and the local dc current density **j**:

$$\mathbf{E} = \mathbf{j}\rho_d(j^2) + [\mathbf{j}\times\mathbf{z}]\rho_h, \tag{43}$$

where **z** is the unit vector normal to the surface of the system. It is assumed that $\rho_d(j^2)$ is a real continuous single-valued function of j^2 and that there exists a region of B, ω, and $\mathcal{P}_{ac}$ in which the spatially nonuniform zero-current state is characterized by a negative dissipative resistivity

$$\rho_d(j^2 = 0) < 0. \tag{44}$$

It is clear that at sufficiently high values of the dc current, $\rho_d(j^2)$ should return to its value in the absence of radiation,

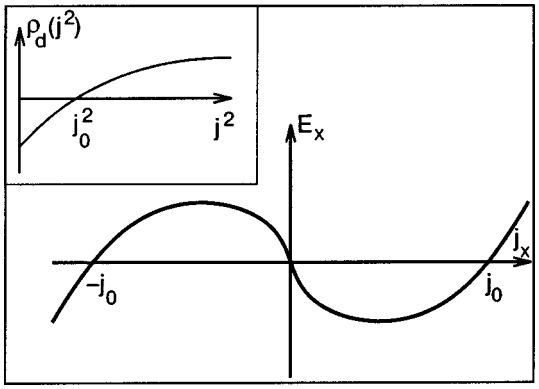

FIG. 18. Proposed form of the dependence of the dissipative component of the local electric field E_x on the current density j_x. The inset shows the dependence of the dissipative resistivity on the current density.

since in that limit the microwave radiation will be a small perturbation of the electron distribution function of the steady state. Thus it follows from continuity that there exists a value $j=j_0$ at which

$$\rho_d(j_0^2)=0, \tag{45}$$

and $\rho_d(j^2)$ has the form shown in the inset to Fig. 18. The main panel of Fig. 18 shows the S-shaped I–V characteristic that follows from the proposed form of the function $\rho_d(j^2)$.

We note that the choice of an S-shaped form of the I–V characteristic corresponds to the requirement of continuity and single-valuedness of the function $\rho_d(j^2)$. In the case of an N-shaped I–V characteristic the function $\rho_d(j^2)$ would be multivalued.

Considering the fluctuation δj around the time-independent uniform state with current j_i and using the continuity equation

$$\frac{\partial n}{\partial t}+\vec{\nabla}\cdot\mathbf{j}=0 \tag{46}$$

and Poisson's equation

$$\mathbf{E}=-\vec{\nabla}\hat{U}n, \tag{47}$$

we obtain the following expression:

$$\nabla(\hat{U}\nabla\cdot\mathbf{j})=\frac{\partial}{\partial t}[\mathbf{j}\rho_d(j^2)+[\mathbf{j}\times\mathbf{z}]\rho_H]. \tag{48}$$

Here n is the electron charge density and $\hat{U}$ is the nonlocal interaction operator, which can be expressed in terms of the Green's function of Laplace's equation with suitable boundary conditions. Importantly, $\hat{U}$ has non-negative eigenvalues (the authors assume that the screening radius is equal to zero and neglect the difference between the electric and electrochemical potentials).

Writing $\mathbf{j}(r,t)=\mathbf{j}_i+\delta\mathbf{j}(r,t)$, linearizing with respect to $\delta\mathbf{j}$, and taking the divergence of both sides of Eq. (48), we obtain

$$\frac{\partial\vec{\nabla}\cdot\delta\mathbf{j}}{\partial t}=(\vec{\nabla}(\tilde{\hat{\rho}}_d+\hat{\rho}_H)^{-1}\vec{\nabla}U)\vec{\nabla}\cdot\delta\mathbf{j}, \tag{49}$$

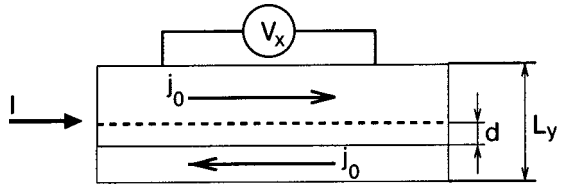

FIG. 19. Simplest possible picture of the current density distribution—a domain wall. Under the influence of the total current I the system adjusts through a shift of the position of the domain wall by a distance d; see text.

where

$$\hat{\rho}_h=\hat{\rho}_h\begin{bmatrix}0 & 1\\ -1 & 0\end{bmatrix}$$

is the usual Hall resistivity tensor,

$$\tilde{\hat{\rho}}_d=\rho_d\hat{1}+\alpha_j\,\mathbf{j}_i\otimes\mathbf{j}_i \tag{50}$$

and

$$\alpha_j=2\frac{dp_d(j)^2}{dj^2}\bigg|_{j^2=j_i^2}. \tag{51}$$

Since the Coulomb interaction operator $\hat{U}$ is positive definite, the stability is determined by the sign of the operator $\vec{\nabla}(\tilde{\hat{\rho}}_d+\hat{\rho}_H)^{-1}\vec{\nabla}$ in front of it. In order for any solution of equation (49) not to grow in time, the following condition must be satisfied:

$$\rho_d(j^2)\geqslant 0,\quad \rho_d(j^2)+\alpha_j j^2\geqslant 0. \tag{52}$$

Obviously, if even one of the quantities ρ_d or $\rho_d+\alpha_j$ is negative, then the state with a uniform current distribution is unstable.

It follows from the analysis in Ref. 30 that almost everywhere in the sample the current density has the value j_0 at which dissipative resistivity vanishes, but the direction of the current density must change in such a way that the total current agrees with the boundary conditions. The distribution of current density should contain regions of singular points, occupying a negligible fraction of the volume, where the current density takes on values different from j_0. The simplest possible form of such a singularity (domain wall) is shown in Fig. 19. It is seen in the figure that any value of the total current I corresponding to a current density much less than j_0 can be obtained by a simple change of the height of the domain wall: if d is the position of the domain wall relative to the center, then $I=2dj_0$ at $V_x=0$. Analogously, the total Hall resistance is the sum of the positive voltage in the upper half of the sample and the negative voltage in the lower half; this leads to

$$V_y=\rho_h\left[j_0\left(\frac{L_y}{2}-d\right)-j_0\left(\frac{L_y}{2}+d\right)\right]=-\rho_H I$$

and agrees with the result in the absence of radiation if the ac field does not influence ρ_H.

The model considered above explains the existence of domains, but because of the assumption of zero screening radius it cannot give the characteristics of the domain walls.

A more detailed model was considered in Refs. 26 and 33. Let us start from the basic principles. The relation between the electron density n and electric field $\mathbf{E}$ is given by Poisson's equation

$$\vec{\nabla}\cdot\mathbf{E}=\frac{4\pi e}{\varepsilon}(n-n_0), \tag{53}$$

where n_0 is the electron density in the uniform case. The current density is equal to

$$\mathbf{j}=\hat{\sigma}\mathbf{E}-e\hat{D}\vec{\nabla}n+\frac{\varepsilon}{4\pi}\frac{\partial\mathbf{E}}{\partial t}. \tag{54}$$

Here the second term is the diffusion current and the third is the displacement current. In a Corbino disk geometry $E_y=0$ all of the quantities depend only on x, and the component j_x is equal to

$$j_x=\sigma(E_x)E_x-eD\partial_x n+\frac{\varepsilon}{4\pi}\partial_t E_x. \tag{55}$$

Eliminating the electron density from (53) and (55), we obtain the partial differential equation

$$j_x=\sigma(E_x)E_x-\frac{D\varepsilon}{4\pi}\partial_x xE_x+\frac{\varepsilon}{4\pi}\partial_t E_x. \tag{56}$$

Together with the continuity equation $\partial n/\partial t+\vec{\nabla}\cdot\mathbf{j}=0$ and the equation specifying the function $\sigma(E_x)$, we obtain a closed system describing the dynamics of the distribution of the modulus of the electric field in the system. In the particular case of a stationary or uniformly moving electric-field domain we have

$$\frac{4\pi}{\varepsilon}j_x=\frac{4\pi}{\varepsilon}\sigma_0(E_x)E_x-D\partial^2_{\xi\xi}E_x-\partial_\xi E_x\left(s-\frac{\sigma_0(E_x)E_x}{en_0}\right). \tag{57}$$

Here $\sigma_0(E_x)=\sigma(E_x)n_0/n$ and $\xi=x-st$. It is assumed that $E_x(x,t)=E_x(\xi)$. Equation (55) is almost exactly the same as the equation describing the Gunn effect. The only difference is the dependence $\sigma_0(E_x)$; in particular, the center of symmetry of the N-shaped part of the I–V characteristic in this case lies at the origin of the coordinates $(E_x\partial_\xi, E_x)$.

6. CONCLUSION

Let us conclude by listing the little-studied aspects of the magnetoresistance oscillations in a magnetic field under irradiation. There has been no convincing study that would describe both the results of the experiments of Refs. 4 and 6 and also the more recent result.[20] The nature of the high activation energy for temperature dependence of the resistance at the minima of the oscillations remains puzzling. The decrease of the amplitude of the Shubnikov–de Haas oscillations in certain intervals of magnetic fields and radiation frequencies in comparison with the case of no radiation remains to be explained. At present all of the studies that have touched upon the formation of electric-field and current-density domains have considered the case of a one-dimensional domain structure. We anticipate the publication of results of numerical simulations of the formation and behavior of two-dimensional domain structures. The model of Ref. 26 utilizes a model form of the I–V characteristic of the 2DES without domains. The majority of the existing microscopic models at best give only the value of the conductance of the system in the linear response theory.

*E-mail: Lyapilin@imp.uran.ru

[1] B. A. Tavger and M. Sh. Erukhimov, Zh. Éksp. Teor. Fiz. **51**, 528 (1966) [Sov. Phys. JETP **24**, 354 (1967)]; V. I. Ryzhiĭ, Fiz. Tekh. Poluprovodn. **3**, 1704 (1969) [Sov. Phys. Semicond. **3**, 1432 (1970)]; V. L. Popovskii, L. P. Pryadko, and A. L. Talapov, J. Phys.: Condens. Matter **2**, 1583 (1990).
[2] V. I. Ryzhiĭ, Fiz. Tverd. Tela (Leningrad) **11**, 2577 (1969) [Sov. Phys. Solid State **11**, 2078 (1970)]; V. I. Ryzhiĭ, JETP Lett. **7**, 28 (1968); A. D. Gladun and V. I. Ryzhiĭ, Zh. Éksp. Teor. Fiz. **57**, 978 (1969) [Sov. Phys. JETP **30**, 534 (1970)].
[3] V. I. Ryzhiĭ, R. A. Suris, and B. S. Shchamkhalova, Fiz. Tekh. Poluprovodn. **20**, 2078 (1986) [Sov. Phys. Semicond. **20**, 1299 (1986)]; A. D. Malov and V. I. Ryzhiĭ, Fiz. Tverd. Tela (Leningrad) **14**, 2048 (1973) [Sov. Phys. Solid State **14**, 1766 (1973)]; V. I. V'yurkov, A. D. Gladun, A. D. Malov, and V. I. Ryzhiĭ, Fiz. Tverd. Tela (Leningrad) **19**, 3618 (1977) [Sov. Phys. Solid State **19**, 2113 (1977)].
[4] M. A. Zudov, R. R. Du, L. N. Pfeiffer, and K. W. West, arXiv: cond-mat/0210034; Phys. Rev. Lett. **90**, 046807 (2003); EP2DS-15, Nara, Japan (2003).
[5] C. L. Yang, M. A. Zudov, T. A. Knutilla, R. R. Du, L. N. Pfeiffer, and K. W. West, arXiv: cond-mat/0303472.
[6] R. G. Mani, J. H. Smet, K. von Klitzing, V. Narayanamurti, W. B. Johnson, and V. Umansky, Nature (London) **420**, 646 (2002); arXiv: cond-mat/0306388; arXiv: cond-mat/0303034; *26th International Conferernce on the Physics of Semiconductors*, Edinburgh, 2002; EP2DS-15, Nara, Japan (2003).
[7] Y. A. Bychkov and E. I. Rashba, J. Phys. C **17**, 6039 (1984); S. Datta and B. Das, Appl. Phys. Lett. **56**, 665 (1990); R. Eppenga and F. H. Shuurmans, Phys. Rev. **37**, 10923 (1988); A. C. Rovwe, J. Nehls, R. A. Stradling, and R. S. Ferguson, Phys. Rev. B **63**, 201307 (2001).
[8] R. M. White, *Quantum Theory of Magnetism*, 2nd ed., Springer, New York (1983), Mir, Moscow (1985).
[9] P. W. Anderson and W. F. Brinkman, arXiv: cond-mat/0302129.
[10] A. C. Durst, S. Sachdev, N. Read, and S. M. Girvin, arXiv: cond-mat/0301569; EP2DS-15, Nara, Japan 2003; Phys. Rev. Lett. **91**, 086903 (2003).
[11] J. Shi and X. C. Xie, arXiv: cond-mat/0302393; Phys. Rev. Lett. **91**, 086801 (2003).
[12] V. Ryzhii and R. Suris, arXiv: cond-mat/0307223.
[13] V. Ryzhii and V. Vyurkov, arXiv: cond-mat/0305199.
[14] A. A. Koulakov and M. E. Raikh, arXiv: cond-mat/0302465; Phys. Rev. B **68**, 115324 (2003).
[15] S. A. Mikhailov, arXiv: cond-mat/0303130.
[16] L. A. Dmitriev, M. G. Vavilov, I. L. Aleiner, A. D. Mirlin, and D. G. Polyakov, arXiv: cond-mat/0310668.
[17] W. Kohn, Phys. Rev. **128**, 1242 (1961).
[18] P. K. Tien and J. P. Gordon, Phys. Rev. **129**, 647 (1963).
[19] K. Park, arXiv: cond-mat/0312084.
[20] E. Vasiliadou, G. M. Muller, D. Heitmann, D. Weiss, K. von Klitzing, H. Nickel, and W. Schlapp, Phys. Rev. B **48**, 17145 (1993).
[21] V. I. Ryzhiĭ, R. A. Suris, and B. S. Shchamkhalova, Fiz. Tekh. Poluprovodn. **20**, 1404 (1986) [Sov. Phys. Semicond. **20**, 1299 (1986)].
[22] C. F. Lavine, R. J. Wagner, and D. C. Tsui, Surf. Sci. **113**, 112 (1982).
[23] D. Stein, G. Ebert, K. von Klitzing, and G. Weimann, Surf. Sci. **142**, 406 (1984).
[24] V. I. Ryzhiĭ, JETP Lett. **7**, 28 (1968).
[25] B. M. Askerov, *Electronic Phenomena in Semiconductors* [in Russian], Nauka, Moscow (1985).
[26] A. F. Volkov and V. V. Pavlovskii, arXiv: cond-mat/0305562.
[27] T. J. Drummond, W. Kopp, H. Morkoç, and M. Keever, Appl. Phys. Lett. **41**, 277 (1982).
[28] E. M. Lifshitz and L. P. Pitaevskii, *Physical Kinetics*, Pergamon Press, Oxford–New York (1981), Nauka, Moscow (1979).
[29] K. W. Chiu and J. J. Quinn, Phys. Rev. B **9**, 4724 (1974).
[30] A. V. Andreev, I. L. Aleiner, and A. J. Millis, arXiv: cond-mat/0302063; Phys. Rev. Lett. **91**, 056803 (2003).
[31] B. R. Nag and P. Das, Phys. Rev. **132**, 2514 (1963).
[32] L. A. Dmitriev, A. D. Mirlin, and D. G. Polyakov, arXiv: cond-mat/0304529.
[33] F. S. Bergeret, B. Huckestein, and A. F. Volkov, arXiv: cond-mat/0303530.

Translated by Steve Torstveit

Neutral and charged excitons in a CdTe-based quantum well

J. A. Gaj,* P. Płochocka, and C. Radzewicz

Institute of Experimental Physics, Warsaw University, Hoża 69, 00-681, Warsaw, Poland

P. Kossacki and W. Maślana

Institute of Experimental Physics, Warsaw University, Hoża 69, 00-681, Warsaw, Poland; Laboratoire de Spectrométrie Physique, CNRS et Université Joseph Fourier-Grenoble, B.P. 87, 38402 Saint Martin d'Héres Cedex, France

J. Cibert and S. Tatarenko

Laboratoire de Spectrométrie Physique, CNRS et Université Joseph Fourier-Grenoble, B.P. 87, 38402 Saint Martin d'Héres Cedex, France

(Submitted July 12, 2004)
Fiz. Nizk. Temp. **30**, 1133–1138 (November 2004)

We present a summary of our spectroscopic studies of the oscillator strength of transitions related to the formation of neutral and positively charged excitons in modulation *p*-doped CdTe-based quantum wells. The hole concentration was controlled in the range from 10^{10} to 10^{11} cm^{-2}. Continuous-wave and time-resolved femtosecond pump–probe absorption measurements were performed. They allowed us to study the interacting system of excitons, trions, and free holes. Characteristic times of the system were determined, such as the trion formation time. A new explanation of so-called oscillator-strength ''stealing'' has been proposed, in terms of spin-dependent screening. Experimental evidence is presented for optical creation of transient spin polarization in the quantum well. © *2004 American Institute of Physics.* [DOI: 10.1063/1.1819859]

INTRODUCTION

The existence of charged excitons (trions) in semiconductors was predicted by Lampert[1] back in the fifties. However, because of a very small dissociation energy, charged excitons were extremely difficult to observe in bulk crystals. A very different situation occurs in doped semiconductor quantum wells, where the confinement leads to a strong increase of the dissociation energy and charged excitons can be easily observed. The first experimental identification of charged excitons in a semiconductor quantum well by Kheng *et al.*[2] opened the field of experimental studies of those complexes. In particular, the optical properties of both *p*- and *n*-doped CdTe-based quantum wells have been extensively studied.[3–6] Transmission, photoluminescence, four-wave mixing, and time-resolved absorption experiments have been performed. Negatively (X^-) and positively charged (X^+) excitons are frequently observed in absorption and often dominate the excitonic photoluminescence of doped quantum wells (both in III–V and II–VI semiconductor systems).[7,8] They appear as absorption or photoluminescence lines a few meV below a neutral exciton transition.

In this paper we present a summary of our studies of positively charged excitons in modulation *p*-doped CdTe-based quantum wells. We had the possibility of controlling the hole concentration by additional illumination in the range up to 10^{11} cm^{-2}. Thus the relative intensity of charged and neutral excitons was controlled. Therefore we were able to investigate the role of the hole gas and the interplay between the charged and the neutral excitons.

EXPERIMENTS

The experimental results were obtained on modulation doped structures consisting of a single 80 Å quantum well (QW) of $Cd_{1-x}Mn_xTe(x \approx 0.0018)$ embedded between $Cd_{0.66}Zn_{0.07}Mg_{0.27}Te$ barriers grown pseudomorphically on a (100) $Cd_{0.88}Zn_{0.12}Te$ substrate. Due to strain and confinement the energy separation between heavy and light hole excitons is larger than 15 meV. Therefore only heavy hole excitons were observed in our experiments. Modulation *p*-type doping was assured by a nitrogen-doped layer placed at 200 Å from the QW. The density of the hole gas in the QW was controlled by an additional illumination with photon energy above the gap of the barriers, provided by a tungsten halogen lamp with a blue filter: the control mechanism and its calibration are described in detail in Ref. 9.

The continuous wave (cw) transmission through the sample was measured as a function of hole gas density. The external magnetic field was applied in a Faraday configuration. We also measured time resolved absorption in a pump–probe configuration. The pulses were generated by a $Ti^{3+}:Al_2O_3$ laser tuned to 765 nm (1620 meV), at a repetition rate of 100 MHz. The duration of the laser pulse was about 100 fs and the spectral width about 40 nm (80 meV), which is much broader than the separation between the neutral exciton line X and the charged exciton line X^+. To excite only one transition (charged or neutral exciton) the pump pulse was shaped to a spectral width less than 1 nm and a duration of about 2 ps, thus creating either X, or X^+ by the binding of an additional hole. We analyzed the dynamics of both transitions by a spectrally broad probe pulse. The pump

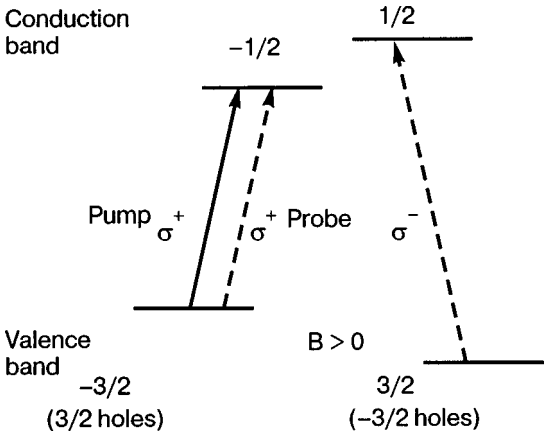

FIG. 1. Optical transitions for pump and probe pulses in magnetic field $B>0$.

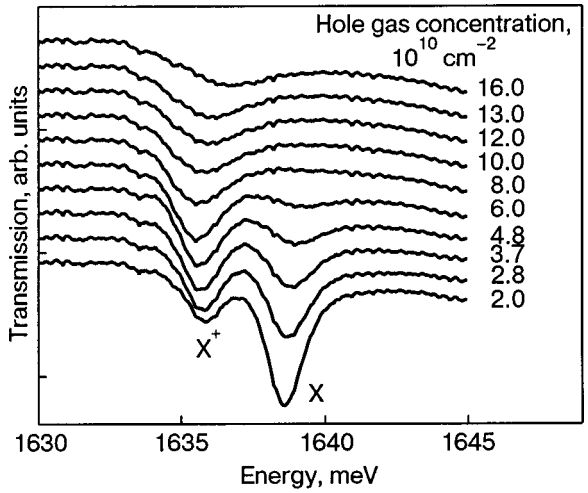

FIG. 2. Transmission through the quantum well measured for different hole concentrations.

and probe pulses were focused on the sample to a common spot of diameter smaller than 100 μm, and the spectrum of the pump pulse transmitted through the sample was recorded as a function of the pump–probe delay. The power of both pulses was controlled independently, the pump-to-probe intensity ratio being at least 20:1. The average power of the pump beam was typically 300 μW, which results in the creation of a few times 10^{10} cm^{-2} excitons by each pulse. The pump beam was polarized circularly (by convention, σ^+, creating electrons with spin $-1/2$ in the conduction band and holes of momentum $+3/2$ in the $-3/2$ spin-down valence subband; Fig. 1). The probe beam was detected behind the sample in both circular polarizations, measuring the absorption associated with the creation of either X or X^+ having electron–hole pairs of the same spin as the pump (σ^+, co-polarized) or opposite (σ^-, cross-polarized). Therefore, we could analyze the influence of the charged exciton on the neutral exciton and separate spin-dependent contribution by separation of the light polarization. Additionally, by applying magnetic field we were able to resolve all four polarization configurations: pump with σ^- and probe with $\sigma^+(-/+)$ or $\sigma^-(-/-)$ polarization, and pump with σ^+ and probe with $\sigma^+(+/+)$ or $\sigma^-(+/-)$ polarization. To analyze the neutral and charged exciton line intensities two Gaussian functions were fitted to the cw or time-resolved spectra. In some experiments difference spectra were analyzed to expose the change in the optical absorption under the influence of the pump pulse.

RESULTS

Continuous wave measurements

Let us start from results obtained in cw transmission measurements. Figure 2 shows the transmission through the quantum well, measured for different hole concentrations. Two absorption lines are observed. The higher-energy line is related to the neutral exciton (X). The second line, lying at lower energy, is related to the positively charged exciton (X^+). A strong influence of the hole gas on intensity of both transitions is observed. The neutral exciton intensity decreases with increasing hole concentration. Simultaneously the charged exciton intensity increases. For low hole concentrations the charged exciton intensity is proportional to the hole concentration in the relevant spin subband. However, for higher hole concentration the intensity of the charged exciton saturates, because states with higher **k** are filled.

The changes of relative intensity of the charged and neutral exciton were observed for both negatively and positively charged excitons.[2,9,10] This effect was called oscillator-strength stealing (OSS) from the neutral exciton by the charged exciton. However, the change of the charged exciton oscillator strength is not equal to the change of the neutral exciton oscillator strength. In this way the sum rule is not applicable; only after taking into account additional optical transitions involving scattering processes is the sum rule approximately obeyed.[3,11] We will show that it is possible to explain the reduction of the neutral exciton intensity by screening: a normal and a spin-dependent one. The two types of screening can be separated by magnetooptical experiments.

Measurements of the cw optical density in external magnetic field were also performed. The selection rules for charged and neutral exciton are the same as for pump–probe experiments, presented in Fig. 1. In Fig. 3a the transmission spectra in both polarizations in magnetic field are shown. In the σ^+ polarization we observe that the neutral exciton line dominates the charged exciton line. In Fig. 3b, where the intensities of the neutral and charged exciton lines are plotted versus magnetic field, the charged exciton line completely disappears at -0.3 T. However, for the σ^- polarization the charged exciton line gets stronger with increasing magnetic field. In magnetic field as low as 0.3 T the hole gas is fully polarized in one spin subband, due to the giant Zeeman effect in the semimagnetic QW. A charged exciton is formed by the binding of an additional hole from the pre-existing gas, with spin opposite to those created by the light. In one polarization trions cannot be formed—there are no pre-existing holes in the opposite spin subband. In the opposite polarization the intensity of the charged exciton dominates, while the intensity of the neutral exciton is smaller. This correlation between charged and neutral exciton intensities became known as intensity or oscillator-strength stealing. No microscopic explanation of this effect has been proposed so far. Using external magnetic field and external illumination

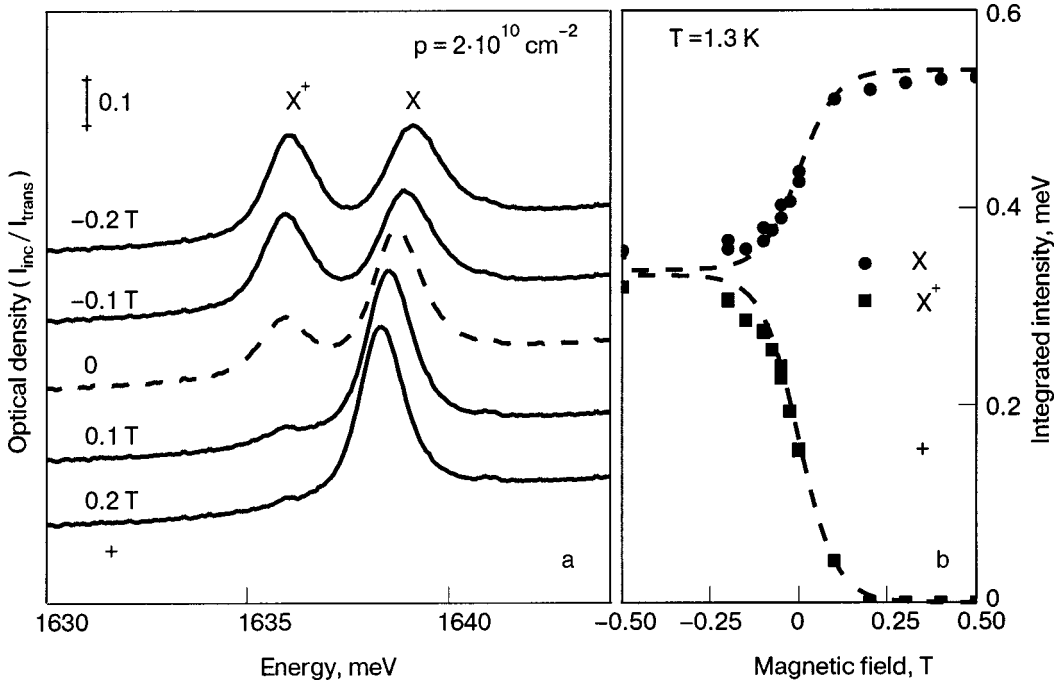

FIG. 3. Optical density of a CdMnTe quantum well in magnetic field (hole concentration was $p=2\times10^{10}$ cm^{-2}) (a). Integrated line intensities as a function of magnetic field (b).

we can control the relative number of charged and neutral excitons. An important conclusion from the cw measurements is that the spin-dependent effects are essential. However, their exact nature still remained unclear. Significant progress was obtained in time-resolved studies.

Time-resolved absorption measurements

We measured the time-resolved absorption[6] hoping to explain the origin of the oscillator-strength stealing. In Fig. 4a the optical density for negative and short positive delays (0.5 ps) is presented. We observe two absorption lines, one related to the charged exciton, the other to the neutral exciton. At zero delay (when the strong pump pulse excites the sample) the intensity of the charged exciton decreases and the intensity of the neutral exciton increases for co-polarized pump and probe pulses. The line intensities are plotted versus pump–probe delay time in Fig. 4b,c. The temporal evolution of the oscillator strength of the charged and neutral excitons is shown Fig. 4b for co- and cross-polarized beams when the pump pulse is tuned to resonance with the charged exciton. Results for pump pulse tuned to the neutral exciton are presented in Fig. 4c.

Let us start the discussion for the case of co-polarized beams. We observe an intensity decrease of the charged exciton, accompanied by an intensity increase of the exciton at zero delay time. This variation is faster when the pump pulse

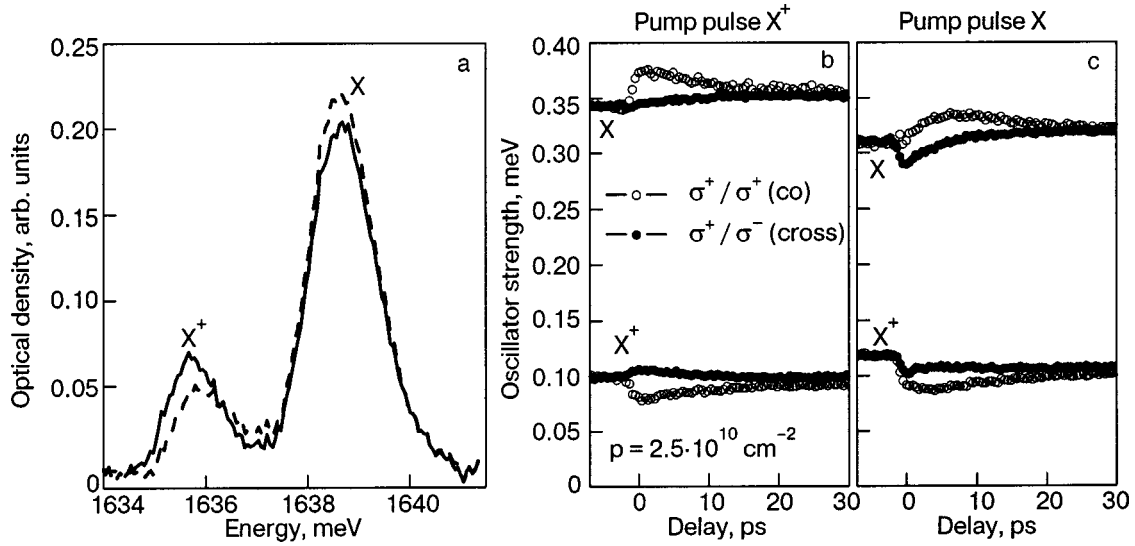

FIG. 4. Optical density for a QW with hole density $p\approx2.5\times10^{10}$ cm^{-2}, at negative delay (-8 ps, solid line) and short positive delays (0.5 ps, dashed line), for a co-polarized pump pulse tuned to X^+ (a); evolution of the X and X^+ oscillator strength with pump pulse tuned to X^+ (b); evolution of X and X^+ with pump pulse tuned to X (c).

is tuned to resonance with the charged exciton; when the pump pulse is tuned to resonance with the neutral exciton, the same effects are observed with a delay. We observe the same behavior as that observed in cw transmission measurements (Fig. 2), with one important difference: now we do not modify the density of pre-existing holes. The only thing that changes in the time-resolved measurements is the occupation of charged exciton states. This fact led us to a new explanation of the oscillator-strength stealing phenomena, in terms of spin-dependent screening. Let us assume that intensity of neutral exciton decreases due to screening by holes with spin opposite to the spin of the hole created by light. In this way we can explain why in cw measurements the increase of the hole density results in a decrease of neutral exciton intensity. In time-resolved results, the holes bound into charged excitons (resonant creation of charged excitons by the pump) cannot screen the neutral exciton any more, and its intensity increases, as shown in Fig. 4b. The decrease of the charged exciton intensity is due to bleaching of the transition: the number of charged excitons created by the pump pulse is comparable with the number of pre-existing holes; therefore the probe pulse with the same polarization cannot form charged excitons—the transition is blocked. The conclusion is that the decrease of neutral exciton intensity is due to screening by holes with spin opposite to that of the holes involved in the neutral exciton—a spin-dependent effect. The second important conclusion is that the binding of holes into charged excitons excludes them from interaction with the rest of the system, specifically from screening the neutral exciton. In the case of pumping into the neutral exciton we observed the same effect, but the increase of the neutral exciton intensity is delayed. In this case the charged exciton is not formed directly. The pump creates neutral excitons, and then some time is needed to bind additional holes and form charged excitons. Therefore the increase of the neutral exciton intensity, when the pump pulse is tuned to resonance with the neutral exciton, occurs with a rise time related to the formation of charged excitons. We found that this rise time depends on hole concentration in the following way: 5, 2, and 1 ps for hole densities of 2.5×10^{10}, 3×10^{10}, and 4×10^{10} cm^{-2}, respectively.[6] The formation time is faster for higher hole concentration, in good agreement with the PL results presented in Refs. 12 and 13.

Let us turn to the situation when the pump and probe pulses are cross-polarized. We observe a completely different time evolution of charged and neutral exciton intensities depending on whether the pump pulse is tuned to resonance with the charged or neutral exciton. In Fig. 4b (pump resonant with X^+) the intensity of the charged exciton increases slightly and the intensity of the neutral exciton remains constant in time. However, when we tune the pump pulse to resonance with neutral exciton (Fig. 4c), the intensity of both transitions decreases at zero delay. This behavior can be explained by spin-dependent screening. When we pump into the charged exciton we bind holes. The charged exciton is sensitive to holes with both spins (because it consists of two holes with opposite spin). The bound holes are excluded from screening trions, which increase in intensity. In co-polarization this effect is masked by the bleaching discussed previously. When we pump the neutral exciton, a decrease in intensity is observed in cross-polarization for both neutral and charged excitons. We explain it by exciton–exciton interaction: screening and phase space filling.

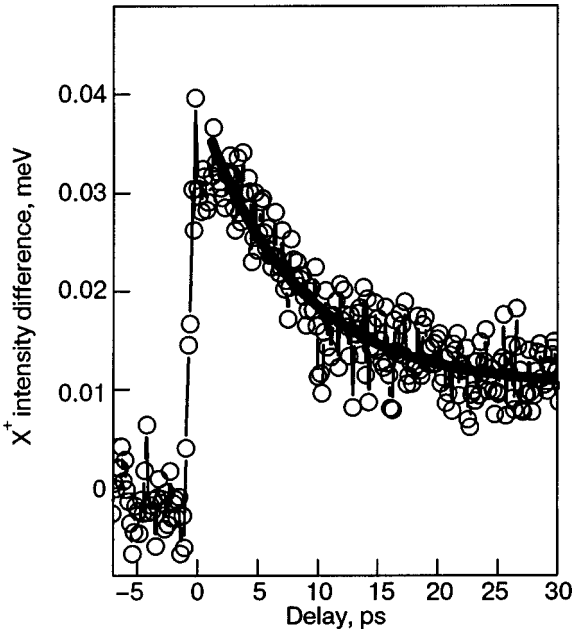

FIG. 5. Temporal evolution of the difference between charged exciton oscillator strengths observed in ''cross'' and ''co'' circular polarizations without external magnetic field. The curve presents a fit by exponential decay with decay time of 8 ps.

We can use the fact that the charged exciton intensity is proportional to the density of holes in the relevant spin subband to find characteristic time of the heavy hole spin flip. Let us assume that a strong pump pulse creates a nonequilibrium population of heavy holes in one spin subband. Then the intensity of the charged exciton when the probe pulse is σ^+ polarized is proportional to the density of holes in the spin 3/2 subband. For σ^- polarization of the probe pulse the intensity of the charged exciton is proportional to the number of heavy holes with spin $-3/2$. Therefore, the time evolution of the difference of the intensities of the charged exciton in the two circular polarizations gives us information about spin relaxation of the heavy holes. In a complicated systems like ours, other spin polarizations (of excitons, trions) can also be responsible for the intensity difference. However, we believe that the hole spin polarization is predominant. In Fig. 5 the temporal evolution of the difference between co- and cross-polarized intensities of the charged exciton is plotted. The decay time is 8 ps, and we found it weakly dependent on the hole concentration in the investigated range. This value is comparable to the spin relaxation times determined for holes bound in excitons and trions. Photoluminescence experiments with much lower excitation power and very similar heterostructures gave values from about 3 ps (Ref. 14) through 20 ps (Ref. 12) up to 35 ps (Ref. 13),

CONCLUSIONS

We have shown that pump–probe time-resolved absorption measurements can be a useful tool for studying interaction mechanisms in the exciton–carrier–trion system. We proposed a new explanation of the known oscillator-strength

stealing effect by spin-dependent screening. We showed experimentally a new optical creation mechanism of spin polarization of a 2D carrier gas in a semiconductor quantum well. Pump–probe absorption experiments enabled us to measure characteristic times of the excitons and carriers, such as the trion creation time or spin relaxation time.

This work has been partially supported by KBN Grants 2 P03B 002 25 and PBZ-KBN-044/P03/2001, and the Polonium program.

*E-mail: Jan.Gaj@fuw.edu.pl

[1] M. S. Lampert, Phys. Rev. Lett. **1**, 450 (1958).
[2] K. Kheng, R. Cox, Y. Merle d'Aubigné, F. Bassani, K. Saminadayar, and S. Tatarenko, Phys. Rev. Lett. **71**, 1752 (1993).
[3] R. T. Cox, R. B. Miller, K. Saminadayar, and T. Baron, Phys. Rev. B **69**, 235303 (2004).
[4] K. Kheng, Ann. Phys. **20**, 229 (1995).
[5] G. V. Astakhov, D. R. Yakovlev, V. P. Kochereshko, W. Ossau, J. Nurnberger, and W. Faschinger, Phys. Rev. B **60**, R8485 (1999).
[6] P. Plochocka, P. Kossacki, W. Maoelana, J. Cibert, S. Tatarenko, C. Radzewicz, and J. A. Gaj, Phys. Rev. Lett. **92**, 177402 (2004).
[7] G. Finkelstein, H. Shtrikman, and I. Bar-Joseph, Phys. Rev. Lett. **976**, 74 (1995).
[8] A. J. Shields, J. L. Osborne, M. Y. Simmons, M. Pepper, and D. A. Ritchie, Phys. Rev. B **52**, 5523 (1995).
[9] P. Kossacki, J. Cibert, D. Ferrand, Y. Merle d'Aubigné, A. Arnoult, A. Wasiela, S. Tatarenko, and J. A. Gaj, Phys. Rev. B **60**, 16018 (1999).
[10] T. Brunhes, R. André, A. Arnoult, J. Cibert, and A. Wasiela, Phys. Rev. B **60**, 11568 (1999).
[11] A. Esser, R. Zimmermann, and E. Runge, Phys. Status Solidi B **227**, 317 (2001).
[12] E. Vanelle, M. Paillard, X. Marie, T. Amand, P. Gilliot, D. Brinkmann, R. Lévy, J. Cibert, and S. Tatarenko, Phys. Rev. B **62**, 2696 (2000).
[13] P. Kossacki, J. Phys. C **13**, R471 (2003), and references cited therein.
[14] C. Camilleri, F. Teppe, D. Scalbert, Y. G. Semenov, M. Nawrocki, M. Dyakonov, J. Cibert, S. Tatarenko, and T. Wojtowicz, Phys. Rev. B **64**, 085331 (2001).

This article was published in English in the original Russian journal. Reproduced here with stylistic changes by AIP.

Magnetotransport probing of the quality of the heterointerfaces and degree of symmetry of the potential profile of quantum wells in the valence band of the $Ge_{1-x}Si_x/Ge/Ge_{1-x}Si_x$ heterosystem

M. V. Yakunin,* G. A. Alshanskii, Yu. G. Arapov, V. N. Neverov, G. I. Harus, and N. G. Shelushinina

Institute of Metal Physics of the Urals Division of the Russian Academy of Sciences, Sofia Kovalevskaya St., 18, Ekaterinburg 620219, Russia

O. A. Kuznetsov

Physicotechnical Institute of Nizny Novgorod State University, Nizhny Novgorod 603600, Russia

A. de Visser and L. Ponomarenko

Van der Waals-Zeeman Institute, University of Amsterdam, The Netherlands
(Submitted June 24, 2004)
Fiz. Nizk. Temp. **30**, 1139–1145 (November 2004)

It is shown that in a periodic system of p-type $Ge_{1-x}Si_x/Ge/Ge_{1-x}Si_x$ quantum wells having a Ge layer more than ~ 30 nm wide, the hole gas in each Ge layer is separated into two two-dimensional sublayers concentrated near opposite boundaries of the layer. This follows from the vanishing of the quantum Hall effect plateau and of the corresponding minimum of the longitudinal magnetoresistance for a filling factor $\nu=1$. Here positive magnetoresistance is observed, which is attributed to the presence of two types of holes with different mobilities. A quantitative analysis shows that these are mainly heavy holes having different mobilities in the sublayers that form. The difference of the mobilities indicates that the opposite heterointerfaces of the Ge layers are of different quality. It follows from an analysis of the shape of the quantum Hall effect plateau for $\nu=2$ that the densities of holes in the sublayers formed are close and, consequently, that the profile of the potential wells is close to symmetric. © *2004 American Institute of Physics.* [DOI: 10.1063/1.1819860]

INTRODUCTION

Heterosystems consisting of layers of Si, Ge, and their solid solutions are of interest in connection with the significant improvements that have been achieved in the parameters of devices based on them (as compared with those made from the analogous bulk materials) for today's applications. Because of this, and also the relatively low cost of these materials, they are promising objects that can compete with other heterosystems.[1,2] For achieving high mobility of the carriers in the layer (which is essential for increasing the working frequency) an important role is played by the quality of the heterointerfaces: its geometric irregularities should be minimized, its sharpness should be maximized, and the fraction of impurities located on and near the interface should be minimized. This last factor is important, since high mobilities are achieved only through selective doping of the barriers, so that the ionized impurities are partitioned from the free carriers in the potential well by an undoped part of the barrier—a spacer. An impurity can diffuse from the nominal doping region and approach the heterointerface and even reach it. An increase in mobility can also be brought about by increasing the width of the well, since the average position of the carriers is then farther away from the heterointerface and from the doped region of the barriers. However, the latter process is prevented by the bending of the bottom of the well that occurs during growth of its width. For all of these reasons it is important to find methods for quality control of heterointerfaces and for monitoring the profile of the potential well.

In the heterosystems under study the potential well is predominantly formed in the valence band of the layer with the larger Ge content.[2] Therefore here the holes mainly form a size-quantized gas.

In studying the quantum Hall effect (QHE) we have found that in a multilayer system of p-type $Ge/Ge_{1-x}Si_x$ at a Ge layer thickness greater than ~ 30 nm the hole gas in each Ge layer separates into two two-dimensional sublayers.[3] On the one hand, this establishes a limit on the existence of a unified quasi-two-dimensional hole gas in the Ge layer (i.e., on the maximum distance of the holes from the heterointerface). On the other hand, since the holes are localized near one of the heterointerfaces in the two-dimensional sublayers that form, and the characteristics of that particular heterointerface influence the mobility of the holes near it, it becomes possible to carry out a comparative analysis of the opposite boundaries of the Ge layers.

SAMPLES AND EXPERIMENT

We shall present the results of measurements of the longitudinal $\rho_{xx}(B)$ and Hall $\rho_{xy}(B)$ magnetoresistivities (MRs) of multilayer $Ge/Ge_{1-x}Si_x$ samples with $x \approx 0.1$, grown on a substrate with the (111) orientation. The central part of the

TABLE I. Parameters of the $Ge/Ge_{1-x}Si_x$ multilayer samples.

Sample	N	d_w, nm	p_s, 10^{15} m^{-3}	μ, m^2/(V·5)
1006	90	12.5	4.9	1.4
1124b3	27	22	2.8	1.0
475a2	37	38	5	1.3
476a4	37	38	5	0.85
476b4	37	38	5.8	0.98

$Ge_{1-x}Si_x$ barriers is doped with boron. The samples differ in the width d_w of the Ge layers, the density p_s of the hole gas in them, and also the hole mobility μ and the number of $Ge/Ge_{1-x}Si_x$ periods N (for the parameters of the samples, see Table I).

The hole mobilities are rather high for observation of a clear picture of the QHE. Figure 1 shows a typical QHE pattern for Ge layers ~ 20 nm thick. (The resistivity in each of the figures is given per conducting Ge layer.) We call attention to the fact that the features of the QHE, i.e., the "shelves" on $\rho_{xy}(B)=h/e^2i$ and the corresponding minima of $\rho_{xx}(B)$, are predominant at even values of i, but features are also observed for $i=1$. Negative magnetoresistance appears in the region of low magnetic fields (due to weak localization effects).

In the samples with Ge layer widths greater than ~ 30 nm the structure of the experimental curves changes substantially: the QHE feature for $i=1$ vanishes (Fig. 2), and a positive magnetoresistance appears which is expressed particularly clearly at low magnetic fields (Fig. 3).

SEPARATION OF THE HOLE GAS INTO TWO TWO-DIMENSIONAL SUBLAYERS

The vanishing of the QHE features for $i=1$ in samples with wide Ge layers indicates that the hole gas in the layers separates into two two-dimensional sublayers concentrated near opposite heterointerfaces.[4] The appearance of such an effect can be expected starting with a certain width of the potential well under the condition that its profile is symmetric (or at least that the deviations from symmetry are small). For the investigated series of samples with different widths of the Ge layer, the QHE feature for $i=1$ vanishes starting at

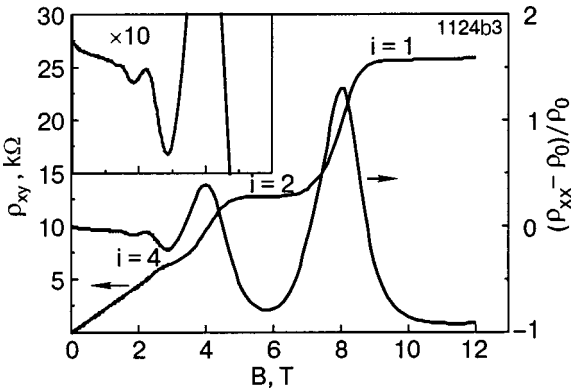

FIG. 1. Quantum Hall effect in sample 1124b3 ($d_w=22$ nm).

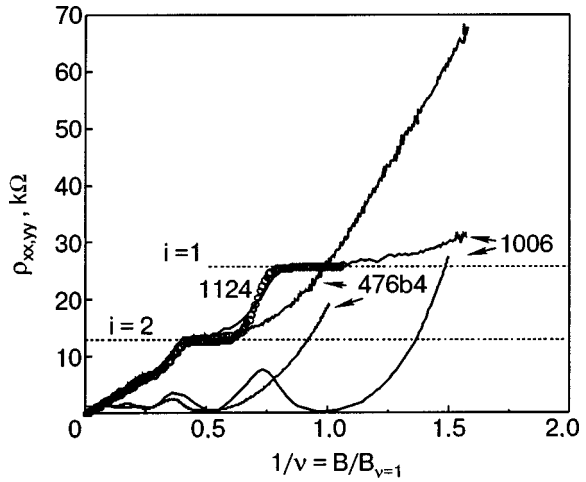

FIG. 2. Quantum Hall effect in Ge layers of different widths. The QHE features with $i=1$ vanish for a width of the Ge layer greater than ~ 30 nm.

$d_w \approx 30$ nm. The vanishing of this feature means that the profile of the potential well is symmetric, since otherwise in a wide asymmetric well the free carriers would simply leak into one of the triangular wells forming near the heterointerface. Such a situation is observed for one-sided doping of a potential well and for isolated wells found near the surface because of the influence of the charged surface states (see, e.g., Ref. 5). The symmetric nature of the profile of the potential wells in the samples that we investigated is probably promoted by their multilayeredness. The structure of the symmetric potential well for sample 475a2, calculated from the joint solution of the Schrödinger equation and Poisson's equation, is presented in Fig. 4. The Fermi level is found near the top of the curved bottom of this well, as is typical for the process of separation of a hole gas. However, the main sign of separation into two independent sublayers is the practically complete coalescence of the lower levels HH1 and HH2. The tunneling gap is practically absent (it amounts to $\sim 1\ \mu$V) because of the large width of the barrier formed and the large mass of the heavy holes.

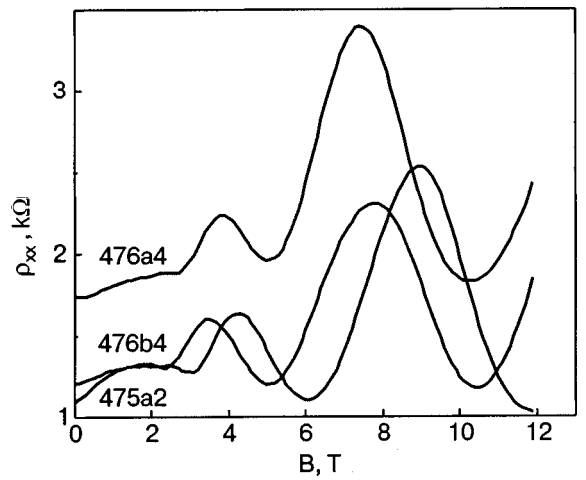

FIG. 3. Positive magnetoresistance in samples with a width of the Ge layer greater than 30 nm.

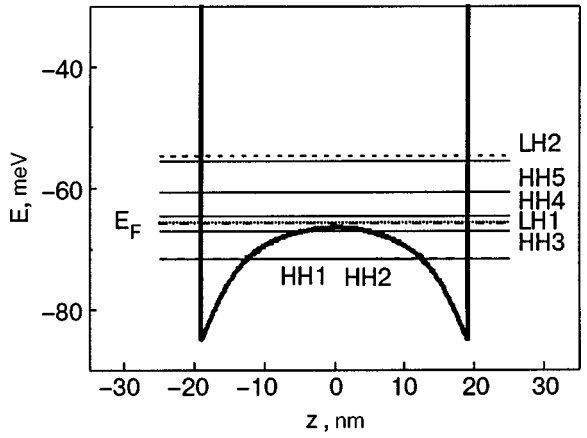

FIG. 4. Calculated potential profile, the energy levels, and the Fermi level of sample 475a2.

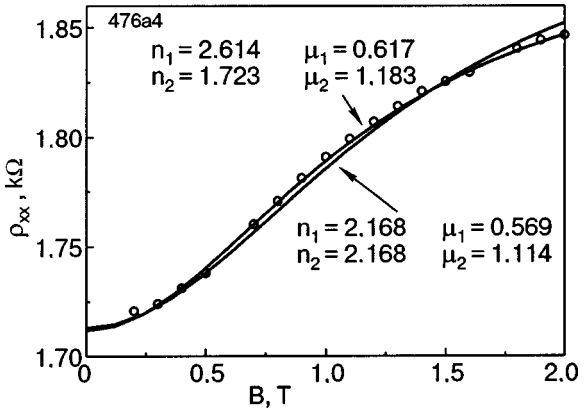

FIG. 5. Magnetoresistance of sample 476a4. Experiment (○); the solid curves were calculated according to formula (1) for two sets of parameters.

POSITIVE MAGNETORESISTANCE: A SIGN THAT THE OPPOSITE HETEROINTERFACES ARE DIFFERENT

The positive magnetoresistance in a perpendicular magnetic field is quite easily described by the participation of two types of carriers, with different mobilities, in the magnetotransport. The fact that positive magnetoresistance arises in samples with wide Ge layers in the same cases when the QHE feature with $i=1$ vanishes, i.e., when the hole gas separates into two two-dimensional sublayers, can be explained by the conjecture that holes with different mobility are found in the different sublayers. Thus the difference of their mobilities indicates that the opposite boundaries of the layer are of different quality. This difference is unsurprising, since these boundaries are formed under different conditions: the heterointerface of the Ge layer on the side farther from the substrate (the normal boundary) grows on a layer of pure elemental Ge, whereas the boundary nearer the substrate (the inverted boundary) grows on a layer of solid solution $Ge_{1-x}Si_x$ and, most importantly, that layer is doped. And although there is nominally an undoped spacer layer between the impurity layer and the heterointerface, in actuality an impurity can ''float up'' during growth, approaching and possibly even reaching the boundary with the Ge layer. It is therefore to be expected that the hole mobility is lower near the inverted heterointerface than near the normal boundary.[6] In relatively narrow layers every hole is sensitive to both boundaries, and therefore the holes all have the same mobility. Upon separation into hole sublayers in the case of a wide Ge layer the holes in each of the sublayers formed can have different mobilities.

The longitudinal and Hall magnetoresistivities in the presence of two types of carriers with different mobilities μ_j are described in the framework of the extremely simple Drude–Lorentz model by the formulas[7]

$$\rho_{xx}=(D_1+D_2)/[(D_1+D_2)^2+(A_1+A_2)^2],$$

$$\rho_{xy}=-(A_1+A_2)/[(D_1+D_2)^2+(A_1+A_2)^2]. \qquad (1)$$

Here $D_j=n_j e\mu_j/(1+\mu_j B)$ is the diagonal term of the conductivity matrix for layer j, $A_j=\mu_j B D_j$ is the corresponding off-diagonal term, and n_j is the density of the 2D hole gas in sublayer j.

The curves of ρ calculated according to formula (1) for sample 476a4 are shown in Fig. 5. It is seen that both for equal densities of the hole gas in the layers, $n_1=n_2$, and also (with a somewhat better agreement with experiment) for $n_1 \neq n_2$ the mobilities in the sublayers must differ by roughly a factor of two.

It also follows from the results of the fitting that this method is rather insensitive to the difference in the densities of the hole gas in the sublayers. In the case of a large number of oscillations of $\rho_{xx}(B)$, which occurs, e.g., in the conventional heterosystem of n-type GaAs/AlGaAs,[8,9] the difference between n_1 and n_2 can be determined from two different series of oscillations. In a hole gas, however, this cannot be done.

ESTIMATE OF THE RATIO OF THE DENSITIES OF THE HOLE GAS IN THE SUBLAYERS FROM THE STRUCTURE OF THE QHE

Let us first answer the question of how the QHE feature can be realized for the Ge layer as a whole at a definite value of i $(=2)$ in the face of such a large difference in the mobilities in the sublayers. Even at equal hole densities in the two sublayers the difference of their resistivities will be proportional to the difference of the hole mobilities, and when the sublayers are connected in parallel into a common circuit the currents flowing along the sublayers will differ by the same factor. If two given sublayers are considered to be isolated from each other, then in each of them the first plateau of $\rho_{xy}(B)$ from the high-field end will correspond to $i=1$, i.e., will have a height $\rho_{xy}=25.813$ kΩ. However, the voltages $U^l_{xy}=\rho_{xy}I^l$ corresponding to them will be different on account of the difference of the currents I^l (the index l numbers the layer). Then if one considers the classical situation for an initially uniform distribution of the current streamlines over the width of the sample, then when the corresponding potential contacts of the sublayers are connected, because of the potential difference across these contacts circulating currents should flow between them, distorting the pattern of streamlines in each sublayer. After these contacts are connected the potentials across them change, and a calculation of the value of the potential difference formed across such

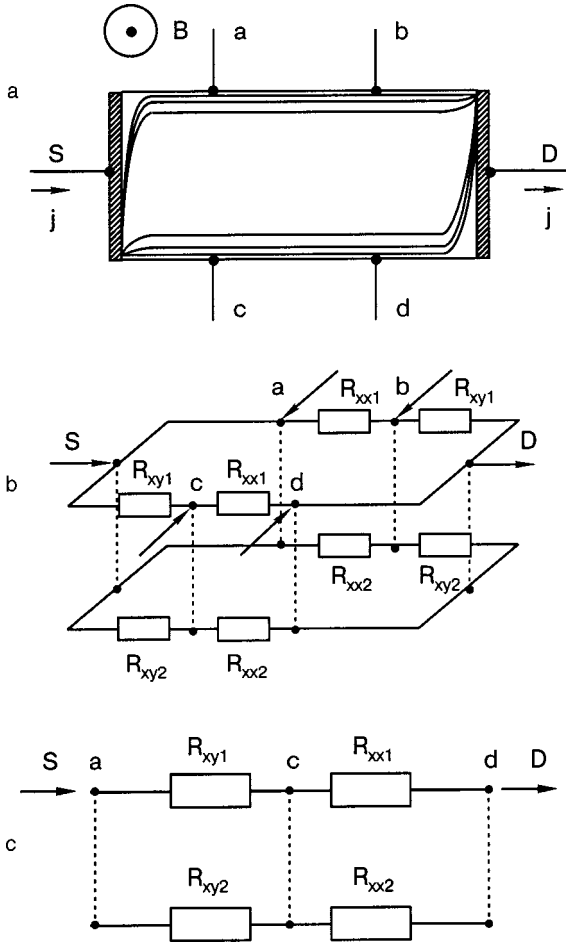

FIG. 6. Equivalent circuit of a system of two layers in the QHE regime. The current streamlines in an isolated 2D layer (a); the distribution of the Hall and longitudinal resistances in the layer (b); the layer resistances connected in parallel (c).

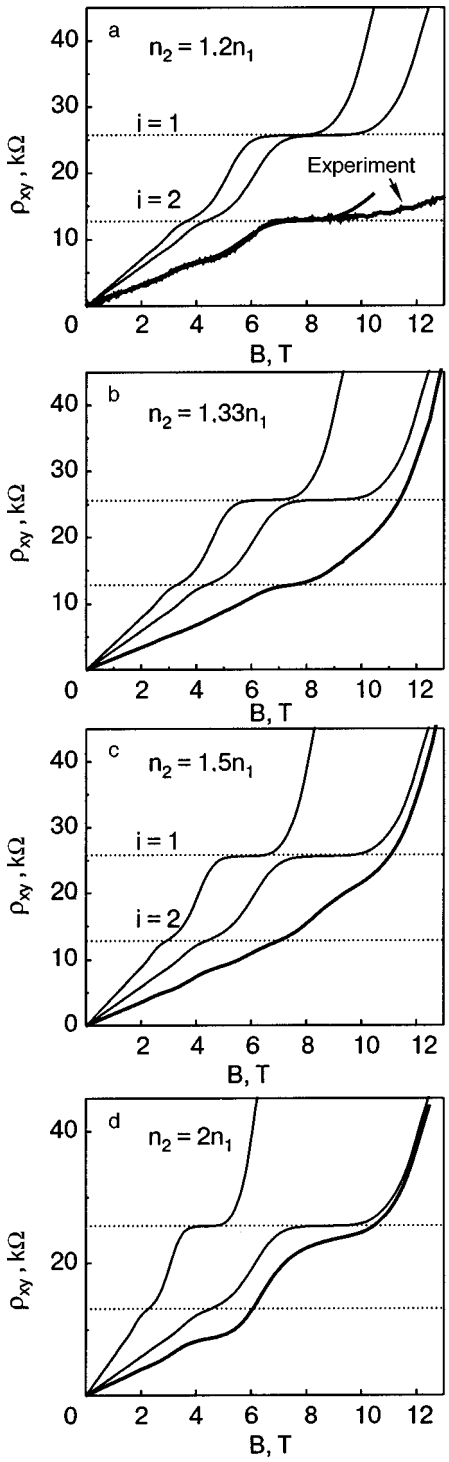

FIG. 7. Transformation of the resultant Hall resistance of two parallel layers for increasing differences of the hole concentrations in them. The top two curves are for the individual layers; the lower curve is the result of their connection in parallel. a) $n_2 = 1.2n_1$; the resultant model curve is compared with the experimental curve for sample 475b4.

joined Hall contacts in a circuit with distributed parameters and currents circulating in the transverse direction is, generally speaking, not a simple problem.

In actuality, in the QHE regime the classical picture of the uniform distribution of current over the cross section does not apply. At zero temperature ideal 2D layers (i.e., in the complete absence of any parallel 3D conduction) in the interval of magnetic fields corresponding to the QHE the potential along the whole perimeter of the sample can take on only two values, so that the difference of these potentials is equal to h/ie^2 (Ref. 10). In this case discontinuity of the equipotential lines occurs only at two points—at the inlet and outlet of the current.[11] This means that even when the end of the sample is completely coated with a conducting material, the current will flow into the body of the sample only at one point—at the edge of the contact of the conducting coating with the sample, and it will flow out only at a single diagonally opposite point (see Fig. 6a, which shows the current streamlines in a rectangular bar in the QHE regime).

In the equivalent circuit of the 2D layer the Hall resistance will be represented by two resistors R_{xyl} corresponding to the aforementioned two discontinuities of the equipotentials (Fig. 6b). Indeed, as is seen in Fig. 6b, the voltage drop across the left resistor R_{xy} in a layer taken separately is equal to the voltage between contacts a–c, and the voltage drop across the right resistor R_{xy} is equal to the voltage between contacts b–d. Thus the Hall potential difference in the QHE regime occurs in a vanishingly small region on the perimeter of the sample. In this scheme all the deviations from the ideal QHE regime, responsible for the nonzero value of the longitudinal resistance in the region of the QHE plateau, accumulate as the current flows along the perimeter from the inlet point to the outlet point. This part is represented on the

equivalent circuit by the resistors R_{xx}. It is these resistors that reflect the finite value of the mobility in the QHE plateau region in a real sample. The given equivalent circuit shows that in the QHE regime one can get away from a problem with distributed parameters. As a result, for layers connected in parallel the Hall resistances R_{xyl} of the different layers turn out to be connected in parallel with each other, just as the longitudinal resistances R_{xxl} are (Fig. 6c). Importantly, here the resultant resistances R_{xy} and R_{xx} turn out to be completely decoupled: they are mutually independent and uniquely determined by the corresponding single-layer components.

Thus for a parallel connection of the 2D layers in the QHE regime the differences in the mobility of the carriers in the individual layers has no effect on the resultant value of the Hall resistance of the system. Consequently, for finding the resultant Hall resistance of the sublayers one can treat them as equivalent irrespective of the differences in mobility. Therefore, in the case of a parallel connection of two identical 2D layers ($n_1 = n_2$) in the magnetic field interval in which each isolated layer has a QHE plateau of height $\rho_{xy} = h/e^2 = 25.814$ kΩ, a two-layer system will have a plateau with $\rho_{xy} = h/2e^2 = 12.907$ kΩ.

If the densities of the two-dimensional carrier gas in the layers are different ($n_1 \neq n_2$), then a two-layer system will exhibit a shortened plateau with $\rho_{xy} = h/2e^2 = 12.907$ kΩ in the field interval in which for the isolated layers the shelves overlap. In the two-layer system the shelf with $\rho_{xy} = h/e^2 = 25.814$ kΩ will be absent (see Fig. 7, where we present the results of a mathematical modeling of this situation).

With increasing difference of the densities of the 2D gas in the sublayers the plateau that initially was clearly discernable around $i = 2$ for the system (Fig. 7a) is first smeared out (Fig. 7b,c) and then reforms, but now around $i = 1$ (Fig. 7d). Our experimental results for sample 475b4 (Fig. 7a) coincide with the resulting model curve for $n_2 = 1.2n_1$ over a wide range of magnetic inductions, so the densities of the 2D gas in the sublayers are not very different. In any case the difference is less than 20%, confirming the conclusion reached above that the potential well has a symmetric profile.

It should be mentioned again that the modeling done is valid only in the fields regions where the constituent sublayers have a QHE plateau on their $\rho_{xy}(B)$ curves. At low fields it is more correct to describe the curves on the basis of formula (1).

CONCLUSION

It has been established from QHE studies that the spontaneous formation of the potential profile of a double quantum well occurs in p-type doped $Ge/Ge_{1-x}Si_x$ heterosystems having widths of over ~30 nm. On the one hand, this opens up some possibilities for seeking and investigating the features inherent to intercoupled two-dimensional layers (i.e., for studying interlayer correlated states). On the other hand, galvanomagnetic effects in this regime can be used for a comparative analysis of the quality of the heterointerfaces on opposite sides of the conducting layer and for assessing the degree of symmetry of its potential profile.

It has been found that the samples had two types of holes with mobilities differing by roughly a factor of two. These cannot be heavy and light holes, since their densities are close, and this effect is not observed in narrow layers of the same heterosystem. Consequently, these are holes localized near the opposite heterointerfaces, and the difference of their mobilities means that the quality of these heterointerfaces is substantially different. This illustrates the possibility of performing quality control of the opposite boundaries of the layer from magnetoresistance studies.

We have shown that the potential profile of the quantum wells in a multilayer system can be symmetric from the start, unlike the known situation for isolated conducting layers, where an external electric field must be applied with the aid of a gate in order to compensate the asymmetry induced by the charges localized on the surface.[12]

This study was supported by the Russian Foundation for Basic Research, Projects 02-02-16401, 04-02-16614 and the ''Physics of Solid State Nanostructures'' program of the Russian Academy of Sciences.

*E-mail: yakunin@imp.uran.ru

[1] H. G. Grimmeiss, Fiz. Tekh. Poluprovodn. **33**, 1032 (1999) [Semiconductors **33**, 939 (1999)].
[2] T. E. Whall and E. H. C. Parker, J. Phys. D **31**, 1397 (1998).
[3] M. V. Yakunin, G. A. Alshanskii, Yu. G. Arapov, V. N. Neverov, O. A. Kuznetsov, L. Ponomarenko, and A. de Visser, in *Proceedings of the 15th International Conference on High Magnetic Fields in Semiconductor Physics*, Oxford, UK 2002, publ. on CD-ROM; Nanotechnology **11,** 351 (2000).
[4] Y. M. Suen, J. Jo, M. B. Santos, L. W. Engel, S. W. Hwang, and M. Shayegan, Phys. Rev. B **44**, 5947 (1991).
[5] S. Sasa, J. Saito, K. Nanbu, T. Ishikawa, S. Hiyamizu, and M. Inoue, Jpn. J. Appl. Phys. **24**, L281 (1985).
[6] S. Sasa, J. Saito, K. Nanbu, T. Ishikawa, and S. Hiyamizu, Jpn. J. Appl. Phys. **23**, L573 (1984).
[7] M. J. Kane, N. Apsley, D. A. Anderson, L. L. Taylor, and T. Kerr, J. Phys. C **18**, 5629 (1985).
[8] J. J. Harris, J. M. Lagemaat, S. J. Battersby, C. M. Hellon, C. T. Foxon, and D. E. Lacklison, Semicond. Sci. Technol. **3**, 773 (1988).
[9] J. M. Lagemaat, G. E. W. Bauer, J. J. Harris, and C. T. Foxon, Phys. Rev. B **38**, 13439 (1988).
[10] M. Buttiker, Phys. Rev. B **38**, 9375 (1988).
[11] É. I. Rashba and V. B. Timofeev, Fiz. Tekh. Poluprovodn. **20**, 977 (1986) [Sov. Phys. Semicond. **20**, 617 (1986)].
[12] G. S. Boebinger, H. W. Jiang, L. N. Pfeifer, and K. W. West, Phys. Rev. Lett. **64**, 1793 (1990).

Translated by Steve Torstveit

Parallel magnetotransport in multiple quantum well structures

E. M. Sheregii,* D. Ploch, M. Marchewka, and G. Tomaka

Institute of Physics, University of Rzeszów, Rejtana 16a, 35-310 Rzeszów, Poland

A. Kolek, A. Stadler, and K. Mleczko

Department of Fundamental Electronics, Rzeszów University of Technology, 35-959 Rzeszów, W. Pola 2, Poland

W. Strupiński, A. Jasik, and R. Jakiela

Institute of Electronic Materials Technology, Wólczyńska 133, 01-919 Warsaw, Poland
(Submitted July 21, 2004)
Fiz. Nizk. Temp. **30**, 1146–1156 (November 2004)

The results of investigations of parallel magnetotransport in AlGaAs/GaAs and InGaAs/InAlAs/InP multiple quantum-well structures (MQWs) are presented. The MQWs were obtained by metalorganic vapor phase epitaxy with different shapes of the QWs, numbers of QWs, and levels of doping. The magnetotransport measurements were performed in a wide region of temperatures (0.5–300 K) and at high magnetic fields up to 30 T (**B** is perpendicular to and the current is parallel to the plane of the QW). Three types of observed effects are analyzed: the quantum Hall effect and Shubnikov—de Haas oscillations at low temperatures (0.5–6 K) and magnetophonon resonance at higher temperatures (77–300 K). © *2004 American Institute of Physics.* [DOI: 10.1063/1.1819862]

1. INTRODUCTION

Electron magnetotransport has been widely investigated in low-dimensional structures (LDSs) since 1980. We can distinguish two type of magnetotransport in LDSs according to the direction of the magnetic field: first—the magnetic field is perpendicular to the plane of the quasi-two-dimensional electron gas (Q2DEG) and parallel to the **z** axis, which is the axis of the layer growth (**B**$\|$**z**), and second—the magnetic field is parallel to the plane of the Q2DEG and perpendicular to the **z** axis (**B**$\perp$**z**). In each of these cases both perpendicular electron transport (current perpendicular to the plane of the Q2DEG) and parallel electron transport (current parallel to the plane of the Q2DEG) are possible. It is well known that Landau quantization occurs in the plane perpendicular to the magnetic field. If the magnetic field **B** is perpendicular to the plane of the Q2DEG (parallel to the **z** axis) the entire value of B works to cause Landau quantization, which means an oscillatory character of density of states. The quantum effects in the Q2DEG—Shubnikov–de Haas oscillations (SdH) and quantum Hall effects (IQH)—are caused by Landau quantization and can be observed in the case of magnetic field perpendicular to the layer (**B**$\perp$**z**) and parallel electron transport.

If **B** is not perpendicular to the plane of the Q2DEG and there is an angle φ between **B** and **z**, the Landau level energy is formed by the value $B_t = B\cos\varphi$. This is a well-known effect of a tilted magnetic field, when the resonance peaks are shifted toward higher magnetic fields if **B** is tilted to the plane of the Q2DEG (the angle φ increases).

No Landau quantization will be observed if **B** is located in the plane of the Q2DEG. Barrier effects can be manifested only in perpendicular electron transport in this case for Q2DEGs in heterostructures or in a single quantum well (QW). Interesting effects are manifested for this geometry if we have a coupled double QW (DQW): in a DQW there will be an effect connected with crossing of the Fermi surfaces.

Both perpendicular and parallel electron transports have very important applications.

Perpendicular electron transport has fundamental applications in lasers and in detectors of electromagnetic radiation. The determination of the Q2DEG parameters under conditions of perpendicular transport is one of the more important aims of research on perpendicular electron magnetotransport.

Parallel electron transport has fundamental application too, namely, om transistors and particularly in special transistors such as i) high power transistors; ii) transistors for high frequency or high-electron-mobility transistors (HEMTs). The conditions for such devices are fulfilled in GaAs/AlGaAs 2D structures produced by MBE technology, as well as MOVPE. Strained quantum wells such as InGaAs/InP (InGaAs/InAlAs) structures are widely used in high-speed semiconductor devices such as InGaAs high-speed transistors or HEMTs[1] and heterojunction bipolar transistors (HBTs).[2–4] Transistors based on InGaAs/InAlAs structures with single QWs have a higher frequency limit and lower noise in comparison with those based on GaAs/AlGaAs. However, the latter structures have a very essential advantage—they can be heated to higher temperature without deterioration of the parameters, which is important for high power devices. Thus for HEMTs based on InGaAs/InAlAs structures it is paramount to obtain wider QWs with sufficient high electron density (lower resistance). On the other hand the wide QW means the appearance of a triangular shape of the QWs in which the Q2DEG is located, making it impossible to increase the electron density without

deterioration of the carrier parameters. A special technology of HEMT structures is required in order to obtain a wide, quasirectangular QW with a Q2DEG of high parameters.[5,6] Therefore, the creation of HEMTs built on InGaAs/InAlAs/InP QW structures of different shape is a problem of considerable importance. The separation of donors from carriers in the QW by a space buffer enables one to decrease the their scattering. The direct doping of QWs is applied for power amplifiers with the aim of decreasing the amplitudes of harmonics in the signal.[3]

LDSs can contain different number of QWs: those with two QWs are called double quantum wells (DQWs); those with several identical (or otherwise) QWs we will call multiple quantum wells (MQWs); those with a large number of identical QWs are called superlattices (SLs). HEMTs can be built on MQWs, too, because the additional channel(s) increase the conductivity and the device power limit. Therefore, research on the parallel electron transport in channels of the MQW structures GaAs/AlGaAS and InGaAs/InP or InGaAs/InAlAs/InP is interesting from the point of view of improving the 2DEG parameters.

2. SINGLE QW (SQW) STRUCTURES

Investigations of structures with single QWs are important to get experience in interpretation of quantum effects: SdH oscillations and IQH. It is necessary to develop methods of calculation of the Landau level energies in SQWs of different shape: rectangular and triangular.

These methods must be verified on real QWs. A detailed description of the engineering of structures and the presentation of the experimental data and their interpretation can be found in the original articles.[7,8] Here we present the main results only.

2.1. Structures

InGaAs/InAlAs/InP structures with single QWs were grown by low-pressure metalorganic vapor phase epitaxy (LP-MOVPE) on semi-insulating (100) InP:Fe substrates. A horizontal quartz reactor (AIX-200R&D) and IR heated graphite susceptor were used. The reactor pressure and temperature were maintained at 100 mbar and at 650 °C, respectively, during the unstrained layer growth. The V/III ratio was unchanged and amounted to 329 for InP, 1040 for $In_{0.52}Al_{0.48}As$ and 198 for $In_{0.75}Ga_{0.25}As$. The partial pressure of SiH_4 (doped barriers) was the same in all of the structures.

Four types of structures were studied. Their parameters are presented in Table I. The first structure (#1093) consisted of (from bottom to top) an undoped 180 nm InP buffer followed by a 400-nm InAlAs buffer layer on an InP:Fe substrate. A delta-doped Si donor layer and 3-nm $In_{0.52}Al_{0.48}As$ spacer were grown on the InAlAs buffer layer. A 13-nm $In_{0.75}Ga_{0.25}As$ channel layer, a 3-nm $In_{0.52}Al_{0.48}As$ spacer, a delta-doped Si donor layer, and a 25-nm $In_{0.52}Al_{0.48}As$ Schottky layer terminated the structure growth.

In the case of the second structure (#1098), the indium content in the channel was changed from 53 to 65% during a time of 25 s, then a constant indium content of 65% was maintained in a 17-nm InGaAs layer, and then the graded layer (from 65 to 53%) was repeated. The parameters of the other layers were unchanged.

TABLE I. Parameters of the structures.

Sample	Channel parameters			δ-doping donor concentrations, 10^{12} cm^{-2}
	compositions, In, %	thickness, nm	profile of QW	
1093	75	20	sharp interface	0.7
1098	65	20	changed compositions in channel	5.0
1607	65	23.5	sharp interface	3.5
1088*	53	20	sharp interface	2.5

Note: 1088*— process with one δ-doping layer.

In comparison with the previous structures the third (#1088) structure has only one delta-doped Si donor layer. A 10-period $(1.8\ nm)In_{0.53}Ga_{0.47}As/(2.5\ nm)In_{0.52}Al_{0.48}As$ superlattice was additionally deposited on the InP as a buffer layer in the case of sample #1607. In order to improve the crystalline quality of the strained layer, the growth rate and temperature values of the 18-nm $In_{0.65}Ga_{0.35}As$ active layer were lower than the ones in the case of the #1098 structure and equal to 4.1 Å/s and 600 °C, respectively.

The structures #1093, #1607, and #1088 have sharp interfaces between the InGaAs channel layer and the InAlAs spacer layers. The doping level was different in these four kinds of structures: minimal for #1093 and maximal for #1098.

2.2. Description of experiment and results

Magnetotransport measurements were performed using a superconducting system giving magnetic fields up to 11 T. The sample was mounted in an anticryostat providing temperatures from 0.4 to 300 K. $U_{xy}(B)$ and $U_{xx}(B)$ records were registered for opposite directions of the magnetic and electric fields. Therefore, eight records were made and averaged for one temperature measurement of both the Hall effect and magnetoresistance.

Figures 1 and 2 show examples of $R_{xy}(B)$ and $R_{xx}(B)$ records for samples #1088, #1607, and #1098.

The formation of Q2DEG in samples #1088, #1607, and #1098 is clearly evidenced by quantum oscillations in $R_{xx}(B)$ and plateaus in $R_{xy}(B)$—the IQH. It is shown that the Hall resistance $R_{xy}(B)$ at temperatures of 0.4 K (0.6 K), 1.6 K, and 2.8 K is quantized according to $h/\nu e^2$, where ν is an integer, h is Planck's constant, and e is the electron charge (in the case of sample #1607 there is a departure from this rule, discussed later). The pronounced maxima of the $R_{xx}(B)$ curve (the SdH oscillations) correspond to beginning of each plateau on the $R_{xy}(B)$ curve. These oscillation peaks decline at temperatures above 10 K. It is necessary to notice that structure of the SdH peaks in the case of sample #1088 is simpler and claerer in comparison with the oscillation peaks for sample #1607. At the temperature of 0.4 K, for sample #1607 there is a long plateau on the $R_{xy}(B)$ curve, which spreads from 4.0 to 6.5 T with the maximum at a magnetic field of about 8.0 T, where the $\nu=5$ plateau should start (this maximum disappears at $T>1.0$ K and the $\nu=5$ plateau becomes observable), while for sample #1098 at

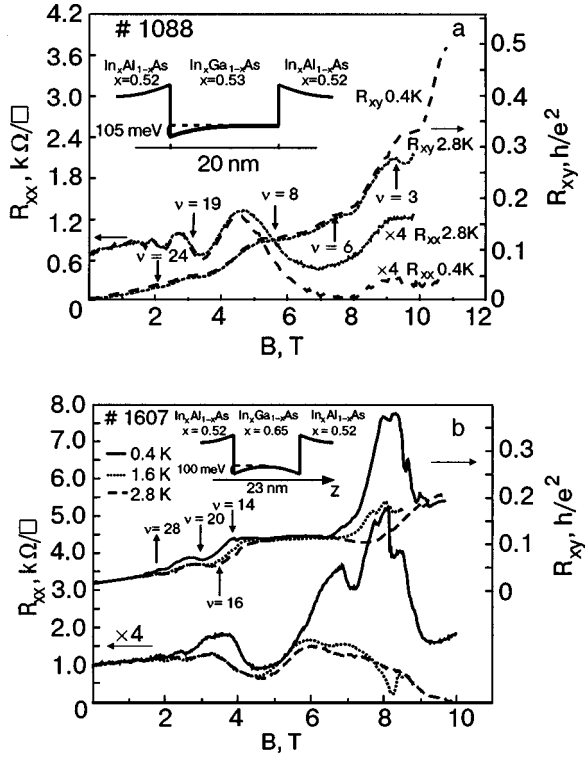

FIG. 1. Records of $R_{xy}(B)$ and $R_{xx}(B)$ for samples #1088 (a) and #1607 (b). The inset shows the band profile of the QW.

$T=0.6$ K a sequence of pronounced plateaus on the $R_{xy}(B)$ curve are observed. Very sharp maxima are also observed on the $R_{xx}(B)$ curve, with undoubtedly periodic behavior versus inverse magnetic field.

Analysis of the positions of the experimental peaks in inverse magnetic field shows the presence of more than one oscillation series: two for sample #1088, and three for sample #1098 (without spin splitting). That means that two subbands in the QW are populated in the cases of sample #1088 and three subbands in case of sample #1098. Another confirmation that the two electron subbands for sample #1088 are populated as well as the three subbands for sample

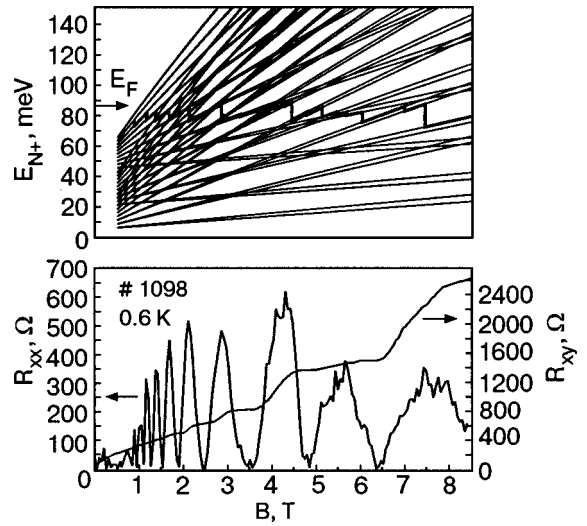

FIG. 2. The Landau level energies calculated for sample #1098 as well as SdH oscillations and the IQH effect at 0.6 K.

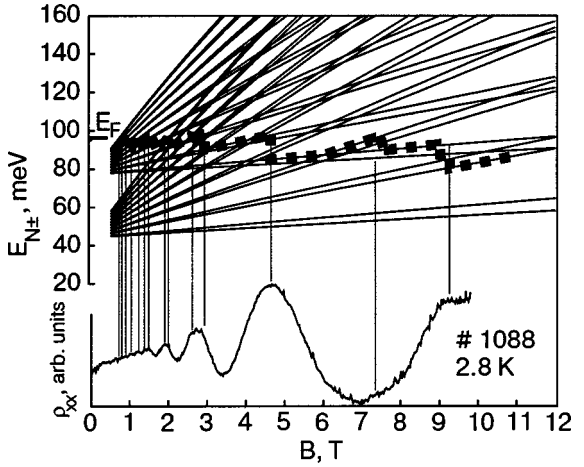

FIG. 3. The Landau level energies calculated for sample #1088 and SdH oscillations at 2.8 K.

#1098 is deduced from the IQH filling factors ν and the calculation of the Landau level energies (see Fig. 3 and 4). Similar analysis for sample #1607 was done by means of the $R_{xx}(B)$ and $R_{xy}(B)$ curves obtained at $T=1.6$ K.

The fundamental fields B_f for this series are presented in Table II. Assuming a circular Fermi surface, a 2D carrier concentration n_s can be extracted from the SdH period:

$$n_s=\sum_i^k \frac{2e(B_f)_i}{h}, \tag{1}$$

where i is the number of the subband in the QW and k is the number of populated subbands. The values of the density n_s are presented in Table II. The carrier mobility values determined from the low-field Hall measurements are also entered here.

In case of sample #1093 the oscillation peaks on the $R_{xx}(B)$ curve are observed too but they are not so pronounced as for the sample described above, and the plateaus on the $R_{xy}(B)$ curve are absent.

2.3. Interpretation

In the case of sample #1088 we have an asymmetric QW. The band profiles of this QW were calculate by Zawadski and Pfeffer[9] (the barrier composition is differs by only

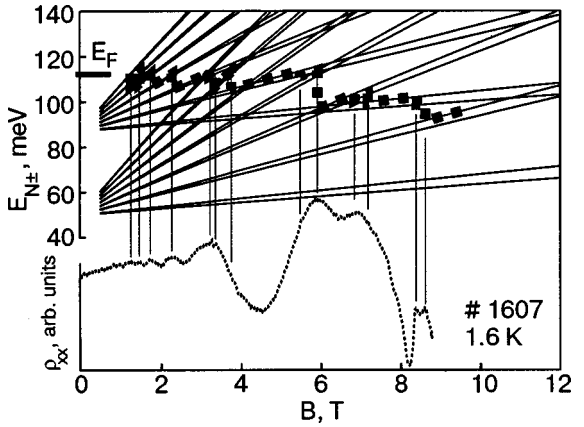

FIG. 4. The Landau level energies calculated for sample #1607 and SdH oscillations at 1.6 K.

TABLE II. The values of fundamental fields B_f of SdH oscillations and 2D carrier density deduced from B_f as well as the carrier mobilities obtained from the damping factor of the SdH oscillations.

Sample	B_f, T			2D carrier density, 10^{12} cm^{-2}	Electron mobility*, 10^5 cm^2/(V·s)
	Number of electronic subbands				
	1	2	3		
1088	2.6	19.6	–	1.07	1.7
1607**	6.4	19.8	–	1.2	3.2
1098	8.3	14.9	18.4	2.0	2.6
1093	6.1	19.4	–	1.0	0.94

Note: *is related to Landau levels in the magnetic field region about 1.5–4 T; **parameters are related to temperatures $T>1.0$ K.

1%) and are presented in Fig. 1a (inset). Since the depth of the triangular well at the edge of the QW for structure #1088 is 105 meV, we can assume that the Q2DEG in this structure is located in a single triangular potential well. The structure #1607 was doped symmetrically, since shape of QW is symmetric too. This shape is shown in Fig. 1b (inset). In case of sample #1607 we have two triangular QWs separated by a barrier of about 95 meV. Thus the Q2DEG in structure #1607 is located in a nearly double triangular QW.

The engineering of structure #1098 is more complicated: the In-content in the channel is increased from 53 to 65% over the 16 nm to compensate the Coulomb interaction with ionized donors in the δ-doped layers. Therefore, the shape of the QW is practically rectangular (see Fig. 5).

To interpret experimental results on the SdH oscillations and IQH plateaus it is necessary to calculate the energy of the Landau levels. We adapted the Zawadzk–Pfeffer quasi-two-band model[10,11] for calculation of the Landau level energies in the subbands of the QW. The description of the adapted model for the different QW shapes is presented in Ref. 8.

The calculated Landau levels are shown in Fig. 3 for sample #1088 (triangular QW) at a temperature of 2.8 K.

The structure of the SdH peaks as well as the plateaus of the IQH effect are interpreted very well for this sample: it is necessary to take the value of Fermi energy equal to 18 meV for subband number $i=1$ and 51 meV for the subband $i=0$ [we define the Fermi level us to be placed between two Landau levels when the plateaus on the $R_{xy}(B)$ curve or the minima (zero) on the $R_{xx}(B)$ curve occur].

The calculated Landau levels are shown in Fig. 2 for the sample #1098 (rectangular QW) at temperature 0.6 K. It is necessary to take the value of the Fermi energy equal to 27.5 meV for subband number $i=2$, 54 meV for subband $i=1$, and 70 meV for the lowest subband $i=0$ to obtain good agreement with positions in magnetic field of the experimental peaks of the SdH oscillations for sample #1098.

In case of sample #1607 satisfactory agreement between the experimental positions of the SdH peaks versus magnetic fields and the theoretical ones at $T=1.6$ K was obtained if the Landau level energies were calculated in the framework of a single triangular QW model. The values of the Fermi level energies are 27 and 63 meV for subbands $i=1$ and $i=2$, respectively. But this model can not be adjusted for the $R_{xy}(B)$ and $R_{xx}(B)$ curves obtained at 0.4 K.

TABLE III. Band-structure parameters of $In_xGa_{1-x}As$ channels of the InGaAs/InAlAs/InP structures.

Sample	x	E_g, eV	m_c^*/m_0	g_c^*	Δ, eV
1088	0.53	0.846	0.0345	−8.16	0.355
1607	0.65	0.723	0.0299	−9.90	0.355
1098	0.65	0.723	0.0299	−9.90	0.355
1093	0.75	0.629	0.0265	−11.36	0.355

The values of the band-structure parameters, energy gap E_g, the effective electron mass at the edge of the conduction band m_c^*, the effective g factor g_c^* used for calculation of the Landau levels energies of the Q2DEG for all structures are presented in Table III.

2.4. Generalization

Four kinds of InGaAs/InAlAs/InP structures with a SQW channel for HEMTs were prepared: with a sharp interface–the structures #1088, #1607 and #1093 and with a variable composition in the channel—the #1098 structure.

Structures with sharp interface have different content of InAs in QW channel: 53% for #1088, 65% for #1607, and 75% for #1093. It is shown that the maximal mobility of the Q2DEG in the InGaAs QW channel was obtained for structure #1088 with a single asymmetric triangular QW. The lowest electron mobility was determined for the structure #1093 with maximal difference of the InAs content in barrier and QW, namely: 53 and 75%, respectively, though the effective mass of electrons in the QW is the smallest. That means that scattering on the interface dislocations is significant and we can assume that this factor is the most important in limiting the electron mobility in the QW.

An interesting case is presented by the structure #1098, in which a smooth transition from the barrier to the QW was prepared with the aim of decreasing the mismatch as well as to form rectangular QW. The calculations confirm that determination of the Landau level energies by the model that applies to the rectangular QW give a better fit to the experimental positions of the SdH peaks than does the model applying to the triangle QW. Thus the InGaAs channel in structure #1098 actually does form a quasi-rectangular QW. The 2D density of electrons in this channel is the highest and the electron mobility is very high too, namely 2.6×10^5 cm^2/(V·s). Therefore, the proposed engineering of this structure appears promising.

The Zawadzki–Pfeffer quasi-two-band model[10,11] adapted for calculation of the Landau level energies in the triangular and rectangular InGaAs/InAlAs QWs enables us satisfactorily to interpret experimental data for the structures #1088 and #1098.

3. DOUBLE QUANTUM WELL

3.1. Motivation

Fabrication of multiple 2D layers in close proximity allows the controlled introduction an additional degree of freedom associated with the third dimension.

TABLE IV. Parameters of the InGaAs/InAlAs DQW structure.

Sample	Composition of two channels In, %	Two channels with thickness of, nm	QW-profile	Three δ-doping layers with donor concentrations, 10^{12} cm^{-2}
2506	65	20	Sharp interface	3.5

The double QW is the simplest of these structures and preserves both high electron mobility and external gating of the electron density in the layers. Interlayer Coulomb interaction in multilayer systems can lead to interesting effects such as Wigner crystals or the absence of plateaus in the IQH for filling factor equal to 1 or 3.[12,13] Experimentally both the integer and fractional Hall effects have been observed in multilayer systems with essential interlayer tunneling. Effects connected to the crossing of the Fermi surfaces of two coupled QWs when B is in the plane of the layers were observed for wide QW with Q2DEG localized in two triangular QWs[14] or for a specially engineered DQW.[15] The problem of the electron–electron interaction for coupled DQWs was investigated experimentally in Refs. 16 and 17 and theoretically by Danhong Huang *et al.*[18] Thus bi-layer two-dimensional systems have been of great research interest in the study of the properties of Q2DEGs at high magnetic fields.

3.2. The structure description and experimental results

Here the experimental results are presented which were obtained for DQWs fabricated at the Institute of Electronic Material Technology in Warsaw. They consisted of two InGaAs QWs of thickness 20 nm, and three InAlAs barriers. In each barrier there were donor δ-doped layers.

The structure was grown on an InP substrate similarly to the SQW. The parameters of the structure are presented in Table IV. The data of magnetotransport measurements at low temperatures are shown in Fig. 6, where the pronounced SdH oscillations on the $R_{xx}(B)$ curve as well as the IQH effect on the $R_{xy}(B)$ curve of are also shown. The SdH oscillations for weak magnetic fields appear starting at 0.5 T. The peaks of the SdH oscillations at higher magnetic fields are split just as has been observed in DQWs by other authors.

This splitting increases towards higher magnetic fields, which means that the energy gap caused by electron interaction within the DQWs is proportional to B, as was shown in Ref. 16. It should be noted that the plateaus on the $R_{xy}(B)$ curve are deformed. There are two possible explanations for that. The first explanation invokes the presence of additional channels of conduction, for instance conduction through three donor δ layers. The second one involves coupling of the QWs.

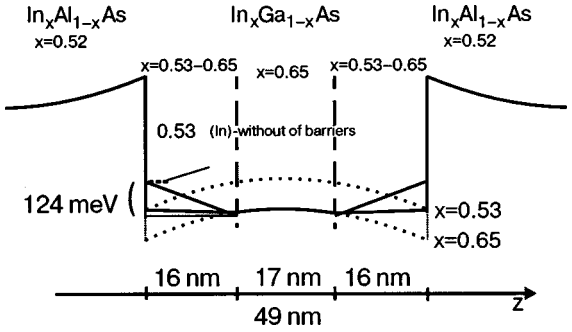

FIG. 5. The band profile of the QW for structure #1098.

3.3. Theory

We use the model proposed in Ref. 18, in which symmetric DQWs separated by a middle barrier were considered. An external magnetic field was assumed to be applied perpendicular to the planes of the QWs. The electron motion was described by the Schrödinger equation containing both the DQW potential and self-consistent Hartree potentials. The in-plane electron motion in each subband in the DQW was assumed to be Landau quantized. The total electron energy including both the in-plane and vertical electron motions can be written as

$$E_{ni}=\left(n+\frac{1}{2}\right)\hbar\omega_c+E_i+V_{ni}^F, \tag{2}$$

where V_{ni}^F is the exchange energy (involving screening) which is given by Eqs. (12)–(18) in Ref. 18. The numerical calculations performed by the authors of Ref. 18 for DQWs based on the well material GaAs and barrier material $A_{0.3}Ga_{0.7}As$ with a well width of 14 nm and a barrier width of 3 nm have shown that there is an approximately linear B dependence for the tunneling gap in the region of magnetic fields $B\leqslant 9$ T. Therefore, the total splitting Δ_t between energy states of two QWs consists of two parts: a constant term Δ_{SAS}, determined by the overlapping of the electron wave functions of the two QWs, and a variable tunneling term V_{ni}^F, involving a screening factor:

$$\Delta_t=\Delta_{SAS}+V_{ni}^F. \tag{3}$$

The last term is a strongly decreasing function of B, and for magnetic fields less than that at which the quantum limit begins can be written as

$$V_{ni}^F=-(K_0-kB), \tag{4}$$

where K_0 is the maximum screening factor in zero magnetic field and $-kB$ is a variable screening factor that decreases with B up until the first Landau level in the two QWs is filled. Generally, the total energy gap Δ_t between symmetric and antisymmetric states in DQW is proportional to the magnetic field, as has been observed experimentally.[16]

We adapted this analysis for our case of an $In_{0.53}Al_{0.47}As/In_{0.65}Ga_{0.35}As$ DQW structure, assuming rectangularity of the QWs. This last enables us to calculate the Landau level energies according to the formulas:

$$\frac{(E-E_\perp)(E_g+E+E_\perp)}{E_g}=\frac{\hbar^2\pi^2(i+1)^2}{2m_c^*a^2k}\pm(\Delta_{SAS}^s+kE_\perp), \tag{5}$$

$$E_\perp=-\frac{E_g}{2}+\frac{E_g}{2}\sqrt{1+\frac{4\mu_B B}{E_g}\left[f_1\frac{m_0}{m_c^*}\left(n+\frac{1}{2}\right)\pm\frac{1}{2}g_0^*f_2\right]}, \tag{6}$$

$$f_1=\frac{(E_g+\Delta)\left(E_\perp+E_g+\frac{2}{3}\Delta\right)}{\left(E_g+\frac{2}{3}\Delta\right)(E_\perp+E_g+\Delta)},$$

$$f_2=\frac{E_g+\frac{2}{3}\Delta}{E_\perp+E_g+\Delta}, \tag{7}$$

where E_g is the energy gap (between the top of valence band and the edge of the conduction band), Δ is the spin–orbital splitting, m_0 is electron mass in vacuum, m_c^* is the effective electron mass at the edge of the conduction band, μ_B is the Bohr magneton, $n=0,1,2,\ldots$ stands for Landau levels, $i=0,1,2,\ldots$ is the number of the subband, $E_\perp$ is the Landau level energy in the absence of the QW (in the Zawadzki–Pfeffer notation), and E is the unknown energy of Landau level n for subband with number i in the QW. The parameter Δ_{SAS}^s is the energy gap determined by the overlap of the wave functions, which is diminished by the screening at zero magnetic field, as follows from (3) and (4):

$$\Delta_t=(\Delta_{SAS}-K_0)+kB\equiv\Delta_{SAS}^s+kB. \tag{8}$$

This parameter has the meaning of the zero-magnetic-field splitting of the subbands and can be determined by extrapolation of the experimental peak splitting of the SdH oscillations to $B=0$. The parameter k (which is in fact the coefficient of proportionality between the total splitting Δ_t and $\hbar\omega_c$) can be determined as a fitting parameter.

3.4. Interpretation

The calculation of the Landau level energies was performed for sample #2506 taking into account the band parameters determined for sample #1098 with single rectangular QW (Table III). Extrapolation of the experimental peaks splitting of the SdH oscillations to $B=0$ gives the value of $\Delta_{SAS}^s=1$ meV. The coefficient of proportionality k between total splitting Δ_t and $\hbar\omega_c$ was determined as fitting parameter and was found to be equal to 0.19.

In Fig. 6 the calculated Landau level energies are shown as functions of magnetic field. It is clearly seen that we have achieved excellent agreement between the experimental data concerning the peak positions and theoretical prediction for the SdH oscillation maxima. It is interesting to note that the value of the total splitting Δ_t is approximately equal to 15 meV at 10 T for $n=1$ and $i=0$ and should increase together with the field up to about 30 T, where the predicted quantum limit should occur. It is necessary to notice that we have not needed to invoke the thermal stresses caused by mismatch to explain the experimental data on the InGaAs/InAlAs/InP DQW.

If we return to Fig. 1b, where the experimental data for sample #1607 are presented, we can notice that the strong maximum at 8 T in the $R_{xy}(B)$ curve obtained for this sample at $T=0.4$ K can be explained by the presence of the second triangular QW in this sample.[1)] As was mentioned above, the SdH oscillation structure at 2.8 K can be explained by means of the single-triangle QW model. This model predicts the value of Fermi energy as to be about 112 meV above the conduction band bottom. This value is a bit greater than the barrier energy height ($\sim$95 meV). This barrier separates two triangular QWs in the conducting channel, and, hence, the Q2DEG in the two triangular QWs constitutes a united electron system. We assume that at 0.4 K the Fermi level falls below the barrier top.

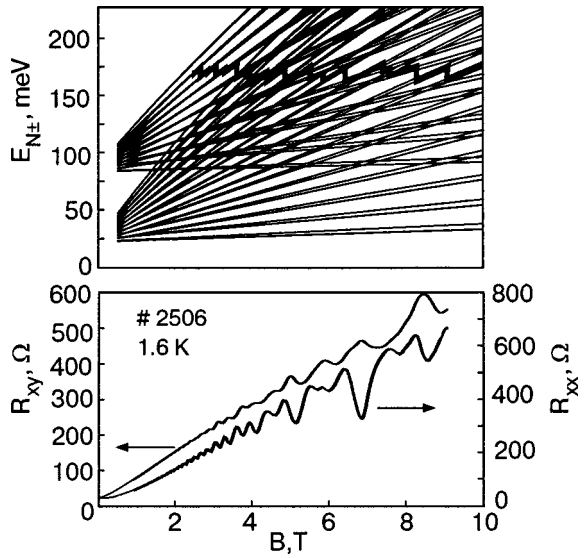

FIG. 6. The Landau level energies calculated for sample #2506 as well as SdH oscillations and IQH at 1.6 K.

Then a new situation occurs in which two correlated electron subsystems are in two separate triangular QWs. Therefore, in this situation the structure should be considered as a DQW.

3.5. Generalization

In parallel and perpendicular magnetotransport in a DQW the following effects connected to the resonance tunneling are manifested:

— the existence of an SAS gap, which means an additional splitting of the electronic states;

— the SAS gap is proportional to B; this proportionality is expected to be reduced in very strong magnetic field.

Excellent agreement was achieved between the experimental data concerning the SdH peak positions and theoretical prediction for the SdH oscillation maxima based on the method of calculating the Landau level energies using the model of the DQW proposed in Ref. 18 and the Zawadzki–Pfeffer quasi-two-band model.[10,11]

The influence of the thermal stresses on parallel electron transport, which can disrupt the magnetoconductivity in a InGaAs/InAlAs DQW, was not observed in this measurement.

4. MULTIPLE QUANTUM WELLS

4.1. Description of structures

Four types of MQW systems were studied. They consisted of ten QWs of GaAs and ten $Al_xGa_{1-x}As$ barriers and were obtained by LP-MOVPE on semi-insulating GaAs at the Warsaw Institute of Electronic Materials. The thickness of the well was 10 and 8 nm; the thickness of the barrier was

TABLE V. Parameters of the GaAs/$Al_xGa_{1-x}As$ MQW structures.

Structures	$L_{GaAs}(nm)/L_{AlGaAs}(nm)$	x	Carrier density, $10^{10}cm^{-2}$
151	10/4	0.3	50
152	10/4	0.3	5
153	8/4	0.3	50
41	10/4	1.0	50

4 nm for all the MQW. GaAs layers were doped with Si to about 5×10^{10} and 5×10^{11} cm^{-3}. The parameters of MQWs are shown in Table V.

Six samples in standard form for Hall measurements obtained by photolithography from #151 MQWs have been measured as well as three, two, and two from #152, #153, and #41, respectively.

4.2. Experimental results: Low-temperature measurements

The data of magnetotransport measurements at low temperatures are presented in Fig. 7 for sample #151. It is seen that there are SdH oscillations on the $R_{xx}(B)$ curve. The oscillation peaks start at a magnetic field of about 4.5 T and consist of three unsplit maxima. The SdH oscillations start at a higher field than that for the QW structures based on InGaAs/AlGaAs, because the electron effective mass in GaAs is two times greater than in $In_{0.65}Ga_{0.35}As$. A single plateau is observed on the $R_{xy}(B)$ curve at 8–9 T; it corresponds to the deep minimum on the $R_{xx}(B)$ curve. Similar curves were obtained at low temperatures for the samples #41 and #152. These curves, on one hand, is evidence of the existence of a Q2DEG in the samples which we studied; on the other hand, they demonstrate clearly that there is no influence of thermal stresses which could split maxima in these MQW structures in the low-temperature measurements.[19] Since the splitting of electron states caused by tunneling in ten coupled QWs didn't appear at low temperatures (1.6 K) in the SdH oscillations and in the IQH effect, they *a fortiori* cannot appear at a temperature higher than 77 K.

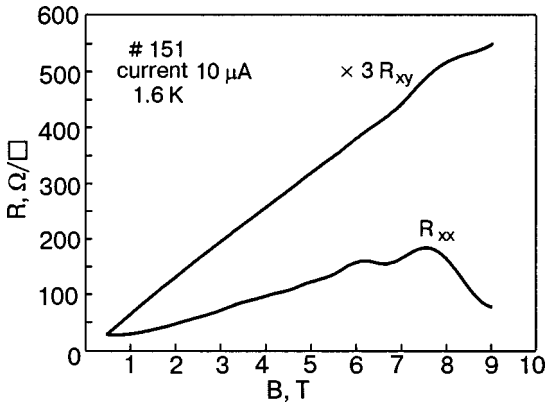

FIG. 7. Records of $R_{xy}(B)$ and $R_{xx}(B)$ for sample #151 obtained at low temperature ($T=1.6$ K).

4.3. EXPERIMENTAL RESULTS: MAGNETOPHONON RESONANCE

The magnetophonon resonance (MPR) appears every time when the phonon frequency ω_{LO} is equal to the cyclotron frequency ω_c of the electron in a magnetic field, multiplied by the same small integer M:

$$\omega_{LO}=M\omega_c, \tag{9}$$

where $\omega_c=eB/m$, e is the electron charge, m is the effective mass, and B is the magnetic induction.

The resonances are manifested in transverse ρ_{xx} and longitudinal ρ_{zz} magnetoresistances. The transverse magnetoresistance ρ_{xx} reaches the maximum at resonance values of magnetic fields, which fulfills the specified resonance condition [Eq. (9)]. There are two papers known in which MPR was reportedly examined in superlattices and structures with MQW in the vertical transport (both the magnetic field and the electric current are perpendicular to the layers).[20,21] The present paper reports results of exploring the MPR and MQW in the parallel transport. In this instance the measurements can be more sensitive to the strain in the layers.[22,23]

The MPR research was performed in pulsed magnetic fields up to 30 T. The pulsed fields were generated by discharging a 10 mF capacitor bank through a copper coil, giving a pulse duration of 4 ms. A transient recorder was used to store the transverse magnetoresistance $\rho_{xx}(B)$ and a voltage $\propto\partial B/\partial t$, which was numerically integrated to find **B**. The induced voltage in the sample leads was compensated for by several additional field coils. There was a good agreement between data taken on the rising and falling sides of the pulse for samples with resistances <300 kΩ. The transverse magnetoresistance was measured between 77 and 340 K and the MPR oscillations extracted by subtracting a voltage linear in magnetic field. The oscillating part of the magnetoresistance $\Delta\rho_{xx}$ was recorded.

In Fig. 8 examples of the $\Delta\rho_{xx}(B)$ curves registered are shown in which the structure of the observed peaks was faithfully represented because of its astonishing repetition for different MPR harmonics at different temperatures.

The broken curves in Fig. 8a show the resonance peaks without the fine structure. As the repetition of individual MPR peaks in the given MQW stands out particularly in the magnetic field interval 0–16 T, where peaks caused by transitions 0–2, 0–3, 0–4, 0–5 and 0–6 were observed simultaneously, the resonance curves within this range of magnetic induction B are represented. Representing them in the whole range of resonance fields together with the transition 0–1 (22.5 T) would lead to disappearance of the interesting structure of the peaks and its repetition for different harmonics.

It should be noted that: i) the fine structure of MPR peaks reappears in each type of MQW, but its character is not the same; ii) with increasing temperature the fine structure becomes more pronounced.

It follows that the occurrence of the observed peak structure depends neither on the two-dimensional density of carriers nor on the size of the quantum wells but can be connected to phonons.

The thicker arrows in Fig. 8 indicate the position of the MPR peaks observed in the single heterostructures

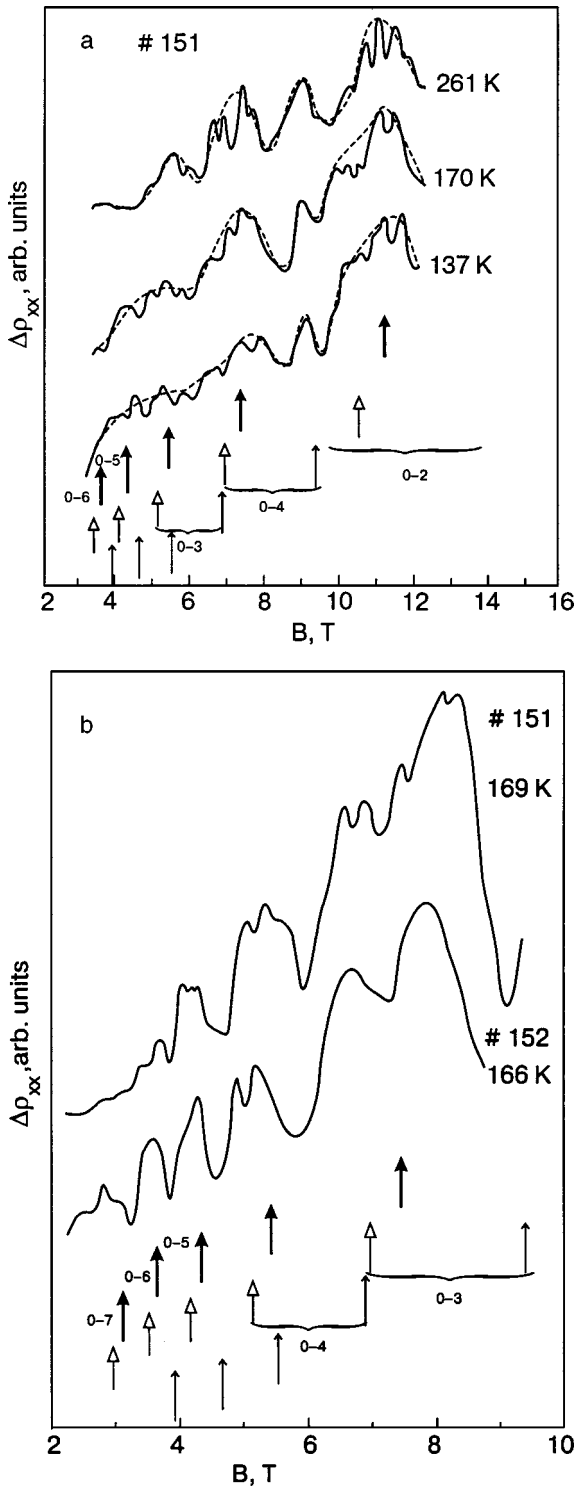

FIG. 8. Experimental recordings of $\Delta\rho_{xx}(B)$ obtained for sample #151 at three different temperatures higher than 77 K (a) and for samples #152 ($T=166$ K) and #151 ($T=169$ K) (b).

GaAs–$Al_xGa_{1-x}As$ at the temperature 130 K to facilitate an interpretation of the observed peak structure.

In the case of MPR in a single heterostructure each transition between Landau levels corresponds with one peak (structureless) and the resonance fields were somewhat smaller than the theoretical position of MPRs involving the bulk LO phonon of GaAs. The authors of Ref. 21, where an examination of MPR in the vertical transport in GaAs–AlAs MQWs was reported, besides oscillations connected with the absorption of the quantum wells GaAs LO phonons also observed the peaks caused by the interaction of electrons with LO phonons of the AlAs barrier. The partly observed peak structure can be explained by the introduction to MPR of two more kinds of barrier phonons. So, the occurrence of a peak at about 9 T can be explained by a transition 0–3 of an electron with the absorption AlAs-like LO phonon. The MPR caused by interaction between an electron and phonons from the barrier made of a GaAs-like lattice, though, manifest themselves as satellites of each main series transition, on the side of lower magnetic fields. It is mostly visible in Fig. 8b, where the fine structure is less prominent.

It is well known that every phonon band in solid solutions of zinc-blend structure consist of four lines[24] which means the existence of the five phonon modes. In case of AlGaAs the average distance between these modes is about $8\ cm^{-1}$ or 1 meV. So, these five modes can generate fine structure of the MPR peaks.

5. SUMMARY

The parallel magnetotransport in SQWs, DQWs, and MQWs is studied at low temperatures and a temperature higher than 77 K.

A method of calculation of the Landau level energies including the tunneling and screening effects in the coupled DQWs, which enable us to interpret the SdH oscillations and the IQH effect, is developed.

The fine structure of the MPR peaks in parallel transport of MQWs can not be explained by destruction of the magnetoconductivity caused by thermal stresses, because at low temperatures this splitting should manifest itself more strongly, but it does not appear in the SdH oscillations and QHE.

The splitting of electron states caused by tunneling in coupling ten QWs does not appear at low temperatures (1.6 K) in the SdH oscillations and QHE, and it therefore cannot appear at temperatures higher then 77 K when MPR is observed.

There is no doubt that the fine structure of the MPR peaks is connected to phonons.

At temperatures less than 1 K, the magnetotransport phenomena in a single symmetric QW of the width greater than 10 nm reveal similar features to those characterising the electron transport in the DQW.

The $In_xGa_{1-x}As/In_xAl_{1-x}As$ (#1098) structure makes an interesting example of QWs where due to a smooth transition from the barrier to the QW a rectangular QW was produced. The calculations confirm that the evaluation of the Landau level energy using rectangular QW model gives better fitting of the experimental positions of the SdH peaks than the triangular QW model. The 2D density of electrons in the channel of the structure in question is very high, as is the electron mobility, which is equal to $2.6\times10^5\ cm^2/(V\cdot s)$.

Therefore, the proposed engineering of this structure appears promising.

*E-mail: sheregii@atena.univ.rzeszow.pl

[1)]The maximum in the plateaus with $\nu=1$ was observed on the $R_{xy}(B)$ curve by M. Kellog *et al.*[17] for a DQW and was explained by involking the drag effect in the IQH effect.

[1] W. J. Schaff, P. J. Tasker, M. C. Foisy, and L. F. Eastman, in *Semiconductors and Semimetals*, Vol. 33, Academic Press, New York (1991), Chap. 2.
[2] F. H. Pollak, in *Semiconductors and Semimetals*, Vol. 32, Academic Press, New York (1990), Chap. 2.
[3] Ming-Ta Yang and Yi-Jen Chan, IEEE Trans. Electron Devices **43**, 1174 (1996).
[4] Y. H. Chen, K. T. Hsu, K. L. Chen, H. H. Lin, and G. J. Jan, Jpn. J. Appl. Phys. **33**, 2448 (1994).
[5] Y. H. Chen and G. J. Jan, J. Appl. Phys. **77**, 6681 (1995).
[6] Y. H. Chen and G. J. Jan, IEEE J. Quantum Electron. **33**, 574 (1997).
[7] G. Tomaka, E. M. Sheregii, T. Kąkol, W. Strupiński, A. Jasik, and R. Jakiela, Phys. Status Solidi A **195**, 127 (2003).
[8] G. Tomaka, E. M. Sheregii, T. Kakol, W. Strupiński, R. Jakiela, A. Kolek, A. Stadler, and K. Mleczko, Cryst. Res. Technol. **38**, 407 (2003).
[9] W. Zawadzki and P. Pfeffer, Proc. NGS-10, IPAP Conf. Ser. 2, p. 219 (2001).
[10] W. Zawadzki, J. Phys. C: Solid State Physics **16**, 229 (1983).
[11] P. Pfeffer and W. Zawadzki, Phys. Rev. B **41**, 1561 (1990).
[12] G. S. Boebinger, H. W. Jiang, L. N. Pfeiffer, and K. W. West, Phys. Rev. Lett. **64**, 1793 (1990).
[13] Y. W. Suen, J. Jo, M. B. Santos, L. W. Engel, S. W. Hwang, and M. Shayegan, Phys. Rev. B **44**, 5947 (1991).
[14] T. Ihn, H. Carmona, P. C. Main, L. Eaves, and M. Henini, Phys. Rev. B **54**, 2315 (1996).
[15] T. Jungwith, T. S. Lay, L. Smrcka, and M. Shayegan, Phys. Rev. B **56**, 1029 (1997).
[16] K. M. Brown, N. Turner, J. T. Nicholls, E. H. Linfield, M. Pepper, D. A. Ritchie, and G. A. C. Jones, Phys. Rev. B **50**, 15465 (1994).
[17] M. Kellog, I. B. Spielman, J. P. Eisenstein, L. N. Pfeiffer, and K. W. West, Phys. Rev. Lett. **88**, 126804 (2002).
[18] D. Huang and M. O. Monosrech, Phys. Rev. B **54**, 2044 (1996).
[19] G. Tomaka, E. M. Sheregii, and T. Kakol, Mater. Sci. Eng., B **80**, 173 (2001).
[20] H. Nogutchi, H. Sakaki, T. Takamasu, and N. Miura, Phys. Rev. B **45**, 12148 (1992).
[21] P. Gassot, J. Genoe, D. K. Maude, J. C. Portal, K. S. H. Dalton, D. M. Symons, R. J. Nicholas, F. Arstone, J. F. Palmier, and F. Lauelle, Phys. Rev. B **54**, 14540 (1996).
[22] G. Tomaka, J. Cebulski, E. M. Sheregii, W. Ściuk, W. Strupiński, and L. Dobrzariski, Acta Phys. Pol. A **94**, 597 (1998).
[23] G. Tomaka, J. Cebulski, E. M. Sheregii, W. Sciuk, W. Strupiński, and I. Dobrzanski, Mater. Sci. Eng., A **288**, 138 (2000).
[24] B. V. Robouch, A. Kisiel, and E. M. Sheregii, Phys. Rev. B **64**, 073204 (2001).

This article was published in English in the original Russian journal. Reproduced here with stylistic changes by AIP.

Nonmonotonic temperature dependence of the resistivity of p-Ge/$Ge_{1-x}Si_x$ in the region of the metal–insulator transition

Yu. G. Arapov, G. I. Harus, N. G. Shelushinina, and M. V. Yakunin

Institute of Metal Physics of the Ural Division of the Russian Academy of Sciences, Sofia Kovalevskaya St., Ekaterinburg 620219, Russia

V. N. Neverov*

Institute of Metal Physics of the Ural Division of the Russian Academy of Sciences, Sofia Kovalevskaya St., Ekaterinburg 620219, Russia; Ural State University, pr. Lenina 51, Ekaterinburg 620083, Russia

O. A. Kuznetsov

Physicotechnical Research Institute, Nizhny Novgorod State University, Nizhny Novgorod 603600, Russia

L. Ponomarenko and A. De Visser

Van der Waals-Zeeman Amsterdam University, Valknierstraat 65, 1018 XE Amsterdam, The Netherlands
(Submitted May 11, 2004)
Fiz. Nizk. Temp. **30**, 1157–1161 (November 2004)

In a two-dimensional (2D) hole system (multilayer p-Ge/$Ge_{1-x}Si_x$) heterostructure with conductivity $\sigma \approx e^2/h$ at low temperatures ($T \approx 1.5$ K) a transition from the insulator phase ($d\sigma/dT > 0$) to a ''metallic'' phase ($d\sigma/dT < 0$) is observed as the temperature is lowered, behavior that is in qualitative agreement with the predictions of the Finkelstein theory. In a magnetic field **B** perpendicular to the plane of the 2D layer one observes positive magnetoresistance depending only on the ratio B/T. We attribute the positive magnetoresistance effect to the suppression of the triplet channel of Fermi-liquid electron–electron interaction by the magnetic field owing to the strong Zeeman splitting of the hole energy levels. © *2004 American Institute of Physics.* [DOI: 10.1063/1.1819865]

INTRODUCTION

In disordered 2D systems at low temperatures there are two types of quantum corrections $\delta\sigma = \delta\sigma_{wl} + \delta\sigma_{ee}$ to the Drude conductivity $\sigma_0 = e^2/h(k_F l)$: $\delta\sigma_{wl}$ is the correction due to inertial effects in the scattering of the electron waves on impurities (weak localization), and $\delta\sigma_{ee}$ is the correction due to the disorder-modified electron–electron interaction.[1,2] In weakly disordered systems with $k_F l > 1$ these corrections are small in the parameter $(k_F l)^{-1}$ (l is the mean free path) and depend logarithmically on temperature.

Experiments to detect[3] and study (see reviews[4,5]) the so-called metal–insulator transition from the change in the carrier density in 2D semiconductor structures with high mobility have stimulated a substantial advance in the theory of electron–electron interaction effects.[6,7] The general theory of quantum corrections to the components of the conductivity tensor of a 2D system owing to electron–electron interaction effects has been developed for the case $kT < E_F$ for an arbitrary relationship between the values of kT and $\hbar/\tau$ (τ is the momentum relaxation time) over the whole range of temperatures from the diffusion regime ($kT\tau/\hbar \ll 1$) to the ballistic regime ($kT\tau/\hbar \gg 1$) both for short-range (point)[6] and for large-scale (smooth)[7] impurity potentials.

For example, the linear growth of the resistivity ρ with temperature in Si-MOSFET structures with high carrier mobility at large values $\sigma_0 \gg e^2/h$, which for the past decade has been considered to be a manifestation of an ''anomalous metallic'' state, is now interpreted as being due to an electron–electron interaction effect in the ballistic regime.[8] However, the nonmonotonic temperature dependence of $\rho(T)$ observed near the proposed metal–insulator transition ($\sigma_0 \approx e^2/h$) still does not have a generally accepted explanation. This has stimulated our investigations into multilayer p-Ge/$Ge_{1-x}Si_x$ heterostructures.

Suppression of the low-temperature conducting phase by a magnetic field *parallel* to the 2D layer (*positive* magnetoresistance) has been observed repeatedly for high-mobility Si-MOSFET[9–15] and p-GaAs heterostructures[16,17] such behavior is explained either by the ''complete polarization'' of the electron (hole) gas[12–14,17,18] or (at low fields) by the Zeeman effect in the quantum correction owing to the electron–electron interaction in both the diffusion[19] and ballistic[8,15] regimes.

We have carried out studies in a magnetic field *perpendicular* to the 2D layer, where together with the Zeeman level splitting it is necessary to take weak localization effects into account. The hole gas in the Ge quantum wells for the p-Ge/$Ge_{1-x}Si_x$ heterostructures studied is described by the Luttinger Hamiltonian with a highly anisotropic g factor in respect to the mutual orientation of the magnetic field and the 2D plane. At the bottom of the lower spatial subband $g_\perp = 6\kappa$ (where for Ge the Luttinger parameter $\kappa = 3.4$)[20] for the *perpendicular* magnetic field and $g_\parallel = 0$ for the *parallel*.[21,22] For interpretation of our experimental $\rho(B,T)$ curves in the samples near the proposed metal–insulator phase transition we invoked a model used for semiconduct-

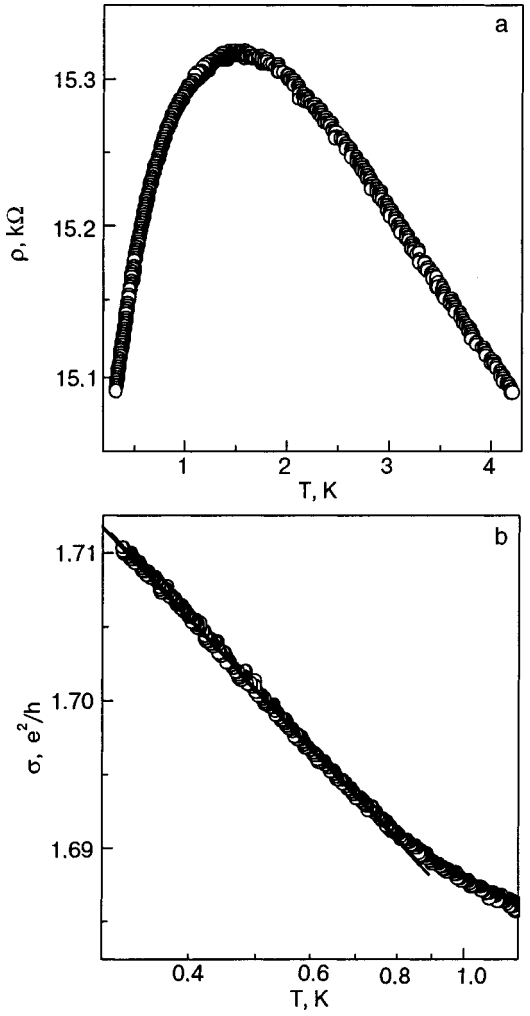

FIG. 1. Temperature dependence of the resistivity (a) and conductivity (b) for $B=0$.

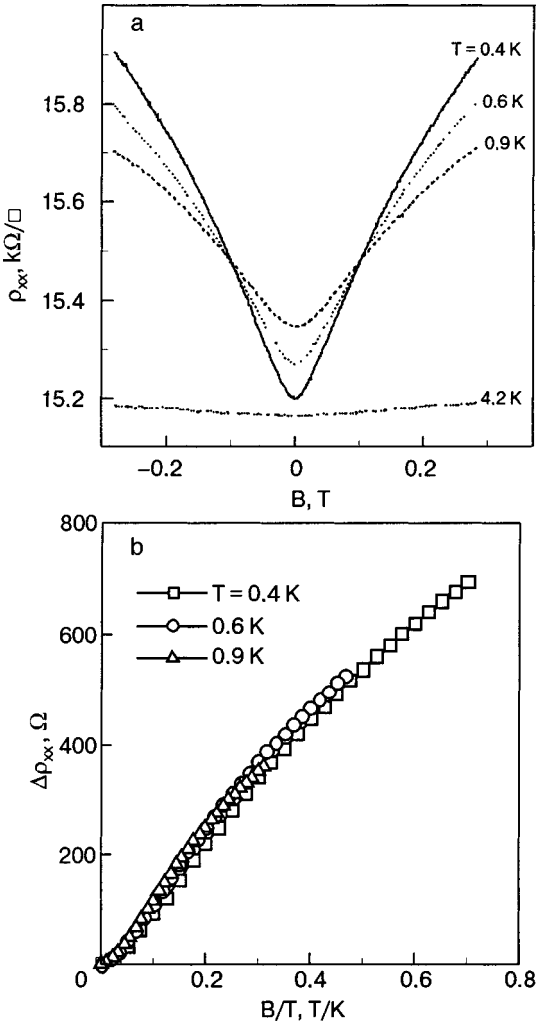

FIG. 2. Resistivity versus magnetic field (a) and magnetoresistivity versus B/T (b) at different temperatures.

ing 2D systems with high mobility.[10,15,19,23,24]

EXPERIMENTAL RESULTS AND DISCUSSION

Measurements of the galvanomagnetic effects in multilayer heterostructures of p-type $Ge/Ge_{1-x}Si_x$ were made in magnetic fields up to 5 T at $T=0.3$–4.2 K. For a sample[1)] with a carrier density of 1.2×10^{11} cm^{-2} and mobility $\mu_p=4\times10^3$ cm^2/(V·s) (parameter $\varepsilon_F\tau/\hbar=0.75$), nonmonotonic low-temperature behavior of the resistivity is observed (Fig. 1a): $\rho(T)$ increases with decreasing temperature from 4.2 to 1.5 K (localization) and then $\rho(T)$ decreases as T is lowered further from 1.5 to 0.3 K (antilocalization). In the antilocalization region for $T\leqslant1$ K the conductivity depends logarithmically on temperature (Fig. 1b). In the whole temperature interval positive magnetoresistance is observed, increasing sharply with decreasing T (Fig. 2a). At low temperatures $T<1$ K in fields $B<0.3$ T the magnetoresistivity $\Delta\rho_{xx}$ is an almost universal function of the ratio B/T (Fig. 2b).

The observed $\rho(B,T)$ curves can be compared with the quantum corrections to the two-dimensional conductivity due to the weak localization effects ($\delta\sigma_{wl}$) and to electron–electron interaction ($\delta\sigma_{ee}$). For the electron–electron interaction effects in the diffusion regime $k_BT\tau/\hbar\ll1$ we have[1,2]

$$\delta\sigma_{ee}(B,T)=\delta\sigma_{ee}(0,T)+\delta\sigma_z(b), \tag{1}$$

where

$$\delta\sigma_{ee}(0,T)=\frac{e^2}{2\pi^2\hbar}(1-3\lambda)\ln\frac{k_BT\tau}{\hbar}, \tag{2}$$

$$\delta\sigma_z(b)=-\frac{e^2}{2\pi^2\hbar}G(b)\quad\left(b=\frac{g\mu_BB}{k_BT}\right). \tag{3}$$

The first term in front of the logarithm in Eq. (2) corresponds to the exchange part of the electron–electron interaction, while the second term corresponds to the Hartree contribution (triplet channel). Here

$$\lambda=\frac{1+\gamma_2}{\gamma_2}\ln(1+\gamma_2)-1, \tag{4}$$

where γ_2 is the Fermi-liquid interaction parameter.[25]

The electron–electron contribution of the magnetic field is given as a function of the ratio B/T by expression (3), where $G(b)$ is a known function describing the positive magnetoresistance due to the splitting of the electron energy levels,[1,26,27] and $g=20.4$ for a 2D hole gas in Ge for $\varepsilon_F\to0$.

For weak localization effects[28]

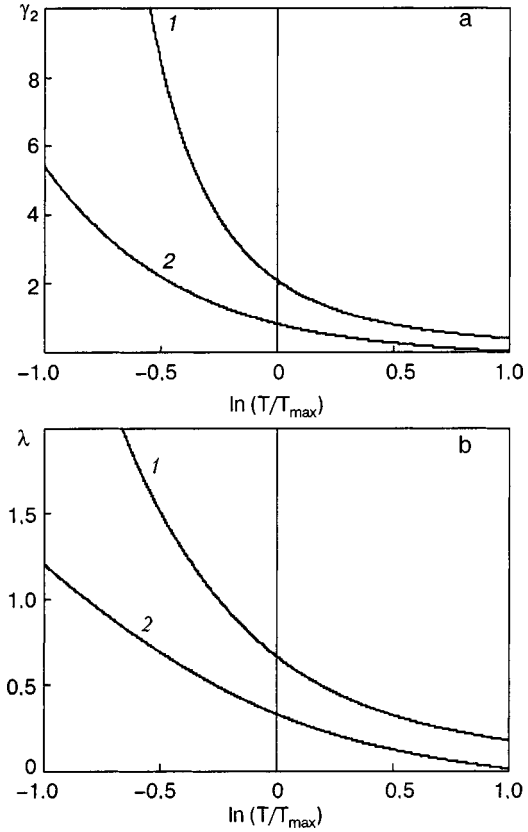

FIG. 3. Temperature dependence of the parameter γ_2 (a) and $\lambda=[(1+\gamma_2)/\gamma_2]\ln(1+\gamma_2)-1$ (b) according to the Finkelstein theory,[25] both with (*1*) and without (*2*) allowance for weak localization effects.

$$\delta\sigma_{wl}(0,T)=\frac{e^2}{2\pi^2\hbar}p\ln\frac{T}{T_0}, \tag{5}$$

and the dependence on magnetic field for $B\ll B_{\rm tr}$, $B_\rho\ll B_{\rm tr}$ ($B_{\rm tr}=\hbar c/4eD\tau$; $B_\varphi=\hbar c/4eD\tau_\varphi$, D is the diffusion coefficient, τ_φ is the dephasing time, which depends on the temperature as T^{-p}, where p is an exponent determined by the scattering mechanism, dimensionality of the sample, etc.) is determined by the expression[28]

$$\delta\sigma_{wl}(B,T)=\frac{e^2}{2\pi^2\hbar}\left[\psi\left(\frac{1}{2}+\frac{B_\varphi}{B}\right)-\ln\frac{B_\varphi}{B}\right]. \tag{6}$$

Formula (6) describes the negative magnetoresistance due to the suppression of interference effects by the magnetic field. We emphasize that $\delta\sigma_{wl}$ depends only on the ratio B/B_φ, and for $p=1$ (the Nyquist mechanism) it is a function of the ratio B/T.

By comparing the dependence $\rho(T)$ in the region of "metallic" conductivity at $T<1$ K (see Fig. 1b) with expressions (2) and (5) for $p=1$ we see that such behavior is possible only when the predominant role is played by the antilocalization contribution of the triplet channel. A fitting gives $\lambda=0.68$, which corresponds to $\gamma_2=2.15$ (in the notation of Ref. 6, $F_0^\sigma=-\gamma_2/(1+\gamma_2)=-0.68$).

The magnetic field dependence (see Fig. 2b) can be described only by the joint influence of two effects: positive magnetoresistance due to the Zeeman splitting (3), and negative magnetoresistance due to dephasing (6), with a slight

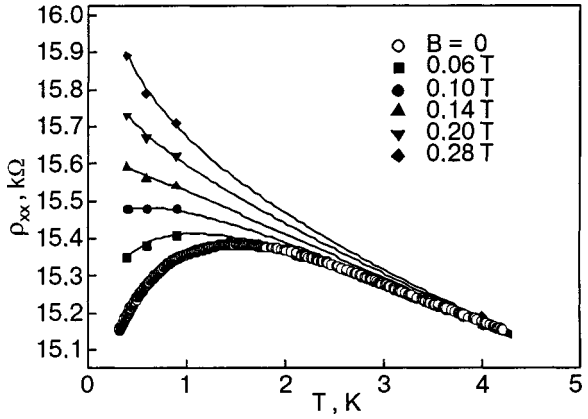

FIG. 4. Temperature dependence of the magnetoresistivity in fixed magnetic fields.

predominance of the first effect. For example, let us give the expression for $\delta\sigma=\delta\sigma_{ee}+\delta\sigma_{wl}$ at low fields $B\ll B_z=k_BT/g\mu_B$, $B\ll B_\varphi$:

$$\delta\sigma(B,T)=\frac{e^2}{2\pi^2\hbar}\left[-0.091\gamma_2(1+\gamma_2)+0.042\left(\frac{B_z}{B_\varphi}\right)^2\right]\times\left(\frac{B}{B_z}\right)^2, \tag{7}$$

where (for $p=1$) the ratio B_z/B_φ is independent of temperature.

By fitting the dependence $\rho(B/T)$ using formulas (3) and (6) in the whole interval of magnetic fields one can determine separately the g factor and $B_\varphi(\tau_\varphi)$. The value found for the g factor, $g=14.2\pm1.4$, is somewhat lower than the theoretical value for $\varepsilon_F\to0$ ($=20.4$), in accordance with the high degree of nonparabolicity of the hole dispersion relation in the ground spatial subband. For the dephasing time a fit gives $k_BT\tau_\varphi/\hbar\approx1$, in good agreement with the theoretical estimate.

Simultaneously taking into account the disorder (localization effects) and the electron–electron interaction leads to renormalization of the parameter γ_2—to monotonic growth of γ_2 with decreasing temperature[25] (Fig. 3). As was shown in Ref. 24, such a renormalization is especially important in the region of the metal–insulator transition, which is determined by the condition $\varepsilon_F\tau/\hbar\approx1$. We assume that the nonmonotonic $\rho(T)$ dependence observed by us is due to just such a renormalization of the parameter γ_2 and, as a result, to a change in sign of the coefficient $(p+1-3\lambda)$ at $T\approx1.5$ K, although we have been unable to describe the effect quantitatively.

CONCLUSIONS

Thus the observed nonmonotonic behavior of $\rho(T)$ and, specifically, the transition from insulating ($d\rho/dT<0$) to "metallic" ($d\rho/dT>0$) behavior with decreasing temperature is attributed by us to enhancement of the role of the triplet channel in the quantum correction to the conductivity due to the electron–electron interaction. The increase of the contribution of the triplet channel with decreasing temperature is apparently due to the renormalization of the electron–electron coupling parameter predicted in the Finkelstein

theory,[25] which is especially substantial for 2D systems in the vicinity of the concentration-induced metal–insulator transition ($\varepsilon_F \tau/\hbar \approx 1$). The Zeeman splitting of the electron energy levels in a magnetic field leads to effective suppression of the triplet channel, thus restoring the insulating behavior of $\rho(T)$ down to the lowest temperatures (Fig. 4).

The authors thank V. I. Okulov and S. G. Novokshonova for a discussion of the results. This study was supported by the Russian Foundation for Basic Research, Grant No. 02-02-16401, 04-02-16614 and was carried out as part of the ''Low-Dimensional Quantum Heterostructures'' program of the Russian Academy of Sciences, the CRDF, and the Ministry of Education of the Russian Federation, Grant Y1-*P*-05-14 (Ek-005[X1]), and a grant for young scientists from the Ural Division of the Russian Academy of Sciences.

*E-mail: neverov@imp.uran.ru

[1)]The technological parameters of the sample were: number of periods (Ge + GeSi) $N=15$; quantum well (Ge layer) width $d_W=80$ Å, and barrier (GeSi layer) width $d_b=120$ Å.

[1] P. A. Lee and T. V. Ramakrishnan, Rev. Mod. Phys. **57**, 287 (1985).
[2] B. L. Altshuler and A. G. Aronov, in *Electron–Electron Interactions in Disordered Systems*, A. L. Efros and M. Pollak (eds.), Amsterdam (1985), p. 1.
[3] S. V. Kravchenko, G. V. Kravchenko, J. E. Furneaux, V. M. Pudalov, and M. D'Iorio, Phys. Rev. B **50**, 8039 (1994).
[4] B. L. Altshuler, D. L. Maslov, and V. M. Pudalov, Physica E **9(2)**, 209 (2001).
[5] E. Abrahams, S. V. Kravchenko, and M. R. Sarachik, Rev. Mod. Phys. **73**, 251 (2001); S. V. Kravchenko and M. P. Sarachik, cond-mat/0309140 (submitted to Rep. Progr. Phys.)
[6] G. Zala, B. N. Narozhny, and I. L. Aleiner, Phys. Rev. B **64**, 214204 (2001); G. Zala, B. N. Narozhny, and I. L. Aleiner, cond-mat/0107333.
[7] I. V. Gornyi and A. D. Mirlin, Phys. Rev. Lett. **90**, 076801 (2003); I. V. Gornyi and A. D. Mirlin, cond-mat/306029.
[8] V. M. Pudalov, M. E. Gerhenson, N. Kojima, G. Brunthaler, A. Prinz, and G. Bauer, Phys. Rev. Lett. **91**, 126403 (2003); cond-mat/0401031.
[9] V. M. Pudalov, G. Brunthaler, and A. Prinz, and G. Bauer, JETP Lett. **65**, 932 (1997).
[10] D. Simonian, S. V. Kravchenko, M. P. Sarachik, and V. M. Pudalov, Phys. Rev. Lett. **79**, 2304 (1997).
[11] M. Y. Simmons, A. R. Hamilton, M. Perer, E. N. Linfield, R. D. Rose, D. A. Ritchie, A. K. Savchenko, and T. G. Griffiths, Phys. Rev. Lett. **80**, 1292 (1998).
[12] T. Okamoto, K. Hosoya, S. Kawaji, and A. Yagi, Phys. Rev. Lett. **82**, 3875 (1999).
[13] A. A. Shashkin, S. V. Kravchenko, V. T. Dolgorolov, and T. M. Klapwijk, Phys. Rev. Lett. **87**, 086801 (2001); cond-mat/0302004.
[14] S. A. Vitkalov, N. Zheng, K. M. Mertez, M. R. Sarachik, and T. M. Klapwijk, Phys. Rev. Lett. **85**, 2164 (2000).
[15] S. A. Vitkalov, K. James, V. N. Narozhny, and M. R. Sarachik, and T. M. Klapwijk, cond-mat/0204566.
[16] J. Yoon, C. C. Li, D. Shahar, D. S. Tsui, and M. Shayegan, cond-mat/9907128.
[17] N. Noh, M. R. Lilly, D. S. Tsui, J. A. Simmons, E. N. Hwang, S. Das Sarma, L. N. Pfeiffer, and K. W. West, Phys. Rev. B **68**, 165308 (2003).
[18] V. T. Dolgopolov and A. Gold, JETP Lett. **71**, 27 (2000).
[19] O. Simonian, S. V. Kravchenko, M. R. Sarachik, and V. M. Pudalov, Phys. Rev. B **57**, R9420 (1998).
[20] J. C. Hensel and K. Suzuki, Phys. Rev. Lett. **22**, 838 (1969).
[21] Yu. G. Arapov, N. A. Gorodilov, O. A. Kuznetsov, V. N. Neverov, L. K. Orlov, R. A. Rubtsova, G. I. Kharus, A. L. Chernov, N. G. Shelushinina, and G. L. Shtrapenin, Fiz. Tekh. Poluprovodn. **27**, 1165 (1993) [Semiconductors **27**, 642 (1993)]; Yu. G. Arapov, O. A. Kuznetsov, V. N. Neverov, G. I. Kharus, N. G. Shelushinina, and M. V. Yakunin, Fiz. Tekh. Poluprovodn. **36**, 550 (2002) [Semiconductors **36**, 519 (2002)].
[22] A. V. Nenashev, A. V. Dvurechenskiĭ, and A. F. Zinov'eva, Zh. Éksp. Teor. Fiz. **123**, 362 (2003) [JETP **96**, 321 (2003)].
[23] P. T. Coleridge, A. S. Sachrajda, and R. Zawadzki, cond-mat/9912041; cond-mat/0011067; Phys. Rev. B **65**, 125328 (2001).
[24] A. Punnoose and A. M. Finkelstein, Phys. Rev. Lett. **88**, 016802 (2002).
[25] A. M. Finkelstein, Z. Phys. B **56**, 189 (1984).
[26] C. Castellani, C. Di Castro, and P. A. Lee, Phys. Rev. B **57**, R9381 (1998).
[27] G. Zala, B. N. Narozhny, and I. L. Aleiner, Phys. Rev. B **65**, 020201 (2001).
[28] S. Hikami, A. I. Larkin, and I. Nagaoka, Prog. Theor. Phys. **63**, 707 (1980).

Translated by Steve Torstveit

Formation of a self-consistent double quantum well in a wide *p*-type quantum well

G. A. Alshanskiĭ* and M. V. Yakunin

Institute of Metal Physics of the Ural Division of the Russian Academy of Sciences, Sofia Kovalevskaya St., 18, Ekaterinburg 620219, Russia
(Submitted August 28, 2004)
Fiz. Nizk. Temp. **30**, 1162–1165 (November 2004)

The process of formation of self-consistent double quantum wells (DQWs) in a wide *p*-type quantum well in the presence of uniaxial strain is investigated. A feature of *p*-type systems is the structure of the valence band, which consists of two branches of energy dispersion—light and heavy holes. It is shown that this feature leads to significant splitting of the subbands of symmetric and antisymmetric states, as a result of which it is difficult to form states of the DQW with a vanishingly small tunneling gap; a uniaxial strain, by lifting the degeneracy of the band, suppresses this property, so that the two ground subbands of the size quantization of the DQW remain degenerate to high energies. © *2004 American Institute of Physics.*
[DOI: 10.1063/1.1819866]

INTRODUCTION

Systems known as double quantum wells (DQWs) or two-layer electron systems consist of two layers of a two-dimensional electron gas (2DEG) separated by a barrier of width comparable to the average distance between electrons in a layer. The 2DEG layers are each bound in their own quantum well or near different edges of a single wide quantum well. The latter system is called a self-consistent DQW.

In a DQW, unlike an ordinary single quantum well, the charge carriers have an additional degree of freedom—they can occupy states in the right or left quantum well (or, in the presence of tunneling, between the layers), which are characterized by a symmetric or an antisymmetric wave function. This additional degree of freedom can be controlled by varying the height and width of the barrier. The latter not only determines the value of the gap between the symmetric and antisymmetric states but also regulates the value of the interlayer Coulomb interaction.

DQWs exhibit a number of effects due to the interlayer electron–electron interaction. The clearest of these is the closing, in a quantizing magnetic field, of the gap between the symmetric and antisymmetric states and the formation of a state of the collective integer quantum Hall effect (QHE). In an experiment the state of the collective integer QHE is manifested in the vanishing of the associated features at even indices.[1] The features of the integer QHE vanish at high magnetic field if the relation $\Delta_{SAS} \leqslant E_c$ is satisfied,[2,3] where Δ_{SAS} is the gap between the symmetric and antisymmetric states, $E_c = e^2/\varepsilon d$ is the characteristic energy of the interlayer electron–electron interaction, $d = d_w + d_b$ is the distance between centers of the quantum wells forming the DQW. A survey of papers on the quantum Hall effect in DQWs can be found in Ref. 3, and a theoretical analysis of the states of the collective integer QHE is presented in Refs. 3–5.

A magnetic field applied parallel to the plane of the structure mixes the symmetric and antisymmetric states, and that leads to distortion of the Fermi surface in the DQW. This is manifested in a shift of the nodal points of the beats of the Shubnikov–de Haas oscillations in a parallel magnetic field.[6]

In this paper we investigate the possibilities and conditions for the formation of a self-consistent double quantum well in a single *p*-type quantum well. Based on the model formulated, which permits taking into account the presence of uniaxial compression in the heterostructure, a technique is developed for carrying out numerical calculations, the results of which enable one to find the solution of the problem posed under the indicated restrictions, and the important role of uniaxial compression is thereby established.

CALCULATION TECHNIQUE

The calculations were done using an isotropic Luttinger model. The dispersion relation, density of states, effective mass at the Fermi level, wave functions, and profile of the self-consistent potential are determined for a series of wells of different widths and charge carrier densities.

The self-consistent system of equations has the form

$$\left[H_{\mathrm{Lut}}\left(k_x, k_y, \frac{1}{i}\frac{\partial}{\partial z} \right) + V(z)\hat{I} \right] G_i(k_x, k_y, z) = E_i G_i(k_x, k_y, z), \tag{1}$$

$$V(z) = V_0(z) + V_{xc}(z) + q\varphi(z), \tag{2}$$

$$\Delta\varphi(z) = -4\pi[\rho_h(z) + \rho_{\mathrm{imp}}(z)], \tag{3}$$

$$\rho_h(z) = \sum_n \int dk g_n(k, \varepsilon_F) |G_{n,k}(z)|^2, \tag{4}$$

where $G_{i,\mathbf{k}}(z)$ is the envelope wave function belonging to the ith subband; $V_0(z)$ is the "zero" potential formed by a discontinuity of the conduction band; $V_H(z)$ is the Hartree self-consistent potential, which satisfies Poisson's equation, $V_{xc}(z)$ is the exchange-correlation potential, the form of which is taken from Refs. 7 and 8; q is the charge of a hole, $q = |e|$; $\rho(z)$ is the charge density in the system consisting of the hole charge density in the quantum well $\rho_h(z)$ and the impurity charge density $\rho_{\mathrm{imp}}(z)$.

The density of states of the spatially quantized holes is given by the relation

$$g_i(\varepsilon,k)=\frac{k}{2\pi}\,\theta(\varepsilon-\varepsilon_i(k)). \tag{5}$$

For simplicity we neglect the dependence of the Luttinger parameter on the coordinate z, which arises because of the difference of the materials of the layers forming the quantum well and barrier. We have included a uniaxial compression along the z direction (the direction of growth of the heterostructure), which is described by the addition of the following term to the Luttinger Hamiltonian inside the layer forming the quantum well:

$$H_\zeta=\begin{bmatrix} -\zeta & 0 & 0 & 0 \\ 0 & \zeta & 0 & 0 \\ 0 & 0 & \zeta & 0 \\ 0 & 0 & 0 & -\zeta \end{bmatrix}, \tag{6}$$

where

$$\zeta=b(S_{11}-S_{12})X.$$

In the latter expression b is the deformation potential, S_{11} and S_{12} are the elastic constants of the material, and X is the applied pressure. Thus uniaxial compression leads to a change of the position of the bottom of the valence band by an amount ζ inside the layer forming the quantum well, whereupon the depth of the quantum well increases for the heavy holes and decreases by the same amount for the light holes.

To solve the eigenvalue problem we use the transfer matrix method.[9]

RESULTS OF THE CALCULATIONS

Calculations were done for a sample with the following parameters: quantum well width $d_w=38$ nm and depth $U_0=100$ MeV, spacer width $d_{sp}=8$ nm, and density of charge carriers in the well $p=5\times10^{11}$ cm^{-1}. Such values correspond to the sample in which the vanishing of the QHE features with even indices was observed in Ref. 10.

A calculation without the uniaxial stress in the layer forming the quantum well shows that the spectrum of charge carriers in the given system is marked by strong nonparabolicity of the bottom two branches of the dispersion relation, which correspond spatially to the quantized heavy holes (Fig. 1). For $k\sim k_F$ one observes significant splitting of the subbands of symmetric and antisymmetric states, making it difficult for states of the DQW with a vanishingly small tunneling gap to form. This raises the question of how such a state can be formed in the given system.

The answer to this question is to include a uniaxial stress in the Ge layer forming the quantum well. Because of the lattice misfit this layer is stretched in the plane perpendicular to the growth plane of the structure; this can be described effectively by a uniaxial compression along the growth direction of the structure. The value of the parameter ζ describing the amount of uniaxial compression was chosen by proceeding from the requirement that the effective mass of the charge carriers on the Fermi surface be equal to the mass determined from the measurements of the Shubnikov–de Haas oscillations. The results of the calculation are given in Fig. 2.

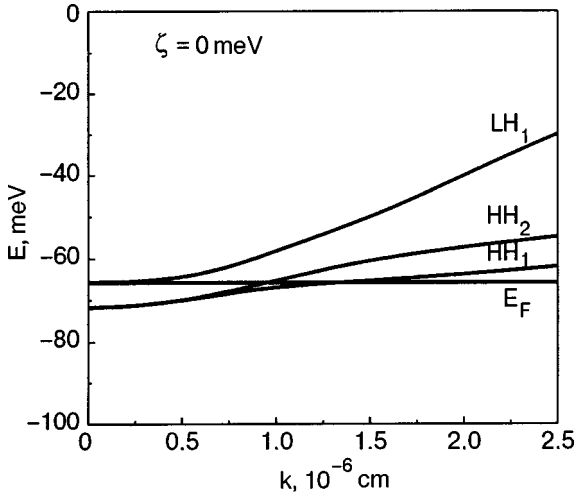

FIG. 1. Dispersion relation of the charge carriers in a p-Ge/GeSi quantum well without allowance for the uniaxial compression; HH_1 and HH_2 show the band of spatial quantization of the heavy holes, LH_1 shows the band of spatial quantization of the light holes.

Uniaxial compression leads to the situation that the ladders of sublevels of the spatial quantization of the heavy and light holes move apart in energy: the levels of the heavy holes are shifted downward while the light-hole levels are shifted upward. As a result, the interaction between the states of the heavy and light holes become weaker, and as a consequence the nonparabolicity of the dispersion relation of the heavy holes decreases, the gap between symmetric and antisymmetric states decreases to a vanishingly small value, and a state of the DQW arises in the system.

CONCLUSIONS

We have shown that the presence of two branches, corresponding to light and heavy holes, in the dispersion rela-

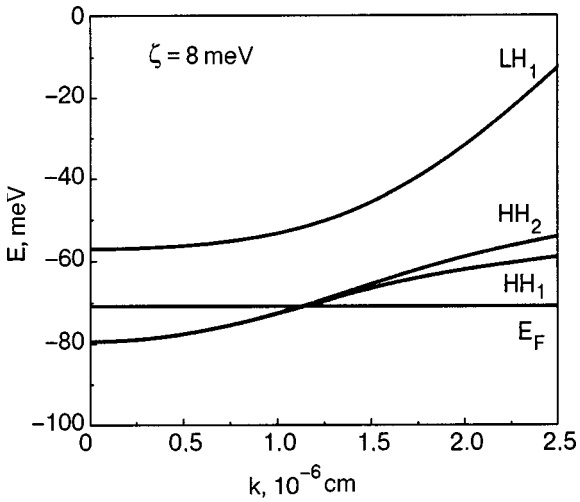

FIG. 2. Dispersion relation of the charge carriers in a p-Ge/GeSi quantum well with the uniaxial compression taken into account; HH_1 and HH_2 show the band of spatial quantization of the heavy holes, and LH_1 shows the band of spatial quantization of the light holes.

tion of the valence band of *p*-type systems leads to significant splitting of the symmetric and antisymmetric states in a wide quantum well, preventing the formation of a system with a DQW. At the same time, we have found that the existence of uniaxial compression in the germanium layer forming the quantum well in a *p*-Ge/GeSi heterostructure substantially expands the possibilities for the formation of a self-consistent double quantum well in a wide *p*-GeSi/Ge/GeSi quantum well.

*E-mail: alshansk@imp.uran.ru

[1] G. S. Boebinger, H. W. Jiang, L. N. Pfeiffer, and K. W. West, Phys. Rev. Lett. **64**, 1793 (1990).
[2] S. Q. Murphy, J. P. Eisenstein, G. S. Boebinger, L. N. Pfeiffer, and K. W. West, Phys. Rev. Lett. **72**, 728 (1994).
[3] K. Yang, K. Moon, L. Belkhir, H. Mori, S. M. Girvin, A. H. MacDonald, L. Zheng, and D. Yoshioka, Phys. Rev. B **54**, 11644 (1996).
[4] R. J. Radtke, P. I. Tamborenea, and S. Das Sarma, Phys. Rev. B **54**, 13832 (1996).
[5] R. J. Radtke, S. Das Sarma, and A. H. MacDonald, Phys. Rev. B **57**, 2342 (1998).
[6] K. Moon, H. Mori, Kun Yang, S. M. Girvin, A. H. MacDonald, L. Zheng, D. Yoshioka, and Shon-Cheng Zhang, Phys. Rev. B **51**, 5138 (1995).
[7] M. Kemerink, PhD Thesis, Technische Universiteit Einhoven, Eindhoven, Nederlands (1998).
[8] P. A. Bobbert, H. Wieldraijer, R. van der Weide, M. Kemerink, P. M. Koenraad, and J. H. Wolter, Phys. Rev. B **56**, 3664 (1997).
[9] C. Yi-Ping Chao and Shun L. Chuang, Phys. Rev. B **43**, 7027 (1991).
[10] Yu. G. Arapov, G. I. Harus, V. N. Neverov, N. G. Shelushinina, M. V. Yakunin, G. A. Alshanskii, and O. A. Kuznetsov, Nanotechnology **11**, 351 (2000).

Translated by Steve Torstveit

Oscillations of the conductivity of a two-dimensional electron gas in the presence of microwave radiation

A. E. Patrakov and I. I. Lyapilin*

Institute of Metal Physics of the Ural Division of the Russian Academy of Sciences, Sofia Kovalevskaya St., 18, Ekaterinburg 620219, Russia

(Submitted June 1, 2004)
Fiz. Nizk. Temp. **30**, 1166–1168 (November 2004)

The conductivity of two-dimensional electrons under microwave irradiation at magnetic fields in the region where the usual Shubnikov–de Haas oscillations do not appear is investigated in the framework of the Boltzmann transport equation. It is shown that under such conditions the microwave radiation gives rise to a new type of oscillations of the components of the conductivity tensor. © *2004 American Institute of Physics.* [DOI: 10.1063/1.1820016]

Interest in theoretical research on nonlinear transport phenomena in two-dimensional electron systems has heightened in connection with the appearance of new experimental data obtained on very pure samples [the characteristic values of the electron mobility and electron density were $\mu = (1.5–2.5)\times 10^7$ cm^2/(V·s) and $n_e \sim 3\times 10^{11}$ cm^{-2}]. In experiments done by two independent groups,[1,2] it has been found that in the presence of microwave radiation in two-dimensional systems at large occupation numbers, oscillations of the longitudinal magnetoresistivity ρ_{xx} appear in the region of magnetic fields in which Shubnikov–de Haas oscillations are not observed. At the same time, the off-diagonal component ρ_{xy} turns out to be insensitive to external radiation.

The most important feature of these experimental results is that the effect is observed under the conditions

$$\hbar/\tau \ll T \simeq \hbar\omega_c \leqslant \hbar\omega \ll \zeta,$$

which implies its quasiclassical nature. Here τ is the momentum relaxation time, ω and ω_c are the radiation frequency and cyclotron frequency, ζ is the Fermi energy, and T is the temperature expressed in energy units. The experiments of Refs. 1 and 2 drew considerable attention, and in a comparatively short time interval many articles had appeared in which various aspects of the observed effects were discussed.[3–5]

In the present paper we consider the diagonal σ_{xx} and off-diagonal σ_{xy} components of the conductivity tensor on the basis of the Boltzmann transport equation, assuming that the main mechanism of electron scattering is elastic scattering on impurities. The ac field of the radiation will be taken into account as a perturbation causing transitions between Landau levels. We shall show that taking these circumstances into account is sufficient for realization of the oscillations mentioned above.

The nonequilibrium nature of the momentum distribution of the electrons is brought about by both dc $\mathbf{E}_{\rm dc}$ and ac $\mathbf{E}_{\rm ac}$ electric fields. We therefore have

$$\left.\frac{\partial f(\mathbf{p})}{\partial t}\right|_{E_{\rm ac}} - e\mathbf{E}_{\rm dc}\frac{\partial f(\mathbf{p})}{\partial \mathbf{p}} - \frac{e}{mc}[\mathbf{p}\times\mathbf{H}]\frac{\partial f(\mathbf{p})}{\partial \mathbf{p}} = I_s[f(\mathbf{p})]. \tag{1}$$

The first term on the left-hand side of Eq. (1) is the rate of change of the distribution function under the influence of radiation due to transitions between Landau levels,

$$\left.\frac{\partial f(\mathbf{p})}{\partial t}\right|_{E_{\rm ac}} = \sum_{\mathbf{p}'} w_{\mathbf{p}\mathbf{p}'}\{f(\mathbf{p}')[1-f(\mathbf{p})] - f(\mathbf{p})[1-f(\mathbf{p}')]\}. \tag{2}$$

Here $w_{\mathbf{p}\mathbf{p}'}$ is the probability of transition of an electron per unit time from a state with kinetic momentum $\mathbf{p}$ to a state with kinetic momentum $\mathbf{p}'$ under the influence of radiation. The second and third terms on the left-hand side of Eq. (1) determine the rate of change of the distribution function due to forces exerted on the electrons by the external electric and magnetic fields. The right-hand side is the collision integral.

We write the nonequilibrium distribution function of the electrons in the form:

$$f(\mathbf{p}) = f_0(\varepsilon(\mathbf{p})) + \mathbf{p}\cdot\mathbf{g}(\varepsilon(\mathbf{p})), \tag{3}$$

where $\mathbf{g}(\varepsilon(\mathbf{p}))$ is an unknown vector function that depends only on energy.

An equation for finding $\mathbf{g}(\varepsilon)$ is obtained by substituting the distribution function (3) into the transport equation (1). We then have

$$\sum_{\mathbf{p}'} w_{\mathbf{p}\mathbf{p}'}[f_0(\varepsilon') - f_0(\varepsilon) + \mathbf{p}'\cdot\mathbf{g}(\varepsilon') - \mathbf{p}\cdot\mathbf{g}(\varepsilon)] - \frac{e}{m}\mathbf{E}_{\rm dc}\cdot\mathbf{p}\frac{\partial f_0(\varepsilon)}{\partial\varepsilon} - \frac{e}{mc}[\mathbf{p}\times\mathbf{H}]\cdot\mathbf{g}(\varepsilon) = -\frac{\mathbf{p}\cdot\mathbf{g}(\varepsilon)}{\tau(p)}. \tag{4}$$

The terms proportional to the second and higher powers of $E_{\rm dc}$ are dropped because they are small.

We seek a solution of equation (4) in the form of a sum of a term that is independent of the radiation power and a term linear in $w_{\mathbf{p}\mathbf{p}'}$. We take into consideration that the main effect of the ac field is to change the energy (and not the momentum) of the electrons. Furthermore, for simplicity we shall assume that the relaxation time is independent of the momentum [$\tau(p) = \tau = \text{const}$]. We now have

$$\mathbf{g}(\varepsilon)=\mathbf{g}_0(\varepsilon)-\left(\frac{\tau}{1+\omega_c^2\tau^2}\right)^2\frac{e}{m}\{(1-\omega_c^2\tau^2)\mathbf{E}_{\rm dc} +2\tau[\omega_c\times\mathbf{E}_{\rm dc}]\}\sum_{\mathbf{p}'} w_{\mathbf{p}\mathbf{p}'}\left(\frac{\partial f_0(\varepsilon')}{\partial\varepsilon'}-\frac{\partial f_0(\varepsilon)}{\partial\varepsilon}\right), \quad (5)$$

where

$$\mathbf{g}_0=\frac{\tau}{1+\omega_c^2\tau^2}\frac{e}{m}\{\mathbf{E}_{\rm dc}+\tau[\omega_c\times\mathbf{E}_{\rm dc}]\}\frac{\partial f_0(\varepsilon)}{\partial\varepsilon}, \quad (6)$$

where $\omega_c=(e\mathbf{H})/(mc)$ and we have taken into account that $\mathbf{E}_{\rm dc}\perp\mathbf{H}$.

Taking into consideration that the change in the electron energy as a result of the interaction with the ac electric field is equal to $\pm\hbar\omega$, we obtain from Eq. (5)

$$\mathbf{g}(\varepsilon)=\mathbf{g}_0(\varepsilon)-\left(\frac{\tau}{1+\omega_c^2\tau^2}\right)^2\frac{e}{m}\{(1-\omega_c^2\tau^2)\mathbf{E}_{\rm dc} +2\tau[\omega_c\times\mathbf{E}_{\rm dc}]\}\sum_{\pm}\rho(\varepsilon\pm\hbar\omega) \times w_{\pm}\left(\frac{\partial f_0(\varepsilon\pm\hbar\omega)}{\partial\varepsilon}-\frac{\partial f_0(\varepsilon)}{\partial\varepsilon}\right). \quad (7)$$

$$w_{\pm}\propto E_{\rm ac}^2\ell^2|\langle n\pm1|x|n\rangle|^2\propto E_{\rm ac}^2 n/\omega_c\propto E_{\rm ac}^2\varepsilon_n/\omega_c^2,$$

where $E_{\rm ac}$ is the amplitude of the ac electric field with frequency ω, $\rho(\varepsilon)$ is the density of states, and $\ell=\sqrt{\hbar/(m\omega_c)}$ is the magnetic length.

Using the expression found for the correction to the distribution function, we calculate the current density caused by the radiation:

$$\mathbf{j}=-\frac{2e}{(2\pi\hbar)^2\rho_0}\int_0^{2\pi}\int_0^{\infty}p'dp'd\varphi\rho(\varepsilon')\mathbf{p}'(f_0(\varepsilon') +\mathbf{p}'\mathbf{g}(\varepsilon')), \quad (8)$$

where $\rho_0=m/(2\pi\hbar^2)$ is the density of states per spin in the absence of magnetic field. Substituting the explicit form of $\mathbf{g}$ from (7) into (8), we find for the diagonal component of the conductivity tensor under conditions of strong degeneracy

$$\sigma_{xx}^{\rm ph}\propto-\frac{\tau^2(\omega_c^2\tau^2-1)}{\omega_c^2(1+\omega_c^2\tau^2)^2}\rho(\zeta)\sum_{\pm}[\zeta^2\rho(\zeta\pm\hbar\omega) -(\zeta\mp\hbar\omega)^2\rho(\zeta\mp\hbar\omega)]. \quad (9)$$

An ideal two-dimensional system in a perpendicular magnetic field is characterized by a discrete energy spectrum that corresponds to a density of states in the form of a set of delta functions. The presence of the random impurity potential causes different points in space to become inequivalent, and the energy of an electron in the magnetic field begins to depend on the position of the center of the cyclotron orbit. This leads to broadening of the peaks on the density of states. We shall assume that the Landau levels have a Lorentzian shape with a width Γ that is independent of the magnetic field. The experimental situation realized is one with a large number of filled Landau levels ($\zeta\gg\hbar\omega_c$), which makes it possibility to write the expression for the density of states in the following form:

$$\rho(\varepsilon)=\left[\hbar\omega_c\pi\ell^2\left(\cos^2\frac{\pi\varepsilon}{\hbar\omega_c}\tanh\frac{\pi\Gamma}{\hbar\omega_c} +\sin^2\frac{\pi\varepsilon}{\hbar\omega_c}\coth\frac{\pi\Gamma}{\hbar\omega_c}\right)\right]^{-1} \quad (10)$$

In the limit of low magnetic fields expression (10) reduces to

$$\rho(\varepsilon)=\rho_0\left(1-\delta\cos\left(\frac{2\pi\varepsilon}{\hbar\omega_c}\right)\right),\ \delta=2\exp(-\pi/(\omega_c\tau_f))\ll1 \quad (11)$$

($\tau_f=1/\Gamma$ is the single-particle relaxation time in the absence of magnetic field).[6] Taking this into account, we obtain for the components of the conductivity tensor

$$\sigma_{xx}^{\rm ph}-\sigma_{xx}^{{\rm ph},SdH}\propto\frac{\omega^2\tau^2(\omega_c^2\tau^2-1)}{\omega_c^2(1+\omega_c^2\tau^2)^2}\delta^2\cos\frac{2\pi\omega}{\omega_c}. \quad (12)$$

Denoting all the cofactors in $\sigma_{xx}^{\rm ph}-\sigma_{xx}^{{\rm ph},SdH}$ except $(\omega_c^2\tau^2-1)\cos(2\pi\omega/\omega_c)$ by a coefficient A (which is proportional to the radiation power), we have

$$\sigma_{xx}^{\rm ph}-\sigma_{xx}^{{\rm ph},SdH}=A(\omega_c^2\tau^2-1)\cos\frac{2\pi\omega}{\omega_c}. \quad (13)$$

Analogous calculations for the Hall photoconductivity give the following result:

$$\sigma_{xy}^{\rm ph}-\sigma_{xy}^{{\rm ph},SdH}=2A\omega_c\tau\cos\frac{2\pi\omega}{\omega_c}. \quad (14)$$

It follows from expressions (13) and (14) that both the diagonal and the off-diagonal components of the photon-assisted conductivity give rise to oscillations as a function of inverse magnetic field: $\propto\cos(2\pi\omega/\omega_c)$. The ordinary Shubnikov–de Haas oscillations, denoted collectively by $\sigma^{{\rm ph},sdH}$ contain the factor $\cos(2\pi\zeta/\hbar\omega_c)$ or $\cos(4\pi\zeta/\hbar\omega_c)$ and by virtue of the inequality $T\simeq\hbar\omega\ll\zeta$ are rapidly damped.

Since the components of the conductivity tensor are known, it is not difficult to find expressions for the diagonal and off-diagonal components of the magnetoresistivity, which are ordinarily measured in experiment. We get

$$\rho_{xx}=\frac{\sigma_{xx}}{\sigma_{xx}^2+\sigma_{xy}^2}=\frac{1}{\sigma_{xx}^0(1+\omega_c^2\tau^2)}+\frac{A}{(\sigma_{xx}^0)^2}\cos\frac{2\pi\omega}{\omega_c} +O(A^2), \quad (15)$$

$$\rho_{xy}=\frac{\sigma_{xy}}{\sigma_{xx}^2+\sigma_{xy}^2}=-\frac{\omega_c\tau}{\sigma_{xx}^0(1+\omega_c^2\tau^2)}+O(A^2). \quad (16)$$

It follows from the expressions given above that the off-diagonal components of the magnetoresistivity ρ_{xy}, unlike the diagonal components ρ_{xx}, are independent of the radiation, as has in fact been observed in experiments.[1,2]

*E-mail: Lyapilin@imp.uran.ru

[1] M. A. Zudov, R. R. Du, L. W. Pfeiffer, and K. W. West, Phys. Rev. Lett. **90**, 046807 (2003).
[2] R. G. Mani, J. H. Smet, K. von Klitzing, and W. B. Jonson, Nature (London) **420**, 646 (2002).

[3] A. C. Durst, S. Sachdev, N. Read, and S. M. Girvin, Phys. Rev. Lett. **91**, 086803 (2003).
[4] L. A. Dmitriev, M. G. Vavilov, I. L. Aleiner, A. D. Mirlin, and D. G. Polyakov, arxiv:cond-mat/0310668 (2003).
[5] S. A. Mikhailov, arxiv:cond-mat/0303130 (2003).
[6] T. Ando, A. B. Fowler, and F. Stern, Rev. Mod. Phys. **54**, 437 (1982).

Translated by Steve Torstveit

Molecular epitaxy and the electronic properties of Ge/Si heterosystems with quantum dots

A. V. Dvurechensky, A. I. Nikiforov, O. P. Pchelyakov,* S. A. Teys, and A. I. Yakimov

Institute of Physics of Semiconductors of the Siberian Division of the Russian Academy of Sciences, pr. Lavrent'eva 13, Novosibirsk 630090, Russia
(Submitted May 25, 2004)
Fiz. Nizk. Temp. **30**, 1169–1179 (November 2004)

We present the results of a study of the processes of preparation and the determination of the electrical and optical characteristics of arrays of Ge nanoislands in Si (artificial ''atoms'') with a discrete energy spectrum, which is manifested all the way up to room temperature. We give a brief analysis of the current ideas about the mechanisms of the initial stage of self-formation and ordering of ensembles of nanoclusters in the heteroepitaxy of Ge on Si. The main factors that determine the spectrum of states are the size quantization and Coulomb interaction of the carriers. It is shown that a new factor arising in an array of quantum dots and which distinguishes it from the situation for an isolated quantum dot is the presence of Coulomb correlations between islands. The rate of emission and the cross section for trapping of holes are determined as functions of the energy level depth. The values of the cross sections are several orders of magnitude greater than the known values in Si. The electron transport along the layers of quantum dots is occurs via hopping conduction, the value of which oscillates as the degree of occupation of the occupation of the islands by holes; this can serve as a working principle for electronic data transmission circuits based on quantum dots. It is shown that Ge quantum dots can be used to construct a photodetector tunable over the near- and mid-IR ranges. © *2004 American Institute of Physics.* [DOI: 10.1063/1.1820017]

INTRODUCTION

In recent years there has been active research on the electronic properties of semiconductor quantum dots, which represent a limiting case of systems with lowered dimensionality: zero-dimensional systems consisting of arrays of nanosize atomic clusters in a semiconductor host.[1,2] The discrete spectrum of energy states in such clusters makes it possible to classify them as artificial analogs of atoms, in spite of the fact that the clusters contain a large number of particles. By varying the size, shape, and composition of the quantum dots by controllable technological means one can obtain analogs of practically all the natural elements.

The nanosize scale of atomic clusters strongly limits the possibilities of using conventional lithographic techniques for preparing the structures, and new approaches must be developed. The idea of using morphological changes of the surface during the growth of mismatched heteroepitaxial systems for the formation of an array of nanosize atomic clusters at the transition from two-dimensional growth to three-dimensional by the Stranski–Krastanov mechanism has proved to be extremely fruitful. This idea was first implemented in 1992 for the Ge/Si system, and it was concluded from the results of a study of that system that one-electron effects are present in this new class of nanostructures.[3] This method of making artificial ''atoms'' has come to be called ''self-organization,'' since it was necessary to explain the observed formation of an array of nanoclusters of a rather uniform size.

Ge nanoclusters in Si are of interest for a number of reasons: 1) progress in the development of the technology of obtaining arrays of Ge nanoclusters of rather uniform size, which is important if they are being considered as artificial atoms for the doping of semiconductors; 2) the sizes of the nanoclusters has been successfully decreased to values such that quantum size effects and electron–electron coupling are manifested all the way up to room temperature; 3) the methods developed are compatible with the existing silicon technology for fabricating discrete devices and circuits.

Studies of the electronic properties of Ge/Si structures have been done with the use of electron tunnel spectroscopy, capacitive spectroscopy, conductance spectroscopy, studies of hopping conductance, and the field effect. The Ge/Si system belongs to the class of type-II heterostructures, in which Ge islands are potential wells for holes. This circumstance dictates the choice of the type of conductivity of the systems studied.

1. GROWTH AND THE FEATURES OF THE ORDERING OF ENSEMBLES OF Ge NANOCLUSTERS

In Ge–Si heterosystems several stages of evolution of the islands is observed as the effective thickness of the film is increased. These stages are different for substrates with the (001) and (111) surface orientations. From the standpoint of creating quantum objects, the (001) surface is unique, since only on it have compact three-dimensional dislocation-free islands with a size of 10–100 nm (Fig. 1) been observed.[1] The appearance of such islands is observed after the formation of a continuous Ge film, superstructural domains of which are easily discerned between islands.

The ordering process causes the islands appearing in the system to have preferred values of their characteristics: their size and shapes, the distance between them, and their mutual

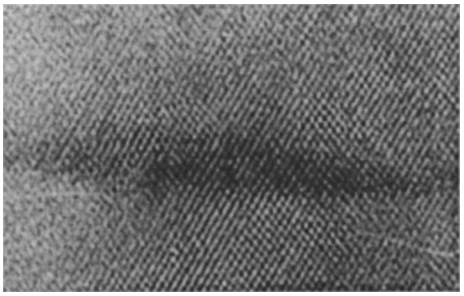

FIG. 1. Direct-resolution TEM image of a ''hut'' cluster of Ge in a Si host.

arrangement. This is a result of minimization of the total free energy of the system. The presence of the preferred characteristics should be manifested in the scattering spectra and electron and x-ray diffraction upon interaction with the surface containing the nanostructures and also in the electron and optical spectra. The size distribution of Ge islands has received a great deal of attention in the literature, since this parameter of a system of quantum dots is extremely important for practical applications. According to the data of Ref. 4, narrower distributions are observed for islands of the ''dome'' type with average sizes of 50–100 nm. The narrower distribution for ''dome'' clusters is explained by the fact that the growth of the elastic strain in the substrate and in the base of the cluster with increasing cluster size causes a slowing of its growth (unlike the development of clusters by the mechanism of Ostwald ripening). For ''hut'' clusters obtained by molecular beam epitaxy (MBE) an analogous regularity is observed: the growth rate of ''hut'' clusters of Ge decreases with increasing size (this effect is investigated in detail in Ref. 5). With the advent of quantum nanostructures (especially structures containing quantum dots) the conventional and technologically well-developed but indirect-gap semiconductors Si and Ge have now become prospective optical materials. This can explain the steady growth of interest in quantum structures based on these substances. The physical effects observed in such structures in recent years will become the basis for creating a new set of basic elements for microwave electronics in the gigahertz and terahertz ranges, optoelectronic devices, and quantum computational technique. In this connection the search for ways of obtaining nanostructures with ultrasmall (<5 nm) Ge quantum dots in Si has taken on a special urgency.

The manifestation of an ordering effect in arrays of islands of nanometer sizes in Ge–Si heterosystems enables one to obtain defect-free quantum dots of relatively small sizes (10–100 nm) with a density of 10^{10}–10^{11} cm^{-2} and have led to a clearer manifestation of atom-like characteristics in the electron and optical spectra of these objects. It was in this system that arrays of nanoclusters were first used to reveal one-electron effects.[3] For progress in the application of structures with germanium and silicon nanoclusters it is very important to look for ways of decreasing their size and increasing their packing density and degree of ordering on the surface.

Analyses of the current conceptual state as to the mechanisms of the initial stage of self-formation and ordering of ensembles of nanoclusters in the heteroepitaxy of Ge on Si have been given in a large number of reviews (see, e.g., Refs. 6–8). For the example of a heterosystem of germanium on silicon the transition from layer-by-layer film growth to the formation of three-dimensional (3D) islands has been investigated in detail. It has been shown that at relatively low synthesis temperatures ($<500\,^{\circ}C$) the interdiffusion of the island and substrate materials can be neglected.[4,9] Such islands do not contain misfit dislocations even after they have substantially exceeded the critical thicknesses, as was first shown in Ref. 6. Besides the difference of the internal and surface energies, lattice parameters, and elastic strains, for epitaxial films and 3D islands of Ge on Si, the key factors influencing the initial stage of heteroepitaxy are the energy of the film–substrate interface and the factors that determine it—the structure and composition of the surface of the silicon substrate.

These factors not only provide morphological stability of a continuous pseudomorphic (wetting) layer of Ge, on the surface of which in the later stages of growth the self-formation of an island film occurs (the Stranski–Krastanov mechanism), but they also influence the shape, size, and spatial distribution of nanoclusters of germanium in the first atomic layers, the coalescence of which leads to the formation of the wetting layer.

Despite a very large number of experimental studies and detailed analytical surveys, until recently[10] there were no indications that it would be possible to obtain a system of ordered nanoclusters in the process of formation of the pseudomorphic wetting layer. In the case of homoepitaxy, when the stresses in the film are minimal, on a clean enough surface the formation of 3D islands does not occur for hardly any semiconductors, and the film growth takes place either through the motion of steps (step–layer growth) or by the formation and growth of two-dimensional islands or nanoclusters. In the very initial stages of heteroepitaxy, in the development of 2D islands, the stresses, as in the case of homoepitaxy, do not play an important role. A more important factor is the state of the substrate surface. For this reason the morphological features of the growth of the first monolayers on atomically clean surfaces are similar for homo- and heteroepitaxy. Thus one can conclude that the self-formation process of nano-islands of extremely small sizes can be observed in the initial stage of growth of the pseudomorphic wetting layer of germanium by a 2D island mechanism. The shape and distribution of those islands can be controlled by varying the structural state of the silicon surface layer.

Experimental confirmation of this conclusion was obtained in Refs. 10–12, where the influence of the superstructural rearrangement of the Si(111)7×7 surface on the formation of Ge nanoclusters having sizes smaller than 5 nm was demonstrated (Fig. 2). It is found that the formation of germanium nuclei occurs predominantly within the half of the 7×7 unit cell that is found in the positions of a stacking fault. Such clusters have considerably temperature stability. Even after annealing at $350\,^{\circ}C$ for 2 hours relatively large fragments of nanoclusters remain on the silicon surface between the germanium islands. To control the character of the ordering of a system of nanoclusters it appears possible to use impurity superstructures having different sizes and structure of the unit cells. Such superstructures on the silicon surface are formed by metal us, in particular. These prereq-

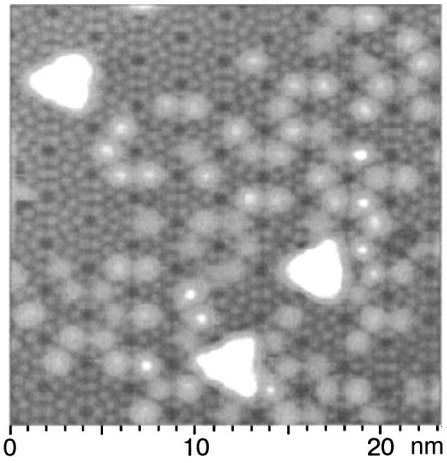

FIG. 2. STM image of Ge nanoclusters on the Si(111)7×7 surface.

uisites do not yet have a satisfactory experimental confirmation and are stimulating further detailed research on the mechanisms of ordering of ensembles of semiconductor nanoclusters by modification of the surface superstructures.

The minimum sizes of the germanium islands self-forming during growth on a clean surface of silicon after formation of the wetting layer is 15 nm. To decrease this size and increase the density one can grow the germanium on an atomically clean oxidized surface prepared directly in the MBE unit. The possibility of creating an oxide layer on the silicon surface under conditions of ultrahigh vacuum has been known for quite some time. It was first demonstrated in Ref. 13 that, depending on the oxygen pressure and the temperature, one could select the regimes of etching and growth of oxide films. The growth of germanium islands on the preliminarily oxidized silicon surface permits a substantial decrease in the size and an increase in the density of the islands. In Refs. 14 and 15 it was shown that in the case of island growth on the oxidized Si(111) surface the lateral size of the islands does not exceed 10 nm, and the density is greater than 10^{12} cm^{-2}. The authors of Ref. 14 assumed that local etching of the silicon oxide by the germanium (the disproportionation reaction) occurs, accompanied by desorption of germanium monoxide. At those places germanium nano-islands, coherently matched with the silicon, are nucleated. However, there are practically no data on the deformation of the islands and its relaxation in the germanium–silicon oxide heterosystem.

In our study the oxidation was done in the MBE unit with oxygen admitted to 10^{-4} Pa and a substrate temperature of 400–500 °C.[16] Then the oxygen was pumped out and the germanium was deposited. The growth of the Ge film was monitored from the high-energy electron diffraction pattern by registering both the qualitative changes in the structure and morphology of the growing surface of the film and quantitative information about the elastic deformation of the surface unit cell. For analysis of the initial stage of germanium film growth on the oxidized silicon surface we registered the change in intensity of specular and 3D diffraction reflections. These quantities are very sensitive to the change in the surface roughness, and the appearance of a 3D reflection indicates the presence of 3D objects on the surface.

The presence of oscillations of the intensity of specular reflection in the case of growth on a clean surface, the extinction of this reflection, and the appearance of a 3D reflection at thicknesses of the germanium film greater than four monolayers indicates the layer-by-layer growth of a wetting layer with the subsequent formation of 3D islands. In the case of the Ge film growth on the oxidized surface the intensity of these reflections changes after the deposition of just one monolayer, and oscillations of the intensity of the specular reflection are not observed. This attests to the absence of such a growth stage as the formation of a wetting layer.

At the time of the deposition of the first monolayer on the SiO_2 surface an adsorption layer of germanium forms, which after the second monolayer transforms into 3D islands. Thus, unlike the Stranski–Krastanov growth mechanism, which is realized on the clean silicon surface, the growth of a germanium film on the oxidized silicon surface occurs by the Volmer–Weber mechanism. From analysis of the deformations of the germanium lattice we measured the change of the 2D unit cell parameter $a_{\parallel}$. For this we registered the change in the distance between reflections of the diffraction pattern, which corresponds to the parameter $a_{\parallel}$. Growth is accompanied by a substantial change in the surface cell of the Ge lattice relative to that parameter for Si, which remains constant. This change reaches 7%, as is observed in the case of growth on the clean Si(100) surface.[16] Initially growth of elastically stressed islands occurs, and then the value of $a_{\parallel}$ decreases to the value for bulk germanium, attesting to the complete plastic relaxation of the islands. The character of the change in the parameter $a_{\parallel}$ is although to that which is observed in the process of heteroepitaxy of germanium on the clean Si(100) surface, but the existence region of the stressed Ge islands is significantly smaller, and the 3D islands that appear after the deposition of only one monolayer of germanium already have the maximum value of the 2D surface cell parameter. Depending on the thickness of the deposited germanium the islands have different sizes and densities. At a film thickness of up to five monolayers the islands have a base size of less than 10 nm and a density of more than 2×10^{12} cm^{-2}. Figure 3 shows a scanning tunneling microscope (STM) image of an array of Ge islands on an oxidized silicon surface, obtained after deposition of three monolayers of germanium at a substrate temperature of 650 °C. Increasing the effective thickness of the deposited germanium leads to the formation of islands with sizes an order of magnitude larger and with a much lower density in addition to the small islands. Such a bimodal distribution of islands in respect to their sizes and densities is observed on the oxidized Si(100) surface at germanium film thicknesses greater than 1 nm, as is also confirmed by electron microscope studies.

2. ELECTRICAL PROPERTIES

2.1. Electron tunneling spectroscopy

The structure to be investigated is in the form of two parallel electrodes (a heavily boron-doped layer of $Ge_{0.3}Si_{0.7}$), between which across a tunnel barrier (an Si spacer) a layer of Ge nanocrystals is inserted.[17] The length of the base of a quantum dot is 15 nm, and the height is 1.5 nm. The density of islands in the array is 3×10^{11} cm^{-2}. When

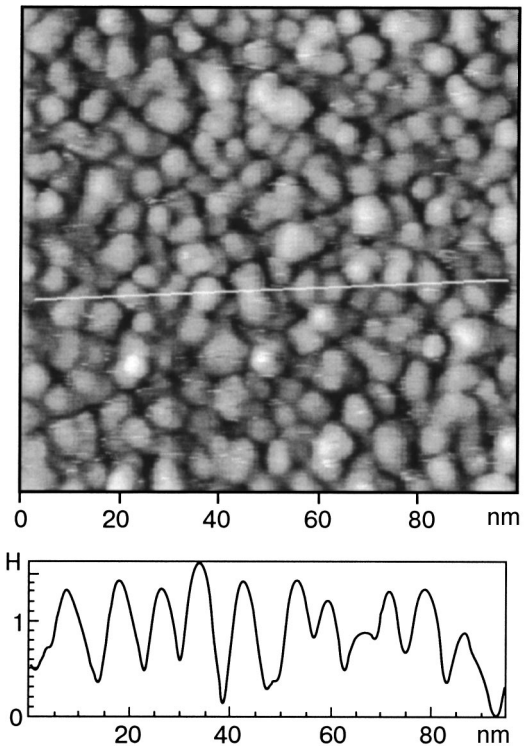

FIG. 3. STM image of Ge island on SiO_2: $T_s = 650\,^{\circ}C$, $d_{Ge} = 3$ ML, $N = 2\times10^{12}$ cm^{-2}.

the Fermi level in the emitter coincides with an allowed level of the carrier in the quantum dot, a resonant increase in the tunneling current should be observed. This method of spectroscopy was first applied to arrays of self-organizing quantum dots in Ref. 3. The voltage dependence of the differential conductance exhibits clear oscillations of the tunneling conductance of the structures, which attest to the existence of a well-resolved discrete spectrum in the Ge islands. The oscillations near zero bias are accompanied by the appearance of a region of negative differential conductance, which is a characteristic feature of resonance tunneling. In the case of a symmetric configuration of barriers the conductance oscillations are almost symmetric about zero and have a characteristic period of $\sim$150 mV, which permits estimation of the distance between size quantization levels in the islands as $\sim 150/2 = 75$ mV. In an asymmetric structure in the region of negative bias a splitting of the conductance peaks into a series of oscillations with a smaller period occurs. With such a polarity of the voltage, in view of the strong difference of the transmission coefficients of the left and right barriers, accumulation of holes occurs in the islands, and processes of Coulomb correlation of carriers due to their interaction become substantial. The correlation interaction lifts the degeneracy of the one-particle levels of the size quantization, since a hole must overcome the energy of electrostatic repulsion of the carriers already found in the quantum dot. A similar effect observed previously in tunnel junction across metallic granules in the form of stepped I–V characteristics was given the name "Coulomb ladder."[18] From the distance between peak of the conductance one can estimate the correlation energy of the holes in the islands: $E_C \approx 36$ meV in the ground state and ≈ 18 meV in the first excited state.

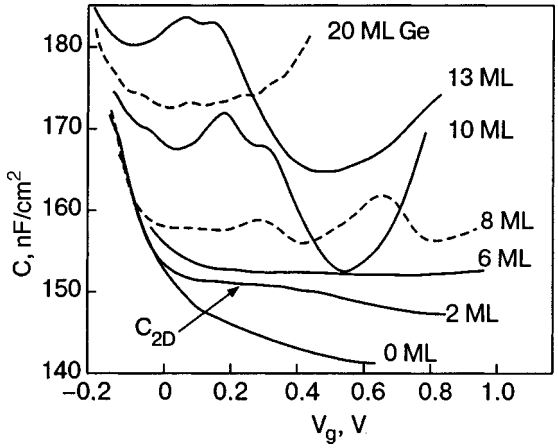

FIG. 4. Capacitance–voltage characteristics of structures with different thicknesses of the Ge layer.

2.2. Capacitive tunneling spectroscopy

Capacitive spectroscopy of quantum dots is based on the fact that the charge in zero-dimensional systems can vary only in a discrete manner by an amount $\delta Q = eN$, where e is the charge of the electron and N is the number of dots in the sample.[19] The structures consisted of the following sequence of layers, starting from the substrate: 1) a p^+-Si substrate with the (100) orientation, which served as the lower electrical contact; 2) a layer of $Si_{0.8}Ge_{0.2}$ with a thickness of $L = 10$ nm, providing a sharp heterointerface for the next Si tunneling barrier; 3) a tunnel-thin Si barrier with $p = 7\times10^{16}$ cm^{-3} and $L = 7$ nm; 4) a layer of Ge nanocrystals; 5) a silicon blocking layer, $p = 7\times10^{16}$ cm^{-3}, $L = 50$ nm; 6) an Al electrode, forming at a Schottky barrier at the boundary with the silicon, for controlling the occupation of the islands; the area of the aluminum pad was $\approx 8\times10^{-3}$ cm^2, according to the size of which a cylindrical mesostructure was etched to a depth of the order of 5 μm. In the investigated structures with a Schottky barrier the thickness of the grown Ge layer, which was measured in monolayers (ML) was varied, which in the case of island formation corresponds to an effective layer thickness d_{eff} (Ref. 20).

The external voltage V_g on the control electrode, shifting the potential in the islands relative to the Fermi level in the contact, which was separated from the island layer by a tunnel-thin barrier, stimulated either the trapping of carriers from the contact to levels of the quantum dot or the emptying of these levels, depending on the polarity of V_g. When the Fermi level in the contact coincides with the energy of a bound state in the quantum dot, the differential capacitance $C(V_g) = dQ/dV_g$ should have a peak indicating the presence of the discrete energy level. The total capacitance of the structure is the sum of two contributions: the first is due to the presence of a space-charge region in the material surrounding the islands (in this case the silicon), and the second contribution C_{QD} is due to the charging of the quantum dots. Since the value of C_{QD} is proportional to the density of states in the quantum dot: $C_{QD} = e(d\mu/dV_g)(dN/d\mu)$, where μ is the chemical potential, one can recover the value of $dN/d\mu$ from the I–C characteristic. The I–C characteristics of structures without a Ge layer had the usual form for a p-type Si depletion layer (Fig. 4). In the case $d_{\text{eff}} = 2$ ML a

plateau appears on the characteristics, typical for a 2D carrier gas. In the region of effective thicknesses of the Ge layer $8\ \text{ML} \leqslant d_{\text{eff}} \leqslant 13\ \text{ML}$ the $C-V$ curves exhibited peaks, the distance between them, their width, and their position on the voltage (energy) scale all depending on d_{eff}: with increasing d_{eff} the peaks become narrower and the energy gap between them decreases. The energy distance between levels corresponding to two capacitance peaks is found from the relation $\Delta E = \Delta V_{gb}/L$ (Ref. 21), where ΔV_g is the distance between peaks on the $C-V$ characteristic, b is the distance between the quantum well and the lower electrode, and L is the distance between the upper and lower electrodes. Calculations give $\Delta E = 87$ meV (for 8 ML), 36 meV (10 ML), and 32 meV (13 ML).[20] The value $\Delta E = 36$ meV for a sample with 10 ML Ge agrees with the value found for the charging energy E_C of the quantum dot in the ground state in the experiments on the resonance tunneling. Therefore the nature of the splitting of the peak has been explained by an electrostatic Coulomb interaction.

We attribute the appearance of capacitance oscillations to the formation of an array of Ge nanocrystals of rather uniform size, in which the density of hole states is a δ function of energy. For a large amount of deposited Ge (20 ML) a relaxation of the elastic stresses occurs, and large islands with dislocations form. This is manifested in the vanishing of the capacitance peaks on the $C-V$ characteristics. With the appearance of threading dislocations and the punchthrough of the space-charge region, apparently due to the strong increase in capacitance, accompanied by a sharp increase in the active part of the conductance at thicknesses greater than 20 ML. The area under each peak on the $C-V$ characteristic, divided by the charge of an electron, is to good accuracy equal to the surface density of Ge islands ($2n_{QD} \approx 6 \times 10^{11}\ \text{cm}^{-2}$). This means that, first, all of the Ge islands are involved in the charge-exchange process in the system and, second, the energy degeneracy is lifted by the Coulomb interaction. Experimental confirmation of the Coulomb nature of the splitting was obtained in measurements of the $C-V$ characteristics with two layers of Ge islands of the same size.[22] In that case the splitting between peaks due to the Coulomb interaction increased.

2.3. Field effect

Oscillations of the hopping conductance under conditions of the field effect have been observed in MIS transistors with an effective Ge thickness of more than 6 ML and containing up to 10^9 Ge islands.[23] The substrate was a high-resistance n-type Si wafer. The change in conductance of MIS transistors in which the conducting channel includes a layer of Ge nanocrystals turns out to be rather informative for studying effects of electron correlations and size quantization.[23] The successive filling of the islands by carriers is brought about by applying a potential to the gate of the transistor. At the densities of Ge islands used the tunneling transitions between states localized in different islands becomes substantial. The probability of "hops" of a hole between quantum dots is determined by: 1) the overlap of the wave functions of the occupied and unoccupied states, and 2) the degree of filling of a given hole shell. If the corresponding level is exactly half filled, then the conductance should

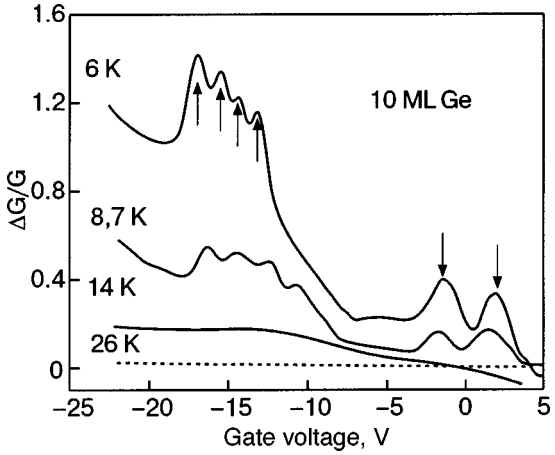

FIG. 5. Relative change of the conductance of the channel of a field-effect transistor containing 10^9 quantum dots, as a function of the gate voltage at different temperatures.

be maximum, and the activation energy of the transitions should be determined by the electrostatic interaction energy of a given hole with all the charges in the nanostructures. When the level is completely filled a carrier in the process of tunneling must make a transition to excited states of the next shell. In that case the activation energy increases by an amount equal to the size quantization energy, and the conductance decreases. Upon further filling of the excited state the activation energy required for a carrier to locate at a given level in the other dots decreases, and again the electron–electron interaction begins to govern; this leads to growth of the hopping conductance, and so on.

Thus the value of the hopping conductance at a fixed temperature and also the average of the activation energy for conduction should oscillate as the gate voltage is varied, thereby reflecting the structure of the spectrum of states. Such oscillations are characteristic only of zero-dimensional systems, in which the electronic spectrum is of a discrete (atom-like) character. In the low-temperature region ($T < 9$ K) the curves of the channel conductance versus gate voltage exhibited oscillations corresponding to the filling of the ground and excited states in the quantum well (Fig. 5). The values obtained for the degeneracy of the states (2 for the ground state and 4 for the excited state) agree with the results obtained by the methods of tunneling and capacitive spectroscopy. The main energy characteristics found in the analysis of the oscillation period (the correlation energy in the ground state $E_C = 28$ meV, in the excited state $E_C \approx 11$ meV, the size quantization energy ≈ 86 meV—all these values are given for $d_{\text{eff}} = 10$ ML) also agree with the results obtained by other methods. In an MIS transistor with a layer of quantum dots formed on a silicon-on-insulator (SIMOX) structure one can minimize the leakage currents through the lower Si layer, as a result of which the conductance oscillations are observed all the way up to temperatures ~ 150 K. The temperature dependence of the conductance turns out to be activational, which indicates that the oscillations occurring are distinct from resonance tunneling and argues in favor of a hopping mechanism of charge transport along the quantum dots. In the general case the temperature dependence of the hopping conductance is described by the

expression $G(T)=G_0\exp[-(T_0/T)^x]$. Approximation of the experimental data by this formula for all the peaks observed gave a value $x\approx 1/2$, which indicates that the activation energy for the hopping conduction in an array of quantum dots is determined by the Coulomb interaction between them.[24] In this case $T_0=6.2e^2/\varepsilon\ell$ (Ref. 25), where ε is the dielectric constant and ℓ is the radius of localization of the carriers in the quantum dots. From the experimental values of the parameter T_0 we found the characteristic size of the wave functions of the holes in the quantum dots: $\ell\approx 15-20$ nm. The value of the activation energy $W=0.5k(T_0T)^{1/2}\approx 11$ meV in the region of relatively high temperatures (~ 100 K), when the ''hops'' of the holes occur via nearest neighbors, is a measure of the contribution of the interaction between dots to the total correlation energy E_C (21 meV). The remaining part (≈ 10 meV) is due to the interaction of holes inside the quantum dots.

2.4. Conductance spectroscopy

Measurements of the complex conductance of silicon Schottky barriers with a buried layer of Ge quantum dots yielded additional information about the structure of the energy spectrum of the quantum dots and the parameters of the hole states.[26] The response from the quantum dots in the given case is represented as the response from a lossy capacitor[27] and is characterized by a time constant $\tau=R_{QD}C_{QD}$. With increasing reverse bias the depletion region penetrates into the interior of the Si, leading to the emptying of the hole levels in the quantum dot. Suppose that the bias is such that an energy level in the quantum dot coincides the Fermi level in the lower p^+-Si contact. Then the ac component of the voltage applied to the sample (V_{ac}) should stimulate the emission of holes into the valence band and the trapping of them back to bound states in the islands, giving rise to an ac conductance. If the frequency of the ac voltage ($\omega=2\pi f$) is high enough ($\omega\tau\gg 1$), then the occupation of the levels will not be able to follow the variation of the voltage, and the quantum dot will not contribute to the measured capacitance (C_{eff}) and conductance (G_{eff}) of the structure. In the opposite case ($\omega\tau\ll 1$) the effective capacitance contains a contribution from the holes accumulated in the island layer and is independent of the frequency. Since this contribution is purely of an electrostatic character, the low-frequency ac conductance is small. It is clear that the conductance should have a maximum when the effective rate of emission τ_i^{-1} from a given level i coincides with the frequency of the ac voltage ($2\pi f\tau_i=1$). This makes it possible to determine the emission time, activation energy, and trapping cross section to the corresponding levels in the quantum well.[28] The curve of the active part of the conductance normalized to the frequency of the ac signal versus the bias voltage has two peaks, at 0.1 and 0.6 V. The amplitude of these peaks is independent of the frequency in the range 10–100 kHz, and the peaks are apparently due to charge-exchange with the wetting layer. In the sample containing quantum dots, four additional peaks are observed, the presence of which has been attributed to charge exchange of the fourfold degenerate first excited state in the Ge nanocrystals.[26] The emission time at a temperature of 90 K was found to have the values [μs]: $\tau_1=5.1\pm 0.1$, $\tau_2=3.0\pm 0.1$, $\tau_3=0.39\pm 0.01$, and $\tau_4=0.29\pm 0.01$. From the temperature dependence of the emission time one can determine the activation energy (the energy level depth, meV): $E_1=201\pm 7$, $E_2=228\pm 7$, $E_3=267\pm 12$, $E_4=288\pm 10$, and also the trapping cross section (Fig. 6). The distance between levels 29 ± 16 meV (the charging energy of the quantum dots) correlates well with the data obtained by other methods. The values obtained for the trapping cross section of carriers to the quantum dots increase with increasing level depth and are many orders of magnitude greater than the known values for deep levels in Si. A possible explanation for this is that the carrier trapping process initially occurs to shallow levels in the thin continuous Ge layer (wetting layer) on which the Ge islands are found and which has dimensions comparable to the size of the structure. Later their successive reflection to deep levels of the quantum dot occurs, accompanied by the emission of phonons.

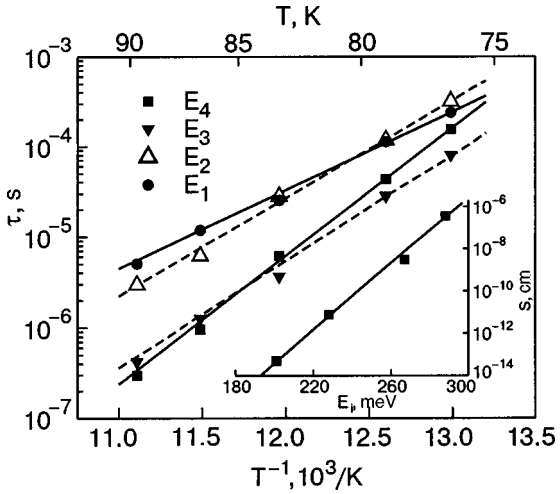

FIG. 6. Temperature dependence of the emission tims of holes from an excited state in the quantum dots. The inset shows the dependence of the trapping cross section to levels in the quantum dots as a function of the energy level depths.

3. OPTICAL PROPERTIES

Interest in the study of the optical properties of quantum dots is motivated by their pronounced practical directionality and by a number of advantages such objects have in comparison with two-dimensional quantum wells. Quantum dots have the following features: first, the spectral band of the photoresponse can be controlled by a preliminary filling of discrete states with the required transition energies; second, the present of lateral quantization in zero-dimensional systems lifts the forbiddenness of of optical transitions polarized in the plane of the photodetector, and that means that it becomes possible to effect absorption of light at normal incidence of the photons; third, in quantum dots one expects a strong increase in the lifetime of photoexcited carriers owing to the so-called phonon bottleneck effect.[28]

3.1. IR absorption

The absorption of photons in the IR region of the spectrum in multilayer Ge/Si heterostructures with self-organizing quantum dots was investigated in Refs. 29 and 30. The dimensions of the islands in the two cases were

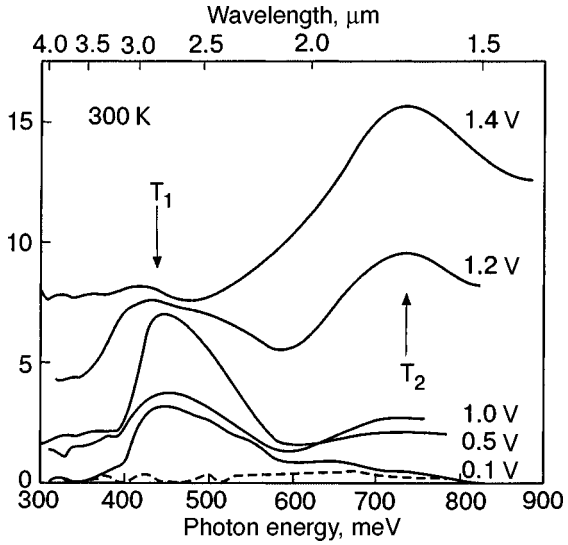

FIG. 7. Photocurrent spectrum of a silicon *p-i-n* diode with Ge quantum dots at different reverse biases. The dashed curve demonstrates the absence of photocurrent in a structure with a continuous layer of Ge.

$\sim$40–50 nm at the base and 2–4 nm in height. The density of islands was $\sim 10^8$ cm^{-2}. The authors of Ref. 29 used boron-underdoped Ge islands in order to fill the ground state of the quantum dots with holes. In the absorption spectra in the wavelength region 5–6 μm a broad ($\sim$100 meV) line was observed, with an amplitude that decreased strongly when the light was polarized perpendicular to the plane of the layers; this was explained by transitions between the two lowest levels of the transverse quantization of the heavy holes in the quantum dot. In Ref. 30 for activation of optical transitions within an undoped quantum dot an additional light pump was used. The photoinduced absorption polarized parallel to the plane of the layers had an asymmetric maximum in the 4.2 μm region and was attributed to a transition of the holes from the ground state of the quantum dot to extended states of the valence band. The value of the absorption cross section determined in Ref. 30 was unusually high (2×10^{-13} cm^2), which is at least an orders of magnitude greater than the known photoionization cross sections for local centers in Si (Ref. 31) and three orders of magnitude greater than the analogous value for InAs/GaAs quantum dots.[32] These data attest to the promise of the Ge/Si system for IR detectors.

3.2. Photoconductance

The detection of a photocurrent generated by photons with energies less than the band gap of silicon in Ge/Si heterostructures with self-organizing quantum dots was first reported in Refs. 33 and 34. The possibility of implementing a quantum-dot photodetector tunable over the near- and mid-IR ranges was demonstrated in Ref. 35. The photodetector was a silicon *p-i-n* diode with a 2D array of Ge nanoclusters inserted in its base. The quantum dots had an average lateral size of 15 nm and a height of 1.5 nm. The spectra of the photocurrent at different reverse biases are shown in Fig. 7. In a sample with a continuous Ge film (6 ML) no photoresponse is seen. In the structure with the quantum dots, two maxima are observed at energies less than the fundamental absorption edge in silicon ($\sim$1.12 eV), at wavelengths of 1.7 and 2.9 μm. The intensity of both maxima dependences strongly on the value of the reverse bias, and these dependences are correlated with each other. When the bias is increased to 1.4 V the response in the mid-IR vanishes (at 2.9 μm, line T_1) and a signal appears in the near-IR (at 1.7 μm, line T_2). The value of the energy at the T_1 maximum (430 meV) corresponds to the energy depth of the ground state of the hole in the quantum dot.[36] Therefore process T_1 was identified as a transition of a hole from the ground state localized in the Ge quantum dot to an extended state of the valence band. When the reverse bias is increased, the hole levels in the quantum dots are filled with electrons. At voltages around 1.4 V a complete discharging of holes from the quantum dot occurs, and the transition T_1 becomes ''forbidden.'' Starting at that value it becomes possible for interband transitions of electrons from the valence band to the conduction band to occur (process T_2). Since the system under study is a type-II heterostructure—the holes are localized in the Ge regions, while for electrons the Ge region is a potential barrier,[37] such an optical transition is indirect in coordinate space and is accompanied by the ejection of an electron from Ge to Si. The transition energy should be determined by the difference between the band gap of Si (1.12 eV) and the energy of the hole state in the Ge quantum dot (0.43 eV), i.e., equal to 700 meV, in agreement with the experimental position of the line T_2 ($\approx$730 meV).

CONCLUSION

Our studies of the fabrication of arrays of Ge nanoislands in Si and measurement of their electrical and optical characteristics permit the conclusion that arrays of artificial ''atoms'' are formed, having a discrete energy spectrum which is manifested all the way to room temperature. The main factors that determine the spectrum of states are the size quantization and Coulomb interaction of the carriers. A new factor that arises in an array of quantum dots as opposed to a single quantum dot is the presence of Coulomb correlations between islands. We have determined the rates of emission and the trapping cross section of holes as functions of the energy level depths. The values of the cross sections exceed the known values in Si by several orders of magnitude. The electron transport along the layers of quantum dots is effected by hopping conductance, the value of which oscillates with changes in the degree of filling of the islands with holes, which may provide a basis for the creation of electronic data transmission circuits based on quantum dots. The possibility of creating a Ge quantum-dot photodetector tunable over the near- and mid-IR ranges is shown.

These studies were supported by the Russian Foundation for Basic Research (Grants 99-02-17019, 03-02-16506, 03-02-16468), by the Ministry of Industry and Science, Grant NSh-533-2003-2, Project Minpromnauk No. 37.029.11.0041, the Interbranch Science and Engineering Program for Physics of Solid State Nanostructuers (Grant 98-1100), and the Intercollegiate Science Program ''Universities of Russia — Basic Research'' (Grant 4103).

*E-mail: pch@isp.nsc.ru

[1] L. Jacak, P. Hawrylak, and A. Wojs, Quantum Dots. Berlin, Springer (1998), p. 196.
[2] N. N. Ledentsov, V. M. Ustinov, V. A. Shchukin, P. S. Kop'ev, Zh. I. Alferov, and D. Bimberg, Fiz. Tekh. Poluprovodn. **32**, 385 (1998) [Semiconductors **32**, 343 (1998)].
[3] A. I. Yakimov, V. A. Markov, and A. V. Dvurechenskii, and O. P. Pchelyakov, Philos. Mag. B **65**, 701 (1992).
[4] T. I. Kamins, G. Medeiros-Ribeiro, D. A. A. Ohlberg, and R. S. Williams, J. Appl. Phys. **85**, 1159 (1999).
[5] M. Kastner and B. Voigtlander, Phys. Rev. Lett. **82**, 2745 (1999).
[6] D. J. Eaglesham and M. Cerullo, Phys. Rev. Lett. **64**, 1943 (1990).
[7] O. P. Pchelyakov, Yu. B. Bolkhovityanov, L. V. Sokolov, A. I. Nikiforov, and B. Foĭkhtlender, Izvestiya Akad Nauk Ser. Fiz. **64**, 205 (2000).
[8] K. Brunner, Rep. Prog. Phys. **65**, 27 (2002).
[9] G. Capellini, M. De Seta, and F. Evangelistib, Appl. Phys. Lett. **78**, 3 (2001).
[10] O. P. Pchelyakov, Yu. B. Bolkhovityanov, A. I. Nikiforov, B. Z. Olshanetsky, L. V. Sokolov, S. A. Teys, and B. Voigtlaender, *Atomistic Aspects of Epitaxial Growth*, M. Kortla *et al.* (eds.), Kluwer Academic Publishers (2002), p. 371.
[11] O. P. Pchelyakov, Yu. B. Bolkhovityanov, A. V. Dvurechenskii, A. I. Nikiforov, A. I. Yakimov, and B. Voigtlaender, Thin Solid Films **367**, 75 (2000).
[12] J. Li, J. Jia, X. Liang, X. Liu, J. Wang, Q. Xue, Z. Li, J. Tse, Z. Zhang, and S. Zhang, Phys. Rev. Lett. **88**, 066101-1 (2002).
[13] J. J. Landerb and L. Morrison, J. Appl. Phys. **33**, 2098 (1962).
[14] A. A. Shklyaev, M. Shibata, and M. Ichikawa, Phys. Rev. B **62**, 1540 (2000).
[15] A. Barski, M. Derivaz, J. L. Rouviere, and D. Buttard, Appl. Phys. Lett. **77**, 3541 (2000).
[16] A. I. Nikiforov, V. A. Cherepanov, O. P. Pchelyakov, A. V. Dvurechenskii, and A. I. Yakimov, Thin Solid Films **380**, 158 (2000).
[17] A. I. Yakimov, V. A. Markov, A. V. Dvurechenskii, and O. P. Pchelyakov, J. Phys.: Condens. Matter **6**, 2573 (1994).
[18] U. Meirav and E. B. Foxman, Semicond. Sci. Technol. **10**, 255 (1995).
[19] R. C. Ashoori, H. L. Stormer, J. S. Weiner, L. N. Pfeiffer, S. J. Pearton, K. W. Baldwin, and K. W. West, Phys. Rev. Lett. **68**, 3088 (1992).
[20] A. I. Yakimov, A. V. Dvurechenskiĭ, A. I. Nikiforov, and O. P. Pchelyakov, JETP Lett. **68**, 135 (1998).
[21] G. Medeiros-Ribeiro, D. Leonard, and P. M. Petroff, Appl. Phys. Lett. **66**, 1767 (1995).
[22] A. I. Yakimov, A. V. Dvurechenskii, A. I. Nikiforov, and O. P. Pchelyakov, Thin Solid Films **336**, 332 (1998).
[23] A. I. Yakimov, C. J. Adkins, R. Boucher, A. V. Dvurechenskii, A. I. Nikiforov, O. P. Pchelyakov, and G. Biskupskii, Phys. Rev. B **59**, 12598 (1999).
[24] B. I. Shklovskiĭ and A. L. Efros, *Electronic Properties of Doped Semiconductors*, Springer-verlag, New York (1984), Nauka, Moscow (1979).
[25] V. L. Nguen (Nguen Van Lien), Fiz. Tekh. Poluprovodn. **18**, 335 (1984) [Sov. Phys. Semicond. **18**, 207 (1984)].
[26] A. I. Yakimov, A. V. Dvurechenskii, A. I. Nikiforov, and O. P. Pchelyakov, Phys. Low-Dimens. Semicond. Struct. **3/4**, 99 (1999).
[27] S. Anand, N. Carlsson, M.-E. Pistol, L. Samuelson, and W. Seifert, J. Appl. Phys. **84**, 3747 (1998).
[28] M. Sugawara, K. Mukai, and H. Shoji, Appl. Phys. Lett. **71**, 2791 (1997).
[29] J. L. Liu, W. G. Wu, A. Balandin, G. L. Jin, and K. L. Wang, Appl. Phys. Lett. **74**, 185 (1999).
[30] P. Boucaud, V. Le Thanh, S. Sauvage, D. Debarre, and D. Bouchier, Appl. Phys. Lett. **74**, 401 (1999).
[31] D. K. Shroder, in *Charge Coupled Devices*, D. F. Barbe (ed.), Vol. 38 of Topics in Applied Physics, Springer-Verlag, Berlin (1980), Mir, Moscow (1982), p. 70.
[32] S. Sauvage, P. Boucaud, J.-M. Gerard, and V. Thierry-Mieg, Phys. Rev. B **58**, 10562 (1998).
[33] G. Abstreiter, P. Schittenhelm, C. Engel, E. Silveira, A. Zrenner, D. Meertens, and W. Jager, Semicond. Sci. Technol. **11**, 1521 (1996).
[34] P. Schittenhelm, C. Engel, F. Findeis, G. Abstreiter, A. A. Darhuber, G. Bauer, A. O. Kosogov, and P. Werner, J. Vac. Sci. Technol. B **16**, 1575 (1998).
[35] A. I. Yakimov, A. V. Dvurechenskii, Yu. Yu. Proskuryakov, A. I. Nikiforov, O. P. Pchelyakov, S. A. Teys, and A. K. Gutakovskii, Appl. Phys. Lett. **75**, 1413 (1999).
[36] S. K. Zhang, H. J. Zhu, F. Lu, Z. M. Jiang, and Xun Wang, Phys. Rev. Lett. **80**, 3340 (1998).
[37] V. Ya. Aleshkin, N. A. Bekin, N. G. Kalugin, Z. F. Krasil'nik, A. V. Novikov, V. V. Postnikov, and H. Seyringer, JETP Lett. **67**, 48 (1998).

Translated by Steve Torstveit

On the nature of the anisotropy of the resistivity of $Nd_{2-x}Ce_xCuO_{4+\delta}$ with different cerium and oxygen concentrations

A. I. Ponomarev,* T. B. Charikova, A. N. Ignatenkov, and A. O. Tashlykov

Institute of Metal Physics of the Ural Division of the Russian Academy of Sciences, Sofia Kovalevskaya St., 18, Ekaterinburg 620219, Russia

A. A. Ivanov

Moscow Engineering-Physics Institute, Moscow 115410, Russia
(Submitted May 28, 2004)
Fiz. Nizk. Temp. **30**, 1180–1186 (November 2004)

The results of a study of the temperature dependences of the resistivity and its anisotropy coefficient in the normal phase of single-crystal $Nd_{2-x}Ce_xCuO_{4+\delta}$ films with different degrees of cerium doping x and oxygen content δ are presented. Two types of films of identical composition are considered, grown with the orientation of the c axis of the crystal perpendicular to and parallel to the plane of the substrate. The parameters found from an analysis of the conductivity and Hall coefficient are presented for the 18 samples studied. © *2004 American Institute of Physics.* [DOI: 10.1063/1.1820018]

1. INTRODUCTION

The anisotropy of the resistivity in the normal state of high-T_c superconducting (HTSC) cuprates has been a subject of research interest since the advent of high-T_c superconductivity and remains a topical problem to this day. While there is agreement that $\rho_{ab}(T)$ exhibits metallic behavior ($d\rho_{ab}/dT>0$),[1–4] the temperature dependence of $\rho_c(T)$ can be of a metallic,[5–7] nonmetallic ($d\rho_c/dT<0$),[2,8] or mixed character.[1,7] Elucidation of the physical causes of the different behavior of $\rho_{ab}(T)$ and $\rho_c(T)$ is an extremely important problem for the construction of a theory of high-temperature superconductivity. Several models for the conduction along the c axis have been proposed, but the agreement among them is not yet satisfactory.

For example, in the band model[9] at any level of doping, HTSC cuprates are anisotropic three-dimensional metals, the conductivity of which should be metallic both in the ab plane and along the c axis. The anomalous (nonmetallic) behavior of $\rho_c(T)$ observed in HTSC crystals attests to the unusual (non-band) nature of the transport between CuO_2 layers. The combination of metallic character of the conduction along the CuO_2 planes $\rho_{ab}(T)$ with the nonmetallic behavior of $\rho_c(T)$ in the c direction ($\rho_c \sim T^{-\alpha}$, where $0<\alpha<2$) was observed in Ref. 8 on crystals of the Y, La, Bi, and Pr systems.

Besides band theory, the Anderson theory,[10] in which the current carriers along the c axis are electrons formed as a result of recombination of holons and spinons in the CuO_2 planes and which tunnel between planes, has been invoked in Ref. 8. If a gap is opened in the spectrum of spin excitations, then the probability of spinon–holon recombination and also the scattering of current carriers on spin fluctuations will be suppressed, and that will lead to a decrease in the conductivity along the c axis and an increase in the conductivity in the ab plane. The presence of a spin gap (pseudogap) has been reliably established in the Y, La, Bi systems,[11] and the Nd system.[12]

In Ref. 13 the optical conductivity and the resistivity along the c axis were calculated in the $t-J$ model on the assumption that the interlayer hops are incoherent. The authors found that at low doping the semiconductor behavior of $\rho_c(T)$ is due to the opening of a pseudogap in the density of states, while in the optimal doping regime one has $\rho_c(T) \sim \rho_{ab}(T)$, i.e., the mechanism of carrier relaxation is common for transport along the layers and in the transverse direction.

In Ref. 14 a bipolar theory of the transport phenomena in copper oxides was proposed, wherein ρ_{ab} and ρ_c are described as functions of temperature and doping. At very low temperatures the authors predict a freezing out of the bipolarons and temperature independence of the anisotropy coefficient $k=\rho_c/\rho_{ab}$, and in a magnetic field—negative magnetoresistivity $\rho_c(B)$. These features have both been observed in LaSrCuO single crystals in magnetic fields up to 61 T.[15]

The authors of Ref. 16 proposed a model for the resistivity along the c axis in cuprates which includes interplanar disorder. It was shown that this disorder stabilizes the metallic state at low temperatures and in the dynamic limit leads to a temperature dependence of the derivative $d\rho_c/dT$ which is negative at low hole densities and positive at high. They also predicted correlations linking the nonlinear resistivity in the plane with the value of the negative $d\rho_c/dT$.

It was shown in Ref. 17 that the anisotropy of the resistivity in an anisotropic medium is the ratio of the phase coherence lengths. In layered crystals, where the interlayer transport is incoherent, the phase coherence length in the c direction is fixed and independent of temperature. This leads to temperature-dependent anisotropy of the resistivity and to the existence of metallic conduction in the plane and nonmetallic conduction in the c direction. This approach presupposes a description of the conduction along the c axis in the

highly nonclassical regime that is characteristic for layered cuprates.

The models mentioned above were developed before the publication of Ref. 18, in which it was established from studies of the angular oscillations of the magnetoresistance in a $Tl_2Ba_2CuO_{6+d}$ crystal that the electron gas is three-dimensional. The Fermi surface has eight parts that correspond to the absence of dispersion along the *c* axis. Such a topography of the Fermi surface can explain the large anisotropy of the properties of the normal and superconducting states in the framework of a standard three-dimensional picture. In other words, the characteristics of the normal state of HTSC cuprates is determined by the usual three-dimensional Fermi particles.

Models for the conduction along the *c* axis in HTSC cuprates have been proposed by Kopaev (at the XXXI Conference on Low Temperature Physics),[19] who treated the crystals as natural superlattices, and by the present authors[20,21] for explaining the conduction in $Nd_{2-x}Ce_xCuO_{4+\delta}$ single crystals, where the crystal was represented as a system of multiple quantum wells (CuO_2 layers $\sim$1.5 Å) separated by selectively doped barriers (NdO layers $\sim$4.5 Å).

The results of a study of the influence of the doping δ on the temperature dependence of $\rho_{ab}(T)$ and $\rho_c(T)$ in $Bi_2Sr_2CaCu_2O_{8+\delta}$ single crystals were reported in Ref. 22. A model for the conduction along the *c* axis was proposed in which the CuO_2 planes are separated by barriers of different height and width. This model successfully describes the temperature dependence $\rho_c(T)$ with the use of a small number of parameters and is able to explain the majority of the features observed in it, e.g., crossover from semiconductor behavior at low doping to almost metallic behavior at a high degree of doping on account of an effective decrease of the barrier height.

It is clear from the review given that the question of the mechanisms of conduction in HTSC cuprates is still topical. In the present paper we report the results of a study of the temperature dependence of the resistivities $\rho_{ab}(T)$ and $\rho_c(T)$ and also of the Hall effect in single-crystal films of $Nd_{2-x}Ce_xCuO_{4+\delta}$.

In the family of cuprate semiconductors, $Nd_{2-x}Ce_xCuO_{4+\delta}$ has many unique characteristics that make it a convenient object of study. It is a superconductor with *n*-type conductivity, it has only one CuO_2 plane per unit cell, it does not have chains (like YBaCuO) nor apical oxygen atoms between adjacent CuO_2 planes, and for that reason has pronounced two-dimensional (2D) properties.[21] Many of the physical properties exhibit ordinary metallic behavior, unlike the anomalous properties of cuprates with *p*-type conductivity (YBaCuO, BiSrCaCuO). For example, in stoichiometric $Nd_{2-x}Ce_xCuO_{4+\delta}$ the temperature dependence of ρ_{ab} is quadratic, $\rho_{ab}\sim T^2$, indicating that the system is an ordinary Fermi-liquid metal.[23] The properties of the $Nd_{2-x}Ce_xCuO_{4+\delta}$ system are extremely sensitive to the oxygen concentration in it. For samples to manifest a superconducting phase ($x=0.14-0.22$) they must be annealed in an oxygen-free medium to remove the nonstoichiometric oxygen δ, which is situated between CuO_2 planes. At optimal annealing ($\delta=0$) the $Nd_{2-x}Ce_xCuO_4$ crystal consists of a set of practically isolated CuO_2 conducting planes separated by a distance of 6 Å and is highly anisotropic, $\rho_c/\rho_{ab}\approx 10^3-10^4$ (Refs. 8, 24, and 25).

The combination of such unique properties in this relatively simple compound affords the possibility of carrying out detailed studies on it and making comparisons with the more complex cuprates, such as YBaCuO and BiSrCaCuO.

The goal of the present study was to investigate the anisotropy of the resistivity in the normal phase and also the temperature dependence of the resistivity of single-crystal $Nd_{2-x}Ce_xCuO_{4+\delta}$ films with different degrees of cerium doping *x* and different oxygen concentrations δ. In contrast to our study of the anisotropy coefficient of the resistivity in nonsuperconducting bulk NdCeCuO crystals,[7] in the present study we investigate two types of single-crystal films of the same composition *x* but with different orientations of the c axis of the crystal with respect to the plane of the substrate:

1. with the *c* axis perpendicular to the plane of the substrate.

2. with the *c* axis parallel to the plane of the substrate and directed along the sample.

2. SAMPLES

Single-crystal films of $Nd_{2-x}Ce_xCuO_{4+\delta}$ were synthesized at the Moscow Engineering Physics Institute by the pulsed laser evaporation on $SrTiO_3$ substrates. Six series of samples $\sim$1200–2000 Å thick were synthesized: three series ($x=0.12$, 0.15, 0.17) with the *c* axis of the crystal oriented perpendicular to the plane of the substrate (001), and three series of the same compositions with the *c* axis oriented parallel to the plane of the substrate $(1\bar{1}0)$. In each series there were three samples with different oxygen content δ. Altogether there were 18 samples studied.

To obtain samples with different δ, films of the same composition were prepared under three different conditions.

"As-grown"—the original ceramic target was evaporated by a focused laser beam and the evaporated target material was deposited on a heated single-crystal substrate (the substrate material was $SrTiO_3$ with the (100) or (110) orientation, with dimensions of $5\times10\times1.5$ mm; the substrate temperature was 800 °C; the pressure during deposition was 0.8 torr, the residual gas was air; the target was a sintered ceramic tablet of $Nd_{2-x}Ce_xCuO_{4+\delta}$ of the given composition).

Annealing in oxygen—the as-grown film was additionally annealed at $T=500$ °C for 60 min at a pressure $p=760$ torr.

Annealing in vacuum (optimal annealing)—the as-grown film was annealed for 60 min at $T=780$ °C and $p=10^{-2}$ torr.

According to x-ray structural data the type-I films, grown on $SrTiO_3$ substrates with the (100) orientation, are epitaxial, with the orientation of the (001) plane of the surface and a degree of misorientation of the domains of less than 1°, which attests to a high degree of structural perfection.

The type-II films, grown on $SrTiO_3$ substrates with the (110) orientation, had the orientation of the surface plane $(1\bar{1}0)$. In some films the plane of the substrate and the plane

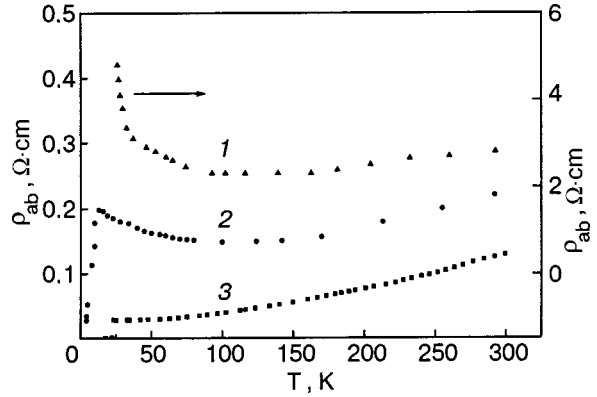

FIG. 1. Temperature dependence of the resistivity ρ_{ab} of $Nd_{2-x}Ce_xCuO_{4+\delta}$ samples ($x=0.15$) annealed under different conditions: in oxygen (*1*) (right-hand scale), as-grown (*2*), and in vacuum (*3*).

of the CuO_2 layer were misoriented by an angle of up to 0.2–0.6°.

A sample shape in the form of a ''double cross'' with a central strip 1 mm wide and a distance between potential contacts of 3 mm was obtained by photolithography. After etching, silver contact pads were deposited on the samples by laser evaporation in vacuum. Thus both $\rho_c(T)$ and $\rho_{ab}(T)$ have been measured by the four-probe method for the first time in the present study.

3. EXPERIMENTAL RESULTS. DISCUSSION

Films with the *c* axis perpendicular to the plane of the substrate

Figure 1 shows the $\rho_{ab}(T)$ curves obtained for samples of $Nd_{1.85}Ce_{0.15}CuO_{4+\delta}$ with different oxygen concentrations (annealed under different conditions). It is seen that with decreasing oxygen concentration from sample No. 1, annealed in oxygen, to sample No. 3, annealed in vacuum, the resistivity ρ_{ab} at temperatures $T<100$ K decreases by approximately 100 times. At $T=300$ K this ratio equals 25. Prior to the superconducting transition, the optimally annealed sample (No. 3) has a resistivity $\rho_{ab}=30\ \mu\Omega\cdot$cm, $T_c=23$ K, $\Delta T<1$ K, a ratio $\rho_{300\,\mathrm{K}}/\rho_{T_c}\cong 5$, which attests to the high degree of structural perfection. This is one of the best characteristics yet reported in the literature.

The $\rho_{ab}(T)$ curve for this sample at $T\geqslant 50$ K is of a metallic character, $d\rho/dT>0$. The condition that must be satisfied for good metallic conduction in a disordered 2D system is $k_F l\gg 1$ (k_F is the wave vector at the Fermi level, l is the mean free path between scatterers). The parameter $k_F l$ is a measure of the disorder of the system and can be found from the experimental value of ρ_{ab}: $k_F l=(hc_0)/\rho_{ab}e^2$ (Ref. 26), where c_0 is the distance between layers ($c_0=6$ Å for $Nd_{2-x}Ce_xCuO_4$), and e is the charge of an electron. For sample No. 3 the parameter $k_F l=56$ ($T=50$ K), which corresponds to a good metal.

The as-grown sample (No. 2), with $k_F l\approx 10$ in the interval $140\leqslant T\leqslant 300$ K, has a metallic trend of the conductivity with temperature. For $T<100$ K its resistivity depends logarithmically on temperature, $\rho_{ab}(T)\sim\ln T$, which can be explained by a weak localization of current carriers as the temperature is lowered,[27] i.e., in this temperature interval the sample is a 2D metal, the resistance of which is determined by quantum interference corrections to the Drude conductivity. The behavior of this sample clearly demonstrates the coexistence of weak localization of current carriers and superconductivity, since the sample undergoes a complete superconducting transition at $T_c=3$ K.

The resistivity of sample No. 1 at low temperatures ($3\ \mathrm{K}\leqslant T\leqslant 45$ K) depends on temperature in an activational manner, $\rho_{ab}(T)\sim\exp(T/T_0)^{1/2}$, which may be due to a hopping mechanism of conduction. For this sample the parameter $k_F l=0.7$, i.e., the sample is found on the insulator side of the metal–insulator transition.

For the compositions $x=0.12$ and $x=0.17$ we observed similar behavior of the resistivity with temperature for the samples annealed in the three different regimes, although the sample with $x=0.12$ does not have a superconducting transition.

The temperature dependence of the resistivity ρ_{ab} of the optimally annealed samples with $x=0.12$, 0.15, and 0.17 in the interval 50–300 K is described well by the polynomial $\rho_{ab}(T)=\rho_0+AT+BT^2$, where $A=(0.7\text{–}2.1)\times 10^{-4}$ mΩ·cm/K and $B=(1\text{–}2.2)\times 10^{-6}$ mΩ·cm/K^2. The observed quadratic temperature dependence of the resistivity can be attributed to the electron–electron (e–e) interaction, which increases strongly because of the 2D nature of superconducting cuprates. The results correspond to the Fermi-liquid description of the normal state of electron-doped copper oxides,[23] where the term linear in T corresponds to the contribution of electron–phonon scattering.[28]

The Hall coefficient of all the samples with $x=0.12$, $x=0.15$, and $x=0.17$ was measured at $T=77$ K and the main parameters of the samples were determined; they are listed in Table I (the values of the resistivity are given at the temperatures corresponding to the minimum of the resistivity $\rho_{\min}$ for each sample). The experimental values of $\rho_{\min}$ and the Hall coefficient R_H are used to find the conductivity per CuO_2 layer $\sigma_s=(\rho_{ab}/c_0)^{-1}$ and the volume density $n=(eR_H)^{-1}$ and surface density ($n_s=nc_0$) of current carriers ($c_0=6$ Å). Using the expression $k_F l=(hc_0)/\rho_{ab}e^2$, where $k_F=(2\pi n_s)^{1/2}$ (Ref. 26), we found the mean free path of the electrons in the samples with different oxygen concentrations.

It was found that the sign of the Hall coefficient is negative in all the samples. It can be seen from Table I that the Hall coefficients of samples Nos. 2 and 3 ($x=0.12$) differ by a factor of two and the resistivities by a factor of 5. This means that the change in the oxygen concentration in these samples due to the different annealing regimes leads mainly to a change in the impurity scattering while having little effect on the current carrier density. At the same time, for sample No. 1, which was annealed in oxygen, the Hall coefficient differs sharply from those for the other samples of this series, exceeding them by more than a factor of 10. This may be due to the fact that the random impurity potential created by the excess oxygen in sample No. 1 is so large that it localizes the current carriers.

In the optimally annealed sample (No. 3) with $x=0.17$ the Hall coefficient, while remaining negative, is an order of magnitude smaller in absolute value than that for the opti-

TABLE I. Main parameters of the samples studied.

Composition, x	Sample No.	$\rho_{ab}\cdot 10^3$, $\Omega\cdot$cm	$\sigma_s\cdot 10^4$, Ω^{-1}	$k_F l$	$R_H\cdot 10^4$, cm^3/K	$n\cdot 10^{-21}$, cm^{-3}	$n_s\cdot 10^{-14}$, cm^{-2}	$k_F\cdot 10^{-7}$, cm^{-1}	l_{ab}, Å	μ, cm^2/(V·5)
	1	1.4	0.4	1.1	−18	3.5	2.1	3.6	3.1	1.5
0.12	2	0.2	3.0	7.8	−17	3.7	2.2	3.7	21	8.5
	3	0.12	6.0	15.6	−18	3.4	2.1	3.6	43	18.2
	1	2.3	0.26	0.7	−63	1	0.6	1.9	3.5	2.7
0.15	2	0.15	4.0	10.4	−5.7	11	6.6	6.4	16.2	3.6
	3	0.03	21.4	56	−2.9	22	13.2	9.15	61.5	10.2
	1	48.0	0.01	0.03	–	–	–	–	–	–
0.17	2	0.05	1.2	32	−1.55	–	–	–	–	–
	3	0.01	5.3	138	−0.37	–	–	–	–	–

Note: The values of ρ_{ab} are given for the temperatures corresponding to $\rho_{\min}$ for each sample.

mally annealed sample (No. 3) of the series with $x=0.15$ and almost two orders of magnitude larger than for sample No. 3 with $x=0.12$. Apparently when the cerium concentration is increased to $x=0.17$ the holes begin to play an important role in the conduction, compensating the electron contribution to a considerable degree. It is clear that in that case it makes no sense to determine the density of current carriers on the basis of a model with one type of carrier.

A similar result indicating an increasing role of holes with increasing doping of $Nd_{2-x}Ce_xCuO_{4+\delta}$ was obtained in Refs. 24 and 29. For example, in Ref. 29, where the dependence of the Hall coefficient on the Ce concentration was investigated in thin films of $Nd_{2-x}Ce_xCuO_{4+\delta}$, it was found that the Hall coefficient at $x=0.15$ is negative, but with increasing Ce concentration it changes sign, and at $x=0.195$ it is positive at all temperatures below 300 K. In Ref. 24 the results of a study of the resistivity and Hall effect for four $Nd_{2-x}Ce_xCuO_{4+\delta}$ single crystals with $x=0.15$ were reported, and it was shown that $R_H>0$ at $T<80$ K for all four crystals. Using a two-band model, the authors of Ref. 24 explained the main features of the behavior of the resistivity and Hall coefficient and conjectured that holes may be responsible for the superconducting transition in NdCeCuO.

Films with *c* axis parallel to the plane of the substrate

The resistivity of films grown along the c axis (ρ_c) also falls off with increasing oxygen concentration, but not by an order of magnitude, as in the case of ρ_{ab}, but by only a few times, and even for the optimally annealed samples with $x=0.12$ and $x=0.15$, ρ_c does not have a metallic temperature trend, i.e., $d\rho_c/dT<0$ (Fig. 2). This result disagrees with band theory,[9] which predicts a metallic trend of $\rho_c(T)$ at any level of doping. In the overdoped samples with $x=0.17$ the behavior of $\rho_c(T)$ is the same as that of $\rho_{ab}(T)$, i.e., $d\rho_c/dT>0$, which can be attributed to the turning on of charge transport between CuO_2 planes and a transition from 2D to 3D type of conduction with increasing dopant concentration. Thus the overdoped $Nd_{2-x}Ce_xCuO_{4+\delta}$ system becomes an anisotropic 3D metal. This result agrees with our previous results obtained on bulk single crystals[7] and also with the results of Ref. 30 on the LaSrCuO system.

For the optimally annealed and as-grown samples with $x=0.15$ in the temperature interval 100–300 K and for the sample annealed in oxygen, the resistivity in the region 200–300 K obeys a $\rho_c(T)\sim 1/T$ law, in agreement with the theory of Ref. 10. At lower temperatures the resistivity of these samples varies by a power law: $\rho_c\sim T^{-0.2}$. Similar behavior of $\rho_c(T)$ is observed for the samples with $x=0.12$ and 0.17.

It was found in all the series of samples that annealing in oxygen leads to growth of the resistivity, apparently because of the appearance of nonstoichiometric ($\delta>0$) oxygen atoms in the lattice and a decrease of the anisotropy coefficient (Fig. 3). At temperatures $T<50$ K the increase in the concentration of oxygen defects in the samples leads to a sharper growth of the resistivity ρ_c with temperature (Fig. 2).

The $\rho_c(T)$ curves for the samples annealed in oxygen manifest the superconducting transition better than the $\rho_{ab}(T)$ curves do (Figs. 1 and 2), but the transition is incomplete ($\rho\neq 0$). This sort of feature was observed in our previous study.[7] It can be understood on the assumption that small superconducting fragments appear in the CuO_2 planes as the temperature is lowered; these have little effect on the conductivity along the planes, but when current is passed along the c axis they can create superconducting "shorts" that will partially shunt the large resistivity ρ_c.

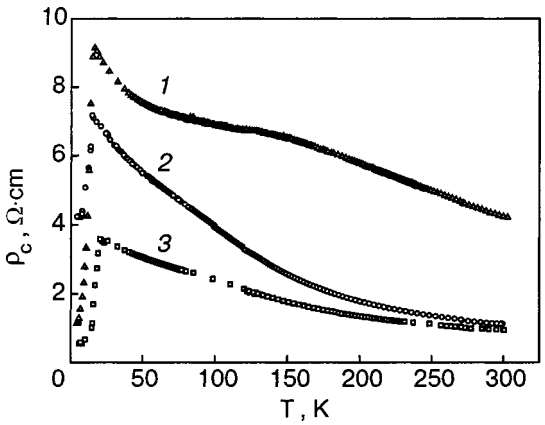

FIG. 2. Temperature dependence of the resistivity ρ_c of $Nd_{2-x}Ce_xCuO_{4+\delta}$ samples ($x=0.15$) annealed under different conditions: in oxygen (*1*), as-grown (*2*), in vacuum (*3*).

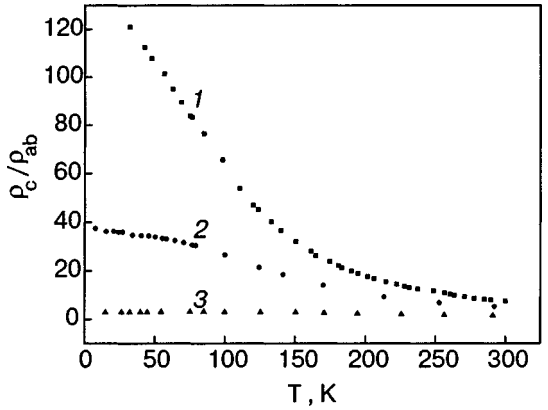

FIG. 3. Temperature dependence of the anisotropy coefficient of the stability for $Nd_{2-x}Ce_xCuO_{4+\delta}$ samples ($x=0.15$) annealed under different conditions: in oxygen (*1*), as-grown (*2*), in vacuum (*3*).

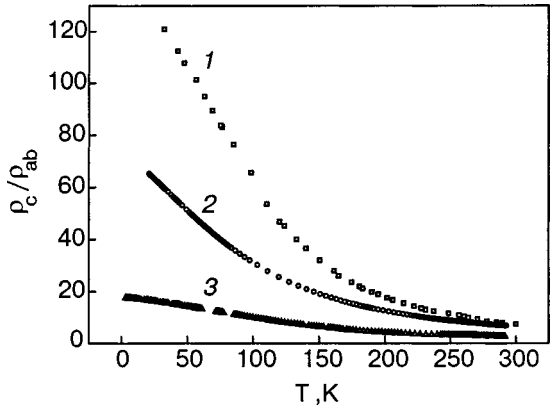

FIG. 4. Temperature dependence of the anisotropy coefficient of the resistivity for optimally annealed $Nd_{2-x}Ce_xCuO_{4+\delta}$ samples with different compositions x: 0.12 (*1*), 0.15 (*2*), 0.17 (*3*).

In the optimally annealed samples ($\delta=0$) the anisotropy coefficient increases with decreasing temperature, and for the sample with $x=0.15$ it reaches $\rho_c/\rho_{ab}=120$ at $T=22$ K (Fig. 3), while in the sample with excess oxygen ($\delta>0$) $\rho_c/\rho_{ab}<10$ and is almost independent of temperature. This value is much less than for the bulk crystals, where the anisotropy coefficient for the optimally annealed samples reaches values of 10^3-10^{-4} (Refs. 8, 24, and 25). This difference may be due to a slight misorientation (less than 0.6°) between the (110) planes of the $SrTiO_3$ and the CuO_2 planes in the type-II films, since in that case there is a component of the conductivity along the ab plane that is many times greater than along the c axis. Nevertheless, the general trend of the resistivity $\rho_c(T)$ with temperature in the samples with $x\leqslant 0.15$ remains semiconducting, i.e., the contribution of ρ_c to the overall resistivity is dominant even in this case. It can be assumed that the negative temperature coefficient of resistance $d\rho_c/dT<0$ is an inherent property of underdoped and optimally doped HTSC cuprates.

Thus we have revealed the following behavior of $\rho_{ab}(T)$ and $\rho_c(T)$.

For all of the as-grown and optimally doped samples of $Nd_{2-x}Ce_xCuO_{4+\delta}$ (for all of the different compositions) a characteristic metallic behavior of $\rho_{ab}(T)$ is observed at $T>100$ K. The $\rho_{ab}(T)$ curves of the samples annealed in oxygen have an insulating trend $d\rho_{ab}/dT<0$ in the entire temperature range for the samples with $x=0.12$ and $x=0.17$ and at $T<120$ K for the sample with $x=0.15$.

The $\rho_c(T)$ curves obtained by us on films with the c axis lying in the plane of the substrate have a negative temperature coefficient of resistance $d\rho_c/dT<0$ for the optimally annealed samples with $x\leqslant 0.15$, while in the overdoped samples with $x=0.17$ the $\rho_c(T)$ curves have a metallic character. A similar result was obtained in Ref. 30, where $La_{2-x}Sr_xCuO_4$ crystals were investigated.

The resistivity ρ_{ab} is much more sensitive to the annealing than ρ_c. This difference is especially noticeable at low temperatures: ρ_c varies severalfold, while ρ_{ab} varies by tens and even hundreds of times.

The anisotropy coefficient reaches the highest values in the optimally annealed films. For example, for the sample with $x=0.15$ at low temperatures $\rho_c/\rho_{cb}=120$. In the optimally doped samples of all compositions the anisotropy coefficient ρ_c/ρ_{ab} is maximum at low temperatures and tends toward unity as the temperature is increased to 300 K (Fig. 4).

The authors thank G. M. Minkov, G. I. Harus, and N. G. Shelushinina for helpful discussions.

This study was supported by the Russian Foundation for Basic Research (RFBR)–Ural Grant 04-02-96084, Government Contract No. 40.012.1.1.1146 (Agreement 12/04), and RFBR Grant 02-02-16942.

*E-mail: ponomarev@imp.uran.ru

[1] S. J. Hagen, T. W. Jiang, Z. Z. Wang, J. Horvath, and N. P. Ong, Phys. Rev. B **37**, 7928 (1988).
[2] S. Martin, A. T. Fiory, and R. M. Fleming, Phys. Rev. B **41**, 846 (1990).
[3] A. I. Ponomarev, A. N. Ignatenkov, T. B. Charikova, A. O. Tashlykov, L. D. Sabirzyanova, N. G. Shelushinina, and A. A. Ivanov, Fiz. Met. Metalloved. **95**, 46 (2003).
[4] S. J. Hagen, X. Q. Xu, W. Jiang, J. L. Peng, Z. Y. Li, and R. L. Green, Phys. Rev. B **45**, 515 (1992).
[5] Y. Iye, T. Tamegai, T. Sakakibara, T. Goto, N. Miura, H. Takeya, and H. Takei, Physica C **153–155**, 26 (1988).
[6] O. Beom-hoan and J. T. Market, Phys. Rev. B **47**, 8373 (1993).
[7] T. B. Charikova, A. I. Ponomarev, A. N. Ignatenkov, G. I. Kharus, N. G. Shelushinina, G. A. Emel'chenko, and A. A. Zhokhov, Fiz. Met. Metalloved. **91**, 46 (2001).
[8] T. Ito, Y. Nakamura, H. Takagi, and S. Uchida, Physica C **185–189**, 1267 (1991); T. Ito, Y. Nakamura, and S. Ishibashi, Nature (London) **350**, 596 (1991).
[9] W. E. Picket, Rev. Mod. Phys. **38**, 43 (1989).
[10] P. W. Anderson and Z. Zou, Phys. Rev. Lett. **60**, 132 (1988); P. W. Anderson, *ibid.* **67**, 3844 (1991).
[11] J. L. Tallon and J. W. Loram, cond-mat/0005063.
[12] E. J. Singley, D. N. Basov, K. Kurahashi, T. Uefuji, and K. Yamada, Phys. Rev. B **64**, 224503–1 (2001).
[13] P. Prelovsek, A. Ramsak, and I. Sega, Phys. Rev. Lett. **81**, 3745 (1998).
[14] A. S. Alexandrov, V. V. Kabanov, and N. F. Mott, Phys. Rev. Lett. **77**, 4796 (1996).
[15] Y. Ando, G. S. Boebinger, A. Passner, T. Kimura, and K. Kishio, Phys. Rev. Lett. **75**, 4662 (1995).
[16] A. G. Rojo and K. Levin, Phys. Rev. B **48**, 16861 (1993).
[17] G. A. Levin and C. C. Almasan, cond-mat/9907306, v. 1.
[18] N. T. Hussey, M. Abdel-Jawad, and A. Carrington, Nature (London) **425**, 814 (2003).
[19] V. V. Kapaev and Yu. V. Kopaev, *XXI Symposium on Low Temperature Physics*, Moscow (1998).
[20] A. I. Ponomarev, A. N. Ignatenkov, L. D. Sabirzyanova, G. I. Harus, and N. G. Shelushinina, in *Proceedings of the International Conference on the*

Physics of Semiconducotors (CD-ROM, Sec. 5 A, N36), Jerusalem (1998).
[21] G. I. Harus, A. N. Ignatenkov, A. I. Ponomarev, L. D. Sabirzyanova, and N. G. Shelushinina, JETP Lett. **70**, 97 (1999).
[22] M. Giura, R. Fastampa, S. Sarti, and E. Silva, Phys. Rev. B **68**, 134505 (2003).
[23] M. V. Sadovskiĭ, Sverkhprovodimost' (KIAE) **8**, 337 (1995).
[24] Z. Z. Wang, T. R. Chien, N. P. Ong, N. P. Ong, J. M. Taraskon, and E. Wang, Phys. Rev. B **43**, 3020 (1991).
[25] A. I. Ponomarev, V. I. Tsidilkovski, K. R. Krylov, and T. B. Charikova, J. Supercond. **9**, 27 (1996).
[26] P. A. Lee and T. V. Ramakrishnan, Rev. Mod. Phys. **57**, 287 (1985).
[27] G. I. Harus, A. I. Ponomarev, T. B. Charikova, A. N. Ignatenkov, L. D. Sabirzyanova, N. G. Shelushinina, V. F. Elesin, A. A. Ivanov, and I. A. Rudnev, Physica C **383**, 207 (2002).
[28] X. Q. Xu, S. N. Mao, Wu Jiang, J. L. Peng, and R. L. Greene, Phys. Rev. B **53**, 871 (1996).
[29] S. Kubo and M. Suzuki, Physica C **185–189**, 1251 (1991).
[30] Y. Nakamura and S. Uchida, Phys. Rev. B **47**, 8369 (1993).

Translated by Steve Torstveit

IMPURITY STATES IN TRANSIENT METAL SEMICONDUCTORS

Mechanisms of radiative and nonradiative recombination in ZnSe:Cr and ZnSe:Fe

M. Godlewski*

Institute of Physics of Polish Academy of Sciences, 32/46 Al. Lotnikow St., Warsaw 02-668, Poland; Department of Mathematics and Natural Sciences College of Science, Cardinal S. Wyszyński University, Warsaw, Poland

M. Surma and V. Yu. Ivanov

Institute of Physics of Polish Academy of Sciences, 32/46 Al. Lotnikow St., Warsaw 02-668, Poland

T. P. Surkova

Institute of Metal Physics of Russian Academy of Sciences, Ural Division, Ekaterinburg, Russia
(Submitted May 25, 2004)
Fiz. Nizk. Temp. **30**, 1187–1193 (November 2004)

Possible applications of ZnSe:Cr in optoelectronics are discussed. It is shown that $2+$ to $1+$ photo-ionization of chromium results in efficient pumping of Cr^{2+} intrashell emission and in energy up-conversion from green to blue. A distinct difference in efficiency of the energy up-conversion is observed between chromium- and iron-doped ZnSe samples. This difference we relate to a very efficient Auger mechanism of photoluminescence quenching in Fe-doped samples. We further demonstrate an anticorrelation of the intensities of mid-infrared Cr emission and up-converted blue emission of ZnSe. © *2004 American Institute of Physics.*
[DOI: 10.1063/1.1820019]

1. INTRODUCTION

Despite concentrated efforts there are difficulties in achieving efficient short-wavelength emission from semiconductor-based light emitting devices. As a consequence, several alternative approaches have been tested, in which green, blue, or violet color emission is obtained due to energy up-conversion, i.e., under optical pumping with photons of a lower energy (longer wavelength).

ZnSe is an attractive candidate for the short wavelength energy up-conversion material, since the ''edge'' (i.e., close to the band gap energy) photoluminescence (PL) of ZnSe is observed in the blue-violet spectral region. Unfortunately, as we have found,[1] two-photon excitation is an inefficient process in the case of undoped ZnSe. The quantum efficiency of the process is very low, about 10^{-6}, i.e., far too low for any practical application. A very different situation was observed in the case of chromium-doped samples.[1,2] Relatively efficient blue up-converted emission was observed under green color optical pumping.

In the following Section we will discuss the mechanism of energy up-conversion in Cr doped ZnSe, and then we will discuss the possibility of tuning of the pumping energy by doping ZnSe with iron or by using alloys of wide-band-gap II–VI semiconductors. Finally, we will discuss the properties of infrared emission in ZnSe:Cr.

2. ZnSe:Cr—MECHANISM OF ENERGY UP-CONVERSION

In Figs. 1 and 2 we show photo-ionization (Fig. 1) and photo-neutralization (quenching, Fig. 2) spectra measured for Cr^{1+} and Fe^{3+} electron spin resonance (ESR) signals in ZnSe. Two complementary Cr ionization transitions were identified in this ESR study as:

- Cr^{2+} + photon to Cr^{1+} + hole in the valence band (band II in Fig. 1),
- Cr^{1+} + photon to Cr^{2+} + electron in the conduction band (direct photo-ionization in Fig. 2),

with Cr^{2+} being the ground charge state of chromium in ZnSe.

The Cr^{1+} signal could also be excited by illumination ionizing acceptor centers of ZnSe (band III in Fig. 1) and, for ZnSe:Fe, Cr, by the $2+$ to $3+$ photo-ionization transition of Fe ions (band I in Fig. 1b, c), i.e., by two transitions generating free electrons in the conduction band of ZnSe. These electrons can be retrapped by chromium resulting in $2+$ to $1+$ charge exchange.

That identity of the ESR excitation and quenching bands was proved in our previous ESR experiments.[3–7] We found that the $2+/1+$ energy level of Cr lies at about 2 eV above the valence band edge of ZnSe.[4] The complementary $1+ \rightarrow 2+$ photo-neutralization transition was also identified, as shown in Fig. 2.

Our previous ESR studies of Cr-doped ZnSe (Ref. 4) and ZnS (Ref. 5) and iron-doped ZnSe (Ref. 6) and ZnS (Ref. 7) indicated high efficiency of these ionization transitions in wide-band-gap II–VI semiconductors. Moreover, we observed that two-step ionization transitions of Cr and Fe ions result in a population of both shallow donors and shallow and deep acceptors.[8]

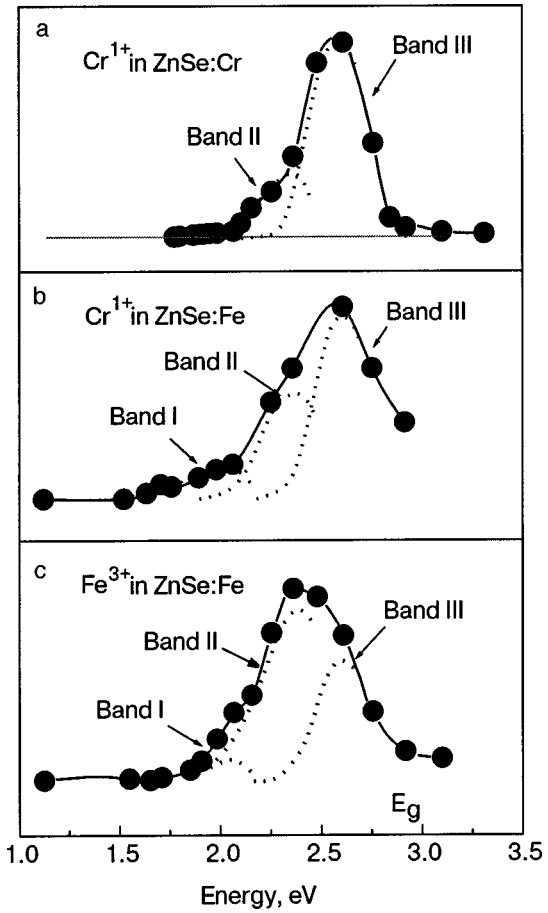

FIG. 1. Low temperature photo-excitation spectra of Cr^{1+} in ZnSe:Cr (a), ZnSe:Fe (b) and Fe^{3+} in ZnSe:Fe (c).

In the $2+ \rightarrow 1+$ chromium photo-ionization transition free holes are photo-generated in the valence band (VB). In the subsequent $1+ \rightarrow 2+$ photo-neutralization transition free electrons are created in the conduction band (CB). These free carriers, if not retrapped by chromium (iron), can then participate in the PL recombination transitions, resulting, e.g., in the appearance of the energy up-converted emission. Not surprisingly, we found that the photoconductivity and photo-ionization (due to $2+$ to $1+$ Cr transition) spectra of ZnSe:Cr both correlate with the excitation spectrum of up-converted emission.[1] Thus, energy up-conversion is explained by efficient photo-generation of free electrons and free holes in two complementary photo-ionization transitions via a deep chromium-related center.

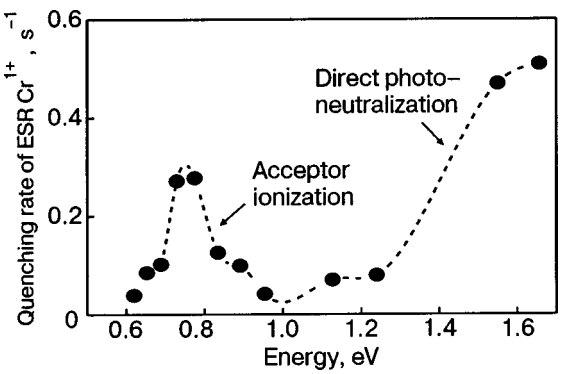

FIG. 2. Low-temperature photo-quenching spectrum of the Cr^{1+} ESR signal in ZnSe:Cr, measured as the spectral dependence of the decay time of the ESR signal under illumination with photons of a given energy. The Cr^{1+} ESR signal was first photo-excited with green color illumination.

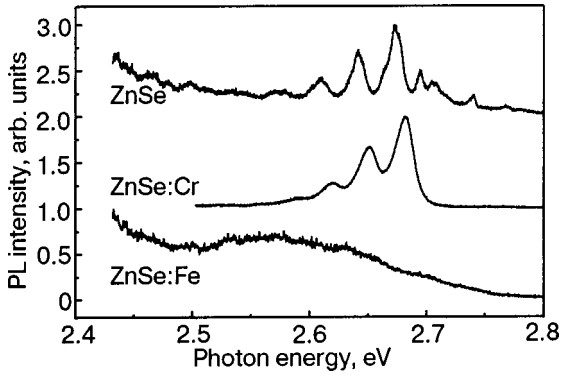

FIG. 3. "Edge" part of the PL in ZnSe, ZnSe:Cr and ZnSe:Fe measured at liquid helium temperature under the green color excitation (for ZnSe:Cr and ZnSe:Fe) or above-band-gap excitation (ZnSe undoped) (after V. Yu. Ivanov *et al.*, Acta Phys. Pol. A **103**, 695 (2003)).

3. ZnSe:Fe — OPTIMIZATION OF OPTICAL PUMPING ENERGY

The blue up-converted emission of ZnSe:Cr is excited by the $2+ \rightarrow 1+$ photo-ionization transition of chromium, which occurs for photon energies larger than about 2 eV, with maximum at about 2.4 eV.[1] Considering possible practical devices, the use of efficient red color GaAs-based laser diodes for optical pumping is preferential. Only in this case can compact devices be constructed, as required for memory storage applications, for example.

Regarding energy up-conversion efficiency, light powers of several mW are required for energy storage applications. Considering that 1 W optical pumping is available, the light conversion efficiency should be not less than few times 10^{-3}.

For ZnSe:Cr the up-conversion efficiency was about 5×10^{-3} at liquid helium temperature, but only for green color optical pumping. For red pumping the up-conversion efficiency was about 10 times lower, i.e., too low for practical applications.

A photo-ESR investigation (Fig. 1) indicated that red color pumping is optimized for $2+$ to $3+$ photo-ionization of iron in ZnSe. We thus turned our attention to this system. In Fig. 3 we show the energy up-converted PL spectra in chromium- and iron-doped ZnSe, as compared to the "edge" PL of undoped ZnSe. The origin of the observed PL emissions in ZnSe and ZnSe:Cr is discussed elsewhere.[1] Weak and broad blue color energy up-converted emission is observed in ZnSe:Fe. Its efficiency is far too low to be of any practical interest. The quantum efficiency of energy up-conversion in ZnSe:Fe we estimated to be two orders of magnitude smaller than that for chromium-doped ZnSe.

Our present investigations indicate that two mechanisms are responsible for the low efficiency of the energy up-conversion process in ZnSe:Fe. First, the photo-ESR investigations indicate that the photo-excited Fe^{3+} charge state of iron decays fast even at low temperatures. The mid-gap level of Fe is not metastably occupied, as is often observed in the case of chromium-doped ZnSe. This relates to the high effi-

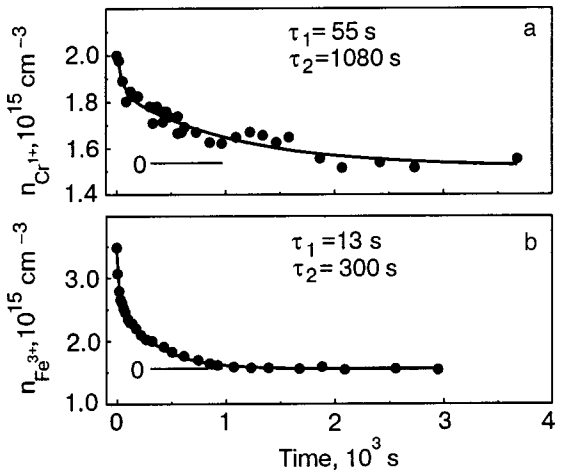

FIG. 4. Decay of Cr^{1+} (a) and Fe^{3+} (b) ESR signals observed at 40 K after the photo-excitation is turned off. Two-exponential decay is observed, with the characteristic times given in the figure.

ciency of carrier trapping processes in iron-doped ZnS and ZnSe.[9–11] The photo-generated Fe^{3+} state has too large a cross section for retrapping of free electrons from the conduction band to be metastably occupied after the photogeneration. The latter we concluded from detailed studies of the kinetics of quenching of photo-excited ESR signals. Examples of relevant ESR results are shown in Figs. 4 and 5 for ZnSe:Fe, Cr. Both the Cr^{1+} and Fe^{3+} ESR signals decayed rapidly to some metastable population after the excitation was turned off. The decay was faster for the Fe ions. In both cases the decay was characterized by the same activation energy, equal to the ionization energy of shallow donors in ZnSe. The latter was surprising in case of Cr^{1+} centers, for which the signal was observed to rise in ZnSe:Cr but to decay in ZnSe:Fe, Cr once electrons were thermally ionized. The reason for this difference we will discuss later on.

We solved simple kinetic equations to explain the evolution of ESR signals under photo-excitation and after the light is turned off:

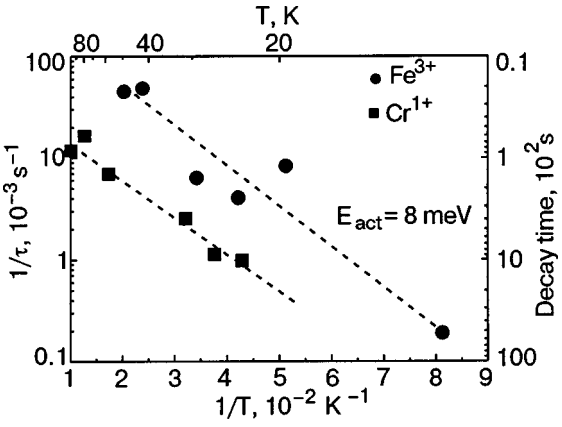

FIG. 5. Temperature dependence of decay of the Cr^{1+} and Fe^{3+} ESR signals observed after the photo-excitation is turned off. Two decay components (see Fig. 4) are characterized by the same temperature dependence with an activation energy of 8 meV.

$$\frac{dn_{\mathrm{Cr}}}{dt} = I\sigma_{OV}(N_{\mathrm{Cr}} - n_{\mathrm{Cr}}) - I\sigma_{OC}n_{\mathrm{Cr}} + n(N_{\mathrm{Cr}} - n_{\mathrm{Cr}})c^e_{\mathrm{Cr}} - pn_{\mathrm{Cr}}c^h_{\mathrm{Cr}},$$

$$\frac{dn}{dt} = I\sigma_{OC}n_{\mathrm{Cr}} - n(N_D - n_D)c^e_D - n(N_{\mathrm{Cr}} - n_{\mathrm{Cr}})c^e_{\mathrm{Cr}},$$

$$\frac{dp}{dt} = I\sigma_{OV}(N_{\mathrm{Cr}} - n_{\mathrm{Cr}}) - p(N_A - n_A)c^h_A - pn_{\mathrm{Cr}}c^h_{\mathrm{Cr}},$$

$$\frac{dn_A}{dt} = p(N_A - n_A)c^e_D - \beta_{\mathrm{AD}}n_An_D - \beta_{\mathrm{ACr}}n_An_{\mathrm{Cr}},$$

$$\frac{dn_D}{dt} = n(N_D - n_D)c^e_D - \beta_{\mathrm{AD}}n_An_D,$$

where: n_{Cr} and N_{Cr} are the concentration of the chromium in the $1+$ charge state and the total concentration of Cr in the sample, respectively; N_A and N_D are the total concentrations of acceptors (A) and donors (D) in the sample, n_A and n_D are the concentrations of populated (neutral) acceptors and donors; n and p are the concentrations of free electrons in the conduction band and free holes in the valence band; σ_{OC} and σ_{OV} are the optical ionization rates for the two complementary ionization transitions of Cr; c^e_D, c^h_A, c^e_{Cr}, and c^h_{Cr} denote the capture rates of electrons (e) by ionized donors, holes (h) by ionized acceptors, and electrons by chromium Cr^{2+} and holes by Cr^{1+}; β_{DAP} describes the average rate of recombination of the DA pairs (DAPs), $\beta_{A\mathrm{Cr}}$ Cr^{1+} describes acceptor tunneling; and, I stands for the light intensity of the photo-excitation. In the equations given above we have omitted terms related to Auger processes, which will be discussed later on.

Detailed analysis of the observed efficiency of photo-excitation for bands II and III in Fig. 1 and rates of signal rise and decay indicated that:

$$\frac{c^e_{\mathrm{Cr}}}{c^e_D} > 25\frac{N_D}{N_A}\frac{\sigma^{\mathrm{Cr}}_{OV}}{\sigma^A_{OC}}.$$

Assuming that our samples are compensated, i.e., that $N_D \approx N_A$, and that:

$$\frac{\sigma^{\mathrm{Cr}}_{OV}}{\sigma^A_{OC}} > \frac{1}{25}$$

as we concluded from the separate study, and also that $\sigma^{\mathrm{Cr}}_{OV}$ is of the same order as $\sigma^{\mathrm{Cr}}_{OC}$, we derive that:

$$\frac{\sigma^{\mathrm{Cr}}_{OV}}{\sigma^A_{OC}} \geqslant \frac{1}{10}$$

and, finally, that $c^e_{\mathrm{Cr}} \geqslant 2c^e_D$. This estimation indicates that Cr centers efficiently retrap photo-generated free electrons from the conduction band. Thus, we must select appropriate relative concentrations of donor and acceptor centers versus chromium concentration to avoid PL deactivation and to achieve efficient energy up-conversion.

For ZnSe:Fe,Cr carrier retrapping is far more efficient. Based on the photo-ESR data, from the observed efficiency of band-I processes (Fig. 1c), we estimate that:

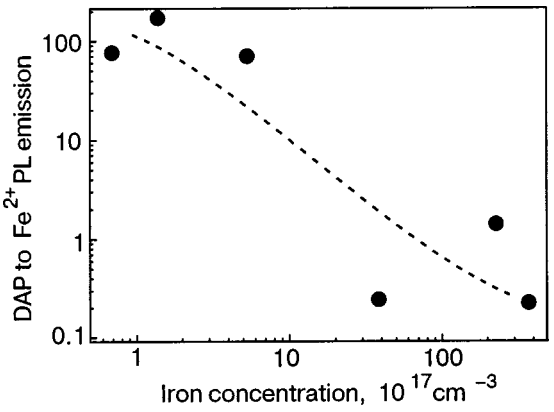

FIG. 6. Concentration dependence of deactivation of donor—acceptor pair emission in ZnSe:Fe.

$$\frac{c^e_{\mathrm{Fe}}}{c^e_{\mathrm{Cr}}}=\frac{N_{\mathrm{Cr}}}{n_{\mathrm{Cr}}}\frac{N_{\mathrm{Fe}}}{n_{\mathrm{Fe}}}\frac{\sigma^{\mathrm{Fe}^{(\mathrm{I})}}_{OC}}{\sigma^{\mathrm{Cr}^{(\mathrm{I})}}_{OC}}$$

so:

$$\frac{c^e_{\mathrm{Fe}}}{c^e_{\mathrm{Cr}}}\gg 1.$$

Moreover:

$$\frac{c^h_{\mathrm{Fe}}}{c^h_A}>\frac{c^e_{\mathrm{Cr}}}{c^e_D}\frac{N_{\mathrm{Cr}}}{n_{\mathrm{Cr}}}\frac{\sigma^{\mathrm{Fe}^{(\mathrm{I})}}_{OC}}{\sigma^{\mathrm{Cr}^{(\mathrm{I})}}_{OC}}>1.$$

These estimates indicate that Fe deactivates (by efficient retrapping of free carriers of both types) all competing recombination transitions in ZnSe, even in the case of a relatively low Fe concentration. This in fact we observed experimentally, as is shown in Figs. 3 and 6.

The second mechanism responsible for a low efficiency of energy up-conversion in ZnSe:Fe relates to very efficient Auger-type nonradiative recombination processes observed in Fe doped wide-band-gap II–VI compounds (see Ref. 2 and references therein). In the Auger process an excited donor acceptor pair decays nonradiatively by energy transfer to a nearby iron center, which is ionized. DAP PL is thus deactivated.

In the case of Fe doped ZnS and ZnSe this process turned out to be efficient, which results in efficient quenching of energy up-converted blue color DAP emission and in shortening of the DAP PL decay time, as we observed for ZnSe:Fe.[2] ''Edge'' DAP emission in ZnSe decays much faster than the relevant DAP emissions in undoped ZnSe and in ZnSe:Cr. This is evidence of very efficient and competing channel of nonradiative recombination in ZnSe:Fe.

Auger-type energy transfer must also take place in chromium doped ZnSe, since in this case also there is an energy overlap between DAP emission and Cr ionization transitions. Such overlaps are required for efficient DAP-to-Cr energy transfer. We performed optically detected magnetic resonance (ODMR) investigations to evaluate the Auger recombination rate in ZnSe:Cr.[12] The ODMR study indicated a fairly low rate of the DAP-to-Cr energy transfer process. This transfer process is rather inefficient in quenching DAP transitions of ZnSe:Cr.

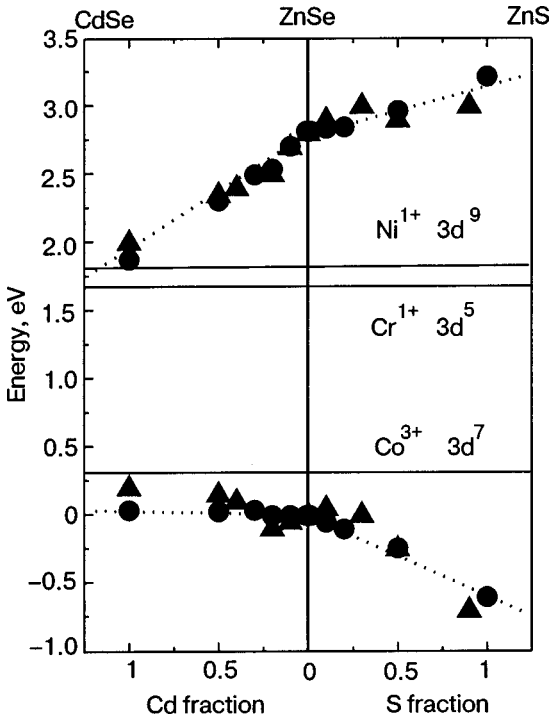

FIG. 7. Band shifts in solid alloys of ZnCdSe and ZnSSe versus energy level positions of three transition-metal-related charge states—nickel, cobalt, and chromium.

4. SOLID ALLOYS OF II–VI:Cr—OPTIMIZATION OF OPTICAL PUMPING ENERGY

The pumping energy of the up-conversion process can be tuned by introducing chromium into solid alloys of ZnCdSe and ZnSSe. Also in these alloys chromium introduces the excited charge state within the band gap, so the alloys turned out to be suitable materials for energy up-conversion. The relevant results are shown in Fig. 7, in which we show the conduction and valence band shifts estimated by us versus the energy level positions of three transition-metal-related charge state levels (nickel, cobalt and chromium) in ZnCdSe and ZnSSe (after Ref. 13). Whereas for alloys with common anion Cr ionization energy changes only a little, it can be changed considerably in alloys of ZnSSe (increases) or ZnCdS (decreases; not shown in Fig. 7). These are important observations, since energy up-conversion in Cr-doped ZnCdS and ZnSSe turned out to be equally efficient as in the case of ZnSe:Cr.

5. TEMPERATURE DEPENDENCE OF UP-CONVERSION PROCESS

There is an additional important consequence of using chromium-doped II–VI alloys. Not only can the excitation (and the energy of up-converted emission) be tuned, but the temperature dependence of the process can also be varied. This is important, since in the case of ZnSe quantum efficiency of the up-conversion process is reduced to about 1% at room temperature.

The photo-ESR investigations indicate that a relatively high quantum efficiency of the energy up-conversion process in ZnSe:Cr (few times 10^{-3}) is related to a metastable population of the Cr^{1+} state, observed at low temperatures. Two-

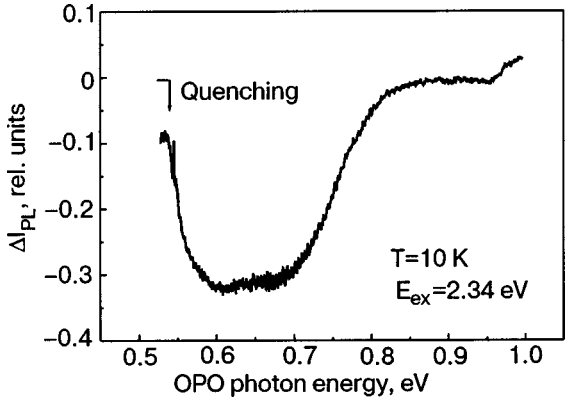

FIG. 8. Photo-quenching of the energy up-conversion process in ZnSe:Cr, observed in the two-color experiment with the OPO system and green color excitation.

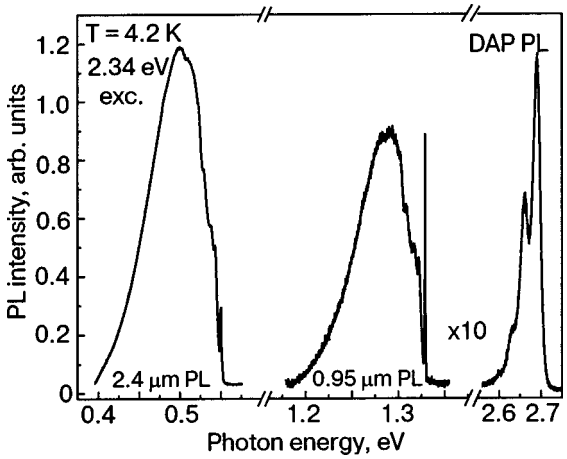

FIG. 9. Two infrared intra-shell emissions of chromium 2+ in ZnSe shown together with the blue energy up-converted DAP emission.

color experiments were performed (Fig. 8) to confirm the role of metastability of the photo-excited Cr^{1+} state. In the two-color experiments, two light sources were simultaneously applied to excite or quench the energy up-converted emission.

First photon, with energy larger than the ZnSe band gap energy, or from the energy range of the Cr 2+ to 1+ ionization transition, excites the blue DAP emission.

The second photon, selected from the range of ionization transitions of ZnSe acceptors. These ionization transitions were first identified from photo-ESR study shown in Fig. 2. The second illumination was obtained from either the OPO system or the free-electron laser (FEL) mid-infrared system. We studied the influence of this second illumination on the intensity of the energy up-converted emission.

For the 2.34 eV illumination and with the second photon within the range of ionization transitions of ZnSe acceptors, illumination quenches the DAP intensity (Fig. 8). Photo-ionization of shallow acceptors reduces also the population of the Cr^{1+} charge state. This is observed as a rapid photo-induced quenching of the Cr^{1+} signal in the photo-ESR study (see Fig. 2).

The up-conversion process is also deactivated when shallow acceptors are thermally ionized. Use of host material with larger acceptor ionization energies is thus profitable. In fact, we observed better temperature stability of energy up-converted DAP emission in ZnCdS:Cr and ZnSSe:Cr than in ZnSe:Cr. This is due to the fact that acceptors are deeper in these two alloys than those in ZnSe lattice.

6. INFRARED INTRA-SHELL EMISSION OF CHROMIUM 2+

In Fig. 9 we show three PL emissions efficiently excited in ZnSe:Cr under Cr the photo-ionization transition. In addition to the blue DAP emission, two infrared emissions, with maximum at about 0.95 μm and 2.4 μm are observed. Both these infrared bands are relatively broad, which can result in optically pumped and tunable laser emission with the wavelength of emission being suitable for some optoelectronic applications, such as lasers for surgery, remote sensing, gas sensing, etc.[14–18]

We found that the all three PL emissions have the same excitation bands and that the two channels of recombination (visible versus infrared) compete. At low temperatures the blue DAP emission dominates, but at increased temperatures the infrared emissions become more pronounced and dominate at room temperature.

The Cr photo-ionization band is characterized by large oscillator strength, i.e., the resulting photo-excitation can be more efficient in excitation of infrared emissions than the direct intra-shell excitation. Thus, such excitation can result in more efficient optical pumping of Cr 2+ intra-shell emissions. This fact is important considering intensive studies on laser action on Cr 2+ intra-shell transitions.

7. CONCLUSIONS AND SUMMARY

Initial interest in ZnSe started from the observation of fairly efficient energy up-conversion. Blue PL emission could be observed under optical pumping with green light. Detailed studies indicated that the process is efficient only at low temperatures. Also the pumping energy was not optimized for excitation with red color laser diodes. Both the temperature stability of the process and the pumping energy can be improved/tuned if we use II–VI solid alloys, such as ZnCdS or ZnSSe. Meanwhile it turned out that the system is suitable for tunable mid-infrared emission, using intra-shell transitions of chromium 2+. Mid-infrared emission with power above 1 W has already been achieved, making the system very attractive for practical applications.

This work was partly supported by the RFBR-Ural (Grant 04-02-96096).

*E-mail: godlew@ifpan.edu.pl

[1] V. Yu. Ivanov, Yu. G. Semenov, M. Surma, and M. Godlewski, Phys. Rev. B **54**, 4696 (1996).
[2] M. Godlewski, A. J. Zakrzewski, and V. Y. Ivanov, J. Alloys Compd. **300/301**, 23 (2000).
[3] M. Godlewski and A. Zakrzewski, in *II–VI Semiconductors*, M. Jain (ed.), World Scientific, Singapore (1993), p. 205.
[4] M. Godlewski and M. Kaminska, J. Phys. C **13**, 6537 (1980).
[5] M. Godlewski, Z. Wilamowski, M. Kaminska, W. E. Lamb, and B. C. Cavenett, J. Phys. C **14**, 2835 (1981).
[6] M. Surma, M. Godlewski, and T. P. Surkova, Phys. Rev. B **50**, 8319 (1994).
[7] M. Godlewski and A. Zakrzewski, J. Phys. C **18**, 6615 (1985).
[8] M. Godlewski, Phys. Rev. B **32**, 8162 (1985).

[9] A. Zakrzewski and M. Godlewski, Appl. Surf. Sci. **50**, 257 (1991).
[10] A. Zakrzewski and M. Godlewski, J. Appl. Phys. **67**, 2457 (1990).
[11] M. Surma and M. Godlewski, Acta Phys. Pol. A **92**, 1017 (1997).
[12] V. Yu. Ivanov, G. Karczewski, M. Godlewski, A. R. Omel'chuk, A. E. Belyaev, and N. V. Zhavoronkov, Acta Phys. Pol. A **103**, 695 (2003).
[13] T. P. Surkova, M. Godlewski, K. Swiatek, P. Kaczor, A. Polimeni, L. Eaves, and W. Giriat, Physica B **273–274**, 848 (1999).
[14] R. H. Page, K. I. Schaffers, L. D. DeLoach, G. D. Wilke, F. D. Patel, J. B. Tassano, Jr., S. A. Payne, W. F. Krupke, Kuo-Tong Chen, and A. Burger, IEEE J. Quantum Electron. **33**, 609 (1997).
[15] S. Bhaskar, P. S. Dobal, B. K. Rai, R. S. Katiyar, H. D. Bist, J.-O. Ndap, and A. Burger, J. Appl. Phys. **85**, 439 (1999).
[16] A. Burger, K. Chattopadhyay, J.-O. Ndap, X. Ma, S. H. Morgan, C. I. Rablau, C.-H. Su, S. Feth, R. H. Page, K. I. Schaffers, and A. Payne, J. Cryst. Growth **225**, 249 (2001).
[17] A. V. Podlipensky, V. G. Shcherbitsky, N. V. Kuleshov, V. I. Levchenko, V. N. Yakimovich, M. Mond, E. Heumann, G. Huber, H. Kretschmann, and S. Kuck, Appl. Phys. B **72**, 253 (2001).
[18] E. Sorokin and I. T. Sorokina, Appl. Phys. Lett. **80**, 3289 (2002).

This article was published in English in the original Russian journal. Reproduced here with stylistic changes by AIP.

Effects of resonance scattering of electrons by donor impurities in semiconductors

V. I. Okulov*

Institute of Metal Physics of the Ural Division of the Russian Academy of Sciences, Sofia Kovalevskaya, 18, Ekaterinburg 620219, Russia

(Submitted September 13, 2004)
Fiz. Nizk. Temp. **30**, 1194–1202 (November 2004)

A generalized formulation of the Friedel approach is given and a theoretical description of the effects of resonance scattering of conduction electrons by donor impurities in semiconductors is developed. The stabilization of the electron density when the Fermi energy reaches the resonance level and the temperature and concentration dependences of the electron mobility and magnetic susceptibility of the localized resonance states are considered in detail. The limits of applicability of the results are discussed. © *2004 American Institute of Physics.* [DOI: 10.1063/1.1820020]

INTRODUCTION

In the study of the energy levels of electrons at donor impurities in semiconductors attention is usually devoted mainly to just one of the possible situations, when those levels lie in the band gap of the host crystal. Then at a low impurity concentration the electronic states are bound, so that the energy values are discrete, and the wave functions are localized at the impurity. In another, more complex situation, but one that has also been studied in detail, when the energies of the electrons on the ionic core of substitutional impurities fall in the energy band of the valence electrons of the crystal, states of hybridization arise, corresponding to collectivization of the electrons on the valence orbitals. A third possible variant of the position of the energies of the impurity electrons has attracted less attention in the existing theoretical treatments: it arises when those levels lie in the conduction band of the crystal, and the impurity states can be hybridized with conducting states. The inadequate development of the theory for this variant has led to a situation where the experimental data obtained under such conditions are interpreted using concepts pertaining to the case when the levels lie in the band gap, i.e., the first of the situations mentioned. If the impurities retain their donor character in the low-temperature limit such an approach is inconsistent, since it presupposes the appearance of conduction electrons owing to thermal ionization of impurities with bound electrons. For a consistent treatment one must start from the fact that the electronic states on the impurities, which are donors in the ground state, are in essence hybridized with states of the conduction band. In this case the donor energy levels are not discrete energy eigenvalues of the bound electrons but resonance energies, according to the terminology of scattering theory. The wave functions of electrons with such energies have both a part that is localized on the impurity and a part describing free motion; this corresponds to hybridization of the impurity and conducting states. A way of describing the hybridization using the concepts of resonance scattering theory is well known in the theory of metals and forms the basis for the approach developed by Friedel in the series of papers whose results are set forth in Ref. 1. We have used such an approach for describing the manifestations of donor electronic states.[2,3] The main problem here is to discover the effects due to resonance scattering of conduction electrons by donor impurities in the concentration dependence and temperature dependence of the electron density, mobility, and magnetic susceptibility. It was shown in Refs. 2 and 3 that resonance scattering leads to stabilization the electron density with increasing number of donors, a concentration maximum of the mobility, and characteristic temperature dependence of the mobility and magnetic susceptibility. Effects of this kind have been observed in experiments on mercury selenide containing iron impurities, and the behavior of the concentration maximum of the mobility has been discussed in detail and is reflected in review articles.[4,5] In searching for an explanation for these facts the authors, relying upon arguments that are now seen to be unjustified, considered it possible to neglect the hybridization of impurity and conducting states despite the low-temperature character of the observed effects. Our experimental data obtained on the same object were presented in Refs. 2 and 3 and were given a quantitative interpretation based on the theoretical concepts of resonance scattering theory; it was shown that this interpretation enjoys advantages over the previously proposed explanations of the concentration maximum of the mobility. In the present article we lay out the theoretical principles of that approach (the results pertaining to the electron mobility have also been presented in Ref. 6) and discuss questions of its justification and applicability.

RESONANCE SCATTERING OF ELECTRONS AND GENERALIZED FRIEDEL SUM RULE

Let us start by giving the known results from the quantum-mechanical theory of the scattering of an electron on a static central potential. The asymptotics of the wave function $\psi(\mathbf{r})$ far from the center is described by the expression

$$\psi(\mathbf{r}) \propto e^{i\mathbf{k}\cdot\mathbf{r}} + f e^{ikr}/r, \tag{1}$$

where the scattering amplitude f depends on the direction of the wave vector $\mathbf{k}$ and the energy $\varepsilon = \hbar^2 k^2/2m$. The wave function (1) is the sum of the asymptotics $\psi_l(r)$ corresponding to definite values of the orbital moment:

$$\psi_l(r) \propto \frac{1}{r}\exp(i\delta_l)\sin\left(kr - \frac{\pi l}{2} + \delta_l\right), \tag{2}$$

which are expressed in terms of the scattering phases δ_l, which depend on the energy ε. A resonance in the scattering is manifested in a characteristic dependence of the derivative with respect to energy of some phase shift $\delta_r(\varepsilon)$ of the set δ_l:

$$\frac{d\delta_r(\varepsilon)}{d\varepsilon} = \frac{\Delta}{(\varepsilon-\varepsilon_r)^2+\Delta^2}. \tag{3}$$

Formula (3) is valid for energies ε close to the resonance energy ε_r; here Δ is the width of the resonance level, which is much less than ε_r. In the limit of small Δ the resonant electronic state has almost the same properties as a bound state, but the form of the asymptotics (1), which contains a contribution from the free motion, remains fundamental. The bound-state wave function $\psi_b(r)$ has exponentially decaying asymptotics:

$$\psi_b(r) \propto \exp(-\gamma r), \tag{4}$$

where γ is a positive real quantity, and the difference of this asymptotic behavior from (1) can be substantial.

Applying these results to the scattering of electrons on substitutional impurities in solids, we reckon the energy from the edge of the conduction band, so that the bound-state energy lies in the energy gap of the crystal. Resonance scattering arises if the impurity potential has an energy level in the conduction band and the impurity is a donor in the ground state, i.e., it gives up an electron without thermal excitation. A resonance donor state is described by formulas (1)–(3) and corresponds to a hybridized state of an electron at an impurity and in the conduction band.

For description of the energy spectrum of the electrons and the scattering potential of the impurities we adopt simple isotropic models. Let the impurity density n_i be small enough that at a distance $r=(3/4\pi n_i)^{1/3}$, equal to the radius of a sphere representing the volume per impurity, the electron wave function is described by the asymptotics (1), (2). Then Friedel's expression[1] is valid for the volume-averaged number density $n(\varepsilon)$ of electrons occupying states with energies from 0 to the given value ε:

$$n(\varepsilon) = n_e(\varepsilon) + n_i z(\varepsilon). \tag{5}$$

in this expression $n_e(\varepsilon)=k^3(\varepsilon)/3\pi^2$ is the density of free electrons obtained by averaging the contribution from the first term in the asymptotic expression (1); the boundary wave vector $k(\varepsilon)$ is determined by the relation $2m\varepsilon/\hbar^2 = k^2(\varepsilon)$. The second term is the contribution to $n(\varepsilon)$ of the inhomogeneous part of the electron density localized near impurity centers because of scattering. The relative fraction $z(\varepsilon)$ of this contribution per scattering center is expressed in terms of the scattering phase δ_l that appears in asymptotic expression (2):

$$z(\varepsilon) = \frac{1}{\pi}\sum_l \nu_l\delta_l(\varepsilon) = \frac{1}{\pi}\sum_l 2(2l+1)\delta_l(\varepsilon). \tag{6}$$

Here we are summing the partial contributions to $z(\varepsilon)$, which are proportional to the scattering phases, from all the electronic states; accordingly, $\nu_l=2(2l+1)$ is the degeneracy multiplicity of the state with the given ε.

The inhomogeneous part of the electron density, localized around the scattering centers, and its contribution to Eq. (5) arise in the resonance scattering. In the absence of resonances the electron wave function upon scattering is unchanged in respect to the character of the spatial distribution, remaining a plane wave, and so in that case the scattering does not affect the average electron density. Therefore, when there are no resonances one should set $z(\varepsilon)=0$, thereby expressing the condition of conservation of the number of electronic states during scattering. According to formula (6), this condition reduces to a definite sum rule for the scattering phases which is obeyed by the scattering potentials of the impurities in the solid. In resonance scattering, on the other hand, a part of the electron density becomes localized at the impurity, and therefore in the scattered wave the fraction corresponding to free motion is different from that in the incident wave. Accordingly, in the average electron density there is a localized fraction in addition to the free-motion fraction, and so $z(\varepsilon)$ is nonzero.

Let us consider the energy dependence of z for the case in which each impurity has one resonance level of energy ε_r. It is not hard to understand that the function $z(\varepsilon)$ describing the occupation of the resonance level has the functional form characteristic for resonance only in a restricted interval around the energy ε_r, i.e., for $\varepsilon_r-\Gamma<\varepsilon<\varepsilon_r+\Gamma$, $\Gamma \ll \varepsilon_r$. Setting aside for now the justification for this assertion and the definition of the parameter Γ, which we shall give below, we note that off resonance on the low-energy side ($\varepsilon<\varepsilon_r-\Gamma$) there is no localized contribution, since $z(\varepsilon)=0$, and consequently

$$\frac{1}{\pi}\sum_l \nu_l\delta_l(\varepsilon)=0, \quad \varepsilon<\varepsilon_r-\Gamma. \tag{7}$$

On the other hand, at high energies ($\varepsilon>\varepsilon_r+\Gamma$) the localized part of the electron density gives a contribution to $n(\varepsilon)$ which corresponds to the total occupation of the resonance level. Then $z(\varepsilon)$ is equal to the degeneracy ν_r of the given level:

$$z(\varepsilon) = \frac{1}{\pi}\sum_l \nu_l\delta_l(\varepsilon) = \nu_r, \quad \varepsilon>\varepsilon_r+\Gamma. \tag{8}$$

Equations (7) and (8) are the Friedel sum rules for the scattering phases. They reflect the fact mentioned above, that the number of states for the motion with nonresonance scattering is equal to the number of states for free motion, since the character of the motion does not change during nonresonance scattering. We emphasize that the application of Eqs. (7) and (8) together with (5) is the basis of the proposed approach for treating just the resonance scattering effects. The contributions of the bound states in such a system of equations could be described formally by phases that are multiples of π and would not lead to any nontrivial energy dependence.

The dependence of z on energy in the resonance interval indicated above is determined by the behavior of the resonance scattering phase. Let us consider Eq. (6) and separate out from the sum on the right-hand side the contribution of the resonance phase, writing

$$\frac{1}{\pi}\sum_l \nu_l\delta_l(\varepsilon)=\frac{1}{\pi}\nu_r\delta_r(\varepsilon)+\frac{1}{\pi}\sum_l{}' \nu_l\delta_l(\varepsilon). \tag{9}$$

The prime on the summation sign means to exclude the contribution mentioned. According to resonance scattering theory, the resonance phase $\delta_r(\varepsilon)$ can be represented as the sum of a sharply varying part, which is obtained from expression (3), and a term $\delta_{sm}(\varepsilon)$ that is slowly varying in the resonance interval. We choose the following form for writing such a sum:

$$\delta_r(\varepsilon)=\frac{\pi}{2}+\arctan\left(\frac{\varepsilon-\varepsilon_r}{\Delta}\right)+\delta_{sm}(\varepsilon), \tag{10}$$

where $\delta_{sm}(\varepsilon_r)=0$. We then have $z(\varepsilon)=(1/\pi)\nu_r\delta_r(\varepsilon)$, and the satisfaction of Eqs. (7) and (8) is ensured by suitable behavior of the function $\delta_{sm}(\varepsilon)$. The resonance contribution (the first two terms) in (10) describe the behavior of the function $\delta_r(\varepsilon)$ for $\varepsilon\to\varepsilon_r$:

$$\delta_r(\varepsilon)=\frac{\pi}{2}+\frac{\varepsilon-\varepsilon_r}{\Delta}. \tag{11}$$

If expression (11) is treated as a linear approximation of the function $\delta_r(\varepsilon)$ in the resonance interval, then one should set $2\Gamma=\pi\Delta$; then the resonance dependence (3) is modeled by a rectangular peak, and the $\delta_{sm}(\varepsilon)$ term is not taken into account. For a more exact description of the behavior of $\delta_r(\varepsilon)$ one must take the term $\delta_{sm}(\varepsilon)$ into account. Since the scale of variation of the function $\delta_{sm}(\varepsilon)$ is large compared to Γ, it can be approximated by the first terms of a Taylor series expansion around ε_r. The linear approximation for $\delta_{sm}(\varepsilon)$ is given by the expression

$$\delta_{sm}(\varepsilon)=\frac{\varepsilon-\varepsilon_r}{\Delta_{sm}}, \tag{12}$$

in which the constant Δ_{sm} is significantly greater than Δ and Γ. Equations (7) and (8) hold in such an approximation, since we adopt the following equation for determining Γ:

$$\frac{1}{\Delta_{sm}}=\frac{\left[\frac{\pi}{2}-\arctan\frac{\Gamma}{\Delta}\right]}{\Gamma}\approx\frac{\Delta}{\Gamma^2}. \tag{13}$$

It follows from Eq. (13) that the width of the resonance interval satisfies the inequalities $\Delta\ll\Gamma\ll\Gamma_{sm}$. The parameters Δ_{sm}, ε_r, and Δ characterize the resonance for scattering on a given impurity potential. In the framework of approximation (12) the boundaries of the resonance interval are modeled by jumps of the derivative of the function $z(\varepsilon)$ from zero to values of the order of $1/\Delta_{sm}$, which are small compared to the resonance values. Thus we have obtained justification for the sharp boundaries of the resonance interval of change in the level occupation $z(\varepsilon)$ and have determined the parameter Γ. It can be seen that this justification involves assumptions about the behavior of the function $\delta_{sm}(\varepsilon)$—that it goes to zero for $\varepsilon=\varepsilon_r$ (this is equivalent to the assumption that the function $z(\varepsilon)$ is symmetric) and that the constant Δ_{sm} is positive. The validity of these assumptions can in turn be linked to the properties of the potential leading to the resonance scattering. The sharp character of the boundaries of the resonance energy interval to which they lead has a simple meaning: resonance localization of the electron density cannot be considered to exist to some degree at all values of energy, but it appears and disappears abruptly at the boundaries of an interval of width 2Γ. As to the nonresonance scattering phases, according to what we have said, relation (9) implies the equation

$$\frac{1}{\pi}\sum_l{}' \nu_l\delta_l(\varepsilon)=0, \tag{14}$$

which is the general Friedel sum rule for all energy values. It must be taken into consideration jointly with the definition (9) and the expression for the resonance phase, which in our approximation looks like

$$\frac{1}{\pi}\delta_r(\varepsilon)=\frac{1}{2}+\frac{1}{\pi}\arctan\left(\frac{\varepsilon-\varepsilon_r}{\Delta}\right)+\frac{\left[\frac{\pi}{2}-\arctan\left(\frac{\Gamma}{\Delta}\right)\right](\varepsilon-\varepsilon_r)}{\pi\Gamma}. \tag{15}$$

Such a statement of the Friedel sum rule allows one to use it efficiently in studying the influence of resonance scattering on the Fermi energy and conductivity.

In substituting into formula (5) the expression obtained for $z(\varepsilon)$, we should take into account that the function $n_e(\varepsilon)$ reflecting the contribution of the free motion to the electron density varies slowly in the resonance interval and is therefore close to the value $n_0=n_e(\varepsilon_r)$. In the linear approximation

$$n_e(\varepsilon)\approx n_0\left[1+\frac{\varepsilon-\varepsilon_r}{\Delta_e}\right],\quad \varepsilon_r-\Gamma<\varepsilon<\varepsilon_r+\Gamma, \tag{16}$$

where $\Delta_e=n_0[dn_e(\varepsilon_r)/d\varepsilon_r]^{-1}$. In this approximation, according to formulas (5) and (12), the function $n(\varepsilon)$ in the resonance interval has the following form:

$$n(\varepsilon)=n_0+n_d\left[\frac{1}{2}+\frac{1}{\pi}\arctan\left(\frac{\varepsilon-\varepsilon_r}{\Delta}\right)\right]+\left(\frac{n_d}{\pi\Delta_{sm}}+\frac{n_0}{\Delta_e}\right)\times(\varepsilon-\varepsilon_r), \tag{17}$$

where $n_d=n_i\nu_r$ is is the density of donor electrons. This formula provides a basis for studying the influence of resonance scattering on the concentration dependence and temperature dependence of the electronic thermodynamic and kinetic parameters. Another basic formula relates the electron mean free path with the resonance scattering phase.

MEAN FREE PATH

In the calculations that follow we use the known expression for the inverse mean free path $\Lambda^{-1}(\varepsilon)$ in terms of the scattering phase, which can be written in the form

$$\Lambda^{-1}(\varepsilon)=2n_i s_0(\varepsilon)\sum_l (l+1)\sin^2[\delta_l(\varepsilon)-\delta_{l+1}(\varepsilon)], \tag{18}$$

where $s_0(\varepsilon)$ is a coefficient that is not related to the scattering. We separate from the sum over l in the above expression the terms containing the resonance phase:

$$(2r+1)\left(\sin^2\delta_r-\frac{1}{2}\sin 2\delta_r\sin 2\varphi\right). \tag{19}$$

Here, assuming that the nonresonance phases $\delta_l (l \neq r)$ are small, we neglect terms containing factors of $\sin^2 \delta_l$ and introduce the notation

$$\sin 2\varphi = (1+c_r)\sin 2\delta_{r+1} + (1-c_r)\sin 2\delta_{r-1}, \qquad (20)$$

where $c_r = 1/(2r+1)$ and, as in Eq. (19), we have dropped the argument ε. We now add the term $\sin^2 \varphi(1-2\sin^2 \delta_r)$ in the parentheses in expression (19). We compensate the nonresonance part by a suitable addition to Eq. (18), and the part with the resonance phase is of the same order of magnitude as the terms that we are ignoring. Then it turns out that expression (19) can be replaced by $(2r+1)\sin^2(\delta_r - \varphi)$, and formula (18) can be written in the approximation we have adopted as

$$\Lambda^{-1}(\varepsilon) = n_d s_0(\varepsilon)[\alpha(\varepsilon) + \sin^2(\delta_r(\varepsilon) - \varphi(\varepsilon))]. \qquad (21)$$

This formula contains the small quantities $\alpha(\varepsilon)$ and $\varphi(\varepsilon)$, which characterize the nonresonance phases. The functions $\alpha(\varepsilon)$ describes the contribution of all the phases off resonance, and $\varphi(\varepsilon)$ reflects the difference between the transport part and the total scattering cross section.

In the analysis of the energy dependence of the mean free path we first separate out a neighborhood of the resonance in which $|\varepsilon - \varepsilon_r| \ll \Gamma$. In this region the $\delta_{sm}(\varepsilon)$ term in the resonance phase can be neglected, since there Eq. (10) takes the form

$$\cot \delta_r(\varepsilon) = (\varepsilon_r - \varepsilon)/\Delta. \qquad (22)$$

Then, taking into account the smallness of $\varphi(\varepsilon)$ in comparison with $\delta_r(\varepsilon)$ in the region under consideration we have

$$\Lambda^{-1}(\varepsilon) = n_d s_0 \left\{ \alpha + \left(1 + \frac{(\varepsilon_r - \varepsilon)^2}{\Delta^2} \right)^{-1} \right\}, \qquad (23)$$

where $s_0 = s_0(\varepsilon_r)$, $\alpha = \alpha(\varepsilon_r)$. Outside the resonance interval, according to Eq. (21), the mean free path is equal to $(n_d s_0 \alpha)^{-1}$. Formula (23) describes the resonance drop in $\Lambda(\varepsilon)$ to a value of the order of $(n_d s_0)^{-1}$ as ε approaches ε_r. This is manifested in concentration dependence and temperature dependence of the conductivity, which we shall discuss below. A necessary condition for the existence of resonance effects is that the parameter α be small compared to unity.

Another characteristic energy region is found near the boundary of the resonance interval. We will be interested in the neighborhood of the upper boundary, $\varepsilon = \varepsilon_r + \Gamma$. In this region the applicability condition for expression (22) does not hold, and the contribution $\delta_{sm}(\varepsilon)$ must be taken into account in the resonance phase. From formula (14) we can obtain the following expression for small $\varepsilon_r + \Gamma - \varepsilon$:

$$\frac{1}{\pi}\delta_r(\varepsilon) = 1 - \frac{\varepsilon_r + \Gamma - \varepsilon}{\pi \Gamma_b}, \qquad (24)$$

where $\Gamma_b = \Delta_{sm}/2 = \Gamma^2/2\Delta$. After expression (24) is substituted into formula (21) we assume that Γ_b is significantly smaller than the characteristic scales for variation of the functions $\alpha(\varepsilon)$ and $\varphi(\varepsilon)$, and these functions can be considered constant in the region under consideration. Then the contribution from φ in the combination $\varphi\Gamma_b$ we include in the boundary energy $\varepsilon_r + \Gamma$, denoting it by ε_b. Then formula (21) for the given case takes the following form:

$$\Lambda^{-1}(\varepsilon) = n_d s_0 \left[\alpha + \sin^2\left(\frac{\varepsilon_b - \varepsilon}{\Gamma_b} \right) \right] \approx n_d s_0 \left[\alpha + \frac{(\varepsilon_b - \varepsilon)^2}{\Gamma_b^2} \right] \qquad (25)$$

The expression obtained for the energy dependence describes the transition of the mean free path at the boundary to the nonresonance value.

ELECTRON DENSITY AND FERMI ENERGY

On the basis of the results presented let us first of all consider the electron density and Fermi energy in the ground state. We take into account that the total electron density $n(\varepsilon)$ is specified by the condition of electrical neutrality or simply by the number of electrons available in the system per unit volume. In our system we should include in this number resonance donor the electrons studied (of density n_d) and the conduction electrons originating from the other donors and from the host (of density n_{0e}). In metals, for which the Friedel theory was developed,[1] the density of conduction electrons varies little with variation of n_d, while for a semiconductor the situation of interest is one in which the number of electrons is almost completely determined by the resonance donors under consideration. In both cases the following equation is valid for the ground state:

$$n(\varepsilon_F) = n_d + n_{0e}, \qquad (26)$$

which serves as the equation for determining the Fermi energy ε_F as a function of the donor density n_d. Under conditions of resonance scattering of electrons the Fermi energy is found in a certain above-resonance interval, and expression (17) for $n(\varepsilon_F)$ should be substituted into Eq. (26). It is easy to see that if the Fermi energy is close to the resonance energy ($|\varepsilon_F - \varepsilon_r| \ll \Gamma$) or significantly larger than it, then the contribution of the energy dependence of the electron density $n_e(\varepsilon)$ in $n(\varepsilon_F)$ is unessential. For studying the dependence on n_d of the value of $n_e(\varepsilon_F)$ itself we must substitute the expression found for the Fermi energy into formula (16). In considering the concentration dependence of the other quantities we can assume that after the resonance is reached the conduction electron density is equal to n_0. In this case the difference $n_0 - n_{0e}$ appears in Eq. (26), and from now on we shall refer to it as n_0. Thus Eq. (26) for the Fermi energy is written in the form

$$\frac{1}{\pi}\delta_r(\varepsilon_F) = 1 - \frac{n_0}{n_d}. \qquad (27)$$

Under the condition $|\varepsilon_F - \varepsilon_r| \ll \Gamma$, from this equation and formula (22) we have

$$\varepsilon_F - \varepsilon_r = \Delta \cot(\pi n_0 / n_d). \qquad (28)$$

The resonance value of the Fermi energy corresponds to $n_d = 2n_0$. With increasing density n_d the Fermi energy increases slowly while remaining inside the resonance interval. Using formula (24), we obtain an expression for ε_F near the boundary of the interval $\varepsilon = \varepsilon_r + \Gamma$:

$$\varepsilon_F = \varepsilon_r + \Gamma - \pi\Gamma_b \frac{n_0}{n_d}. \qquad (29)$$

Thus in the limit of high densities of donor impurities the Fermi energy and the conduction electron density go to the

values $\varepsilon_r+\Gamma$ and $n_e(\varepsilon_r+\Gamma)$, which are practically equal to the exact resonance values. In this lies the well-known ''seizing'' of the Fermi energy, a description of which is obtained here on the basis of the resonance scattering theory.

ELECTRON MOBILITY

Let us consider the dependence of the electron mobility on the density of donor impurities in the resonance interval. This interval is bounded below by the value close to n_0, so that the ratio n_0/n_d with increasing n_d changes from unity to small values. Let us write formulas for the mobility in the characteristic regions discussed above for which formulas (28) and (29) pertain. In the first of them the density n_d takes on values close to the resonance value $2n_0$ and above it under the condition $\cot(\pi n_0/n_d)\ll\Gamma/\Delta$. Using formulas (23) and (28) we obtain the following expression for the mobility μ in the given region:

$$\mu=\mu_0(n_0/n_d)[\alpha+\sin^2(\pi n_0/n_d)]^{-1}, \tag{30}$$

where μ_0 is the mobility at a mean free path $1/(n_0 s_0)$. The resonance effect consists primarily in a drop of the value of the mobility from the nonresonance value $\mu_0(n_0/n_d)/\alpha$ to values of the order of μ_0. However the contribution of the resonance phase $\sin^2(\pi n_0/n_d)\approx 1-\pi^2/2(1/2-n_0/n_d)^2$ near resonance varies slowly, and therefore the minimum of the mobility at $n_d\approx 2n_0$ can be called strongly smeared. With a subsequent rise in the density n_d the mobility grows because the contribution of the resonance phase decreases until it reaches values of the order of α. Since after that, the drop in mobility because of nonresonance scattering begins, the concentration maximum of the mobility occurs at such values of n_d. This maximum quite pronounced by virtue of the smallness of α. It is described particularly clearly by the formulas obtained from expression (30) under the condition that the ratio n_0/n_d is small:

$$\mu=\mu_0\frac{n_0}{n_d}\left[\alpha+\left(\frac{n_0}{n_d}\right)^2\right]^{-1}=\frac{\mu_0\nu}{\pi\sqrt{\alpha}(1+\nu^2)}, \tag{31}$$

where $\nu=n_d\sqrt{\alpha}/(\pi n_0)$. The maximum at $\nu=1$ corresponds to values of n_d that are inversely proportional to the value of α. Therefore for its description at small α the applicability condition of the initial formulas (23) and (28) might not be satisfied. However, it turns out that the expression for the mobility obtained on the basis of formulas (24) and (29) at small n_0/n_d agrees with Eq. (31). Thus it can be assumed that formula (30) describes the concentration dependence of the electron mobility in the whole resonance interval.

The maximum in the concentration dependence of the electron mobility is one of the main effects of resonance scattering by donor impurities. Its origin is essentially due to the stabilization of the electron density as the concentration of donor impurities is increased in the resonance interval. In the course of the filling of the localized states the effective charge of each impurity decreases, and, as a result of this, the scattering of electrons weakens and the mobility increases. The growth continues until the nonresonance scattering, which is characteristic for practically neutral impurities, becomes prevalent, which again leads to a drop of mobility with increasing density of scatterers and ultimately to the appearance of a maximum of the mobility.

The concentration maximum is reflected in the temperature dependence of the electron mobility. Let us consider the ratio of the mobility $\mu(T)$ to its value at $T=0$. We write an initial expression for this ratio in the form

$$\frac{\mu(T)}{\mu}=\int d\varepsilon\left(-\frac{\partial f}{\partial\varepsilon}\right)\frac{\Lambda(\varepsilon)}{\Lambda(\varepsilon_F)}=\int dE\left[4\kappa T\cosh^2\left(\frac{E}{2\kappa T}\right)\right]^{-1}\frac{\Lambda(E)}{\Lambda(0)}, \tag{32}$$

where f is the Fermi function, $E=\varepsilon-\varepsilon_F$, and κ is Boltzmann's constant. The integration in this expression is over the resonance energy interval. As we are interested in the concentration anomalies of the temperature dependence, let us first discuss the comparatively simple limiting case of high impurity concentrations, when the ratio n_0/n_d is small and formulas (24) and (29) are valid. For this case expression (32) takes the form

$$\frac{\mu(T)}{\mu}=\int_{-\infty}^{\theta/T}dx[2\cosh(x/2)]^{-2}(1+\nu^2)\times\left[\left(\frac{Tx}{\theta}-1\right)^2+\nu^2\right]^{-1}, \tag{33}$$

where $\theta=\Gamma_b\sqrt{\alpha}/\nu\kappa$. The formula obtained describes a dependence which in the limit of low temperatures goes to a constant value and which falls off above a certain threshold temperature that is not always clearly defined. The scale of the falloff is determined by the temperature θ and decreases with increasing impurity density. The threshold temperature is defined approximately as the largest of the values of θ and $\nu\theta$, and therefore with increasing concentration, initially it is close to θ and then to the ν-independent temperature $\nu\theta$. Here it is clear that at concentrations less than a certain boundary value the threshold is smeared (the scale of the falloff and the threshold temperature are of the same order of magnitude) and with increasing concentration it becomes more and more pronounced. The boundary for the appearance of the threshold is the value $\nu=1$, which corresponds to the concentration maximum of the mobility.

Similar relationships are described by expressions for the temperature-dependent mobility of electrons at impurity concentrations close to the resonance value. Under the applicability conditions of formulas (23) and (28) one can write the following expression for the function $\Delta(E)/\Lambda(0)$ that appears in definition (32):

$$\frac{\Lambda(E)}{\Lambda(0)}=\left[1+\frac{1}{\alpha}\sin^2\left(\frac{\pi n_0}{n_d}\right)\right]\times\left\{1-\frac{1}{\alpha}\left[\left(\frac{E}{\Delta}+\cot\left(\frac{\pi n_0}{n_d}\right)\right)^2+1+\frac{1}{\alpha}\right]^{-1}\right\}. \tag{34}$$

The temperature dependences obtained with the use of this definition have been used for describing experimental data in Ref. 2, where examples of curves demonstrating the influence of the concentration maximum of the mobility on the

threshold values of the temperatures are presented. We stress that these kinds of relationships are in essence due to the stabilization of the electron density in the resonance interval, which was discussed above.

MAGNETIC SUSCEPTIBILITY

Let us now consider the magnetic susceptibility of a system of electrons scattering on by impurities. According to what we have said above, under resonance conditions there exists a localized electron density around each impurity. Like electrons in an atom, such a system possesses a spin magnetic moment. The set of such localized moments of resonance states gives a separate contribution to the magnetic susceptibility. For calculating it we take as the initial formula the well-known form of the expression for the electron spin susceptibility taking into account on a simplified level the influence of the electron–electron interaction:

$$\chi_r = \mu^2 \eta/(1+\psi\eta). \tag{35}$$

The term χ_r is to be added to the magnetic susceptibility of the conduction electrons, which we shall not discuss, as we are interested only in the contribution of the resonance states. The value of η is expressed in terms of the resonance part $g_r(\varepsilon)=n_i z'(\varepsilon)$ of the electron density of states $g(\varepsilon)$, given by formula (5):

$$g(\varepsilon)=\frac{dn(\varepsilon)}{d\varepsilon}=\frac{dn_e(\varepsilon)}{d\varepsilon}+n_i z'(\varepsilon), \tag{36}$$

$$\eta=-2n_i\int d\varepsilon\, z'(\varepsilon)\frac{df(\varepsilon)}{d\varepsilon}=2n_i\int d\varepsilon\, z'(\varepsilon) \times\left[4\kappa T\cosh^2\left(\frac{\varepsilon-\varepsilon_F}{2\kappa T}\right)\right]^{-1}. \tag{37}$$

Here $f(\varepsilon)$ is the Fermi function without temperature dependence of the chemical potential, the latter being assumed to be only unessentially different from ε_F in the region under consideration. The parameter ψ describes the exchange interaction of electrons in states localized at impurities, and μ^2 includes factors that reflect the role of the interaction between electrons in localized and conducting states, and the difference of the effective spin of a localized state from the spin of the free electron. If an ionized donor is spinless ($S=0$) then the following simple formula for μ^2 is valid:

$$\mu^2=\mu_0^2(1+\psi_{ed})=4\mu_0^2\frac{\langle s^2\rangle}{3}(1+\psi_{ed}), \tag{38}$$

where μ_0 is the Bohr magneton, ψ_{ed} is the coupling constant, $\langle s^2\rangle=s(s+1)=3/4$. For the more pertinent case of nonzero ion spin S, we generalize the second expression in Eq. (38), introducing the spin s_d of the localized state:

$$\mu^2=4\mu_0^2\frac{\langle s_d^2\rangle}{3}(1+\psi_{ed}),\quad S>0. \tag{39}$$

The value of $\langle s_d^2\rangle$ is the parameter of the completely filled localized state, which for an impurity is on the whole close to the state of the un-ionized donor. Here if, together with the spin S of the ionized impurity, one also knows the spin S_a of the un-ionized donor, then one can determine s_d by employing a certain sum rule. For example, at $S_a<S$ we set

$$\langle s_d^2\rangle=\langle S^2\rangle-\langle S_a^2\rangle=S(S+1)-S_a(S_a+1). \tag{40}$$

In more-complex situations when the proposed method of determining the effective moment is inapplicable, the effective moment will remain a phenomenological parameter.

The character of the dependence of η on temperature and impurity concentration depends on the value of the energy κT compared to Δ and of ε_F compared to ε_d. We shall assume that all of the electrons originate from the donors under discussion and in that case their density is such that the Fermi energy exceeds ε_d. Then upon further growth in the donor concentration the Fermi energy varies little, and the conduction electron density $n_e(\varepsilon_F)$ remains close to the value n_0. Calculating the value of η for low and high temperatures, we easily obtain the following simple formulas for the susceptibility:

$$\chi_r=\frac{\mu^2 n_i\sin^2(\pi n_0/n_i)}{\Delta_1+\psi n_i\sin^2(\pi n_0/n_i)},\quad T\ll\frac{\Delta}{\kappa}, \tag{41}$$

$$\chi_r=\frac{\mu^2(n_i-n_0)}{\kappa T+\psi(n_i-n_0)},\quad T\gg\frac{\Delta}{\kappa}, \tag{42}$$

where $\Delta_1=\pi\Delta/2$. The main qualitative feature of these formulas consists in unusual concentration dependences that reflect the fact that the electron density is stabilized in resonance scattering on donor impurities. It is manifested in the terms containing the limiting density n_0 both in the susceptibility without allowance for the interaction and in the parameters characterizing the exchange interaction in localized states. The theoretical confirmation that the susceptibility of resonance donor states at high temperatures obeys the Curie–Weiss law is quite important. This susceptibility χ_r is a constituent of the total magnetic susceptibility of the crystal, which, in addition to the contribution of the electrons, contains a contribution from the localized moments of ionized impurities, which also obeys the Curie law, and the weakly temperature-dependent susceptibility of the host.

RESULTS AND CONCLUSIONS

In this article we have described in detail the effects of resonance scattering of electrons by donor impurities on the basis of the application of a certain generalization of the Friedel approach. It is shown that the given theory predicts stabilization of the electron density, a concentration maximum of the electron mobility, the Curie law for the magnetic susceptibility of resonance donor states, and other features of the conductivity and magnetic susceptibility. Such effects have been observed in mercury selenide containing iron impurities, and in Refs. 2 and 3 a consistent quantitative interpretation of the experimental data was given on the basis of the theoretical results presented here. Moreover, it should be noted that the many experimental studies done on mercury selenide containing iron impurities have for many years provided material that has been used in developing theoretical concepts of a completely different kind, based on the assumption that it is possible to neglect the hybridization of electronic states on impurities and in the conduction band when their energies coincide. Without dwelling on the detailed analysis and a comparison of the theories, which would require voluminous discussion, we shall give only an

argument that bears directly on the present study. We are talking about the basis for the idea that hybridization does not need to be taken into account. In essence it reduces to two assertions. First, that resonance scattering leads to a drop in mobility and cannot lead to its growth. This statement is refuted by the results of the present paper. Second, that the matrix element that determines the width of the resonance level in perturbation theory is very small, practically equal to zero. This assertion is based on a misunderstanding. It is assumed that this matrix element is calculated between wave functions belonging to a single site. But that kind of matrix element should be calculated between wave functions of different sites, as is well known in the theory of s-d hybridization, so that there are no serious grounds for speaking of an extremely small width of the resonance level. Consequently, these statements and others like them based on similar lines of argumentation are essentially unsound. It seems likely that there is every reason to apply the resonance scattering theory to the study of the various phenomena in the mercury selenide and in other objects; this could be a subject for further study.

This study was supported by the Russian Foundation for Basic Research, Grant No. 03-02-16246.

*okulov@imp.uran.ru

[1] J. Friedel, Nuovo Cimento, Suppl. **2**, 287 (1958).
[2] V. I. Okulov, L. D. Sabirzyanova, K. S. Sazonova, and S. Yu. Paranchich, Fiz. Nizk. Temp. **30**, 441 (2004) [Low Temp. Phys. **30**, 328 (2004)].
[3] V. I. Okulov, G̀. A. Alshanskii, V. L. Konstantinov, A. V. Korolev, E. A. Pamyatnykh, Ė. A. Neifeld, L. D. Sabirzyanova, and S. Yu. Paranchich, Fiz. Nizk. Temp. **30**, 558 (2004) [Low Temp. Phys. **30**, 417 (2004)].
[4] I. M. Tsidil'kovskiĭ, Usp. Fiz. Nauk **35**, 85 (1992) [Sov. Phys. Usp. **35**, 85 (1992)].
[5] Z. Wilamowski, Acta Phys. Pol. A **77**, 133 (1990).
[6] V. I. Okulov, http://xxx.lanl.gov/archive/cond-mat/0401174.

Translated by Steve Torstveit

Electrophysical properties of semimagnetic solid solutions $Hg_{1-x}Mn_xTe$

I. M. Nesmelova* and V. N. Ryzhkov

Federal Research and Production Center NPO "State Institue of Applied Optics," Kazan 420075, Russia

M. I. Ibragimova and V. Yu. Petukhov

Kazan Physicotechnical Institute, Kazan Research Center of the Russian Academy of Sciences, Kazan 420029, Russia

(Submitted May 28, 2004)
Fiz. Nizk. Temp. **30**, 1203–1208 (November 2004)

A comprehensive study of the electrophysical properties of the semimagnetic ternary solid solution $Hg_{1-x}Mn_xTe$, an alternative material to $Hg_{1-x}Cd_xTe$, is reported. The charge-carrier scattering, optical, photoelectric, and magnetic properties of the material are investigated. Values are obtained for the effective masses of electrons and holes, the ionization energy of the acceptor level, and the g factor of the charge carriers as functions of the manganese telluride concentration and the densities of electrons and holes at temperatures of 300 and 77 K. It is shown that the methods of radio spectroscopy can be used for diagnostics of the semimagnetic material. Photodiode structures having characteristics close to the values for working in the background-limited regime are obtained by the use of Schottky barriers, diffusion in mercury vapor, and implantation of B^+ ions into p-$Hg_{1-x}Mn_xTe$ samples. © *2004 American Institute of Physics.* [DOI: 10.1063/1.1820021]

The main material now used for optoelectronic elements in the IR region of the spectrum are the ternary solid solutions $Hg_{1-x}Cd_xTe$ (MCT). However, experimental and theoretical studies have shown that the presence of Cd in the MCT lattice lowers the ionicity of the Hg–Te bond, causing a strong decrease of the activation energy for the formation and diffusion of defects; this leads to significant temperature and temporal instability of the electrophysical properties of the material and of the optoelectronic photoelements based on it. One of the alternative materials to MCT is the semimagnetic solid solution $Hg_{1-x}Mn_xTe$ (MMT); the presence of the Mn ions strengthens the Hg–Te bond, permitting the production of a material with stable properties and a more perfect crystal structure.[1–3]

The electrophysical properties of MMT have not been adequately studied. It is necessary to investigate the processes of charge-carrier scattering and to refine some of the parameters of the band structure. The presence of the Mn ions in MMT permits studying the magnetic properties of the material, providing additional diagnostic possibilities.

At low magnetic fields and high temperatures $T>40$ K the main electrophysical properties of MMT are determined by the energy structure near the Γ point of the Brillouin zone; in calculations it is necessary to take into account at least three close-lying zones: Γ_6, Γ_7, and Γ_8. The strongly localized d level of the Mn^{2+} ions lies 3 eV below the top of the valence band and has practically no influence on the electrophysical properties of MMT.

We have investigated the electrical, optical, magnetic, and photoelectric properties of n- and p-type MMT with $x=0.09-0.19$ at temperatures of 77–300 K. Studies were done on samples obtained by recrystallization from a two-phase mixture with replenishment of the melt and on epitaxial films of MMT obtained by LPE from tellurium fluxed melts. The as-grown samples had p-type conductivity, hole concentrations of the order of 10^{17} cm^{-3}, and hole mobilities $\mu_p=(2-5)\times10^2$ $cm^2/(V\cdot s)$ at 77 K. To reduce the hole density and obtain materials with n-type conductivity the grown films were subjected to a prolonged annealing in mercury vapor. As a result we obtained samples with a hole density of not more than $10^{15}-10^{16}$ cm^{-3} and samples with n-type conductivity with an electron density of the order of 10^{15} cm^{-3} or even less and an electron mobility $\mu_n=10^4-10^5$ $cm^2/(V\cdot s)$ at 77 K.

To elucidate the main mechanisms of electron and hole scattering in MMT solid solutions we studied the dependence of the mobility of the charge carriers on their density and the temperature. Figure 1 shows a plot of the electron mobility μ_n as a function of the electron density for two groups of samples with Mn concentrations $0.07<x<0.075$ (dots) and $0.09<x<0.095$ (crosses) at liquid nitrogen temperature. Common to both plots are a slight increase of the electron mobility in the region of densities $n=(2-3)\times10^{15}$ cm^{-3} and a decrease in μ_n at high electron densities. Theoretical calculations of the electron mobility at 77 K were done with allowance for the scattering on polar optical phonons, ionized centers, and microscopic fluctuations of the composition. An analysis of the temperature dependence of the electron and hole mobilities in MMT with $x\sim0.1$ showed that in the high-temperature region the mechanism of scattering on polar optical phonons is dominant, while at low temperatures the dominant mechanism is scattering on ionized acceptor and donor centers. An analogous situation takes place in MCT solid solutions. It has been shown that both n-type and p-type samples are compensated, the total densities of acceptor and donor centers being equal in order of magnitude with a value $\sim10^{16}$ cm^{-3}.

The optical properties of the samples were investigated

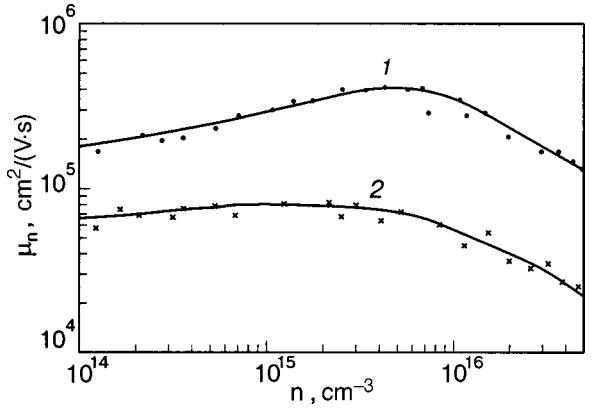

FIG. 1. Dependence of the electron mobility on the electron density at 77 K for two groups of n-type MMT samples with $0.07<x<0.075$ (*1*) and $0.09<x<0.095$ (*2*); the dots and crosses are experimental, the curves are calculated.

on the basis of their absorption and reflection spectra in the region 3–40 μm. It was shown that the MMT samples are more homogeneous in composition as compared to the MCT solid solution. Growth of the absorption on the short-wavelength side of the spectrum is due to interband transitions of the charge carriers at the Brillouin zone center. The absorption edge shifts to longer wavelengths with decreasing temperature and to shorter wavelengths with increasing x. The temperature coefficients of the band gap dE_g/dT were determined as functions of composition. The temperature coefficient of E_g is positive and decreases linearly with increasing x according to the law

$$dE_g/dT=(4.19-18.66x)\times 10^{-4}\ \text{eV/K}.$$

The absorption beyond the main band edge is due to the interaction of radiation with free charge carriers—scattering of free charge carriers on acoustic and optical phonons and ion ionized impurities. In the p-type material this absorption is an order of magnitude larger than in the n-type samples; this is due to transitions of holes between subbands of the valence band. As was shown in Ref. 4, in semiconductors with a Kane band structure this absorption can also be observed in n-type materials, since the real crystals are partially compensated. The absorption coefficient α in n-type single crystals on the long-wavelength side of the main band increases with increasing free electron density n and with increasing temperature (Fig. 2). Three scattering mechanisms were taken into account in the calculations: on acoustic phonons (α_{ac}), optical phonons (α_{opt}), and ionized impurities (α_{ion}). All three scattering mechanisms can be assumed independent and the value of α_{tot} calculated as the sum: $\alpha_{tot}=\alpha_{ac}+\alpha_{opt}+\alpha_{ion}$.

It was assumed in the calculations that the ionized impurities have unit charge (are singly ionized) and that the free charge carrier density is equal to the density of ionized impurities. The values of the band parameters needed in the calculation were taken from Refs. 1 and 5. The calculated spectra are presented in Fig. 2. It is found that for the n-type MMT at 300 K the main contribution to the absorption beyond the edge of the main band is due to the scattering of electrons on optical phonons; the scattering on acoustic phonons and ionized impurities is small. Additional absorption in the spectral region 8–20 μm can be explained by transitions of the charge carriers between subbands of light and heavy holes in the valence band (α_{V1V2}). At $T=80$ K the main contribution to the absorption of free charge carriers is from scattering on ionized impurities, and α_{ac} and α_{opt} are small.

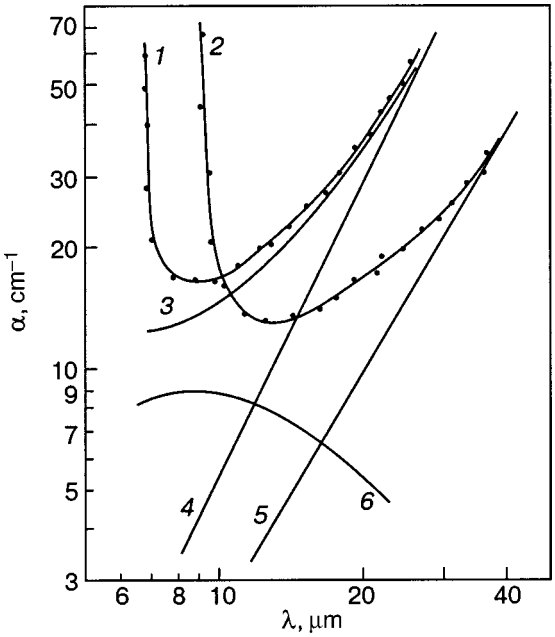

FIG. 2. Absorption spectra of an n-$Hg_{0.9}Mn_{0.1}Te$ sample with $n=4\times10^{16}$ cm^{-3} at 300 K (*1*) and 80 K (*2*); *1,2*—experiment; *3–6*—calculation; *3*—$\alpha_{tot}=\alpha_{ac}+\alpha_{opt}+\alpha_{ion}+\alpha_{V1V2}$ (300 K), *4*—$\alpha_{ac}+\alpha_{opt}+\alpha_{ion}$ (300 K), *5*—$\alpha_{ac}+\alpha_{opt}+\alpha_{ion}$ (80 K), *6*—α_{V1V2} (300 K).

In the p-type materials with a Kane band structure the absorption on the long-wavelength side of the main band edge ($h\nu<E_g$) is due mainly to transitions of holes between subbands of the valence band. It is shown in the monograph cited as Ref. 4 that for InAs, InSb, and CdHgTe this absorption plays a significant role. The theoretical processing of the experimental spectra permits determination of the dispersion relation and the effective masses of both heavy and light holes. The samples chosen for study were p-MMT with $x>0.12$, since for such compositions the absorption at transitions of the charge carriers between the heavy- and light-hole subbands (α_{V1V2}) does not mask the fundamental band–band absorption edge. Figure 3 shows the absorption spectra of a sample with $x=0.186$. It is seen in Fig. 3 that additional absorption is observed in the region of absorption by free carriers ($\lambda>4$ μm). With decreasing temperature the absorption increases and develops a more complex structure. This is often due to the fact that the degree of ionization of the acceptor level decreases with decreasing temperature, and the role of impurity absorption increases both in the conduction band and in the valence bands. We have calculated the absorption coefficient due to transitions of charge carriers between the heavy-hole V1 and light-hole V2 subbands, α_{V1V2}. The calculations were done according to the Kane theory ($E_g<\Delta$) with allowance for the nonparabolicity of the light-hole band and the corrections to the dispersion relations of the holes in bands V1 and V2 for the influence of the more remote bands lying above the conduction band and below the valence band. The effects of higher and lower

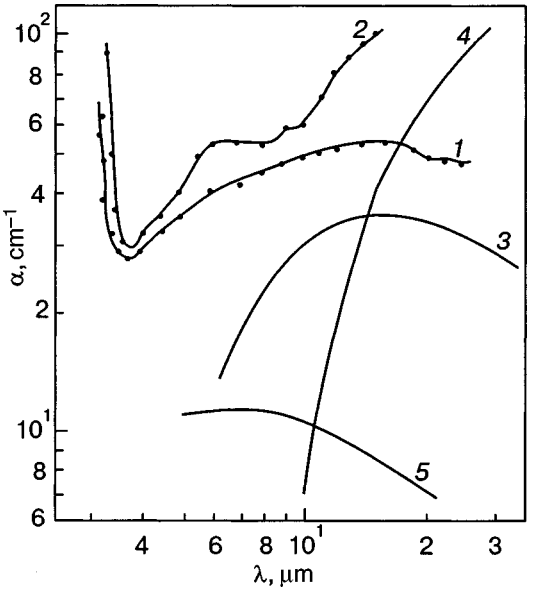

FIG. 3. Absorption spectra of a p-type $Hg_{1-x}Mn_xTe$ sample with $x=0.186$: experiment (*1*,*2*); calculation with (*3*,*4*) and without (*5*) the higher bands taken into account; $T=300$ K (*1*,*3*,*5*) and 80 K (*2*,*4*).

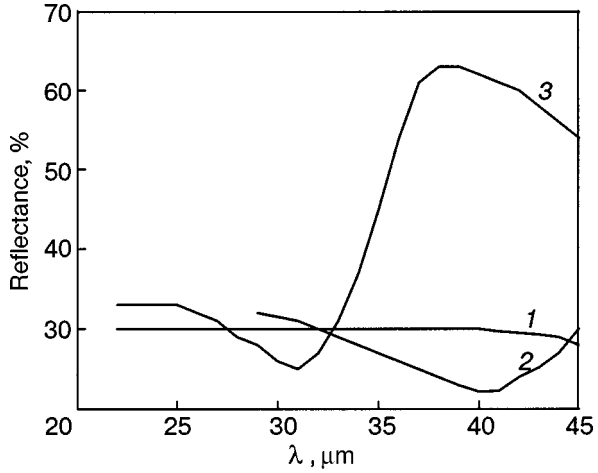

FIG. 4. Reflection spectra of n-$Hg_{1-x}Mn_xTe$ samples (300 K): $n=6\times10^{16}$ cm^{-3}, $x=0.09$ (*1*); $n=1.5\times10^{17}$ cm^{-3}, $x=0.06$ (*2*); $n=5.5\times10^{17}$ cm^{-3}, $x=0.10$ (*3*).

bands were estimated using second-order perturbation theory. The best agreement of the theory with experiment was obtained with the use of the band parameters reported in Ref. 6 (curves *3* and *4* in Fig. 3). The values of the effective masses of the heavy (m_1) and light (m_2) holes were calculated. The results of the calculations in the vicinity of the Γ point for concentrations $x=0.119$, 0.135, and 0.186 at $T=300$ and 80 K are given in Table I. Analysis of the low-temperature spectra permitted estimation of the ionization energy E_a of the acceptor level as a function of the manganese telluride concentration (see Table I).

The reflection spectra of the n-type MCT samples were studied in order to determine the effective masses of the electrons as functions of the electron density and the manganese telluride concentration. Measurements were made at 300 K on an IKS-21 spectrometer in the spectral region 20–45 μm. The samples studied had uncompensated donor densities $n=(6-60)\times10^{16}$ cm^{-3} and were grown by LPE from a tellurium flux. The reflection spectrum of several of the samples are presented in Fig. 4. For samples with $n>10^{17}$ cm^{-3} the characteristic plasma minima λ_{min} were observed, and from their positions the effective masses of the electrons were calculated. The experimental and calculated values of the effective masses of the electrons are given in Table II.

Studies of the magnetic properties of MMT single crystals were done by the ESR method on a Varian E-12 radio spectrometer in the frequency ranges ~9.5 and 37 GHz at sample temperatures of 300 and 77 K. The samples were carefully oriented in the resonant cavity to reduce the nonresonant energy losses, as could be done in this case because all of the ESR spectra observed were practically isotropic. We obtained ESR spectra at room temperature for all of the n- and p-type MMT samples studied with manganese ion concentrations in the solid solution in the range $x=0.074-0.135$. Figure 5 shows the ESR spectrum of a MMT sample $Hg_{0.9}Mn_{0.1}Te$, which consists of only one, rather broad line due to the manganese ions. The absence of hyperfine structure in the spectrum may attest to a strong interaction between magnetic ions or to a large scatter of the local crystalline fields in the MMT solid solution. Lowering the temperature of the measurements to 77 K and recording the ESR spectra at frequencies of 37 GHz at 300 K did not lead to resolution of the hyperfine structure.

Analysis of the spectra showed that the value of the g factor and the ESR absorption linewidth depend on the composition of the samples. With increasing x the value of the g factor decreases from 1.93 to 1.86, while the linewidth changes from 300 to 500 Oe. Such an increase in the absorp-

TABLE I. Band parameters of ternary solid solutions p-$Hg_{1-x}Mn_xTe$ (m_0 is the mass of a free electron).

Composition, x	T, K	m_1/m_0	m_2/m_0	E_g, eV	E_a, eV
0.119	300	0.27	0.0286	0.217	
	80		0.0261	0.175	0.062
0.135	300	0.27	0.0320	0.253	
	80		0.0304	0.228	0.073
0.186	300	0.27	0.0446	0.387	
	80		0.0435	0.376	0.128

TABLE II. Electrical parameters and effective masses of electrons in the solid solutions $Hg_{1-x}Mn_xTe$ (300 K).

Composition, x	$n\cdot10^{-17}$, cm^{-3}	$\mu_n\cdot10^{-4}$, cm^2/(V.s)	λ_{min}, μm	ε_∞	m_n/m_0 exp.	m_n/m_0 calc.
0.09	0.6	8.0	–	13.68	–	0.0194
0.06	1.5	5.0	40.5	13.68	0.0162	0.0190
1.00	5.5	1.3	31.0	13.10	0.0360	0.0345

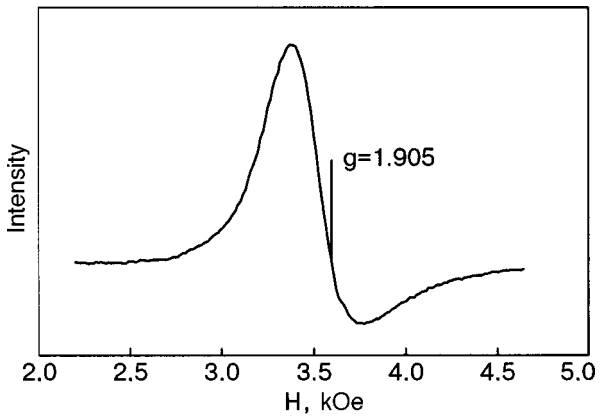

FIG. 5. Room-temperature ESR spectrum of a $Hg_{0.9}Mn_{0.1}Te$ sample at a frequency of 9.5 GHz.

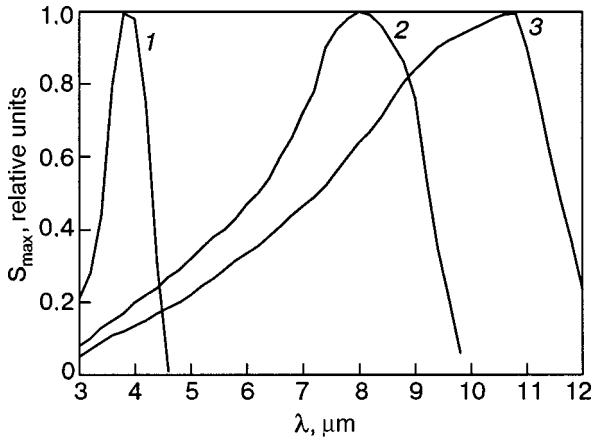

FIG. 6. Spectral distribution of the sensitivity $S_{\lambda,\max}$ of photodiode structures based on $Hg_{1-x}Mn_xTe$ solid solutions obtained by ion implantation (77 K): $x=0.16$ (*1*), 0.11 (*2*), 0.10 (*3*).

tion linewidth in the ESR spectra from the manganese ions attests to growth of distortions in the crystal lattice of MMT with increasing concentration of Mn ions.

The MMT epitaxial films were used to prepare photodiode structures by the Schottky-barrier method, by diffusion in mercury vapor, and by implantation of boron ions into a *p*-type samples. The ion-implantation experiments were carried out in the vacuum chamber of the ILU-3 ion-beam accelerator. As the dopant impurity we used singly charged boron ions B^+ with an energy of 40 keV. The dose of implanted ions was varied over the range $10^{14}-6\times10^{15}$ ions/cm^2. The samples were not subjected to post-implantation thermal annealing.

The photosensitive elements were made in the form of mesa structures by a photolithographic method on the surface of MMT wafers (which had hole densities of $2\times10^{15}-10^{16}$ cm^{-3} at 77 K in the initial material) that had been subjected to ion implantation. Experiments were done on *p*-MMT samples with compositions corresponing to the spectral regions 3–5 and 8–12 μm. Photosensitive diode structures were obtained at all implantation doses. The main electrophysical parameters characterizing the photodiodes structure were investigated: the product of the resistance at zero bias times the area of the sensitive element, R_0A, the voltage sensitivity $S_{\lambda,\max}$, and the detecting power $D^*_{\lambda,\max}$. We obtained the spectral dependence of the photosensitivity of the $p-n$ junctions (Fig. 6). The diode structures had the following parameters:

—$R_0A=130\ \Omega\cdot$cm^2, $S_{\lambda,\max}=1300$ V/W (for the spectral region 3–5 μm);

—$R_0A=1.7\ \Omega\cdot$cm^2, $S_{\lambda,\max}=40$ V/W (for the spectral region 8–12 μm).

The detecting power of the photodiodes was close to the value in the background-limited regime.

The recombination processes in single crystals and epitaxial films of MMT have been investigated in a number of studies (see, e.g., Ref. 7). It was shown that they have much in common with the well-studied photoelectric properties of MCT. Thus one can hope to obtain photoelements based on MMT with parameters like those that are now achievable in MCT.

In summary, we have done a comprehensive study of the electrophysical properties of the promising semimagnetic solid solution manganese–mercury telluride, an alternative material to the widely used cadmium–mercury telluride solid solution but with better stability of the electrophysical parameters.

*E-mail: eugene@mi.ru

[1] A. Rogalski, Infrared Phys. **31**, 117 (1991).
[2] N. G. Garbuz, S. V. Kondrakov, S. A. Popov, E. V. Susov, A. V. Filatov, R. A. Khazieva, and E. N. Kholina, Neorg. Mater. **26**, 536 (1990).
[3] A. Wall, C. Caprile, A. Franciosi, R. Reifenberg, and U. Debska, J. Vac. Sci. Technol. **4**, 818 (1986).
[4] I. M. Nesmelova, *Optical Properties of Narrow-Gap Semiconductors* [in Russian], Nauka (Siberian Division), Novosibirsk (1992).
[5] P. I. Baranskii, O. P. Gorodnichii, and N. V. Shevchenko, Infrared Phys. **30**, 259 (1990).
[6] I. I. Lyapilin and I. M. Tsidil'kovskiĭ, Usp. Fiz. Nauk **146**, 35 (1985).
[7] N. S. Baryshev, *Properties and Application of Narrow-Gap Semiconductors* [in Russian], Unipress, Kazan' (2000).

Translated by Steve Torstveit

PHASE TRANSITIONS AND STRUCTURE OF SEMICONDUCTOR COMPOUNDS

Nonequilibrium processes and ferroelectric phase transition in PbGeTe(Ga) crystals

B. A. Akimov, V. V. Pryadun, and D. R. Khokhlov*

Physics Department, M. V. Lomonosov Moscow State University, Moscow 119992, Russia

L. I. Ryabova and V. I. Shtanov

Chemistry Department, M. V. Lomonosov Moscow State University, Moscow 119992, Russia

E. I. Slynko

Chernovtsy Division of the Institute of Problems of Semiconductor Materials Science, National Academy of Sciences of Ukraine, ul. I. Vil'de 5, Chernovtsy 274001, Ukraine

(Submitted May 25, 2004)
Fiz. Nizk. Temp. **30**, 1209–1213 (November 2004)

The impedance of single-crystal samples of PbTe(Ga) and $Pb_{1-x}Ge_xTe(Ga)$ ($0 \leqslant x \leqslant 0.095$) is investigated in the frequency range from 10^2 to 10^6 Hz and temperature range 4.2–300 K. The temperature dependence of the capacitance of all the $Pb_{1-x}Ge_xTe(Ga)$ samples studied exhibited two types of features. These are a pronounced peak at a temperature $T=T_p$, caused by a dielectric anomaly at the ferroelectric phase transition, and a characteristic strong frequency dependence of the rise in capacitance in the temperature region $T<100$ K. The amplitude of the low-temperature effect decreases monotonically with increasing frequency f, and for $f>10^5$ Hz the effect practically vanishes. This behavior of the capacitance at such low frequencies may be associated with charge exchange processes in the impurity subsystem. The experimentally determined value of T_p is substantially higher than the characteristic temperatures for the appearance of long-term relaxation processes, in particular, the delayed photoconductivity. Consequently, the change of the charge states in the impurity subsystem is not accompanied by dielectric anomalies of the crystal lattice as a whole, and the possible restructuring of the lattice is of a local character. © *2004 American Institute of Physics.* [DOI: 10.1063/1.1820022]

INTRODUCTION

By doping lead telluride with gallium one can obtain crystals and epitaxial films in which the density of charge carriers is close to its values in pure bulk samples at low temperatures. This possibility is due to the stabilization of the position of the Fermi level (FL) within the forbidden band (approximately 70 meV below the bottom of the conduction band). All of the known solid solutions based on lead telluride in which the FL stabilization effect has been successfully observed upon doping with gallium are also semiinsulating. The majority of the theoretical concepts that have been proposed for explaining the set of properties of gallium-doped PbTe crystals presuppose the presence of an electron–lattice correlation that appears thanks to a local rearrangement of the nearest-neighbor crystalline environment of the impurity center upon a change of its charge state. Correlation processes cause a variable valence of gallium in the PbTe host, the formation of a system of impurity levels lying both inside the gap (the ground state) and in the conduction band (metastable impurity state), and the presence of long-term relaxation processes, in particular delayed photoconductivity, at temperatures $T<T_C \sim 80$ K. Together with the notions of local rearrangement of the crystal lattice, the idea of a ferroelectric phase transition at $T=T_C$ has been considered for explaining these properties.[1]

Direct experimental information about the behavior of the permittivity and the presence of a phase transition can be obtained in a study of the temperature dependence of the active and reactive components of the total impedance. Since the samples of gallium-doped solid solutions of lead telluride are quite highly resistive, measurements of the reactive component of the impedance can be carried out directly on uniformly doped crystals without a specially prepared $p-n$ junction. As objects of study we chose single-crystal samples of $Pb_{1-x}Ge_xTe(Ga)$, the electrophysical and photoelectric characteristics of which have been studied in detail.[2–6] The phase transition temperature in undoped of $Pb_{1-x}Ge_xTe$ is well known.[7,8]

SAMPLES AND EXPERIMENTAL TECHNIQUE

Single-crystal samples of $Pb_{1-x}Ge_xTe(Ga)$ ($0<x<0.095$) were obtained by sublimation from the vapor phase. An impurity of 1.5 mol. % GaTe was introduced directly into the growing stock. The composition of the samples was determined by the x-ray diffraction method. The values of the lattice constant are presented in Table I. The samples intended for impedance measurements were in the form of rectangular slabs with an area of $\sim 4 \times 4$ mm and thickness ~ 1 mm. The surface of the slabs was coated by a 95%In+4%Ag+1%Au alloy. For the measurements the

TABLE I. Characteristics of the samples studied.*

N	a, Å	x	T_p, K (lit.)	T_p, K (exp.)	$E_g(T_p)$, meV	E_A, meV	T_{cap}, K
1	6.4642	0	–	–	190 ($T \to 0$)	55	–
2	6.4426	0.046	136	140	265	75	70
2	6.4260	0.080	196	165	297	140	90
4	6.4196	0.095	224	190	313	150	100

*The lattice constant a [Å] $= 6.4642 - 0.47018x$, the band gap $E_g(T_p)$ [meV] $= 190 + 0.55T_p$ (Refs. 7 and 8).

samples were placed in a chamber that shielded them from stray light. The measurements were made with E7-12 and MIT 9216A ac current bridges at frequencies f from 10^2 to 10^6 Hz in the temperature interval 4.2–300 K. The temperature dependence of the resistivity ρ was measured in dc on samples $1 \times 1 \times 5$ mm in size under conditions of shielding and under illumination by IR radiation sources.

EXPERIMENTAL RESULTS

The typical shape of the temperature curves of the resistivity ρ for $Pb_{1-x}Ge_xTe(Ga)$ samples measured in dc under conditions of shielding and under illumination by a light-emitting diode at wavelength $\lambda = 1$ μm is shown in Fig. 1 for samples with $x = 0.046$ and 0.08. Similar curves had been observed previously for solid solutions of various compositions.[2–6] The characteristic feature distinguishing the $\rho(T)$ curve for $Pb_{1-x}Ge_xTe(Ga)$ from that for PbTe(Ga) is the presence of a maximum and a region of decline with decreasing temperature even under conditions of shielding. In lead telluride containing gallium $\rho(T)$ increases monotonically with decreasing temperature all the way down the lowest temperatures of the experiment. Delayed photoconductivity is observed at $T < T_C \sim 80$ K, where T_C is independent of the composition x of the solid solution. In Refs. 2 and 4–6 a correlation was noted between the the composition x of the solid solution and the temperature T_m corresponding to the maximum on the $\rho(T)$ curves obtained under conditions of shielding. This suggested that the maximum is due to a phase transition,[4–6] the temperature of which is shifted by approximately 80 K downward on the temperature scale because of the presence of the dopant. However, the possibility of such a substantial change in phase transition temperature for such an insignificant impurity concentration has raised valid objections.[2,3]

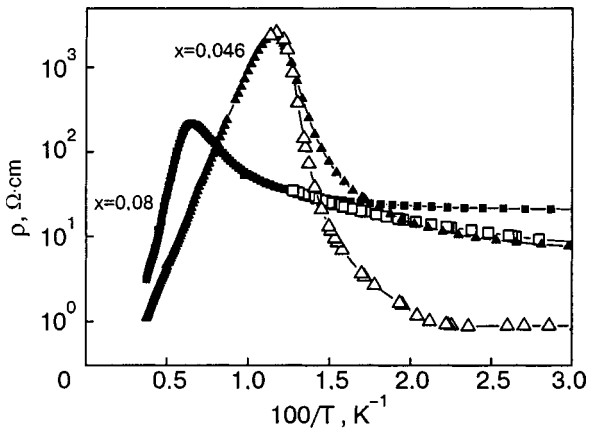

FIG. 1. Temperature dependence of the resistivity of $Pb_{1-x}Ge_xTe(Ga)$ samples, measured under conditions of shielding (▲, ■) and under illumination by an LED at wavelength $\lambda = 1$ μm (△, □).

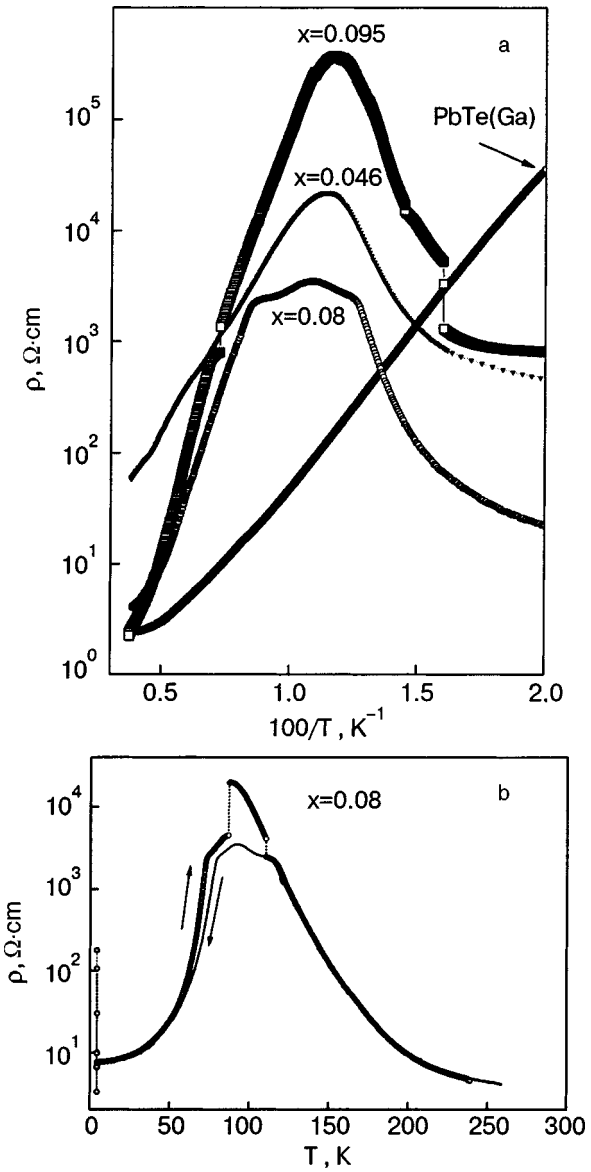

FIG. 2. Temperature dependence of the resistivity of $Pb_{1-x}Ge_xTe(Ga)$ samples prepared for impedance measurements, under conditions of shielding (a) and for a $Pb_{0.92}Ge_{0.08}Te(Ga)$ sample on cooling (line) and on subsequent heating (points) (b).

Figure 2 shows the temperature dependence of the resistivity ρ measured in dc for $Pb_{1-x}Ge_xTe(Ga)$ samples intended for impedance measurements, i.e., having a configuration for capacitance measurements: a large area of the slabs and a comparatively small distance between them. As can be seen in Fig. 2a, no explicit correlation between T_m and the sample composition x is observed. Moreover, in a heating-and-cooling cycle in the region of the maximum one observes instabilities and irreproducibility of the data at low temperatures (Fig. 2b).

In the high-temperature region the $\rho(T)$ curves for all the samples studied exhibited a segment corresponding to an activational character of the conductivity. The activation en-

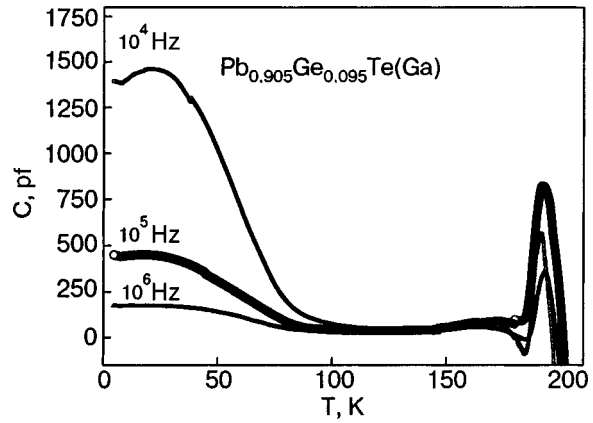

FIG. 3. Typical form of the temperature dependence of the capacitance C of $Pb_{1-x}Ge_xTe(Ga)$ samples, measured at different frequencies f.

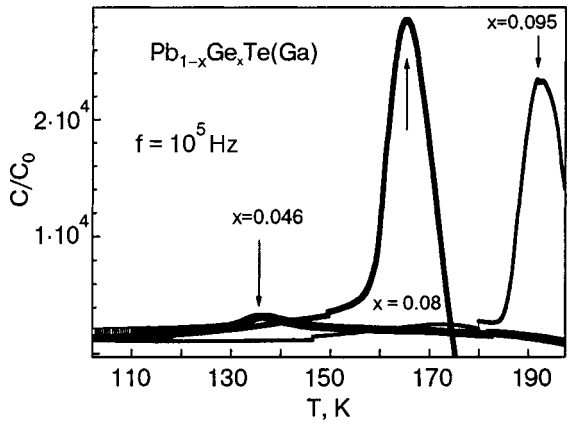

FIG. 4. Temperature dependence of the relative capacitance C/C_0 (C_0 is the geometric capacitance) of $Pb_{1-x}Ge_xTe(Ga)$ samples of different composition at a frequency $f=10^5$ Hz.

ergies E_A calculated from the relation $\rho \propto \exp(E_A/kT)$ are given in Table I. It should be noted that the values of the activation energy obtained previously[2–6] are practically equal to the data of the present study and do not depend on the shape and size of the sample.

At frequencies below 10^5 Hz the real part of the impedance Z' is practically equal to ρ. At a frequency of 10^6 Hz the value of Z' in the peak region is somewhat lower.

An example of the typical temperature dependence of the capacitance C for all of the $Pb_{1-x}Ge_xTe(Ga)$ ($x>0$) samples studied for measurements at different frequencies is shown in Fig. 3 for the sample with $x=0.095$. Since the crystals studied were not completely isolated, especially in the high-temperature region, in the processing of the experimental data the capacitance of the crystals was calculated from the values of the real Z' and imaginary Z'' parts of the impedance in the approximation of an equivalent circuit in the form of a parallel R–C chain. As is seen in Fig. 3, for $T=T_p$ the $C(T)$ curves clearly exhibit a peak with a position that is practically independent of frequency.

Table I also gives the values of the phase transition temperature for undoped $Pb_{1-x}Ge_xTe$ crystals, according to published data (T_p lit.) and according to the experimental data of the present study (T_p). The temperature at which the peak is observed on the $C(T)$ curve is somewhat lower than the temperature of the transition from the cubic to the rhombohedral phase for the undoped alloy of the same composition but is substantially higher than the temperature of the maximum on the $\rho(T)$ curves. It should be noted that the lowering of the phase transition temperature by an amount that is quite comparable with the data of the present study has also been observed upon doping of $Pb_{1-x}Ge_xTe$ alloys with indium.[8] Importantly, the peak on the $C(T)$ curves is rather sharp, indicating good homogeneity of the samples in respect to composition.

In the temperature region $T<T_{cap}$ (T_{cap} is the temperature at which low-frequency anomalies appear) a strong frequency dependence of the capacitance is observed. At low frequencies ($f\sim10^3$ Hz) one observes a sharp, practically jumplike increase in the capacitance by almost an order of magnitude. With increasing f the amplitude of the jump decreases, and at $f=10^5$ Hz the $C(T)$ curve becomes rather smooth. In the temperature region $T<70$ K the capacitance of PbTe(Ga) single crystals is practically independent of both temperature and the frequency f. Figure 4 shows the temperature dependence of the ratio C/C_0 for $Pb_{1-x}Ge_xTe(Ga)$ samples of various composition (C_0 is the geometric capacitance, defined as the ratio of the area of the contacts on the sample to the distance between them). If it is assumed that the sample is a flat capacitor, then the value of C/C_0 corresponds to the permittivity ε. For all the $Pb_{1-x}Ge_xTe(Ga)$ samples studied we find $\varepsilon\sim1300$ in the temperature interval $T_{cap}<T<T_p$ for all f and in the interval 4.2 K$<T<T_p$ for $f>10^5$ Hz.

The additional contribution to the capacitance observed in $Pb_{1-x}Ge_xTe(Ga)$ in the low-frequency range for $T<T_{cap}$ cannot be attributed to processes due to polarization or resonance effects of the crystal lattice itself. The characteristic frequencies of such effects are many orders of magnitude higher than 10^6 Hz. The most probable cause of the increase in capacitance may be processes involving charge exchange between impurity centers. An analogous effect in the same frequency range has been observed previously in the heterojunctions of germanium–silicon diodes and was explained as being the contribution to the capacitance of the heterojunction from charge exchange between boundary states.[9]

CONCLUSION

In this study we have established experimentally that the phase transition temperature T_p in $Pb_{1-x}Ge_xTe(Ga)$ is substantially higher than the characteristic temperatures for the appearance of delayed photoconductivity ($T_C\sim80$ K), the temperatures of the inflection points on the $\rho(T)$ curves, and the temperatures at which the low-frequency anomalies appear on the temperature curves of the capacitance (T_{cap}). The data show that processes involving charge exchange between impurities are characterized by only a local restructuring of the lattice, unaccompanied by the frequency-independent dielectric anomalies observed at transitions to the ferrophase.

This study was supported in part by Grants Nos. 04-02-16397 and 02-02-17057 from the Russian Foundation for Basic Research and by INTAS Grant No. 2001-0184.

*E-mail: khokhlov@mig.phys.msu.ru

[1] B. A. Volkov, L. I. Ryabova, and D. R. Khokhlov, Usp. Fiz. Nauk **172**, 875 (2002).
[2] B. A. Akimov, A. V. Albul, I. I. Ivanchik, L. I. Ryabova, E. I. Slyn'ko, and D. R. Khokhlov, Fiz. Tekh. Poluprovodn. **27**, 355 (1993) [Semiconductors **27**, 194 (1993)].
[3] B. A. Akimov, V. V. Pryadun, L. I. Ryabova, and D. R. Khokhlov, Fiz. Tekh. Poluprovodn. **38**, 293 (2004) [Semiconductors **38**, 281 (2004)].
[4] E. P. Skipetrov, E. A. Zvereva, L. A. Skipetrova, V. V. Belousov, and A. M. Musaitin, J. Cryst. Growth **210**, 292 (2000).
[5] E. P. Skipetrov, E. A. Zvereva, V. V. Belousov, L. A. Skipetrova, and E. I. Slynko, Phys. Status Solidi B **221**, 549 (2000).
[6] E. P. Skipetrov, E. A. Zvereva, O. S. Volkova, E. I. Slynko, and A. M. Musaitin, Mater. Sci. Eng., B **91–92**, 416 (2002).
[7] S. Nishi, H. Kawamura, and K. Murase, Phys. Status Solidi B **97**, 581 (1980).
[8] A. I. Lebedev and Kh. A. Abdullin, Fiz. Tekh. Poluprovodn. **18**, 624 (1984) [Sov. Phys. Semicond. **18**, 388 (1984)].
[9] J. P. Donnelly and A. G. Milnes, IEEE Trans. Electron Devices **ED-14**, 63 (1967).

Translated by Steve Torstveit

Ultrasonic investigation of a phase transition in ZnSe:Ni

V. V. Gudkov* and S. B. Petrov

Russian State Professional-Pedagogical University, ul. Mashinostroiteleĭ 11, Ekaterinburg 620012, Russia

A. T. Lonchakov, I. V. Zhevstovskikh, V. I. Sokolov, and N. B. Gruzdev

Institute of Metal Physics of the Ural Division of the Russian Academy of Sciences, Sofia Kovalevskaya, St., 18, Ekaterinburg 620219, Russia

(Submitted June 1, 2004)
Fiz. Nizk. Temp. **30**, 1214–1218 (November 2004)

Ultrasonic experiments on ZnSe and ZnSe:Ni crystals with impurity concentrations of 5.5×10^{19} cm^{-3} have revealed precursor phenomena at temperatures much higher than the temperature of the structural transition ($T_c=14.5$ K). It is found that the elastic constant C_{44} softens while C_{11} and C_{12} become stiffer as T_c is approached from above; the strains associated with the order parameter are transverse deformations of the ε_4 type. A brief symmetry analysis of the possibilities of formation of a tetragonal phase is given. The Jahn–Teller effect and displacement of the charge density on the chemical bonds are discussed as probable causes of the low-temperature phase transition. © *2004 American Institute of Physics.*
[DOI: 10.1063/1.1820023]

INTRODUCTION

The growing interest in research on type II–VI semiconductors doped with $3d$ elements is due to the possible ordering of the magnetic moments of the impurities and to the use of these materials in spintronic devices. Recently a low-temperature structural transition due to a nickel impurity was observed in zinc selenide by neutron diffractometry supplemented with ultrasonic studies.[1] The currently available data indicate that this is a second-order transition from a cubic structure of the zinc blende type to a tetragonal structure. The nature of the transition observed is not completely clear, since it is due to impurities at an anomalously low density (5.5×10^{19} cm^{-3}).

In the description of phase transitions one considers physical quantities that are derivatives of thermodynamic potentials with respect to thermodynamic coordinates. The experimentally obtained dependence of these derivatives on the thermodynamic parameters yields useful information about the type of transition and its kinetics and also serves as a touchstone for both phenomenological and microscopic theoretical concepts. One such physical quantity is the tensor of elastic constants, which is the second derivative of the free energy F (for an isothermal process) or the internal energy U (for an adiabatic process) with respect to the components of the strain tensor ε_i. (Here and below we use the Voigt notation.) At structural phase transitions the components of the order parameter tensor Q_j are associated with the strains ε_i in a definite way. In was shown in Ref. 2 that for the elastic constants in the region of a second-order structural transition the temperature dependences described by different terms in the expansion of F are qualitatively different, since those terms reflect different characters of the coupling of Q_j and ε_i. In the case of a transition from a cubic to a tetragonal phase the order parameter is a scalar $Q=(c-a)/a$, where a and c are the parameters of the tetragonal unit cell. Thus from the shape of the experimental curves of the temperature dependence of the different components of the elastic constant tensor one can establish which of them undergo the greatest change in the transition region, determine the type of strains associated with the order parameter, and indicate the character of their coupling. The elastic constants can be measured in two types of experiments: static and dynamic. Experiments of the first type presuppose a change in length of the sample when static stresses are applied to it. The second type of experiments is based on the propagation of acoustic waves in the ultrasonic range. The elastic constants thus measured are dynamic, i.e., they contain a frequency-dependent, in general complex, contribution and they determine the phase velocity v and absorption Γ of the ultrasonic wave:

$$v_{\langle klm\rangle,p}=\sqrt{\frac{C_{\langle klm\rangle,p}}{\rho}},$$

$$\Gamma_{\langle klm\rangle,p}=\frac{\omega}{2v_{\langle klm\rangle,p}}\frac{\mathrm{Im}\{C_{\langle klm\rangle,p}\}}{\mathrm{Re}\{C_{\langle klm\rangle,p}\}}=\frac{\omega}{2\rho v^3_{\langle klm\rangle,p}}\mathrm{Im}\{C_{\langle klm\rangle,p}\},\quad(1)$$

where the index p indicates the type of normal mode propagating along the axis $\langle klm\rangle$: in the case of the principal crystallographic axes one has $p=\ell$ for a wave of longitudinal polarization and $S1$ and $S2$ for the two transverse modes; ρ is the density of the material, $C_{\langle klm\rangle,p}$ is an effective elastic constant; ω is the angular frequency of the wave. The elastic-constant tensor of a cubic crystal has three independent components. In a Cartesian coordinate system tied to the principal crystallographic axes, these are C_{11}, C_{12}, and C_{44}.

In Ref. 1 longitudinal ultrasonic waves propagating along the $\langle110\rangle$ axis were used. In that case the effective

elastic constant is a linear combination of all three independent components defined in a coordinate system tied to the principal crystallographic axes:

$$C_{\langle 110\rangle,\swarrow}=\frac{1}{2}(C_{11}+C_{12}+2C_{44}). \tag{2}$$

The effective transverse elastic constants for this direction are

$$C_{\langle 110\rangle,S1}=\frac{1}{2}(C_{11}-C_{12}),C_{\langle 110\rangle,S2}=C_{44}, \tag{3}$$

and therefore, in order to get a more complete picture of the kinetics and the character of the phase transition in ZnSe:Ni, in addition to the curves for longitudinal waves[1] we also investigate on the same samples the temperature dependence of the absorption and of the velocity of transverse modes propagating along the ⟨110⟩ axis.

EXPERIMENT

Measurements of the phase velocity and absorption of ultrasound were made on an ultrasonic device operating on the principle of a frequency-tunable ultrasonic bridge,[3] at frequencies $f\approx 52$ and 154 MHz in the temperature interval $T=4.2$–160 K. The ZnSe:Ni samples were in the form of parallelepipeds with sides of $5\times 7\times 15$ mm. Ultrasonic waves were excited and detected by $LiNbO_3$ piezoelectric transducers. In this method the relative change of the balance frequency f of the bridge is related to the changes of the phase velocity and the path length L traversed by the wave as

$$\frac{\Delta f}{f_0}=\frac{\Delta v}{v_0}-\frac{\Delta L}{L_0}, \tag{4}$$

where $\Delta f=f(T)-f_0$, $\Delta v=v(T)-v_0$, $\Delta L=L(T)-L_0$, and v_0, f_0, and L_0 are quantities defined at a certain temperature T_0 (in our case $T_0=90$ K). The measurement error $\Delta f/f_0$ did not exceed 10^{-6}. Using the results of Ref. 4 for the coefficient of linear thermal expansion determined at $T=100$ K ($\alpha=2.5\times 10^{-6}$ K^{-1}), we found that above 60 K the value of $\Delta L/L_0$ is negligible in comparison with $\Delta f/f_0$. Below 60 K the neutron-diffraction data[1] indicate that the unit cell volume is unchanging (within the accuracy of the measurements) both before and after the transition. Since there is no preferred direction in the sample, in the tetragonal phase it should consist of regions having different directions of the c axis. It is natural to suppose that these axes are equiprobably oriented along the fourfold crystallographic axes of the high-temperature cubic phase. Then it follows from the condition of conservation of the unit cell volume that the linear dimensions of the sample remain constant. Thus if $\Delta v/v_0$ is determined on the basis of relation (4), one may safely neglect the term $\Delta L/L_0$ in the whole temperature interval.

RESULTS AND DISCUSSION

The temperature dependence of the absorption and velocity of transverse sound polarized along the ⟨100⟩ axis (in accordance with formula (3) this is $S2$) measured by us in the Ni-doped crystal is analogous to that for longitudinal waves. The differences are of a quantitative character: the absorption peak is significantly higher and the change in the ultrasound velocity prior to the transition on the high-temperature side is considerably larger. Qualitative differences are seen in the curves for the transverse ultrasonic wave of the $S1$ type (i.e., polarized along the ⟨110⟩ axis): the absorption peak is absent (see Fig. 1b) and the temperature dependence of the velocity is monotonic.

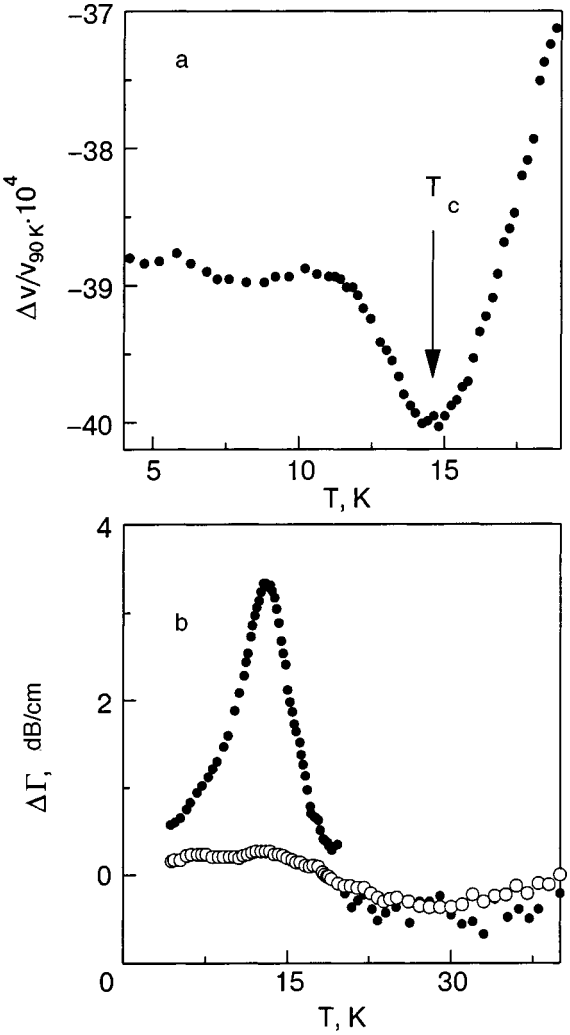

FIG. 1. Temperature dependence of the velocity (a) and absorption (b) of transverse ultrasonic waves in ZnSe:Ni: (●)—polarization along ⟨100⟩, (○)—⟨110⟩. $\Delta V=v(T)-v(90\text{ K})$, $\Delta\Gamma=\Gamma(T)-\Gamma(40\text{ K})$.

Knowing the temperature dependence of all the effective elastic constants for the ⟨110⟩ direction, one can recover the temperature dependence of $C_{11}(T)$, $C_{12}(T)$, and $C_{44}(T)$. Our apparatus also permits measurement of the absolute values of the ultrasound velocity, but to significantly lower accuracy. Therefore in order to express our results on the absolute scale we used the results of Ref. 5, in which the values of the elastic constants of the ZnSe crystal and their temperature dependence $C_{ij}(T)$ in the interval 77–300 K were measured to high accuracy. The temperature intervals of our measurements and the measurements reported in Ref. 5 partially overlap. This made it possible to represent the temperature dependence of the elastic constants of the impurity-free ZnSe crystal on the absolute scale over a wide temperature interval. Assuming that the curves for the pure and doped crystals coincide at high temperatures, we constructed the

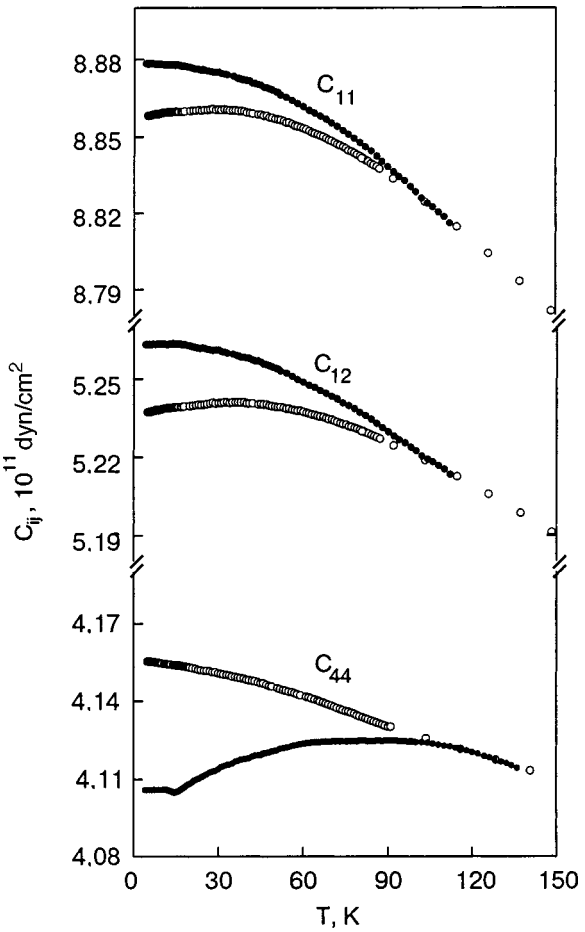

FIG. 2. Temperature dependence of the elastic constants of ZnSe:Ni (●) and ZnSe (○) crystals.

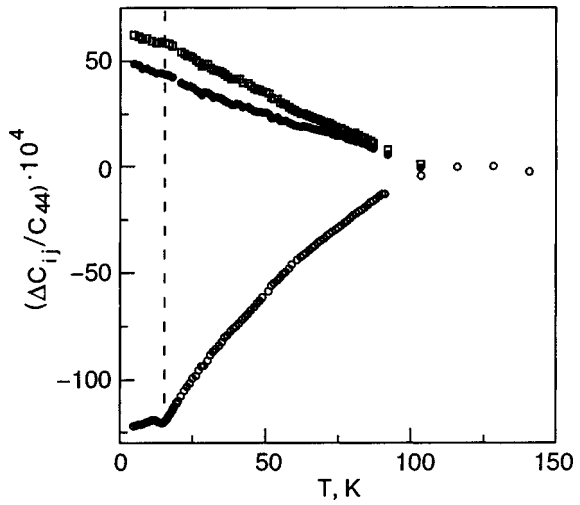

FIG. 3. Temperature dependence of the difference of the elastic constants of the doped (C_{ij}^{Ni}) and pure (C_{ij}^0) crystals, $\Delta C_{ij}=C_{ij}^{\mathrm{Ni}}-C_{ij}^0$, in relative units: (○)—ΔC_{44}, (●)—ΔC_{11}, (□)—ΔC_{12}. The vertical line corresponds to $T=T_c$.

temperature dependence of the elastic constants for the doped crystal (see Fig. 2). We recall that below 14.5 K the ZnSe:Ni sample is no longer of cubic symmetry, that it has a different set of elastic constants and, moreover, is not monocrystalline. Therefore, in the temperature region corresponding to the new phase the data for the doped sample must be understood as being the result of a certain averaging.

In order to get a clearer picture of the differences of the elastic constants of the doped and pure crystals, in Fig. 3 we have plotted on a relative scale the difference of the elastic constants of each given type, $C_{ij}^{\mathrm{Ni}}-C_{ij}^0$, where C_{ij}^0 is the elastic constant of the pure crystal and C_{ij}^{Ni} is the same for the Ni-doped crystal.

The main results obtained on the basis of the experimental data given above can be stated as follows.

1. The temperature dependence of the elastic constants for the doped and pure crystals are different below ≈ 100 K, indicating that precursor phenomena are observed over a wide interval range.

2. Doping leads to a softening of the elastic constant C_{44} and a linear hardening (with decreasing temperature) of the elastic constants C_{11} and C_{12} relative to the pure crystal.

3. The temperature dependence of C_{11} and C_{12} for the pure ZnSe crystal is not monotonic: an indistinct maximum is observed around 40 K. Such behavior can be considered anomalous, since a monotonic hardening of the elastic constants with decreasing temperature is normal for insulators. In the quasiharmonic approximation[6] $C_{ij}(T)$ is proportional to $-T^4$ for $T\to 0$ and to $-T$ at moderately low temperatures.

4. Since nonmonotonic dependence is observed for the doped crystal in the phase transition region only for C_{44}, one can associate a strain of the ε_4 type with the order parameter. The general appearance of the $C_{44}(T)$ curve is similar to the dependence given in Ref. 2, which corresponds to a linear relation between the order parameter and the strains.

A symmetry analysis based on the neutron-diffraction data shows that the transition to the tetragonal phase cannot occur with a wave vector $\mathbf{k}=0$. A tetragonal phase arises only via transition channels of the Lifshitz stars $\{k_8\}$ and $\{k_{10}\}$ in the Kovalev notation.[7] The star $\{k_{10}\}$ forms a tetragonal phase upon a transition along one arm or any two arms, while the star $\{k_8\}$ does so for a certain set of arms, a list of which is given in the monograph cited as Ref. 8. For all the transition channels a tetragonal phase is obtained by displacements of the Se atoms except for one of the channels of the star $\{k_8\}$, which has the greatest (a 16-fold) increase in the unit cell volume. In this last transition channel a tetragonal phase can be obtained by a displacement of both the Se and Zn atoms. What we have said above means that the transition to the tetragonal phase should occur with the formation of superstructure. For confirmation of this conclusion it will be necessary to do further detailed neutron-diffraction studies.

In considering the probable causes of the phase transition in the ZnSe crystal induced by such a low impurity concentration, we turn our attention to the Jahn–Teller effect and to the change in the value and position of the maximum of the charge density on the chemical bonds near the impurity.

The Jahn–Teller effect (see the review[9]) consists in a lifting of the degeneracy of the energy levels of $3d$ elements found originally in a high-symmetry environment. The degeneracy is lifted on account of local deformations of the crystal lattice which lower the symmetry. The Ni^{2+} ions substituting for Zn in the ZnSe crystal have an orbitally degenerate ground state $^3T_1$ in a tetrahedral environment.[10] This

state admits tetragonal distortions of the lattice owing to the interaction of $3d$ electrons of the nickel with acoustic phonons of E symmetry. Although the Jahn–Teller effect can lead to local distortions of the lattice, it is unclear how these distortions would propagate in the crystal, leading to the phase transition.

As a mechanism having longer range one might consider the redistribution of the charge density between an impurity center and the nearest-neighbor environment. This redistribution is manifested in a change in the position and value of the maximum of the charge density on the chemical bond, and this charge has a long-range influence in ionic–covalent crystals.[11] The redistribution of the charge on the bond can be tracked in the series Ge, GaAs, ZnSe, and CuBr. These substances have approximately equal bond lengths and, except for Ge, crystallize in a structure of the zinc blende type. In Ge the maximum of the charge density on the bond is largest and is equidistant from the ions, while in GaAs, ZnSe, and CuBr the maximum of the charge density decreases and is shifted toward the anion. Thus the given series corresponds to a decrease in covalence and an increase in ionicity from the covalent Ge to the most ionic substance in this series, CuBr. For this series of crystals with decreasing degree of covalence and increasing degree of ionicity there occurs a noticeable decrease in the elastic modulus of C_{44}: Ge–6.71, GaAs–5.92, ZnSe–4.91, CuBr–1.51 in units of 10^{11} dyn/cm^2. In ZnSe crystals the Ni impurity leads to an increase in the degree of ionicity of the bond at an impurity center, and at the same time below 100 K a softening of the constant C_{44} is observed experimentally. If it is assumed that these effects are related, then the softening of the elastic constant, the lattice instability caused by it, and the structural transition occurring at low temperatures are of an electronic nature.

CONCLUSION

On the basis of the data obtained we can state the following conclusions.

In ultrasonic experiments on ZnSe and ZnSe:Ni crystals with an impurity concentration of 5.5×10^{19} cm^{-3}, we have observed precursor phenomena at temperatures below 100 K, i.e., almost an order of magnitude higher than the temperature of the structural transition, $T_c=14.5$ K. We have established that the elastic constant C_{44} softens and C_{11} and C_{12} harden as T_c is approached from the high-temperature side; the strains associated with the order parameter are transverse strains of the ε_4 type. A symmetry analysis permits the conclusion that the transition to the tetragonal phase should occur with the formation of a superstructure. The Jahn–Teller effect and the displacement of the charge density on the chemical bonds are likely candidates for the cause of the low-temperature phase transition.

This study was done with the financial support of the Russian Foundation for Basic Research (Grant No. 04-02-96094-p2004 Ural_a).

*E-mail: gudkov@imp.uran.ru

[1] V. I. Sokolov, S. F. Dubinin, S. G. Teploukhov, V. D. Parkhomenko, A. T. Lonchakov, V. V. Gudkov, A. V. Tkach, I. V. Zhevstovskikh, and N. B. Gruzdev, Solid State Commun. **129**, 507 (2004).
[2] W. Rehwald, Adv. Phys. **22**, 721 (1973).
[3] V. V. Gudkov, Dep. VINITI, 22.08.90 No. 4741 [deposited ms., in Russian], *All-Union Institute of Scientific and Technical Information, Moscow (1990)*.
[4] *Physics of II–VI and I–VII Compounds, Semimagnetic Semiconductors*, Vol. 17b of Landolt-Börnstein Series, O. Madelung (ed.), Springer-Verlag, Berlin, Heidelberg (1982).
[5] B. Y. Lee, J. Appl. Phys. **41**, 2984 (1970).
[6] J. A. Garber and A. V. Granato, Phys. Rev. B **11**, 3990 (1975).
[7] O. V. Kovalev, *Irreducible Representations of Space Groups* [in Russian], Izd-vo Akad Nauk Ukr. SSR, Kiev (1961).
[8] Yu. A. Izyumov, V. E. Naĭsh, and R. P. Ozerov, *Neutron Diffractometry of Magnets* [in Russian], Atomizdat, Moscow (1981).
[9] M. D. Sturge, *The Jahn–Teller Effect in Solids*, Vol. 20 of Solid State Physics, Academic Press, London (1967).
[10] H. A. Weakliem, J. Chem. Phys. **36**, 2117 (1962).
[11] W. Weber, Phys. Rev. B **15**, 4789 (1977).

Translated by Steve Torstveot

Dynamics of the insulator–conductor transition initiated by high pressure in ammonium halides

G. V. Tikhomirova* and A. N. Babushkin

A. M. Gorky Ural State University, pr. Lenina 51, Ekaterinburg 620083, Russia
(Submitted June 1, 2004)
Fiz. Nizk. Temp. **30**, 1219–1224 (November 2004)

A comparative study is made of the influence of high pressures (15–50 GPa) on the conductance of the ammonium halides NH_4X (X=F, Cl, Br) at temperatures of 77 K and above. It is found that the application of high pressure induces a phase transition which is manifested in a sharp (jumplike) change in the resistance by several (more than three) orders of magnitude and is accompanied by hysteresis typical of a first-order phase transition. The values of the pressure P_{c1} correlate with the density of the material and are approximately 40, 27, and 15 GPa for NH_4F, NH_4Cl, and NH_4Br, respectively. The relaxation times of the resistance depend strongly on the pressure: in the transition region the relaxation time is increased significantly (from several hours to days). At pressures much higher than P_{c1} it is several minutes. © *2004 American Institute of Physics.* [DOI: 10.1063/1.1820024]

1. INTRODUCTION

Ammonium halides are analogous to transition metal halides, in which the structural transitions at high pressures and the accompanying changes of their optical and electrical properties, including the appearance of metal-like states, have been well studied.[1–4] In ammonium halides the role of the alkali metal is played by the $(NH_4)^+$ ion. The phase diagram of ammonium halides is a unique combination of the phases characterizing dynamic orientational disorder (phases I and II) and phases with different types of orientational ordering of the ammonium ions—''antiferromagnetic'' (phase III) and ''ferromagnetic'' (phase IV). The richness of the phase diagram and the series of features of the orientational phase transitions and lattice dynamics have been stimulating interest in the study of these materials (see, e.g., Ref. 5). Structural studies of these materials have been done at pressures up to 9 GPa.[6–8] Measurements of the conductance together with the data of structural and optical studies yield information about the onset and dynamics of the phase transitions and the changes in the electronic structure. A study of transport phenomena can provide substantial information about critical phenomena at high pressures.[9,10] The goal of the present work was to do a comparative study of the influence of high pressures (15–50 GPa) on the value and relaxation time of the conductance of the ammonium halides NH_4X (X=F, Cl, Br) at temperatures of 77 K and higher.

2. EXPERIMENTAL TECHNIQUE

The measurements were made in a high-pressure cell with diamond anvils of the ''rounded cone–plane'' type made from synthetic polycrystalline carbonado (black) diamonds.[11,12] These anvils are good conductors of electrical current and can be used as electrical contacts to the sample. The resistance of the short-circuited anvils is 7–12 Ω and varies weakly with temperature. The method of estimating the pressures with the use of data on the mechanical properties of the material being compressed and of the diamond and the geometry of the anvil has been tested on a large group of materials over a wide range of temperatures and pressures and is described in Refs. 3, 4, 13, and 14. The technique used allows one to study the same sample upon successive increase and decrease of pressure and also to hold the sample under load for a long time. The samples studied, obtained by compression in the high-pressure cell had a diameter of ~0.2 mm and a thickness of 10–30 μm. Measurements were made in the linear part of the current–voltage characteristic. The voltage across the samples was kept to 10 mV or less to avoid electric breakdown. Because the intrinsic resistance of the measurement circuit was around 100 MΩ, we measured samples with resistances of 10 MΩ or less. The temperature of the high-pressure cell was registered by a copper–Constantan thermocouple.

3. GENERAL FEATURES OF THE BEHAVIOR OF THE RESISTANCE OF AMMONIUM HALIDES UNDER HIGH PRESSURES

In all of the ammonium halides studied the resistance exhibited hysteresis as a function of pressure (Fig. 1). At low pressures the resistance of the investigated samples exceeded 10 MΩ. At a certain critical pressure P_{c2} the resistance of the ammonium halides studied decreased sharply (with a jump). During a subsequent lowering of the pressure the return to a state with high resistance is observed at a critical pressure $P_{c1}<P_{c2}$. [An analogous sharp (jumplike) transition is observed on the temperature dependence of the resistance R at pressures close to the critical (Fig. 2).] Hysteresis is also observed on the temperature dependence of the resistance. The size of the hysteresis loop of the resistance in pressure and temperature decreases with increasing number of compression–decompression cycles and/or increasing duration of the hold under pressure. This shows that a rather long high-pressure treatment of these ammonium halides is necessary in order for them to reach a stable state, and sometimes a static hold at a fixed pressure is insufficient, and several successive compression–decompression cycles are

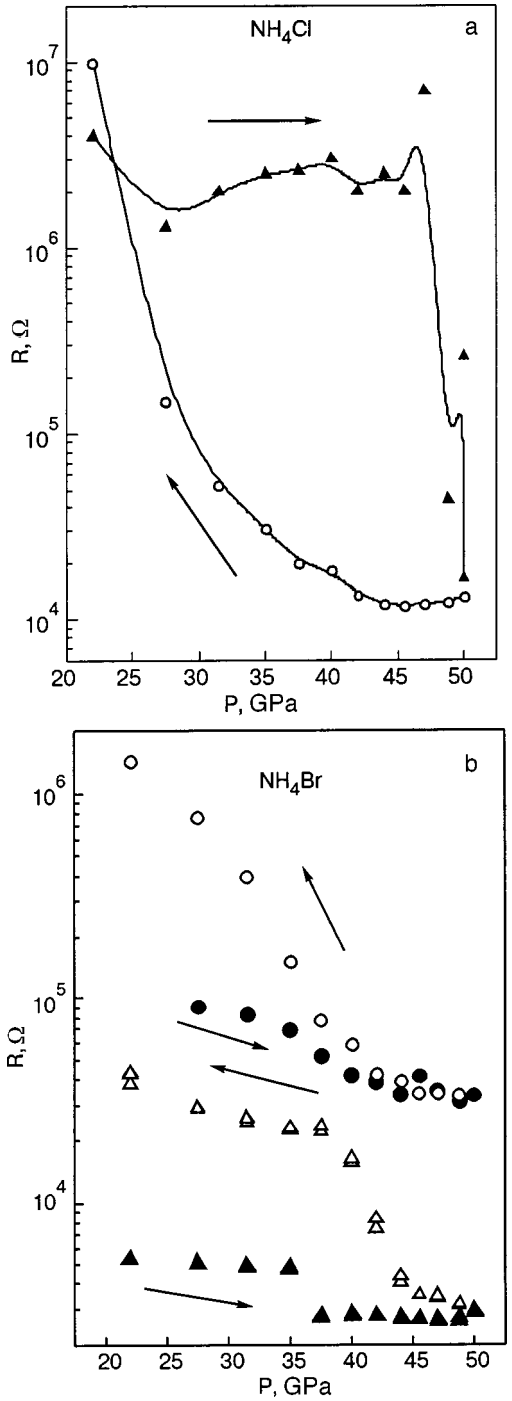

FIG. 1. Pressure dependence of the resistance of NH_4Cl (a) and NH_4Br (b) at room temperature: the circles are for the initial compression and decompression; the triangles are for after a long hold of the sample under pressure.

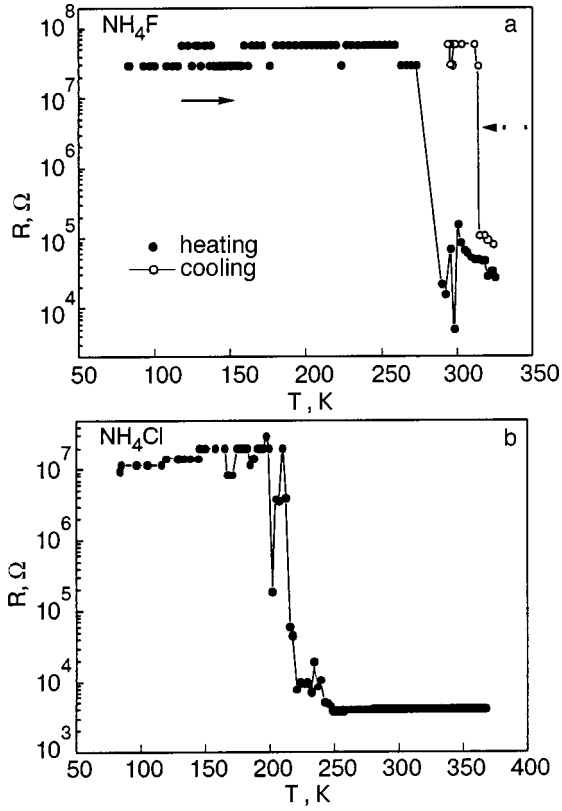

FIG. 2. Temperature dependence of the resistance of NH_4F at a pressure of 50 GPa (a) and of NH_4Cl at $P=27$ GPa (b).

necessary. A correlation is observed between the duration of the necessary preliminary pressure treatment and the density of the material (the atomic weight of the halogens F, Cl, and Br). The critical pressure of the transition between the insulator and low-resistance state in ammonium halides decreases with increasing atomic weight of the halogen.

It was found that the relaxation time of the electrical resistance of the samples upon a change in pressure depends on the applied pressure. Near the pressures of the transition from the low-resistance to the high-resistance (>100 MΩ) state the relaxation time increases substantially.

At pressures $P>P_{c1}$ (in the region of the conducting phase) the temperature dependence and pressure dependence of the resistance exhibit features indicative of the formation of intermediate states. All three ammonium halides at pressures above P_{c1} (after a preliminary hold under pressure) pass into a state characterized by growth of the resistance with temperature. Below we report the features of the behavior of the resistance in each of the three materials studied.

Ammonium fluoride

During the initial application of pressure at room temperature the NH_4F samples pass into a state with a resistance of less than 10^7 Ω only at $P=P_{c2}\approx 50$ GPa, and a prolonged hold (of the order of a month) under pressure is required for this. Figure 2a shows $R(T)$ for an NH_4F sample at a pressure $P=50$ GPa on heating and cooling. It is seen that for 77 K$<T<$270 K the resistance exceeds 30 MΩ. As the temperature is increased, the resistance decreases in a jump by at least three orders of magnitude. On subsequent cooling the sample again passes into the high-resistance state but at somewhat higher temperatures. An additional hold of the sample under a pressure of 50 GPa leads to further decrease of R (by tens of ohms). At pressures of ~ 40 GPa the NH_4F samples undergo a transition to a state with megohm resistance independently of the prehistory of the sample.

The temperature dependence of the resistance of NH_4F is characterized by the presence of hysteresis, which is due, as will be shown, to the long relaxation times. On heating the $R(T)$ curve has a metal-like character up to a certain critical temperature T_{c1}, after which the resistance remains practically unchanged. The critical temperature on cooling, T_{c2}, is practically constant. A long hold (for several weeks) under

pressure leads to vanishing of the hysteresis, and the conduction become metal-like in the entire temperature interval studied (see Ref. 5).

Ammonium chloride

On the initial application of pressure, samples of NH_4Cl undergo a transition to a state with a resistivity of less than $10^7\ \Omega$ only after a hold of the order of a week under a pressure of 50 GPa. In a hold at a lower pressure (44 GPa) the time necessary for transition of the sample to a state of high conductance increases to 17–20 days. It is because of the long time for relaxation to the steady-state conductance of NH_4Cl (just as for NH_4F) that it has not been possible to determine precisely the critical pressure P_{c2} at which the transition from the high-resistance (above $10^7\ \Omega$) to the conducting state occurs. The return to the high-resistance state on decreasing pressure occurs at $P_{c1} \approx 25-27$ GPa independently of the prehistory of the sample.

At pressures near the critical an analogous sharp (jumplike) transition is observed on the $R(T)$ curve of NH_4Cl samples (Fig. 2b). A jump in resistance by more than 3 orders of magnitude indicates the presence of a phase transition. The nonmonotonicities (jumps) of the resistance near the transition are due to the nonuniformity (polycrystalline structure) of the sample and are apparently due to processes of nonuniform compaction of the structure under pressure.

Thus the observed transition of NH_4Cl (like that of NH_4F) from the high-resistance to a low-resistance state upon application of pressure is accompanied by hysteresis typical of a first-order phase transition. The size of the hysteresis loop depends on the duration of the hold at different pressures and is evidently due to the long relaxation times of the conductance.

In the existence region of the conducting phase there exists a temperature hysteresis of the resistance that vanishes (as in the case of NH_4F) after a long hold of the sample under pressure. In the first compression–decompression cycles the temperature dependence of the resistance looks like activation. After a long (two-month) hold of the samples under pressure the temperature coefficient of the resistance changes sign.

When the pressure is reduced to values close to 27 GPa the form of the $R(T)$ curves changes noticeably. A common feature of those curves, independent of the duration of the preliminary pressure treatment, is a minimum of $R(T)$ at a certain critical temperature (see Figs. 3 and 4 of Ref. 15). Below that temperature the resistance obeys the law of activation, while at higher temperatures the temperature coefficient of the resistance is positive, i.e., one observes a ''semiconductor–metal'' transition.

The charge carrier density in the state with the positive temperature coefficient of resistance, estimated from measurements of the thermopower, does not exceed $10^{27}\ m^{-3}$, which is two orders of magnitude lower than the electron densities in metals. The sign of the thermopower remains unchanged in the region of metal-like conduction and indicates an n-type conductivity.

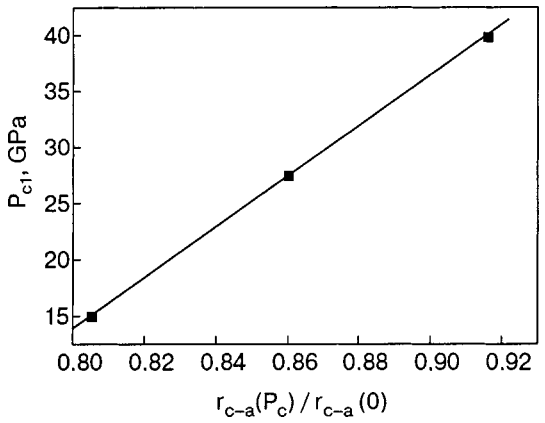

FIG. 3. Dependence of the critical pressure on the cation–anion distance.

Ammonium bromide

For ammonium bromide NH_4Br, unlike the fluoride and chloride, the resistance is already no higher than 1–2 MΩ at pressures $P \sim 15$ GPa. Figure 1b shows the results of a measurement of $R(P)$ in the first compression–decompression cycle (circles) and after a long hold of the sample at high pressure (triangles). It is seen that in the first cycle as the pressure is increased from 15 to 30 GPa the resistance decreases by at least 2 orders of magnitude. Upon further increase in pressure the resistance changes only slightly. After a long hold under pressure the $R(P)$ curve displays a feature at $P \sim 40$ GPa, indicating the formation of a new state of the sample.

We note that the resistance of NH_4Br is larger on decreasing pressure than on increasing pressure, i.e., the effect is opposite to that observed in NH_4F and NH_4Cl. All the pressure curves of the resistance of NH_4Br characteristically exhibit a decrease in the width of the hysteresis loop for $P > 40$ GPa and a noticeable increase of R at lower pressures.

As to the pressures P_{c1} and P_{c2} of the transition between the high-resistance and low-resistance states, it is clear that P_{c1} lies below the lower boundary of our measurements, 15 GPa. The pressure P_{c2} could not be determined because of the sharp growth in the relaxation time of the resistance in the pressure interval 15–22 GPa.

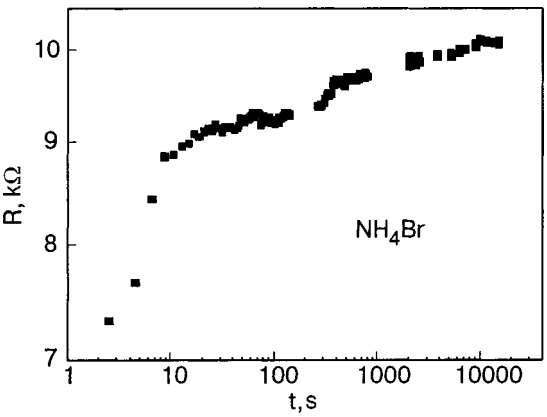

FIG. 4. Variation of the resistance of NH_4Br with time after a lowering of the pressure from 27 to 22 GPa.

The $R(T)$ curves of NH_4Br have a positive temperature coefficient of resistance at 77–300 K. At pressures of 40–44 GPa one observes features indicating the transition of the sample to a different state. We note that both the temperature dependence and pressure dependence of the conductance of ammonium bromide differ substantially from those for the other ammonium halides. Similar features have been observed previously for other alkali metal bromides as well.[2]

The foregoing results show that all the ammonium halides studied exhibit a phase transition between states with high and low resistance. Figure 3 shows the dependence of the critical pressure P_{c1} on the cation–anion distance r_{c-a} at the corresponding pressure. This distance was calculated from the universal equation of state of Schlosser, Ferrante, and Vinet [formula (2.44) in Ref. 16], which gives the dependence of the relative volume V/V_0 on P. The cation–anion distance r_{c-a} is assumed equal to $(V/V_0)^{1/3}$. The dependence $r_{c-a}(P_c)$ turns out to be linear, which shows that these are all transitions of the same type.

4. RELAXATION OF THE CONDUCTANCE IN AMMONIUM HALIDES

The main difficulty in the the measurements of the resistance of ammonium halides as a function of pressure or temperature is the presence of long relaxation times. Unless this circumstance is taken into account the results of measurements can be strongly distorted. The long-term relaxation of the resistance is especially important near the critical pressures.

The relaxation of the resistance near the transition from the high-resistance to the low-resistance state is characterized, as a rule, by two times. Figure 4 shows the dynamics of the change in the resistance of an NH_4Br sample in the time following a lowering of the pressure from 27 to 22 GPa. It is seen that the change in resistance occurs with two markedly different times. The short time amounts to a few seconds, while the long time is a number of hours (or even days). The long time can vary depending on the duration of a preliminary hold of the sample under pressure and the value of the applied pressure (on by how much the applied pressure exceeds the critical pressure). At pressures considerably higher than P_{c1} the relaxation time amounts to several minutes.

At pressures much higher than P_{c1} the relaxation of the conductance of NH_4Cl and NH_4Br obeys an exponential law of the form

$$R(t)=R_s+A\exp(-t/\tau),$$

where $R(t)$ is the resistance at time t, R_s is the steady-state value of the resistance, τ is the characteristic relaxation time, and A is a coefficient.

When the critical pressure is approached, the relaxation of the resistance becomes essentially nonexponential and nonmonotonic (Fig. 5).

Figure 6 shows the pressure dependence of the relaxation time of the conductance τ for NH_4Cl and NH_4Br. It is seen that at pressures near P_{c1} the relaxation time increases noticeably. The $\tau(P)$ curve for ammonium bromide also displays a feature near 40 GPa, which correlates with the features on the pressure dependence and temperature dependence of the resistance.

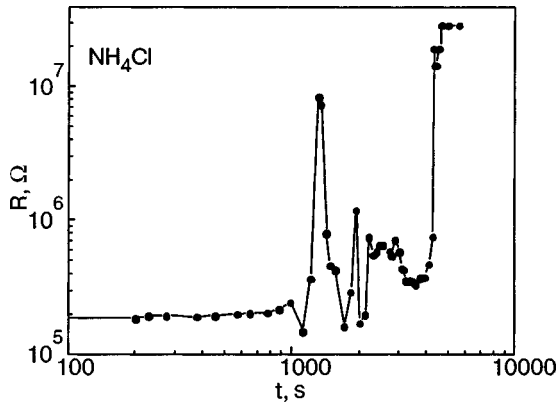

FIG. 5. Variation of the resistance of NH_4Cl with time after a lowering of the pressure from 35 to 27.5 GPa.

5. CONCLUSION

The ammonium halides NH_4X (X=F, Cl, Br) have a phase transition at high pressure. The transition is manifested in a sharp (jumplike) change in resistance by several (more than three) orders of magnitude, and the resistance exhibits hysteresis typical of a first-order phase transition. The values of P_{c1} correlate with the density of the material (with the cation–anion distance) and are 40, 25–27, and 15 GPa for NH_4F, NH_4Cl, and NH_4Br, respectively. An analogous jumplike transition is observed on the temperature dependence of the resistance at pressures near the critical. The relaxation

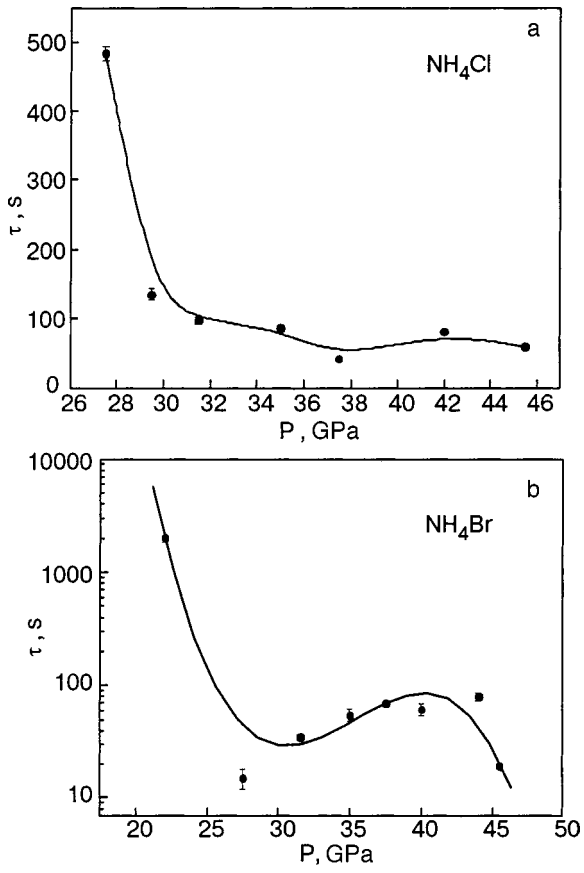

FIG. 6. Pressure dependence of the relaxation time of the conductance to a steady state after the pressure is lowered for samples of NH_4Cl (a) and NH_4Br (b).

time of the resistance depends substantially on the pressure: in the transition region the relaxation time increases strongly (up to a few hours to days). At pressures significantly higher than P_{c1} it amounts to several minutes.

The nonmonotonicity of $R(T)$, which decreases with increasing time of a preliminary hold under pressure, indicates the existence of intermediate (metastable) states. Like alkali metal halides, all of the ammonium halides studied, when subjected to pressures above P_{c1} and a certain hold under pressure, exhibit a transition to a state characterized by growth of the resistance with temperature.

This study was supported in part by a grant from the Russian Foundation for Basic Research–Ural No. 01-03-96494 and the program ''Basic Research and Higher Education'' (Grant No. EK-005-X1) funded by the U.S. Civilian Research and Development Foundation (CRDF), the Ministry of Education of the Russian Federation, and the Administration of the Sverdlovsk Region under the auspices of the Ural Research and Education Center for Advanced Materials.

*E-mail: Galina.Tikhomirova@usu.ru

[1] L. F. Vereschagin, E. N. Yakovlev, and B. V. Vinogradov, JETP Lett. **20**, 540 (1975).
[2] A. N. Babushkin and G. V. Babushkina, Fiz. Khim. Obrab. Mater. **3**, 19 (1996).
[3] A. N. Babushkin, G. V. Babushkina, and O. A. Ignatchenko, in *Proceedings of IHPS3*, Warsaw, September 13–16, 1999, W. Lojkowski (ed.), J. High Pressure School **1**, 32 (1999).
[4] Ya. Yu. Volkova, G. V. Babushkina, and A. N. Babushkin, *Metastable States and Phase Transitions* [in Russian], Collected Scientific Works of the Institute of Thermal Physics of the Urals Division of the Russian Academy of Sciences, issue 5, 198 (2001).
[5] N. G. Parsonage and L. A. Staveley, *Disorder in Crystals*, Oxford University Press (1979), Mir, Moscow (1982).
[6] A. M. Heyns, K. R. Hirsh, and W. P. Holzapfel, J. Chem. Phys. **73**, 105 (1980).
[7] A. M. Balagurov, D. P. Kozlenko, B. N. Savenko, V. P. Glazkov, and V. A. Somenkov, Fiz. Tverd. Tela (St. Petersburg) **40**, 142 (1998) [Phys. Solid State **40**, 127 (1998)].
[8] A. M. Balagurov, B. N. Savenko, D. P. Kozlenko, V. P. Glazkov, V. A. Somenkov, and S. Hull, Physica **265**, 92 (1999).
[9] W. Paul and D. M. Warschauer (eds.), *Solids under Pressure*, McGraw-Hill, New York (1963), Mir, Moscow (1966).
[10] V. V. Shchennikov, Fiz. Met. Metalloved. **67**, 93 (1989).
[11] L. F. Vereshchagin, E. N. Yakovlev, T. N. Stepanov, K. Kh. Bibaev, and B. V. Vinogradov, JETP Lett. **16**, 169 (1972).
[12] L. F. Vereschagin, E. N. Yakovlev, B. V. Vinogradov, G. N. Stepanov, K. Kh. Bibaev, T. J. Alaeva, and V. P. Sakun, High Temp. - High Press. **6**, 99 (1974).
[13] A. N. Babushkin, G. I. Pilipenko, and F. F. Gavrilov, J. Phys.: Condens. Matter **5**, 8659 (1993).
[14] A. N. Babushkin, Y. A. Kandrina, O. L. Kobeleva, S. N. Schkerin, and Y. Y. Volkova, in *Frontiers of High Pressure Research II: Application of High Pressure to Low-Dimensional Novel Electronic Materials*, H. D. Hochheimer, B. Kuchta, P. K. Dorhout, and J. L. Yarger (eds.), Kluwer Acad. Publ., Dordrecht–New York–London (2001), p. 131.
[15] G. V. Tikhomirova and A. N. Babushkin, Defect and Diffusion Forum **208–209**, 271 (2002).
[16] S. S. Batsanov, *Structural Chemistry. Facts and Relationships* [in Russian], Dialog-MGU, Moscow (2000).

Translated by Steve Torstveit

Statistical strained-tetrahedron model of local ternary zinc blende crystal structures

B. V. Robouch*

Laboratori Nazionali di Frascati INFN, DAFNE-L, C.P.:13, 00044 Frascati (RM), Italy

E. M. Sheregii

Institute of Physics, Rzeszow University, Rejtana 16A, 35-310 Rzeszow, Poland

A. Kisiel

Instytut Fizyki, Universytet Jagiellonski, Reymonta 4, 30-059 Krakow, Poland

(Submitted June 1, 2004)
Fiz. Nizk. Temp. **30**, 1225–1234 (November 2004)

The statistical strained-tetrahedron model was developed to overcome two common assumptions of previous models: 1) a rigid undistorted ion sublattice of regular tetrahedra throughout all five configurations, and 2) a random ion distribution. These simplifying assumptions restrict the range of applicability of the models to a narrow subset of ternary alloys for which the constituent binaries have equal or quasi-equal values of their lattice constants and standard molar enthalpies of formation ($\Delta_f H_0$). Beyond these limits the predictions of such models become unreliable, in particular, when the ternary exhibits site occupation preferences. The strained-tetrahedron model, free from rigidity and stochastic limitations, was developed to better describe and understand the local structure of ternary zinc blende crystals, and interpret experimental EXAFS and far-IR spectra. It considers five tetrahedron configurations with the shape and size distortions characteristic of ternary zinc blende alloys, allows nonrandom distributions and, hence, site occupation preferences, conserves coordination numbers, respects stoichiometry, and assumes that next-neighbor values determine preferences beyond next-neighbor. The configuration probabilities have three degrees of freedom. The nineteen inter-ion crystal distances are constrained by tetrahedron structures; to avoid destructive stresses, we assume that the average tetrahedron volumes of both sublattices relax to equal values. The number of distance free-parameters $\leqslant 7$. Model estimates, compared to published EXAFS results, validate the model. Knowing the configuration probabilities, one writes the dielectric function for far-infrared absorption or reflection spectra. Constraining assumptions restrict the number of degrees of freedom. Deconvolution of the experimental spectra yields values of the site occupation preference coefficient and/or the specific oscillator strengths. Validation again confirms the model. [DOI: 10.1063/1.1820025]

1. INTRODUCTION

The abundance of articles in the literature devoted to sphalerite (zinc blende) ternary semiconductors is ample evidence of the interest paid to them. In the hope of better understanding their local structure, we considered the interpretation of extended x-ray absorption fine structure (EXAFS) (see theoretical considerations[1,2] since 1981) and vibrational spectra observed in the far-infrared region (FIR spectra).

EXAFS was applied soon after[3,4] with, alas, no review paper covering the abundant literature devoted to it. For literature on the FIR spectra, see, for instance, the review articles[5–7] and book.[8] With that aim we developed the statistical strained-tetrahedron model, validating it on published EXAFS zinc blende data[9,10] and, after an adaptation, on intermetallide materials.[11] The model was then extended to describe and interpret FIR spectra.[12]

We propose to briefly recall here the model developed and its validation and then to dwell more on FIR-spectrum interpretation, applicability, and limits.

2. THE STATISTICAL STRAINED-TETRAHEDRON MODEL

To create any model, one has to 1) describe as closely as possible the object under study, using proper parameters for that; 2) reduce the set of these parameters through motivated constraints to determine the minimum number of degrees of freedom/parameters; 3) check the model-predicted values against experimental ones; 4) consequently, discard the model or retain it as valid depending on the reproducibility thus obtained. With this in mind we recall our modeling.

2.1. The object under study

Zinc blende fcc structures are tetrahedrally coordinated, characterized by a central ion surrounded by four nearest-neighbor (NN) ions (first shell) defining the four vertices of a tetrahedron, and 12 next-nearest-neighbor (NNN) ions (second shell). Binary compounds AZ (we use A, B, ... for cations, and Z, Y, ... for anions), have their successive shells alternately fully filled by A then Z ions. All tetrahedra are symmetric, regular, and identical; thus, by simple trigonometry, equal interbond angles $\alpha(\mathrm{A{:}Z{:}A}) = \alpha(\mathrm{B{:}Z{:}A})$

TABLE Ia. NNN SOP-coefficients in terms of NN SOPs: All possible NNN distributions and resulting SOP-coefficients for ternary. $0 \leqslant 0 \leqslant \{W_k\}_{k=1,3} \leqslant 4/k$, while $W_0 = W_4 = 1$. Zinc blende $A_{1-x}B_xZ$ with a B or A as central ion.[9]

k	All 12 possible NNN B-ion fills of the 4 tetrahedra	Resulting B-weights ${}^{B}w^{[12]}_{k} = \Sigma_{j=0,4}\{{}^{B}M_{j,k} W^{[4]}_{j}\}$	Resulting A-weights ${}^{A}w^{[12]}_{k} = \Sigma_{j=0,4}\{{}^{A}M_{j,k} W^{[4]}_{j}\}$
0	0 0 0 0	W_1	$W_0 = 1$
1	0 0 0 1	$(3W_1 + W_2)/4$	$(3W_0 + W_1)/4$
2	0 0 0 2/0 0 1 1	$(5W_1 + 2W_2 + W_3)/8$	$(5W_0 + 2W_1 + W_2)/8$
3	0 0 0 3/0 0 1 2/0 1 1 1	$(6W_1 + 4W_2 + W_3 + W_4)/12$	$(6W_0 + 4W_1 + W_2 + W_3)/12$
4	0 0 1 3/0 0 2 2/0 1 1 2/1 1 1 1	$(5W_1 + 7W_2 + 3W_3 + W_4)/16$	$(5W_0 + 7W_1 + 3W_2 + W_3)/16$
5	0 0 2 3/0 1 1 3/0 1 2 2	$(4W_1 + 3W_2 + 3W_3 + 2W_4)/12$	$(4W_0 + 3W_1 + 3W_2 + 2W_3)/12$
6	0 0 3 3/0 1 2 3/1 1 1 3/0 2 2 2/1 1 2 2	$(4W_1 + 6W_2 + 6W_3 + 4W_4)/20$	$(4W_0 + 6W_1 + 6W_2 + 4W_3)/20$
7	0 1 3 3/0 2 2 3/1 1 2 3	$(2W_1 + 3W_2 + 3W_3 + 4W_4)/12$	$(2W_0 + 3W_1 + 3W_2 + 4W_3)/12$
8	0 2 3 3/1 2 2 3/1 1 3 3/2 2 2 2	$(W_1 + 3W_2 + 7W_3 + 5W_4)/16$	$(W_0 + 3W_1 + 7W_2 + 5W_3)/16$
9	0 3 3 3/1 2 3 3/2 2 2 3	$(W_1 + W_2 + 4W_3 + 6W_4)/12$	$(W_0 + W_1 + 4W_2 + 6W_3)/12$
10	1 3 3 3/2 2 3 3	$(W_2 + 2W_3 + 5W_4)/8$	$(W_1 + 2W_2 + 5W_3)/8$
11	2 3 3 3	$(W_3 + 3W_4)/4$	$(W_2 + 3W_3)/4$
12	3 3 3 3	$W_4 = 1$	W_3

TABLE Ib. Intermetallides $M_3(XX')_1$ around X or X′.[11]

	$\{{}^{X}w_k = \Sigma_{j=0,4}\, {}^{X}M_{kj} W_j\}_{k=0,6}$
${}^{X}w_0 =$	$\frac{1}{3}W_1 + \frac{2}{3}W_2$
${}^{X}w_1 =$	$\frac{10}{36}W_1 + \frac{23}{36}W_2 + \frac{3}{36}W_3$
${}^{X}w_2 =$	$\frac{16}{72}W_1 + \frac{41}{72}W_2 + \frac{13}{72}W_3 + \frac{2}{72}W_4$
${}^{X}w_3 =$	$\frac{6}{36}W_1 + \frac{15}{36}W_2 + \frac{11}{36}W_3 + \frac{4}{36}W_4$
${}^{X}w_4 =$	$\frac{2}{72}W_1 + \frac{13}{72}W_2 + \frac{41}{72}W_3 + \frac{16}{72}W_4$
${}^{X}w_5 =$	$\frac{3}{36}W_2 + \frac{23}{36}W_3 + \frac{10}{36}W_4$
${}^{X}w_6 =$	$+\frac{2}{3}W_3 + \frac{1}{3}W_4$

	$\{{}^{X'}w_k = \Sigma_{j=0,4}\, {}^{X'}M_{kj} W_j\}_{k=0,6}$
${}^{X'}w_0 =$	$\frac{1}{3}W_0 + \frac{2}{3}W_1$
${}^{X'}w_1 =$	$\frac{10}{36}W_0 + \frac{23}{36}W_1 + \frac{3}{36}W_2$
${}^{X'}w_2 =$	$\frac{16}{72}W_0 + \frac{41}{72}W_1 + \frac{13}{72}W_2 + \frac{2}{72}W_3$
${}^{X'}w_3 =$	$\frac{6}{36}W_0 + \frac{15}{36}W_1 + \frac{11}{36}W_2 + \frac{4}{36}W_3$
${}^{X'}w_4 =$	$\frac{2}{72}W_0 + \frac{13}{72}W_1 + \frac{41}{72}W_2 + \frac{16}{72}W_3$
${}^{X'}w_5 =$	$\frac{3}{36}W_1 + \frac{23}{36}W_2 + \frac{10}{36}W_3$
${}^{X'}w_6 =$	$+\frac{2}{3}W_2 + \frac{1}{3}W_3$

$= 109.47°$, and the inter-ion distances (${}^{ij}d$) are defined in terms of the lattice constant a (known from x-ray diffraction analysis): ${}^{AZ}d = 3^{1/2}a/4$, ${}^{AA}d = {}^{ZZ}d = a/2^{1/2}$.

For ternary $A_{1-x}B_xZ$ (or AY_yZ_{1-y}), in the binary compound AZ, cations A are partially substituted by B ions. This, leads to five different elementary tetrahedra $\{T_k\}_{k=0,4}$ where the subscript k indicates the number of B ions at the vertices of the tetrahedron, with $(4-k)$ A-ions [T_0(Z:^{4}A), T_1(Z:^{3}A+^{1}B), T_2(Z:^{2}A+^{2}B), T_3(Z:^{1}A+^{3}B), T_4(Z:^{4}B).] Prior to ours, simulations had considered the five $\{T_k\}_{k=0,4}$ tetrahedra as externally rigid with the central ion free to be displaced. The ion distribution fillings (k B-ions into a shell with N sites, from relative contents x and $1-x$) were assumed stochastic and defined by the random Bernoulli binomial polynomials

$$p_k^{[N]}(x) = N!/[k!(N-k)!]x^k(1-x)^{N-k} \quad \text{with} \quad k = 0, ..., N.$$

Thus around a central Z ion the first shell four A/B ions are described by $p_k^{[4]}(x)$, while the second shell contains twelve Z ions! On the other hand, around an A or B ion, the first shell contains four Z ions, while the second-shell distribution of the twelve ions A/B is described by $p_k^{[12]}(x)$. This allows approximate evaluations, avoiding analytical difficulties.

However, to assume a stochastic filling with ions A and B around Z means that the Z-ion preference for either is the same. Thermodynamically this implies that the enthalpies of formation of AZ and BZ pairs are identical. But we are aware that in nature equality is the exception that confirms the rule of inequality. Indeed, the standard molar enthalpies of formation of binaries, $\Delta_f H_0$, kJ/mol, are generally different. That is why the stochastic approach is unable to describe the site occupation preferences (SOPs) reported experimentally!

2.2. Statistical strained-tetrahedron model assumptions

We build our model discarding both restrictions: 1) deviating from stochastic filling of ions, and 2) freeing the tetrahedra of the unnatural constraint of rigidity.

The price for such a more general model is the number of parameters needed to describe the crystal structure. But as we shall demonstrate, realistic assumptions (checked at the end) reduce the degrees of freedom to an acceptable value.

To quantify results departing from stochastic distribution, we attribute to each Bernoulli binomial a SOP weight coefficient. This leads to five NN terms $W_k\, p_k^{[4]}(x)$, thirteen NNN terms ${}^{A}w_k\, p_k^{[12]}(x)$ (for central A ions), and thirteen ${}^{B}w_k\, p_k^{[12]}(x)$ terms (for central B ions), a total of 31 parameters! Fortunately it is the Z ion that determines the choices,

and we claim that *all* higher shell fillings are determined by linear expressions of the five NN SOP coefficients $\{W_k\}_{k=0,4}$. But binary tetrahedron configurations T_0, T_4 have *no* preferences. Thus $W_0=W_4\equiv 1$ (!) and we are left with only $\{W_1,W_2,W_3\}$.

The probabilities of finding B and A ions in a configuration T_k are proportional to $\{kW_k\}_{k=0,4}$ and to $\{4-kW_k\}_{k=0,4}$, respectively (conservation of coordination numbers). As probabilities cannot be negative, we have $0\leqslant W_k\leqslant 4/k$. There are thus only *three* bounded free parameters $\{W_1,W_2,W_3\}$.

Expressions $\{{}^{A}w_k\}_{k=0,12}$, $\{{}^{B}w_k\}_{k=0,12}$ for the NNN shell, are determined by combinatorial probabilities in terms of those around the Z ions of the NN shell. This hypothesis leads for the zinc blende structure, to the linear expressions of the NNN SOP coefficients ${}^{A}w_k$ and ${}^{B}w_k$ as functions of the three W_k's given in Table Ia.[9] To illustrate that the assumption is general and applies to other crystal structures also, the expressions for intermetalides $M_3(X_{1-x}X'_x)_1$ are given in Table Ib.[11]

A random integer ion distribution (k and $4-k$) fully respects stoichiometry. With SOP coefficients $W_k\neq 1$ the situation departs from stochastic equilibrium, with a consequent attenuation of the ternary configuration populations caused by the observed scarcity of one of the two ion populations

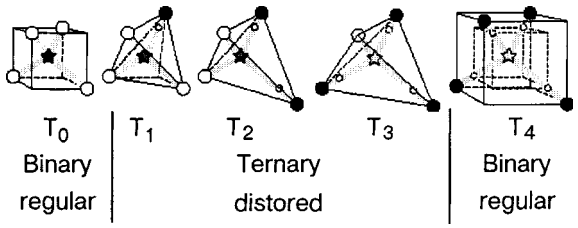

FIG. 1. Aspect of the five elementary tetrahedron configurations $\{T_k\}_{k=0,4}$ of $A_{1-x}B_xZ$ (or AY_yZ_{1-y}) ternary alloys.[9] Small open circles indicate the would-be ion positions as per the rigid tetrahedron hypothesis.

$$\{P_k^{[4]}(x)=C_k p_k^{[4]}(x)\}_{k=1,3} \text{ for ternary } T_k$$

with $\{C_k(W_k)\}_{k=1,3}$, corrective weight factors imposed by stoichiometry

$$0\leqslant\{C_k=\min[W_k,1,(4-kW_k)/(4-k)]\}_{k=1,3}\leqslant 1$$

$W_k<1$ enhances the binary AZ populations and $W_k>1$ that of binary BZ, i.e.

$$P_0^{[4]}(x)=p_0^{[4]}(x)+\sum_{k=1,3}\{\max(0,1-W_k)p_k^{[4]}(x)\}$$

for binary AZ configuration T_0,

TABLE II. Expressions of average pair coordinations $\langle {}^{ij}\mathrm{CN}(x)\rangle$ and distances $\langle {}^{i:j}d(x)\rangle$, as a function of x, for any two-ion pair $i{:}j=\{$AZ, BZ, BB, BA, AA, ZAZ, ZBZ$\}$ of zinc blende $A_{1-x}B_xZ$ ternary.[9]

Average	Coordination numbers for NN ion pairs AZ, BZ
$\langle {}^{BZ}\mathrm{CN}(x)\rangle =$	$\Sigma_{k=0,4}\{\, kW_k\ p^{[4]}{}_k(x)\}$
$\langle {}^{AZ}\mathrm{CN}(x)\rangle =$	$\Sigma_{k=0,4}\{(4-kW_k)p^{[4]}{}_k(x)\} = 4-\langle {}^{BZ}\mathrm{CN}(x)\rangle$
	For NNN ion pairs BB, BA, AA
$\langle {}^{BB}\mathrm{CN}(x)\rangle =$	$\Sigma_{k=0,12}\{k\ {}^{B}w_k\ p^{[12]}{}_k(x)\}$
$\langle {}^{AB}\mathrm{CN}(x)\rangle =$	$\Sigma_{k=0,12}\{k\ {}^{A}w_k\ p^{[12]}{}_k(x)\}$
$\langle {}^{AA}\mathrm{CN}(x)\rangle =$	$12-\langle {}^{AB}\mathrm{CN}(x)\rangle =\Sigma_{k=0,12}\{(12-k\ {}^{A}w_k)\ p^{[12]}{}_k(x)\}$
$\langle {}^{BA}\mathrm{CN}(x)\rangle =$	$12-\langle {}^{BB}\mathrm{CN}(x)\rangle = \Sigma_{k=0,12}\{(12-k\ {}^{B}w_k)\ p^{[12]}{}_k(x)\}$
$\langle {}^{ZBZ}\mathrm{CN}(x)\rangle =$	$\Sigma_{k=0,4}\{3\ k\ W_k\ p^{[4]}{}_k(x)\} = 3\langle {}^{BZ}\mathrm{CN}(x)\rangle$
$\langle {}^{ZAZ}\mathrm{CN}(x)\rangle =$	$\Sigma_{k=0,4}\{3\ (4-kW_k)\ p^{[4]}{}_k(x)\} = 3\langle {}^{AZ}\mathrm{CN}(x)\rangle$
Average	Distances for NN ion pairs AZ, BZ
$\langle {}^{BZ}d(x)\rangle =$	$\{\Sigma_{k=1,4}\{k\ C_k\ {}^{BZ}d_k + 4\ \mathrm{Max}\ [0,\ k(W_k-1)/(4-k)]\ {}^{BZ}d_4\}\ p^{[4]}{}_k(x)\}$ / $\{\Sigma_{k=1,4}\{k\ C_k + 4\ \mathrm{Max}\ [0,\ k(W_k-1)/(4-k)]\}\ p^{[4]}{}_k(x)\}$
$\langle {}^{AZ}d(x)\rangle =$	$\{\Sigma_{k=0,3}\{(4-k\ C_k)\ {}^{AZ}d_k + 4\ \mathrm{Max}\ [0,(1-W_k)]\ {}^{AZ}d_0\}\ p^{[4]}{}_k(x)\}$ / $\{\Sigma_{k=0,3}\{(4-k\ C_k) + 4\ \mathrm{Max}\ [0,(1-W_k)]\}\ p^{[4]}{}_k(x)\}$
	For NNN ion pairs Z:A:Z or Z:B:Z
$\langle {}^{ZBZ}d(x)\rangle =$	$\{\Sigma_{k=1,4}\{k\ C_k\ {}^{ZBZ}d_k + 4\ \mathrm{Max}\ [0,\ k(W_k-1)/(4-k)]\ {}^{ZBZ}d_4\}\ p^{[4]}{}_k(x)\}$ / $\{\Sigma_{k=1,4}\{k\ C_k + 4\ \mathrm{Max}\ [0,\ k(W_k-1)/(4-k)]\}\ p^{[4]}{}_k(x)\}$
$\langle {}^{ZAZ}d(x)\rangle =$	$\{\Sigma_{k=0,3}\{(4-k\ C_k)\ {}^{ZAZ}d_k + 4\ \mathrm{Max}\ [0,(1-W_k)]\ {}^{ZAZ}d_0\}\ p^{[4]}{}_k(x)\}$ / $\{\Sigma_{k=0,3}\{(4-k\ C_k) + 4\ \mathrm{Max}\ [0,(1-W_k)]\}\ p^{[4]}{}_k(x)\}$

TABLE III. $GaAs_xP_{1-x}$ complete set: determined SOP coefficients, distances, angles and volumes for all five elementary configuration tetrahedra. Eleven fit parameters (bold) [3 SOP+8 distance (PGaP NNN data not reported)] to check VRC. Thirty-seven available experimental points from a set of 16 measurements.[9]

Configurations	T_0	T_1	T_2	T_3	T_4
k	0	1	2	3	4
W_k	1	**0.93**	**1.15**	**1.07**	1
^{BZ}d [Å]	–	**2.42**	**2.43**	**2.44**	2.450
^{AZ}d	2.359	**2.37**	**2.37**	**2.38**	–
^{BZB}d	–	–	**3.90**	**3.90**	4.001
^{AZA}d	3.852	3.88	3.98	–	–
^{BZA}d	–	3.91	3.90	3.99	–
^{ZBZ}d	–	3.95	3.97	3.98	4.001
^{ZAZ}d	3.852	3.87	3.87	3.89	–
α(B:Z:B) [deg]	–	–	106.7	106.9	109.47
α(A:Z:A)	109.47	109.7	114.3	–	–
α(B:Z:A)	–	109.3	107.36	112.0	–
$<Vol_{B.centred}>$ [Å^3]	–	7.28	7.37	7.41	7.55
$<Vol_{A.centred}>$	6.74	6.84	6.86	6.91	–
$<Vol_{Z.sublattice}>$	6.74	6.95	7.12	7.29	7.55
$<Vol_{Z.centred}>$	6.74	6.95	7.07	7.28	7.55
|Difference| [%]	0.0	0.1	0.1	0.2	0.0

$$P_4^{[4]}(x)=p_4^{[4]}(x)+\sum_{k=1,3}\{\max(0,\ k(W_k-1)/(4-k))p_k(x)\}$$

for binary BZ configuration T_4. (1)

In the random case, when $\{W_k\equiv 1\}_{k=1,3}$, $\{P_k(x)\rightarrow p_k(x)\}_{k=0,4}$.

Note, however, that even if the SOPs enhance the two binary populations with respect to corresponding populations of the random case, it by no means leads to clustering, since the spatial distribution remains perfectly stochastic.

Ion-pair and configuration populations are *now* determined with due account of the SOPs. This allows us to interpret local crystal structures.

We have five tetrahedra freed from any constraint, two of which (T_0 and T_4) are binary, regular, different sized, and well defined (as remarked above), and three (T_1, T_2, and T_3) ternary and distorted (strained tetrahedra), with *nineteen* unequal interionic distance parameters ^{ij}d and, consequently, altered interbond angles (see Fig. 1, taken from Ref. 9). The geometrical symmetry of each configuration T_k yields three constraints each, which reduces the number of independent distance parameters from nineteen to *ten*.

Material strength considerations lead us, to avoid destructive intercrystal stresses, to impose the condition that the average tetrahedron volume of the four vertex tetrahedra be equal to the central one (one constraint per configuration), leaving us with only $(10-3)=7$ distance parameters, while for SOP extreme values, configurations disappear, and their distances become virtual, i.e., $\leqslant 7$.

Indeed $\leqslant$, as for extreme SOP values configurations disappear, and their distances become virtual!

On the basis of the above probabilities, expressions for the average pair coordination $\langle^{i:j}\mathrm{CN}(x)\rangle$ and distances $\langle^{i:j}d(x)\rangle$ as functions of x, for any two-ion pair $i:j=\{\mathrm{AZ, BZ, BB, BA, AA, ZAZ, ZBZ}\}$ of zinc blende ternary alloys $A_{1-x}B_xZ$ are given in Table II.[9]

On the basis of these, deconvolving a given set of EXAFS data such as $GaAs_yP_{1-y}$ (Ref. 13), one obtains the dimensions of all the elementary tetrahedra involved: the inter-ion distances and angles (see Table III).

Having defined a $31+19$ parameter model and identified the relative constraint relations, we have reduced the problem to $3+7$ independent parameters. The model is ready for confrontation of its estimations with experimental data.

2.3. Model verification

To confirm the validity of the model and its assumptions, we checked the quality of the model with its restricted free parameters.

1. Comparing the experimental distance-EXAFS points and error bars reported in the literature with model fit curves

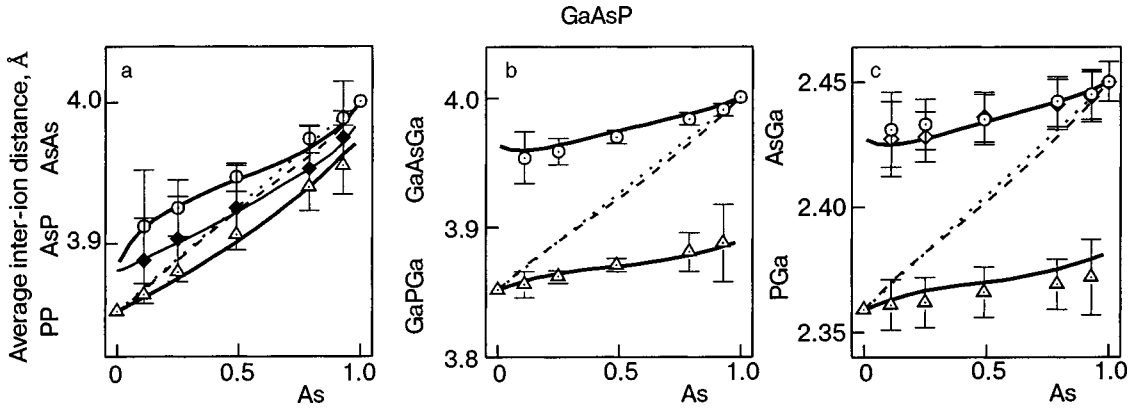

FIG. 2. Average inter-ion distances, Å, as a function of relative content x for $GaAs_xP_{1-x}$ (Ref. 13) comparison of model best fit curves versus reported experimental data. Points are (circles) for As-related (top curves), (triangles) for P-related (bottom curves), and (diamond) for mixed AsP ion distances. Linear combination of weighted average distances (LCWAD) curves (thin dashed lines) and corresponding reference Vegard law lines (thin dotted) are all reported in Ref. 9.

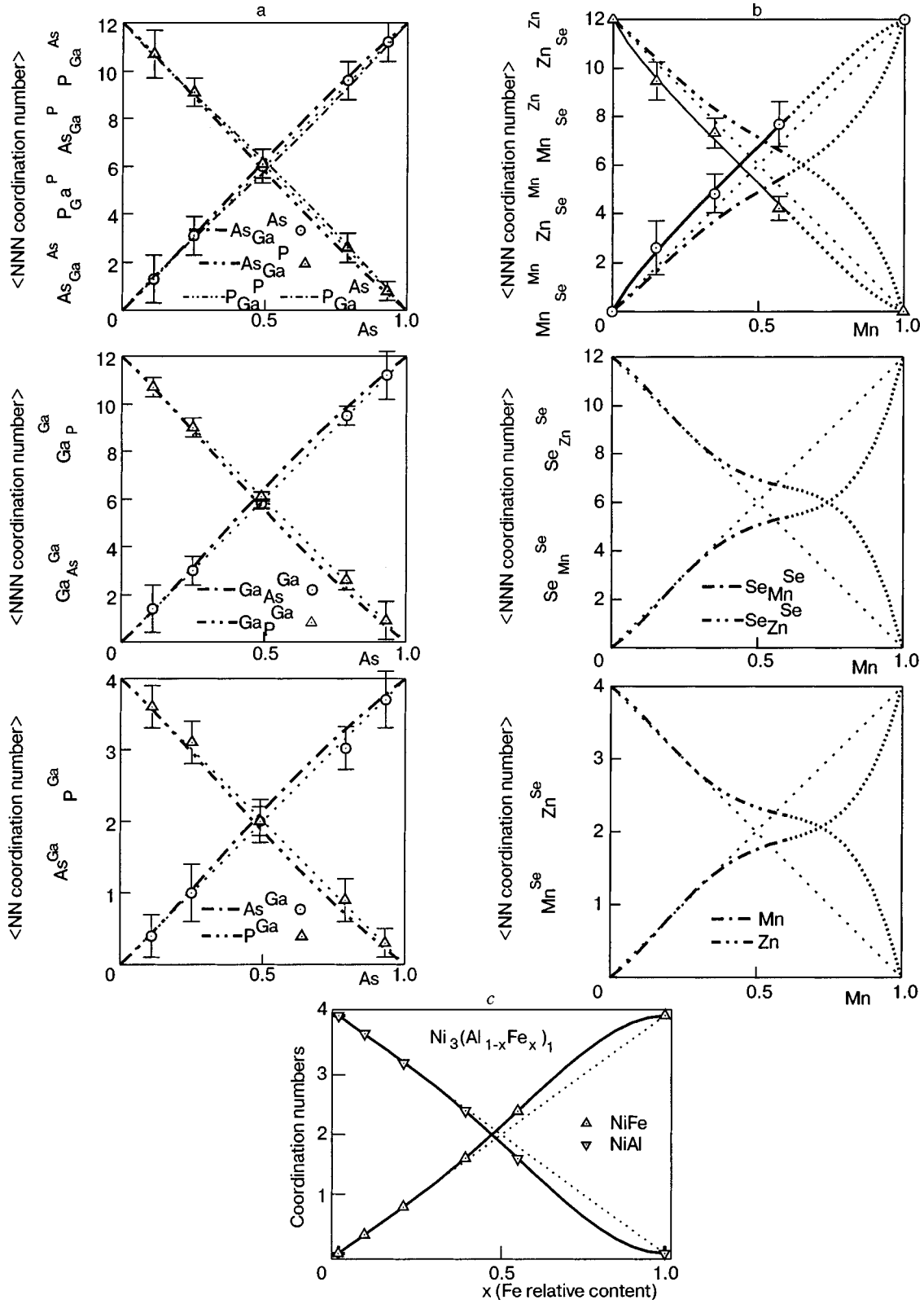

FIG. 3. Average coordination numbers as a function of relative content x: comparison of model best fit curves using SOP values deduced from distance measurements [{0.98,1.07,1.03} $GaAs_xP_{1-x}$ (Ref. 9) (a); {0.62, 1.67, 0} $ZnMn_xSe_{1-x}$ (Ref. 10) (b); {1.01, 0.86, 1.33} $Ni_3(Al_{1-x}Fe_x)_1$ (Ref. 11) (c)] versus independently measured coordination number data.

[see Fig. 2 (36 points with 10 free parameters) and the curves reported in Refs. 9–11].

2. Comparing the ''coordination number'' curve predictions on the basis of SOP values obtained from distance-EXAFS measurement analysis, against independently measured coordination number values (see Fig. 3 and also Refs. 9–11).

3. Checking for a correlation between the thermody-

TABLE IV. Standard molar enthalpies of formation, $\Delta_f H^0$, kJ/mol, of materials and corresponding SOP coefficients. Column (§) gives the origin and comments for reported SOP-coefficient values derived from: *c*—coordination number data, *d*—distance data, 0*—assumed $W_3=0$ value.[10]

Material ABZ/AYZ	components AZ+BZ/AZ+AY	$\Delta_f H^0$, kJ/mol AZ		BZ/AY	SOP W_0	W_1	W_2	W_3	W_4	(§)
ZnMnSe	ZnSe +MnSe	−163.0 [a]	<	−106.7 [b]	1	0.67	1.67	0.04	1	*c*
					1	0.62	1.70	0	1	*d*
GaInAs	GaAs +InAs	−71.0 [a]	<	−58.6 [a,c]	1	0.58	0.25	1.05	1	*d*
GaAsP	GaP +GaAs	−88 [a]	<	−71.0 [a,c]	1	0.93	1.15	1.07	1	*d*
ZnMnS	ZnS +MnS	−206.0 [a], −205.98 [c]	>	−214.2 [a,c], −207.0 [b]	1	1.78	0	0.01	1	*d*
ZnMnTe	ZnTe +MnTe	−92.7 [a,c], −120.5 [b]	<	−94.7 [b]	1	0.25	2.0	0.01	1	*d*
CdMnTe	CdTe +MnTe	−102.5 [b]	<	−94.7 [b]	1	0.68	1.33	0*	1	*d*+0*

namic standard molar enthalpies of formation, $\Delta_f H^0$, kJ/mol, of materials (Table IV)[10] and the corresponding values obtained for the SOP coefficient.

The validity of the model with its restrictive assumptions is thus confirmed.

3. FIR DIELECTRIC FUNCTION $\varepsilon(\omega,x)$ FOR TERNARY ZINC BLENDE ALLOYS

The dielectric function

$$\varepsilon(\omega)=\varepsilon_\infty+\sum_{j=1,n}\{S_j\omega_j^2/[(\omega^2-\omega_j^2)+i\omega\Gamma_j]\}$$

of the phonon spectra of solids can be extracted from experimental reflectivity or transmission coefficients of a crystal, fitting the measured spectra via the Kramers–Kronig (KK) analysis. The KK output $\mathrm{Im}[\varepsilon(\omega)]$ directly yields the maxima for each oscillator line, assumed Lorentzian, with its three parameters $\{\omega_j, \Gamma_j, \text{ and } S_j\}$, respectively, the frequency, the line half-width, and the oscillator strength (OS). Note that while $\{^{iZ}\omega_k\}$ and $^{iZ}\Gamma_k\}$ are prime values, $\{^{iZ}S_k\}$ are sums over all the specific OSs $\{^{iZ}\omega_k\}$ multiplied by the relative ion-pair populations, taking into account ion-pair multiplicities [Eq. (4)], and by three SOP parameters $\{W_1,W_2,W_3\}$, which express the thermodynamics of the alloy considered. The introduction of SOPs links them to the OS of each ternary line. The sum

$$\mathrm{Im}[\varepsilon(\omega,x)]=\sum_{j=1,n}\frac{S_j\omega_j^2\omega\Gamma_j}{(\omega^2-\omega_j^2)^2+\omega^2\Gamma_j^2} \tag{2}$$

describes the total activity of all the oscillators over the frequency range considered. In zinc blende ternary $A_{1-x}B_xZ$ (or AY_yZ_{1-y}) compounds, each vibrating ion dipole pair AZ and BZ from each of the five elementary tetrahedron configurations $\{T_k\}_{k=0,4}$ contributes a phonon line to the spectrum (this idea was first presented by Verleur and Backer,[14] who proposed a pioneering single-parameter model; the limits of the model were later discussed by us in Ref. 15). Thus $\mathrm{Im}[\varepsilon(\omega,x)]$ of the $A_{1-x}B_xZ$ spectra can be written as

$$\begin{aligned}\mathrm{Im}[\varepsilon(\omega,x)]=&\frac{4\,{}^{AZ}s_0\,{}^{AZ}\omega_0^2\,{}^{AZ}\Gamma_0\omega}{(\omega^2-{}^{AZ}\omega_0^2)^2+{}^{AZ}\Gamma_0^2\omega^2}P_0(x) && \text{binary AZ}\\ &+\sum_{k=1,3}\left\{\frac{k\,{}^{BZ}s_k\,{}^{BZ}\omega_k^2\,{}^{BZ}\Gamma_k\omega}{(\omega^2-{}^{BZ}\omega_k^2)^2+{}^{BZ}\Gamma_k^2\omega^2}+\frac{(4-k)\,{}^{AZ}s_k\,{}^{AZ}\omega_k^2\,{}^{AZ}\Gamma_k\omega}{(\omega^2-{}^{AZ}\omega_k^2)^2+{}^{AZ}\Gamma_k^2\omega^2}\right\}P_k(x) && \text{ternary ABZ}\\ &+\frac{4\,{}^{BZ}s_4\,{}^{BZ}\omega_4^2\,{}^{BZ}\Gamma_4\omega}{(\omega^2-{}^{BZ}\omega_4^2)^2+{}^{BZ}\Gamma_4^2\omega^2}P_4(x) && \text{binary BZ}\end{aligned} \tag{3}$$

with the $P_k(x)$'s defined in Eqs. (1).

Thus, the OS $^{iZ}S_k$ of each mode can be expressed by

$$^{BZ}S_k(x)=\,^{BZ}s_k k P_k(x) \quad \text{and}$$

$$^{AZ}S_k(x)=\,^{AZ}s_k(4-k)P_k(x), \tag{4}$$

with the *specific* OS $^{AZ}s_0=\,^{AZ}s$ and $^{BZ}s_4=\,^{BZ}s$ proper to the two binary constituents, and to $\{^{AZ}s_k\}_{k=0,3}$ and $\{^{BZ}s_k\}_{k=1,4}$ of the three ternary configurations.

If all four specific OSs for a given iZ pair are equal and independent of x, i.e.,

$$\{^{BZ}s_k\}_{k=1,4}=\,^{BZ}s \quad \text{and} \quad \{^{AZ}s_k\}_{k=0,3}=\,^{AZ}s$$

for a random distribution of A and B ions, the total OS of the respective modes AZ and BZ of $A_{1-x}B_xZ$ alloys is reduced identically to two linear functions of x,

$$\sum_{k=0,4}^{BZ} S_k(x) = 4x\,{}^{BZ}s \quad \text{and}$$

$$\sum_{k=0,4}^{AZ} S_k(x) = 4(1-x)\,{}^{AZ}s, \tag{5}$$

often referred to as the linear dependence on x.

To treat FIR spectra we make two FIR assumptions.

1. Specific OSs relative to a given ion pair is the same for all configurations,

$$\{{}^{BZ}S_k\}_{k=1,4} = {}^{BZ}s, \quad \{{}^{AZ}S_k\}_{k=0,3} = {}^{AZ}s. \tag{6}$$

2. Analogously, we assume that for each of the two constituent ion pair populations, the linewidths Γ of any given composition spectrum are invariant:

$$\{{}^{AZ}\Gamma_k\}_{k=0,3} = {}^{AZ}\Gamma \quad \text{and} \quad \{{}^{BZ}\Gamma_k\}_{k=1,4} = {}^{BZ}\Gamma. \tag{7}$$

Thus to deconvolve a ternary spectrum with its 8 lines/spectrum, we have *three* SOP coefficients and *two* OS coefficients! As was shown, the true tetrahedron populations in crystal lattices are determined by the alloy composition x (or y for AY_yZ_{1-y} compounds) and the three SOP coefficients $\{W_1, W_2, W_3\}$.

To assess the credibility of the model FIR assumptions, a best-fit test is carried out to "derive" the two binary OS $\{{}^{AZ}s, {}^{BZ}s\}$ values from the $GaAs_yP_{1-y}$ spectra (Fig. 4)[14] that

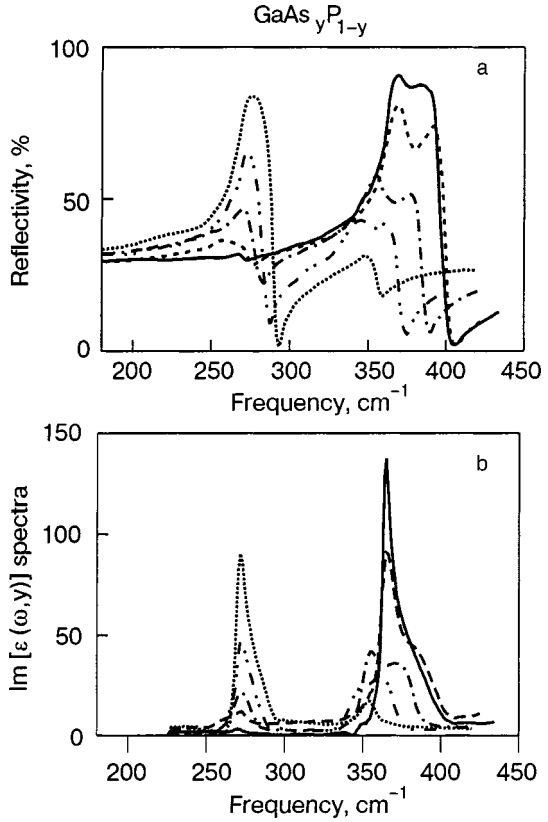

FIG. 4. $GaAs_yP_{1-y}$: reflectivity [%] spectra[14] (a); corresponding normalized Im[$\varepsilon(\omega,y)$] Kramers–Kronig derived spectra (b). Curves: $y=0.01$ (solid), 0.15 (dashed), 0.44 (dash-dotted), 0.72 (dash-dot-dotted), 0.94 (dotted).

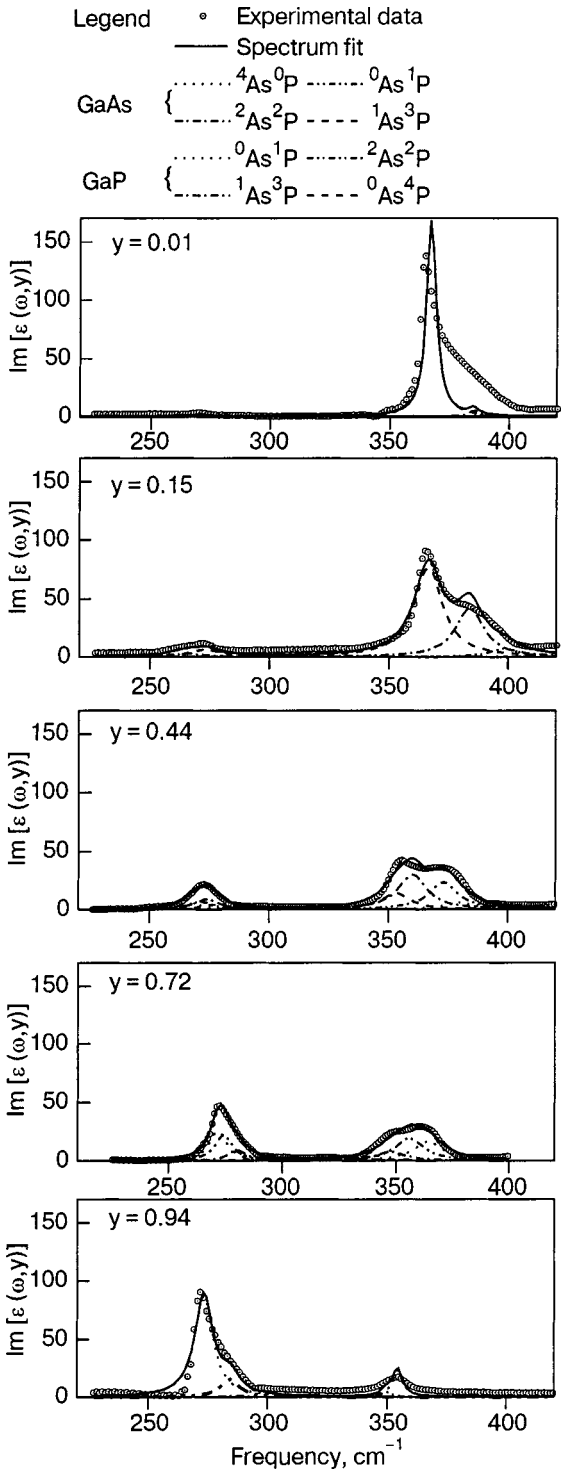

FIG. 5. Model best fit deconvolution of $GaAs_yP_{1-y}$ Im[$\varepsilon(\omega,y)$] spectrum for SOP coefficients $\{W_1=0.98,\ W_2=1.07,\ W_3=1.03\}$. The four line bands of $\{{}^{GaAs}\omega_k\}_{k=1,4}$ and of $\{{}^{GaP}\omega_k\}_{k=0,3}$ are distinctly seen below and above $\omega=300\ \text{cm}^{-1}$, respectively; experimental points (circles), best fit (solid lines), deconvolved lines (various discontinuous lines); the frequencies and intensities obtained are given in Table V.

TABLE V. Individual deconvolution of $GaAs_yP_{1-y}$ spectra for each spectrum parameter $\{^{iGa}\omega_k, ^{iGa}\Gamma_{i=As,P;k=0,4}$ and $\{^{GaAs}s, ^{GaP}s\}$ taken as free. $\{W_1=0.975,\ W_2=1.0715,\ W_3=1.034$, as per Wu *et al.* data$\}$: table of best fit parameter values for the dipoles GaAs $k=1,4$ and GaP $k=0,3$. Amplitudes are given to two decimals.

Phonon dipole configuration ≈		GaAs				GaP			
		$^4As^0P$	$^3As^1P$	$^2As^2P$	$^1As^3P$	$^0As^4P$	$^1As^3P$	$^2As^2P$	$^3As^1P$
		$k=4$	3	2	1	0	1	2	3
	y_{As}								
ω [cm^{-1}]	1%	257.8	261.9	264.3	268.4	363.5	365.5	377.0	379.0
	15%	259.6	261.6	263.6	271.2	362.9	364.9	366.9	381.0
	44%	265.1	269.2	271.2	273.2	350.7	352.7	363.6	373.9
	72%	269.7	271.7	273.7	279.6	342.8	344.8	350.9	360.6
	94%	269.5	271.5	278.5	280.5	345.8	347.8	349.8	351.8
Γ [cm^{-1}]	1%	8.64				4.06			
	15%	10.04				6.58			
	44%	10.74				11.52			
	72%	6.00				9.24			
	94%	3.99				11.50			
A	1%	0.00	0.00	0.00	0.04	1.84	0.05	0.00	0.00
(given	15%	0.02	0.01	0.08	0.17	1.05	0.55	0.09	0.01
to two	44%	0.13	0.21	0.28	0.12	0.26	0.57	0.42	0.11
decimals)	72%	0.52	0.46	0.18	0.02	0.02	0.13	0.31	0.26
	94%	1.63	0.28	0.02	0.00	0.00	0.00	0.03	0.17

have a rich documentation in EXAFS,[13] yielding SOP values.

4. SUMMARY AND CONCLUSIONS

The spectrum of any pure canonical, zinc blende ternary ABZ (or AYZ) material with its 5 tetrahedron configurations $\{T_k\}$ exhibits 8 phonon lines ($4AZ+4BZ$). The number of lines can be less than 8 when in pure defect-free materials extreme preferences prevent the formation of some configuration; this is observed[10,11] with a transient element in B $=\{$Mn, Fe,…$\}$: ZnMnSe lacks one, ZnMnS lacks two; however, GaAlN also lacks one with another nearly evanescent.[16] Thus only 6, 4, 4 intense $+2$ weak phonon lines, respectively. More than 8 lines are observed when point defects occur (antisites, vacancies, etc.), which are responsible for the extra lines (as reported[17] for HgCdTe). Thus FIR admits the detection of defects: vacancies, intersites, antisites, H-loading deformations, quantifying amount of impurity ions.[18]

The *statistical model of the optical dielectric function* is applied to five $GaAs_yP_{1-y}$ (of the type AY_xZ_{1-x}) FIR spectra[14] (see Fig. 4). In spite of the restricted number of parameters, the results show a good fit of the spectra (Fig. 5, Table V); but most importantly, the best-fit values obtained for ^{GaAs}s and ^{GaP}s overlap with published values within the uncertainty bars (Table VI).

Such a satisfactory reproduction validates the model assumptions and gives confidence the model is useful in giving a deeper understanding of the FIR results. Equations, tables and figures taken from our previous publications (as referenced) are documented there in greater detail.

Part of the work was supported by the EU TARI Project contract HPRI-CT-1999-00088.

TABLE VI. Individual deconvolution of $GaAs_yP_{1-y}$ spectra, $\{W_1=0.975,\ W_2=1.0715,\ W_3=1.034\}$: table of best fit values $\{^{GaAs}s_y, ^{GaP}s_y\}$, their average values, and comparison to values in the literature. An asterisk indicates unreliable low-signal values.

y_{As}	GaAs	GaP
1%	*	1.97
15%	2.18	1.98
44%	1.68	2.49
72%	1.58	2.77
94%	2.00	*
All 5 together (global values)	1.75	1.98
Aver. experimental	1.84±0.11	2.24±0.17
Aver. literature	1.815±0.21	2.06±0.16
ratio	0.90±0.14	1.15±0.17

*E-mail: Robouch@lnf.infn.it

[1] P. A. Lee, P. H. Citrin, P. Eisenberger, and B. M. Kincaid, Rev. Mod. Phys. **93**, 769 (1981).
[2] B. K. Teo, *EXAFS: Basic Principles and Data Analysis*, Springer Verlag (1986).
[3] J. C. Mikkelsen and J. B. Boyce, Phys. Rev. B **28**, 7130 (1983).
[4] A. Balzarotti, M. T. Czyzyk, A. Kisiel, N. Motta, M. Podgorny, and M. Zimnal-Starnawska, Phys. Rev. B **30**, 2295 (1984); **31**, 7526 (1985).
[5] A. S. Barker and J. Sievers, Rev. Mod. Phys. **47**, 51 (1975).
[6] D. W. Taylor, in: Dynamical Properties of Solids, vol. **2**, G. H. Horton and A. A. Maradudin (eds.), North-Holland, New York (1975).
[7] D. W Taylor, in *Optical Properties of Mixed Crystals*, R. J. Elliot and I. P. Ipatova (eds.), Elsevier Science Publishers B. V. (1988), p. 35.
[8] Sadao Adachi, *Optical Properties of Crystalline Solids and Amorphous Semiconductors. Materials and Fundamental Principles*, Kluwer Academic Publishers, Boston (1999).
[9] B. V. Robouch, A. Kisiel, and J. Konior, J. Alloys Compd. **339**, 1 (2002).
[10] B. V. Robouch, A. Kisiel, and J. Konior, J. Alloys Compd. **340**, 13 (2002).
[11] B. V. Robouch, E. Burattini, A. Kisiel, A. L. Suvorov, and A. G. Zaluzhnyi, J. Alloys Compd. **359**, 73 (2003).
[12] B. V. Robouch, E. M. Sheregii, and A. Kisiel, Phys. Status Solidi (in print).
[13] Z. Wu, K. Lu, Y. Wang, J. Dong, H. Li, Ch. Li, and Zh. Fang, Phys. Rev. B **48**, 8694 (1993).
[14] H. W. Verleur and A. S. Barker, Phys. Rev. **149**, 715 (1966).

[15] B. V. Robouch, A. Kisiel, and E. M. Sheregii, Phys. Rev. B **64**, 73204 (2001).
[16] B. V. Robouch, A. Kisiel, I. Kutcherenko, and L. K. Vodopyanov, Appl. Phys. Lett. (submitted).
[17] S. P. Kosyrev, L. K. Vodopyanov, and R. Triboulet, Phys. Rev. B **58**, 1374 (1998).
[18] A. Kisiel, B. V. Robouch, E. Burattini, A. Marcelli, M. Piccinini, M. Cestelli Guidi, P. Calvani, A. Nucara, E. M. Sheregii, J. Polit, and J. Cebulski, *Book of Abstracts, 5th International Ural Seminar on Radiation Damage Physics of Metals and Alloys*, Snezhinsk, Russia (2003).

This article was published in English in the original Russian journal. Reproduced here with stylistic changes by AIP.

Wavelet analysis and its application in tunneling and x-ray spectroscopy

M. V. Chukalina* and Yu. V. Dubrovskii

Institute of Problems of Microelectronic Technology and Especially Pure Materials, Russian Academy of Sciences, Chernogolovka, Moscow Region 142432, Russia

H. Funke

European Synchrotron Radiation Facility ESRF, German National Station ROBL, Department of the Institute of Radio Chemistry, Forschungszentrum Rossendorf, Grenobl 38043, France
(Submitted May 25, 2004)
Fiz. Nizk. Temp. **30**, 1235–1243 (November 2004)

The capabilities and limitations of wavelet analysis are demonstrated for the illustrative case of two practial applications: investigation of magneto-tunneling signals and the extended x-ray absorption fine structure (EXAFS) of uranium. A brief introduction to wavelet analysis is given. The term ''window size'' of the mother wavelet function is defined; this concept underlies one of the ideas for a criterion of optimal choice of the mother wavelet function. The capabilities of a software package developed by the authors are demonstrated; this software was used for all the calculations done in the course of this study. © *2004 American Institute of Physics.*
[DOI: 10.1063/1.1820026]

INTRODUCTION

The mathematical processing of the measured signals is an important step for interpreting the results of measurements and explaining the physical processes taking place in the samples under investigation. A new integral transform—the wavelet transform—was developed theoretically in the 1990s and has since come to be used for solving a wide range of scientific problems[1], in particular, for processing oscillating signals.

Here we present original results on two completely different physical phenomena. Common to both is that the use of wavelet analysis for processing experimental data proved to be essential for obtaining new physical results.

First, we investigated tunneling processes in double-barrier AlGaAs/GaAs/AlGaAs heterostructures in a magnetic field perpendicular to the heterolayers in a wide range of energies of the tunneling electrons. As a result of the measurements and the subsequent careful analysis we were able for the first time to detect and identify the two-dimensional magnetopolaron states associated with Landau levels of indices $N>3$ and on up to $N=7$.

Second, as a result of extended x-ray absorption fine structure (EXAFS) studies of uranium (IV) we succeeded for the first time in characterizing the atomic structure of its complexes with the carboxyl groups of acetic, formic, and glycolic acids. The problem of indentifying the scattering centers found in one coordination sphere has been solved only with the use of the wavelet transform, which has the property of locality in both real space and reciprocal space.

This paper is organized as follows. In the first Section we present the basic concepts of wavelet analysis. In the the second Section we describe the investigation of the magneto-tunneling spectra for purposes of studying the interaction of electrons with longitudinal optical phonons in polaron semiconductors, where the formation of magnetopolaron states can occur. Next the results of studies of the x-ray absorption spectra of uranium (IV) are presented. In the final Section of the paper we discuss topics connected with the properties of the wavelet transform itself.

A BRIEF INTRODUCTION TO WAVELET ANALYSIS

If a function $f(t)$ is considered as an analog signal with a finite energy defined by the norm

$$\|f\|_2=\left[\int_{-\infty}^{\infty} f(t)^2 dt\right]^{1/2},$$

then the Fourier transform

$$\hat{f}(\omega)=\int_{-\infty}^{+\infty} f(t)\exp(i\omega t)dt \tag{1}$$

of the function is the spectrum of that signal. Here ω is the frequency, t is a measurable quantity (the time, voltage, etc.). However, formula (1) is inconvenient for a certain class of signals, since it does not reflect the dynamics of the frequencies of the spectrum in time. Figure 1 shows a signal containing three frequency components, 1, 2, and 3 Hz, on a given time interval. Figure 2 shows the modulus of its Fourier transform, which has only two maxima, inadequately reflecting the reality of the situation. If instead of using infinite waves ($\sin \omega t$, $\cos \omega t$) as the kernel of the integral equation (1) one uses waves having the property of locality, e.g., $\sin \omega t \exp(-(t^2/2\sigma))$, where σ is some parameter, then it should be possible to analyze signals whose frequency components are unstable in time. Such a method was proposed by Gabor in 1946. However, the window size by which the wave is bounded remains constant for all wavelengths generalized in the signal, and that is not very convenient, because for different wavelengths a different number of periods fall within the window. One would like to have a flexible frequency–time window that would automatically contract in the neighborhood of high-frequency centers and expand

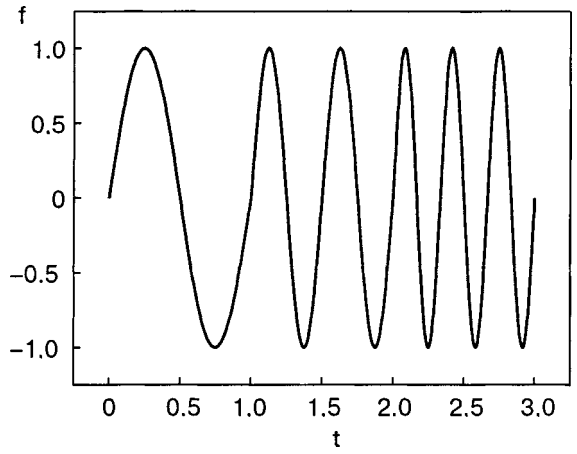

FIG. 1. An example of a signal containing three frequency components, 1, 2, and 3 Hz, which are unstable in time.

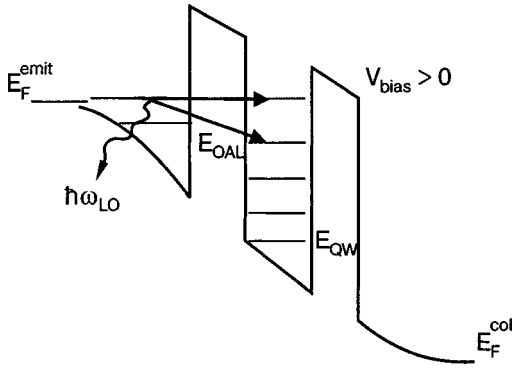

FIG. 3. Diagram illustrating the tunneling process, when electrons in a two-dimensional emitter occupy only one ground Landau level. The first is elastic tunneling to the Landau levels in the quantum well with conservation of energy. The second is inelastic tunneling with the emission of optical phonons.

around low-frequency centers. A transform that has the ability to contract and expand in this way is the integral wavelet transform:[1]

$$W_f^{\psi}(a,b)=\frac{1}{\sqrt{a}}\int_{-\infty}^{\infty} f(t)\,\psi^*\left(\frac{t-b}{a}\right)dt, \tag{2}$$

where a is the scaling parameter, b is the translaiton parameter, ψ is the basis wavelet function, and the asterisk * denotes the complex conjugate. We note that $\psi((t-b)/a)$ is obtained from a single wavelet function $\psi(t)$ as a result of its translation by b and scaling by a factor of a. In practice the function ψ can be used as the basis wavelet only if there exists an inverse transformation:

$$f(t)=\frac{1}{C_{\psi}}\int_{-\infty}^{\infty}\int_{-\infty}^{\infty} W_f^{\psi}(a,b)\,\frac{1}{a^2}\,\psi\left(\frac{t-b}{a}\right)dadb. \tag{3}$$

Here

$$C_{\psi}=\int_{-\infty}^{\infty}\frac{|\hat{\psi}(\omega)|^2}{|\omega|}d\omega.$$

It follows that the function $\hat{\psi}(\omega)$ [the Fourier transform of the function $\psi(t)$] goes to zero at the coordinate origin, or, in other words

$$\int_{-\infty}^{\infty}\psi(t)dt=0.$$

This is the so-called admissibility condition. We note that the same kernel, to within complex conjugation, is used for the integral transformations (2) and (3).

Thus the result of the wavelet transform is a frequency–time spectrum of the signal, the analysis of which in some cases helps one find a solution to a problem. Examples of two such problems are discussed below.

USING THE WAVELET TRANSFORM FOR ANALYSIS OF MAGNETO-TUNNELING SPECTRA

In polaron semiconductors such as GaAs, electrons can efficiently interact with longitudinal optical (LO) phonons to form polarons, i.e., the ''original'' (in neglect of the interaction with phonons) electronic states become renormalized. In a magnetic field perpendicular to the plane of a quantum well (QW), the two-dimensional (2D) continuous electronic states split into discrete Landau levels (LLs) with index N. Here the interaction of the electrons with optical phonons becomes particularly efficient when the condition $n\hbar\omega_{LO}=m\hbar\omega_c$ is met. Here n and m are integers, $\hbar\omega_{LO}$ is the energy of a longitudinal optical phonon, and $\hbar\omega_c$ is the cyclotron energy, equal to the distance between discrete Landau levels. In this case one speaks of the appearance of magnetopolaron states.

Tunneling spectroscopy enables one to determine the electron density of states in the QW. As is shown in Fig. 3, at a sufficiently high magnetic field, when the electrons in the 2D emitter occupy only the one ground Landau level, two tunneling processes can occur: elastic tunneling to the Landau levels in the quantum well, with conservation of energy, and inelastic tunneling, with the emission of optical phonons. From the position of the peaks of the tunneling current as a function of voltage (which is linearly related to the energy of the electronic states in the quantum well) and magnetic field (Fig. 4), one can recover the energy spectrum of the electronic states in the quantum well. Figure 4 shows the so-called fan diagram that would be obtained in the absence of electron–phonon coupling. It reflects the superposition of two unperturbed spectra of electronic states shifted by the energy of the optical phonon. However, as we have said,

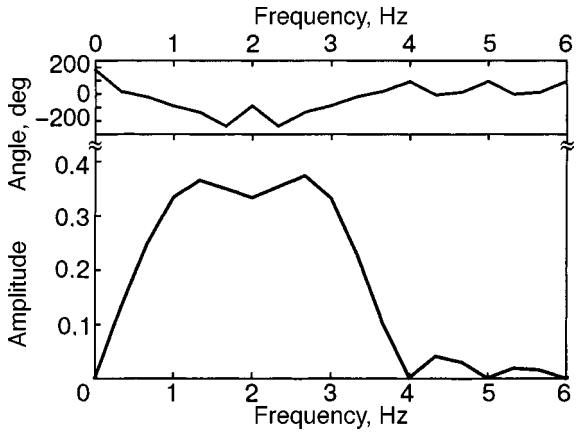

FIG. 2. Model transform of the Fourier signal shown in Fig. 1.

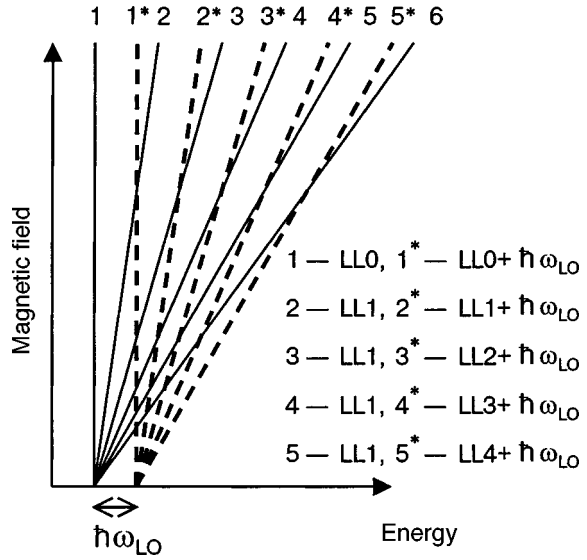

FIG. 4. Fan diagram in the absence of electron–phonon coupling.

under the condition $n\hbar\omega_{LO}=m\hbar\omega_c$ a strong renormalization of the electron spectrum occurs, right where the lines intersect on the fan diagram. In the intersection regions one should observe anticrossing. Typical signs of this phenomenon are exchanges of intensities and frequencies of the oscillations. In an experiment one measures the dependence of the tunneling current on magnetic field at constant voltage, i.e., the density of states in the well is scanned at a fixed energy. By measuring the magneto-tunneling spectra at different bias voltages one can reconstruct the total picture of the electronic states in the entire range of magnetic fields. A typical magneto-tunneling spectrum obtained at a constant bias voltage of 230 mV is presented in Fig. 5. The spectrum has peaks which are periodic in the inverse magnetic field and correspond to the two different oscillations (Fig. 6). To recover the spectrum of electronic states it is necessary to identify each peak and associate it to an elastic tunneling process to Landau levels in the quantum well or to inelastic tunneling with the emission of an optical phonon. Figure 7 shows the results of a calculation of the wavelet transform for bias voltages of 162, 175, and 187 mV. The result of the calculation of the wavelet transform is a frequency–time

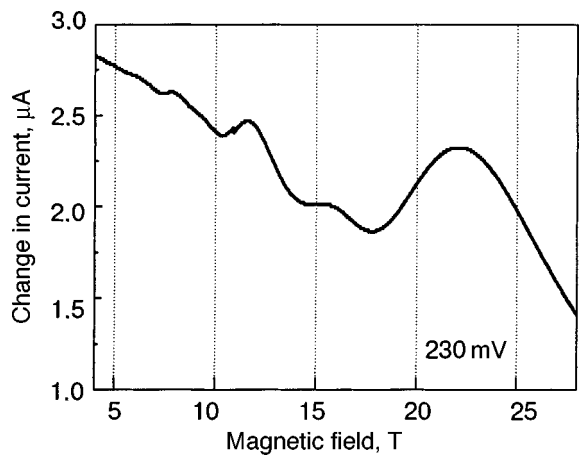

FIG. 5. Typical magneto-tunneling spectrum obtained at a constant bias voltage of 230 mV.

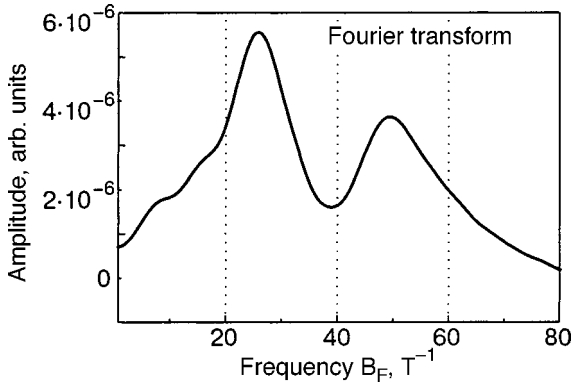

FIG. 6. Fourier transform (model) of the signal shown in Fig. 5.

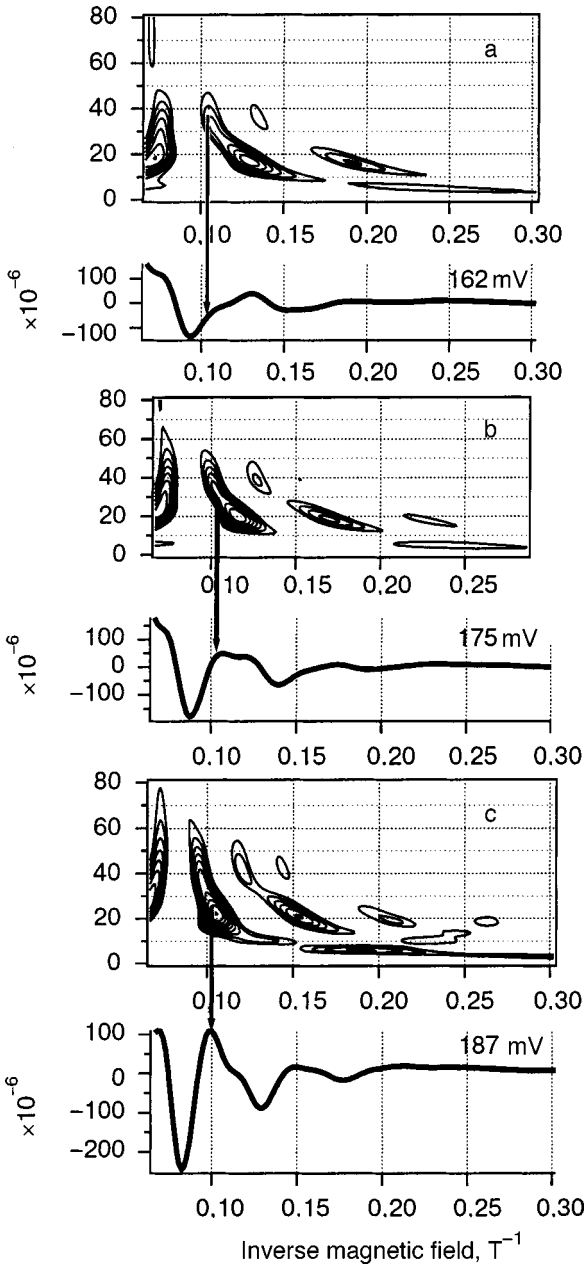

FIG. 7. A set of signals and their wavelet transforms. Illustration of the dynamics of the frequency components of the local maximum found in the region of 0.1 T^{-1}.

map of the signal. The signal and its wavelet transform are placed one above the other, and the X axis in both cases is the inverse magnetic field. The Y axis in the frequency–time map corresponds to the frequency axis of the Fourier transform. Equal-level lines are drawn on the map according to the results of the calculation of the wavelet transform. Analysis of the frequency–time map of the signal enables one to draw a conclusion as to the nature of each oscillation of the signal, i.e., to determine the spectral composition of each oscillation individually. The arrows mark the dynamics of the behavior of the frequency components of the local maximum of the signal found in the 0.1 T^{-1} region. It is seen that along with the exchange of intensities an exchange of frequencies also occurs.

As a result of such an analysis we succeeded in identifying for the first time the magnetopolaron states associated with Landau levels up to $N=7$. A more detailed exposition of the physical properties of the investigated magnetopolaron states can be found in Ref. 2.

WAVELET ANALYSIS OF THE EXAFS SPECTRA

The traditional first step in the interpretation of the EXAFS spectra is to use a Fourier transformation. The idea of using that method of analysis was first proposed and examined in detail in the papers by Stern, Lytle, and Sayers,[3–6] where a model function describing the oscillations of the absorption coefficient of the central absorbing atom as a function of the energy of the exciting x rays was constructed. This function has the form

$$\chi(k)=S_0^2(k)\sum_{i=1}^{n}\frac{N_i}{R_i^2}\frac{F_i(k)}{k}\exp\left(-\frac{2R_i}{\lambda}\right)\times\exp(-2\sigma_i^2k^2)\sin(2kR_i+\Psi). \quad (4)$$

Here χ is the measured spectrum normalized to the atomic absorption, k is the electron wave vector, S is the amplitude attenuation factor, n is the number of coordination spheres, N_i is the number of atoms in the ith coordination sphere, R_i is the average radius of the ith coordination sphere, and F_i is the backscattering amplitude. The factor $\exp(-2R_i/\lambda)$ describes the inelastic scattering of a photoelectron by the environment of the absorbing atom in traversing a distance $2R_i$; λ is the electron mean free path, and Ψ is the total phase shift at the central and scattering atoms. The factor $\exp(-2\sigma_i^2k^2)$ is introduced in view of the necessary of taking thermal vibrations of the scattering atoms into account. If the phase shift is neglected, then the calculation of the Fourier transform enables one to determine the number of nearest coordination spheres and their radii. The values of the backscattering amplitude, total phase shift, and mean free path are taken from a table in Ref. 7. For determination of the exact values of the radii of the coordination spheres, the number of atoms in the coordination spheres, and the factor σ, a fitting procedure is used. Great difficulties in interpreting the spectra arise in the case when the coordination sphere contains different types of atoms, i.e., when scattering processes on different types of atoms are superposed in one peak of the Fourier transform.

It was precisely for such cases that it was proposed several years ago[8] to use the wavelet transform together with the Fourier transform. The idea is based on the fact that the function that describes the amplitude of the backscattering of atoms of a given type has a local maximum in energy (wavevector) space (Fig. 8a). The position of the maxima depends on the type of atoms, i.e., if we consider not the frequency spectrum but the frequency–time spectrum of the measured signal, then we can separate the contributions from the different types of atoms if there is more than one kind of atom in a given coordination sphere.

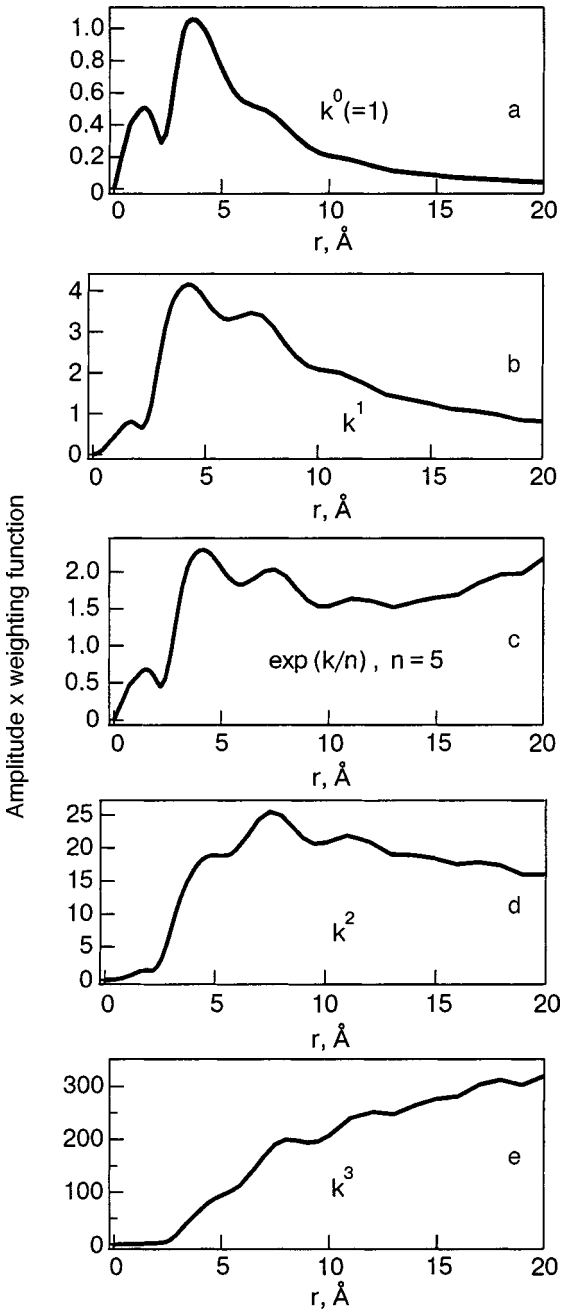

FIG. 8. Example of a function describing the backscattering amplitude for phosphorus (a). The results of multiplying the amplitude by various weighting functions of k (b–e).

Let us explain this idea in more detail using as an example the following experiment, which was done on the ROBL beamline of the European Synchrotron Radiation Facility in Grenoble, France. For measurement of the EXAFS spectra at room temperature we prepared three solutions

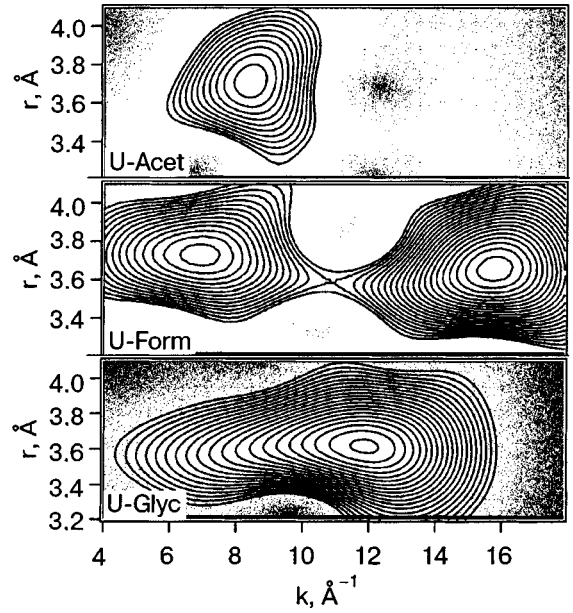

FIG. 9. Fragments of the frequency–time maps for different samples. U-Acet—sample No. 1, U-Form—sample No. 2, U-Glyc—sample No. 3.

of the following composition. Sample No. 1, based on acetic acid: [U(VI)]=0.025 mole/liter, [acetic acid] =0.5 mole/liter, pH=4.5. Sample No. 2, based on formic acid: [U(VI)]=0.053 mole/liter, [formic acid] =1.0 mole/liter, pH=4.5. Sample No. 3, based on glycolic acid: [U(VI)]=0.02 mole/liter, [glycolic acid] =0.25 mole/liter, pH=8. The EXAFS spectrum was measured at the energy of the U L_{III} edge. The spectra were processed in accordance with the standard processing procedure using the software packages EXAFSPAK[9] and FEFF8.[10] The following results were obtained: for sample No. 2 a broad peak was observed in the region r =3.1–4.0 Å in Fourier space; this peak could not be interpreted uniquely with the use of the fitting procedure. To refine the interpretation of the local maximum in Fourier space for the given sample we calculated the wavelet transform for all three samples. Figure 9 shows the parts of the frequency–time maps for all three samples in the range 3.2–4.1 Å (U-Acet—sample No. 1, U-Form—sample No. 2, U-Glyc—sample No. 3). The spectrum of sample No. 1 is dominated by multiple scattering on the carbon atoms, while the spectrum of sample No. 3 reveals the pure U–U scattering.[11] The result of the wavelet transform of sample No. 2 shows two distinct, separate maxima, i.e., two scattering events on a light element and a heavy element at approximately the same distance ($\Delta r=0.1$ Å). Both types of scattering are registered—multiple scattering on carbon and U–U scattering. From the results of the wavelet analysis we can say that the two structure elements U–O_{ax}–U and U–O_{eq}–C are both present and that the formation of multinuclear complexes does occur.[11]

In closing we would like to call attention to the choice of weighting functions. By virtue of the fact that the amplitude of the vibrations falls off rapidly from the beginning to the end of the spectrum, it is common practice to multiply by an additional weighting factor before calculating the spectrum.

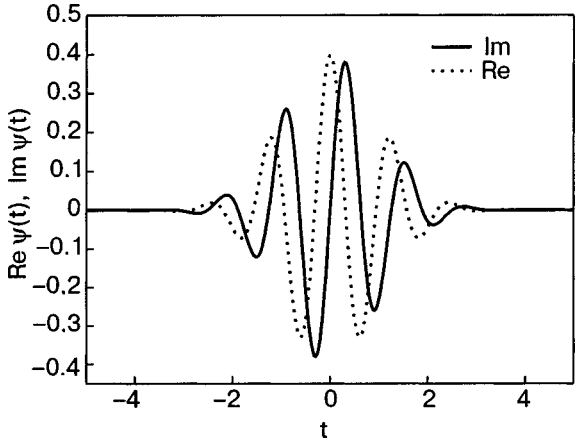

FIG. 10. Real and imaginary parts of the Morlet function (5). The values of the parameters are $\eta=5$ and $\sigma=1$.

As a rule, this is a function of the form k^3. Turning back to Fig. 8, which shows the result of multiplicatoin of the function describing the backscattering amplitude by various weighting functions. After multiplication by k^2 the maximum is shifted from 4 Å to 7 Å, and after multiplication by k^3 the pattern is fundamentally altered. This means that if atoms of phosphorus and of a heavier element having a local maximum of its backscattering amplitude lying 4 Å to the right are located in one of the coordination spheres of the sample, the frequency–time map of the signal when weighted by a function k^3 will no longer show two features. For this reason the choice of the weighting function must be done correctly. One must check that the properties of locality of the function describing the backscattering amplitude are preserved.

SOME PROPERTIES OF THE WAVELET TRANSFORM WITH THE USE OF THE MORLET FUNCTION

In both of the problems elaborated above the wavelet function used was the Morlet function, which has the form

$$\psi(t)=\frac{1}{\sqrt{2\pi}\sigma}\left[\exp(i\eta t)-\exp\left(-\frac{\eta^2}{2}\right)\right]\exp\left(-\frac{t^2}{2\sigma^2}\right). \tag{5}$$

The parameter η specifies the number of oscillations under the Gaussian envelope in the case when $\sigma=1$. The introduction of the constant $-\exp(-\eta^2/2)$ guarantees that the admissibility condition will be satisfied. Figure 10 shows the real and imaginary parts of the Morlet function for $\eta=5$ and σ =1. The main criterion for choosing the mother wavelet function (as the wavelet function is still called) is that the functional dependence of the frequency components appearing in the signal be close to the form of the chosen wavelet function.

We begin our discussion of the resolution properties for the wavelet transform with the determination of the window size of the wavelet function. Suppose that the function $\psi(t)$ and its Fourier transform $\hat{\psi}(\omega)$ are rather rapidly damped, i.e., that they are window functions.[1] The center of the window for any function ψ from $L^2(R)$ is defined as

$$t^*=\frac{1}{\|\psi\|_2^2}\int_{-\infty}^{\infty} t|\psi(t)|^2 dt$$

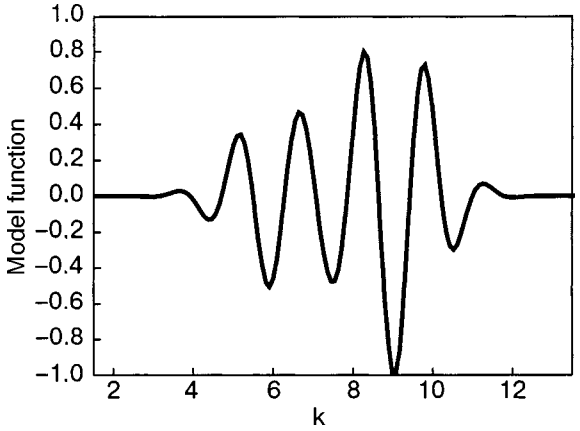

FIG. 11. Model function calculated according to formula (8).

and the radius of the window is defined as

$$\Delta_\psi = \frac{1}{\|\psi\|_2}\left\{\int_{-\infty}^{\infty}(t-t^*)\left|\psi(t)\right|^2 dt\right\}^{1/2}.$$

Thus the integral wavelet transform of the analog signal (2) localizes it in a time window $[b+at^*-a\Delta_\psi, b+at^*+a\Delta_\psi]$ having its center at $b+at^*$ and a width of $2a\Delta_\psi$. In signal analysis this is called time localization. The frequency window is specified by the formula

$$\left[\frac{\omega^*}{a}-\frac{1}{a}\Delta_{\hat\psi}, \frac{\omega^*}{a}+\frac{1}{a}\Delta_{\hat\psi}\right].$$

The center of the window is located at the point ω^*/a and the width of the window is $2\Delta_{\hat\psi}/a$. A detailed analysis and derivation of the formulas are given in Chui's book.[1]

The size of the frequency–time window we have introduced,

$$[b+at^*-a\Delta_\psi, b+at^*+a\Delta_\psi] \times\left[\frac{\psi^*}{a}-\frac{1}{a}\Delta_{\hat\psi}, \frac{\omega^*}{a}+\frac{1}{a}\Delta_{\hat\psi}\right] \quad (6)$$

varies depending on the position of its center in frequency–time space. The window narrows at high-frequency centers and expands at low-frequency centers. All the while the area of the frequency–time window remains constant, equal to $4\Delta_\psi\Delta_{\hat\psi}$.

The size of the frequency–time window for the Morlet wavelet in our calculations is

$$\left[t-\frac{\eta\sigma}{\sqrt{2}\omega}, t+\frac{\eta\sigma}{\sqrt{2}\omega}\right]\times\left[\omega-\frac{\omega}{\sqrt{2}\eta\sigma}, \omega+\frac{\omega}{\sqrt{2}\eta\sigma}\right]. \quad (7)$$

Let us illustrate the use of the above formula for analysis of the resolution. The model calculations were carried out in the course of solving the problem of interpretation of the EXAFS spectra, and for that reason the axis of measurement is the axis of wave vectors k and the frequency axis is the axis of interatomic distances r.

Figure 11 shows the model function

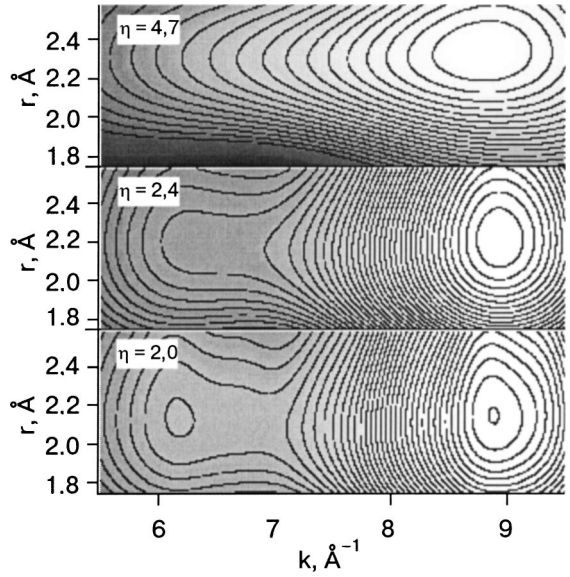

FIG. 12. Result of a calculation of the wavelet transform of the model function shown in Fig. 11. Illustration of the criterion for choosing the parameter of the Morlet function in accordance with the size of the frequency–time window.

$$f(k) = 0.5\sin(2rk+\delta_1)\exp\left(-\frac{(k-C_1)^2}{2}\right)+\sin(2rk+\delta_2)\exp\left(-\frac{(k-C_2)^2}{2}\right). \quad (8)$$

The transition from the variables of formula (7) to the variables used in formula (8) is simple: $t\Rightarrow k$; $\omega\Rightarrow 2r$. The following parameter values were used in the modeling: $r=2.1$ Å, $\delta_1=\delta_2=0$, $C_1=6$, $C_2=9$. The result of the calculation of the wavelet transform for different values of the Morlet wavelet parameter ($\eta=4.7$, 2.4, and 2.0) is presented in Fig. 12. The calculation shows that the two centers of localization of the wave processes cannot be resolved if the lateral size of the frequency–time window is larger than the distance between centers of localization. In the given example the distance ΔC between localization centers is equal to 3. In accordance with formula (7), for the parameter value $\eta=4.7$ the lateral size of the frequency–time window is equal to 3.35. The maxima cannot be resolved if the distance between them is less than the lateral size of the frequency–time window. According to formula (7), the lateral size of the window is determined by the position of the center of the window in frequency–time space and the parameters of the Morlet wavelet function. By decreasing the parameter η we arrive at the situation where the distance between localization centers becomes larger than the lateral size of the frequency—time window, and the maxima on the frequency–time map become resolved.

CONCLUSION

We have carried out a detailed study of magnetotunneling processes in double-barrier AlGaAs/GaAsAlGaAs heterostructures. We have for the first time identified the two-dimensional magnetopolaron states associated with the Landau levels with indices $N>3$ up to $N=7$. In addition, with the aid of EXAFS spectroscopy we have for the first

time characterized the atomic environment of uranium (IV) in complexes formed with the carboxyl groups of acetic, formic, and glycolic acids. Both problems could be solved only thanks to the application of the wavelet transform, which has the property of locality in both real space and reciprocal space. The calculations were done using a software package developed by the present authors and which is available on the Internet.[12] For those who have found this method of analysis useful for signal processing, we would recommend that they also become acquainted with Ref. 13.

This study was done with the financial support of the Russian foundation for Basic Research; M. Chukalina also obtained partial support from the Forschungszentrum Rossendorf, Germany.

*E-mail: chukalinamarina@mail.ru

[1] C. K. Chui, *Introduction to Wavelets*, Academic Press, San Diego (1992), Mir, Moscow (2001).

[2] M. V. Chukalina, Yu. V. Dubrovskii, V. A. Volkov, L. Eaves, D. Yu. Ivanov, E. E. Vdovin, J.-C. Portal, D. K. Maude, M. Henini, and G. Hill, *Proceedings of the Conference "Nanostructures: Physics and Technology"* (2003), p. 183.

[3] D. E. Sayers and E. A. Stern, Phys. Rev. Lett. **27**, 1204 (1971).

[4] E. A. Stern, Phys. Rev. B **10**, 3027 (1974).

[5] E. A. Stern, D. E. Sayers, and F. W. Lytle, Phys. Rev. B **10**, 4836 (1975).

[6] F. W. Lytle, D. E. Sayers, and E. A. Stern, Phys. Rev. B **11**, 4825 (1975).

[7] B. K. Teo, *EXAFS: Basic Principles and Data Analysis*, Springer, Berlin, Heidelberg, New York, Tokyo (1986).

[8] H. Funke and M. Chukalina, Reports No. 343, Forschungszentrum Rossendorf (2002), p. 45.

[9] G. N. George and I. J. Pickering, Stanford Synchrotron Radiation Laboratory (1995).

[10] L. Ankudinov, B. Ravel, J. J. Rehr, and S. D. Conradson, Phys. Rev. B **58**, 7565 (1998).

[11] A. Rossberg, Ph. D. Thesis, Technical University Dresden (2002).

[12] www.esrf.fr/exp_facilities/BM20/BM20_RCH_e/software/wavelet.html

[13] I. M. Dremin, O. V. Ivanov, and V. A. Nechitaĭlo, Usp. Fiz. Nauk **171**, 465 (2001).

Translated by Steve Torstveit